Microfluidic Approaches for the Study of Yeast Chemotropism, Hypoxia, and Mouse Embryonic Development.

BY

MARIE-ELENA BRETT
B.S., University of New Hampshire, 1998

THESIS

Submitted as partial fulfillment of the requirements for the
degree of Doctor of Philosophy in Bioengineering
in the Graduate College of the
University of Illinois at Chicago, 2013

Chicago, Illinois

Defense Committee:

David T. Eddington, Chair and Advisor
Michael Cho
Jun Cheng
David E. Stone, Biological Sciences
Bradley Merrill, Biochemistry and Molecular Genetics

Acknowledgements

I would like to expressly thank my husband Kyle for allowing me the luxury of returning to school. Many thanks to my family, especially my mom Marie, who supported me every step of the way. The many mentors I have been lucky to work with and for, including Dr. David Eddington, Dr. David Stone, and Dr. Brad Merrill and all my amazing labmates who I have had the pleasure of sharing my life and my work with over the last four years.

Abstract

Microfluidic techniques have become a valuable tool to study individual cells as well as whole tissues. Biological problems can be can be elucidated in the micro-scale to attain fast and high throughput data collection. There are many methods to create micro-scale devices most of these methods employ some form of soft photolithography. Soft photolithography is a technique in which a master, silicon, is spin coated with a photoresist. A pattern is resolved by exposing the resist to ultraviolet light through a high density transparency containing the desired structure of the microfluidic device or stamp [1]. The master is then used to replica mold the desired device or stamp in polydimethylsiloxane (PDMS) [2-4]. Devices fabricated through soft photolithography allow for spatial and temporal control of environmental conditions as well as the alteration of surface chemistry for specific applications [4, 5]. These techniques can be utilized to create devices that accomplish everything from patterning proteins and cells [6] to creating complex bioreactors [7, 8]. Here, the techniques are employed to fabricate a manually actuated on-chip valve; develop a 6 well hypoxic insert that can be used to subject veins to hypoxic conditions; and study chemotropism in the yeast cell line *Saccharomyces cerevisiae* through the creation of a rotating gradient device for *in vitro* study of single cell as well as microposition cells through patterning to study *in vivo* mating mixtures. These techniques are also employed to create a microfluidic device to culture mouse embryos ex vivo, with the ultimate goal of studying how chemical and mechanical factors affect development. To reach these goals novel microfluidic devices have been designed, fabricated, and validated to control flow within microfluidic channels

with a small footprint valve; induce hypoxia in saphenous veins; systematically induce chemotropism in yeast for quantitative analysis; and to culture mouse embryos *ex vivo*. While these are distinct applications, the common theme is developing novel microfluidic tools to allow new experimental possibilities.

Summary

Microfluidic techniques have become a valuable tool to study individual cells as well as whole tissues. Biological problems can be can be elucidated in the micro-scale to attain fast and high throughput data collection. There are many methods to create micro-scale devices most of these methods employ some form of soft photolithography. Soft photolithography is a technique in which a master, silicon, is spin coated with a photoresist. A pattern is resolved by exposing the resist to ultraviolet light through a high density transparency containing the desired structure of the microfluidic device or stamp [1]. The master is then used to replica mold the desired device or stamp in polydimethylsiloxane (PDMS) [2-4] Devices fabricated through soft photolithography allow for spatial and temporal control of environmental conditions as well as the alteration of surface chemistry for specific applications [4, 5] These techniques can be utilized to create devices that accomplish everything from patterning proteins and cells [6] to creating complex bioreactors [7, 8] Here, the techniques are employed to fabricate a manually actuated on-chip valve; develop a 6 well hypoxic insert that can be used to subject veins to hypoxic conditions; and study chemotropism in the yeast cell line *Saccharomyces cerevisiae* through the creation of a rotating gradient device for *in vitro* study of single cell as well as microposition cells through patterning to study *in vivo* mating mixtures. These techniques are also employed to create a microfluidic device to culture mouse embryos *ex vivo*, with the ultimate goal of studying how chemical and mechanical factors affect development. To reach these goals novel microfluidic devices have been designed, fabricated, and validated to control flow within microfluidic channels with a small footprint valve; induce hypoxia in saphenous veins; systematically induce chemotropism in yeast for

quantitative analysis; and to culture mouse embryos *ex vivo*. Ultimately, the priority of this research is to control flow in a microfluidic device with a small footprint on-chip valve; determine if hypoxia in saphenous veins is linked to vasoocclusion and constriction; further elucidate the chemotropic pathway in yeast; as well as define factors that affect development in mouse embryos. While these are distinct applications, the common theme is developing novel microfluidic tools to allow new experimental possibilities.

There is a need for a simple method to control fluid flow within microfluidic channels. To meet this need, soft photolithography was used to create a simple push pin with a polydimethylsiloxane (PDMS) tip. This valve was integrated into microfluidic networks to obstruct flow. This novel valve design can attain on/off control of fluid flow without an external power source using readily-available, low-cost materials. The valve consists of a 14 gauge (1.6mm) one inch piece of metal tubing with a PDMS pad at the tip to achieve a fluidic seal when pressed against a microfluidic channel's substrate. The metal tubing or pin is then either manually pushed down to block or pulled up to allow fluid flow. The valve was validated using a pressure transducer and fluorescent dye to determine the breakthrough pressure the valve can withstand over multiple cycles. In the first cycle, the median value for pressure withstood by the valve was 8.8 psi with a range of 17.5 - 2.7 psi. The pressure the valves were able to withstand during each successive trial was lower suggesting they may be most valuable as a method to control the initial introduction of fluids into a microfluidic device. These valves can achieve flow regulation within microfluidic devices, have a small dead volume, and are simple to fabricate and use, making this technique widely suitable for a range of applications.

Microfluidic approaches for the study of yeast chemotropism, vein hypoxia, and embryonic development.

Microfluidic techniques are suitable to many applications. As in the previous example, where soft photolithography was used to find a unique solution to fluid flow in microfluidic channels, here soft photolithography was used to create a six well insert for a standard culture dish that can exert spatial and temporal control of the oxygen concentration within a 3 mm high region. This insert can be used to induce hypoxic conditions on vein sections. Saphenous veins are commonly used in coronary artery bypass surgery (CABG) [9]. Unfortunately, many of the grafts fail due to vasoocclusion or constriction. Hypoxia is thought to be the cause of many of these negative outcomes. In chapter two, a 6 well hypoxic insert was fabricated and tested to determine if this device could be used to create a hypoxic environment in which to study saphenous vein hypoxia. The data garnered through the fabrication and testing of the 6 well hypoxic insert indicated that the device could be easily calibrated to determine the amount of oxygen present in the bottom of a 6 well plate. Upon calibration, the device established a desired concentration of oxygen, ranging from 0-21%, and these concentrations could be maintained over time.

In the two previous examples, soft photolithography was used to create platforms that exert control over the flow of gas or liquid. This microfluidic technique can also be employed to establish varying microenvironments within the same culture area. In chapter three, soft photolithography, along with several other microfluidic techniques, was employed to fabricate novel microfluidic device to establish a rotating chemical gradient. This gradient was utilized to study the yeast chemotropic pathway.

Microfluidic approaches for the study of yeast chemotropism, vein hypoxia, and embryonic development.

Haploid budding yeast exposed to mating pheromone produced by cells of the opposite mating type stop dividing and polarize their growth, thereby forming a mating projection, or “shmoo.” Cells treated with pheromone under isotropic conditions form mating projections adjacent to their last bud site. This is called default shmooing. In contrast, mating cells interpret complex pheromone gradients and polarize their growth in the direction of the closest partner [10, 11]. This is called chemotropism, the directed growth of a cell in response to a chemical gradient. Chemotropism plays an important role in a broad range of biological phenomena, including metazoan development [12], pollen tube formation [13], and fungal infection. A well characterized example of chemotropism in mammals is axon growth cone guidance, which is essential for formation of the proper neuronal connections during brain development [14]. It is notable that growing axons follow complex pathways as they track morphogenic gradients en route to their intended targets.

The yeast chemotropic response can be induced *in vitro*, as well as in mating mixtures. The first demonstration of yeast chemotropism in an artificially generated pheromone gradient was reported by Segall [15], who dispensed a continuous source of pheromone from a moving pipet. Unfortunately, the shape of the gradient cannot be controlled using this method and only cells closest to the pipet tip grew toward it [15, 16]. Nevertheless, both orientation and reorientation were observed in this experiment. One other study of yeast chemotropism using Segall’s apparatus was published [16], but due to the experimental difficulty of this method, our understanding of yeast gradient tracking has largely been left at the phenomenological level since its discovery in 1993.

Microfluidic approaches for the study of yeast chemotropism, vein hypoxia, and embryonic development.

Recently, several groups have applied the precise microscale control afforded by microfluidic devices to study yeast chemotropism [17-20]. However, most of these experiments were limited to stimulation from a single direction. In the exceptional cases, the gradient direction was rotated a full 180° by reversing the inputs of medium with and without pheromone. Here, microfluidic techniques were employed to design, fabricate, and characterize a microfluidic device that creates and rotates a chemical gradient by 90°. After characterizing the gradient created by the device and testing the polystyrene coating, the validity of the device was tested through the induction of orientation in wild type *S. cerevisiae* and compared the angle of orientation to a negative control. The device was able to induce orientation, with an angle of 56.9°, compared to the negative control which showed no discernible orientation. Ultimately the goal of this work is to induce reorientation. The rotating gradient device was able to induce reorientation in 83.6% of cells in a systematic and measurable fashion. The advantage of this device is its ease of use and ability to create and rotate chemical gradient to further study *S. cerevisiae* and its mutants to further elucidate the chemotropic mechanisms involved in mating projection growth.

The rotating gradient device was then used to test the ability of GβP- cells to orient in a chemically manufactured α factor gradient. The comparison of the angle of orientation measured in GβP- cells versus wt cells in a gradient or treated with isotropic pheromone highlighted the GβP- cells inability to sense the direction of a gradient. To obviate the need for the PS coating several non-porous substrates were tested to determine if the rotating gradient design could be replicated in a substrate that would not absorb small hydrophobic compounds into its bulk. Through

this testing it became clear that hot embossing of PMMA is a good solution to replace the PS coating.

Finally, the ability to induce a manufactured α factor gradient was conferred to an agarose pad using the automated chemical delivery device (ACDD). Preliminary results from orientation studies in this device suggest that the ACDD can be used to induce orientation. Ultimately, this device will be used to subject mating mixtures to a manufactured α factor gradient in the hopes that a confusion assay can be developed to further elucidate the chemotropic pathway.

In chapter four, microfluidic techniques were employed to culture 6.5 day embryos *ex vivo* for 24 hours through the gastrulation phase of mammalian development. The study of gastrulation in mouse embryos is important to elucidate the pathway of early development in mammalian embryos. Currently, the study of whole embryos is limited to collecting data at static time points and inferring development between these periods [21, 22]. The dependency of embryos on the support of the uterine environment has been a challenge in culturing embryos *ex vivo*. At the present time, a roller-bottle method allows for the *ex vivo* culture of embryos, but not continuous visualization or imaging of embryos [22], leaving the problem of taking data at static time points. Jones *et al*. devised a way to culture mouse embryos under continuous monitoring but were unable to culture embryos less that 8.5 days postcoitum (dpc) [21].

Briefly, gastrulation is the developmental process by which the pluripotent cells of the embryo begin to commit to defined cell lineages. This process requires

expansive cell movements that must occur in the correct spatial and temporal pattern to set up the basic body plan of the embryo [23]. Typically, any defect or failure in gastrulation results in significant morphological defects and/or embryonic lethality. The goal of this research is to design a microfluidic device that allows for the direct examination of the cell movements that occur in the embryo during gastrulation.

Two devices, one for incubator culture and one for bench-top culture, were designed, fabricated and characterized for the ex vivo culture of gastrulation stage embryos. The primary, immediate application of these devices described in chapter four is to enable live imaging of cellular events during gastrulation in mice. Devices were tested for the ability to support embryogenesis at the stage of primitive streak (PS) induction, when cell lineage decisions are coordinated with elaboration of a basic body plan. The ability to mount the device on either a full thickness glass slide or a coverslip, make the embryo culture devices amenable for imaging with a wide range of microscopy systems. The embryo culture methods described here can be combined with low magnification stereomicroscope systems to elucidate the spatiotemporal dynamics of the morphogenesis of structures that define stages of gastrulation. Combined with more powerful microscopes and fluorescent labels, the device now enables real time tracking of cell movements, shape changes, and proliferation through gastrulation.

Although each of the platforms described vary in design and usage, they display the extensive number of applications that can be devised using microfluidic techniques. The significance of this research lies in the ability to gaining understanding of

biological elements. Microfluidics enables the creation of platforms that enhance the ability to generate robust data and explore areas that are unable to be reached with larger scale technologies.

Microfluidic approaches for the study of yeast chemotropism, vein hypoxia, and embryonic development.

Table of Contents

List of Figures

List of Tables

Abbreviations

AVE	anterior visceral endoderm
BMP	bone morphogenic proteins
CABG	coronary artery bypass graft
CH	continuous hypoxia
dpc	days post coitum
DSML	digital scanned laser light sheet fluorescence microscope
FITC	fluorescein isothiocyanate
FOXY	fluorescent oxygen sensor (ruthenium based)
HIF	hypoxia-inducible factor
HP	head process
h-PDMS	hard PDMS
HPMM	high precision micromilling
IH	intermittent hypoxia
ME	mesoectoderm
Nodal	protein encoded by the *NODAL gene*
NE	neuroectoderm
PAF	posterior amniotic fold
PDMS	polydimethylsiloxane
PS	polystyrene (chapter 3)
PS	primitive streak (chapter 4)
ROS	reactive oxygen species
SR101	sulforhodamine 101

TGFβ	transforming growth factor beta signaling pathway
TURN	tape underlayment rotary-node
TWIST valves	torque-actuated valves
U2OS	osteosarcoma cells
Wnt	signalling pathway named for Int1 (integration 1) and Wg (wingless) genes
wt	wild type
XC/Bud	exocoelomic cavity/bud
YPD	yeast peptone dextrose

Microfluidic approaches for the study of yeast chemotropism, vein hypoxia, and embryonic development.

Chapter 1 Controlling Flow in Microfluidic Channels with a Manually Actuated Pin Valve

1.1 Abstract

There is a need for a simple method to control fluid flow within microfluidic channels. To meet this need, a simple push pin with a polydimethylsiloxane (PDMS) tip has been integrated into microfluidic networks to obstruct flow within the microchannels. This new valve design can attain on/off control of fluid flow without an external power source using readily-available, low-cost materials. The valve consists of a 14 gauge (1.6mm) one inch piece of metal tubing with a PDMS pad at the tip to achieve a fluidic seal when pressed against a microfluidic channel's substrate. The metal tubing or pin is then either manually pushed down to block or pulled up to allow fluid flow. The valve was validated using a pressure transducer and fluorescent dye to determine the breakthrough pressure the valve can withstand over multiple cycles. In the first cycle, the median value for pressure withstood by the valve was 8.8 psi with a range of 17.5 - 2.7 psi. The pressure the valves were able to withstand during each successive trial was lower suggesting they may be most valuable as a method to control the initial introduction of fluids into a microfluidic device. These valves can achieve flow regulation within microfluidic devices, have a small dead volume, and are simple to fabricate and use, making this technique widely suitable for a range of applications.

1.2 Introduction

Precise control of fluid flow within microfluidic channels is necessary for many applications. This chapter details a simple on chip valve consisting of a manually actuated pin that can directly block fluid flow within microfluidic channels. Researchers typically rely on either off chip flow control [24, 25] or on chip valving schemes [24, 26-28]. Off chip control is simple, but creates a large dead volume between the valve and the channel, while on-chip control requires complex, multilayered microfluidic networks. Though there are a multitude of successful demonstrations of microfluidic valves [24], many of these require intricate and expensive setups, extensive device modification, or complex fabrication schemes such as incorporating multiple layers to the design [27, 28]. One such example published by Carl Hansen and Stephen R. Quake, is a multi-layer valving scheme in which additional layers of channels sandwiched between thin membranes are added to actuate flow using pressure to deflect the membranes. The flexibility of these thin membranes allows for flow control of adjacent channels. Quake's group has also used these additional layers of channels to fabricate a micro-rotary pump [27]. A number of other examples use outside power sources [25], multiple series of channels [26, 28, 29], and biosensors or hydrogels [29-32] to control flow.

One well-defined demonstration of a manual valve utilizes screws embedded in a polyurethane compartment which avoids these intricate design factors and achieves a simple manually controlled valve [26]; however the footprint of these valves are quite large due to the thickness of the polyurethane compartment, limiting their implementation in microfluidic devices. There are several types of screw valves that

allow for manually actuated, on-chip control. Two of the most prominent are the tape underlayment rotary-node or TURN valve and the TWIST valve [33, 34]. When compared to these two screw valves the pin valve has an additional advantage, the simplicity of its actuation, a manual push, results in instantaneous On/Off flow control. The TURN valve uses a screw driver to reduce and/or increase the flow with each turn [33]. The simple push of the valve with a finger closes the valve and stops flow immediately. Like the screw based TWIST valve, the pin valve can also be used to keep channels closed without any additional force [34]. To open, the valve is simply pulled up to become flush with the top of the channel. However, there is one disadvantage to this simplicity, unlike the TURN valve, the pin valve only has On/Off control it lacks the graded control the screw based TURN and TWIST valves share [33, 34].

This chapter demonstrates a simple valve that can be incorporated into a multitude of channel layouts and does not require modifications to microfluidic device design. A hole can simply be bored into any size channel to insert the pin valve for flow control. The valve described here, like screw, pneumatic, or solenoid valves can be prefabricated before it is needed in batches of multiple (1-96) valves in each fabrication [35]. This allows for the pin valve to be easily integrated into any device through the simple act of boring a hole into the device using a sharpened metal pin, slightly larger than the channel diameter, over the channel in which flow control is desired. Like other prefabricated valves, the pin valve reduces the intricacy and time consumption of device fabrication [35]. The advantage of the pin valve over other prefabricated valves is that it generally has a smaller footprint. Recently published reports state that the footprint of a screw valve or pneumatic valve is approximately

3.5 x 3.5mm, and the footprint of a solenoid valve is approximately 10x10mm [35]. This is in contrast to the pin valve, which in the circumstances of this study the footprint of the pin valve was approximately 2.05mm in diameter (circular footprint). This sized valve was used on a channel 1mm in width. The same process could be used to fabricate smaller pins and smaller holes could be bored to accommodate smaller channels, thus reducing the footprint of the pin valve even further. This smaller footprint is an advantage for both imaging of the device as well as the ability to control closely adjacent channels.

The pin valve is created from a metal pin filled with PDMS (Sylgard 184, Dow) that is directly inserted into a microfluidic channel to control flow as shown in Figure 1.1. The valve consists of a one inch long metal cylinder filled with PDMS and fabricated to include a PDMS tip on the interface end. When the PDMS is pressed against the substrate of a microfluidic channel, a seal is created and flow is blocked. This seal can be easily broken by simply pulling the pin up to achieve on-off flow control within the channel. In this chapter the fabrication, testing and application of this simple on/off valve for microfluidic devices is described. This valve was fabricated using simple techniques and readily available materials which will allow easy implementation in a variety of laboratories.

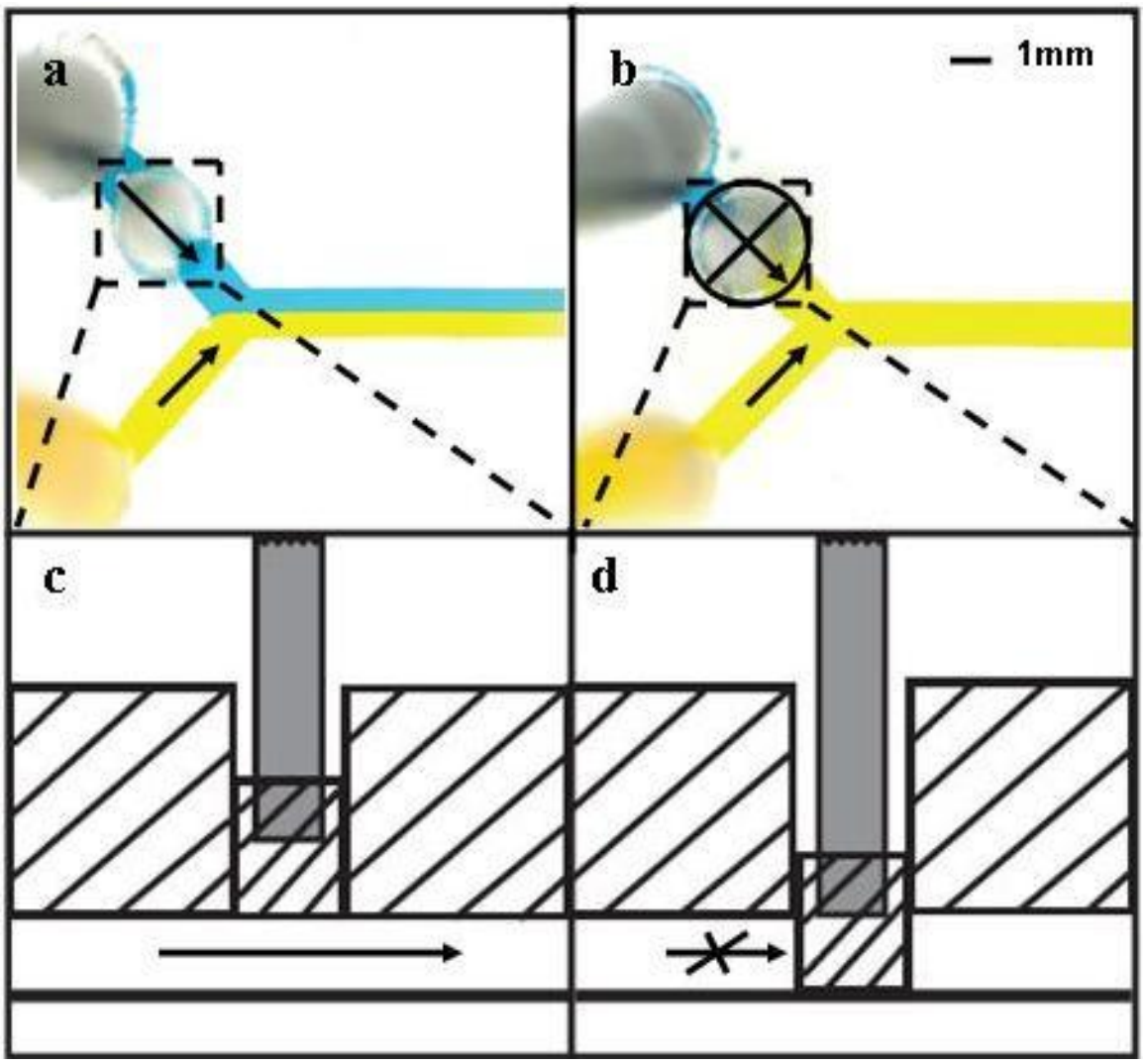

Figure 1.1: Image and schematic of pin valve in ON & OFF-positions. (a) Top down image of the pin valve in is the ON-position, allowing both yellow and blue vegetable dyes to flow simultaneously in the 1 mm x 375 µm PDMS channel. (b) Top down image of the pin valve in OFF position. The flow of blue dye is completely blocked and only yellow dye is permitted to flow into the channel. (c) Schematic representation of the pin valve being inserted into the channel until the PDMS tip of the pin is flush with the PDMS at the top of the channel. (d) Schematic representation of the pin valve being pushed through the channel until the PDMS tip of the pin is pressed against the glass bottom of the channel (glass slide).

1.3 Materials and Methods

1.3.1 Fabrication of the Pin Valve

The pin valve is created from a hollow metal pin filled with PDMS (Sylgard 184) that can be directly inserted into a microfluidic channel to control flow as shown in Figure 1.1. To fabricate the pin valve, 14 gauge (1.6mm) stainless steel tubing was cut in one inch sections. Once sections were cut the ends of the metal portion of the valve were buffed to remove any unevenness or roughness from the edges. The metal pins were then set in a 96 well plate in which the bottoms of the wells were pre-bored, covered with scotch tape (3M) and filled with degassed PDMS mixed at a 10:1 ratio of pre-polymer to curing agent. Upon filling the 96 well plate with PDMS the set up was degassed again as shown in Figure 1.2. Scotch tape was then placed on the top surface of the 96 well plate and a dental probe (McMaster-Carr) was used to form a hole above each well. Metal pins were placed vertically in individual wells and moved up and down to fill the lumen of the pin with PDMS. The entire setup was then baked at 75°C for 2 hours and allowed to cool to room temperature overnight. Pins with cured PDMS were removed from each well of the 96 well plate. Excess PDMS was trimmed from above the pad area and the PDMS plug was cut to 1 mm beyond the length of the metal portion of the pin. Each pin was cut to size to avoid differences in length introduced during processing. In order to cut the bottom plane of the pad orthogonal to the central axis of the pin we used the markings on a cutting mat (Vantage). The diameter of the PDMS plug was then reduced using an 11 gauge (2.30mm) punch as shown in Figure 1.2.

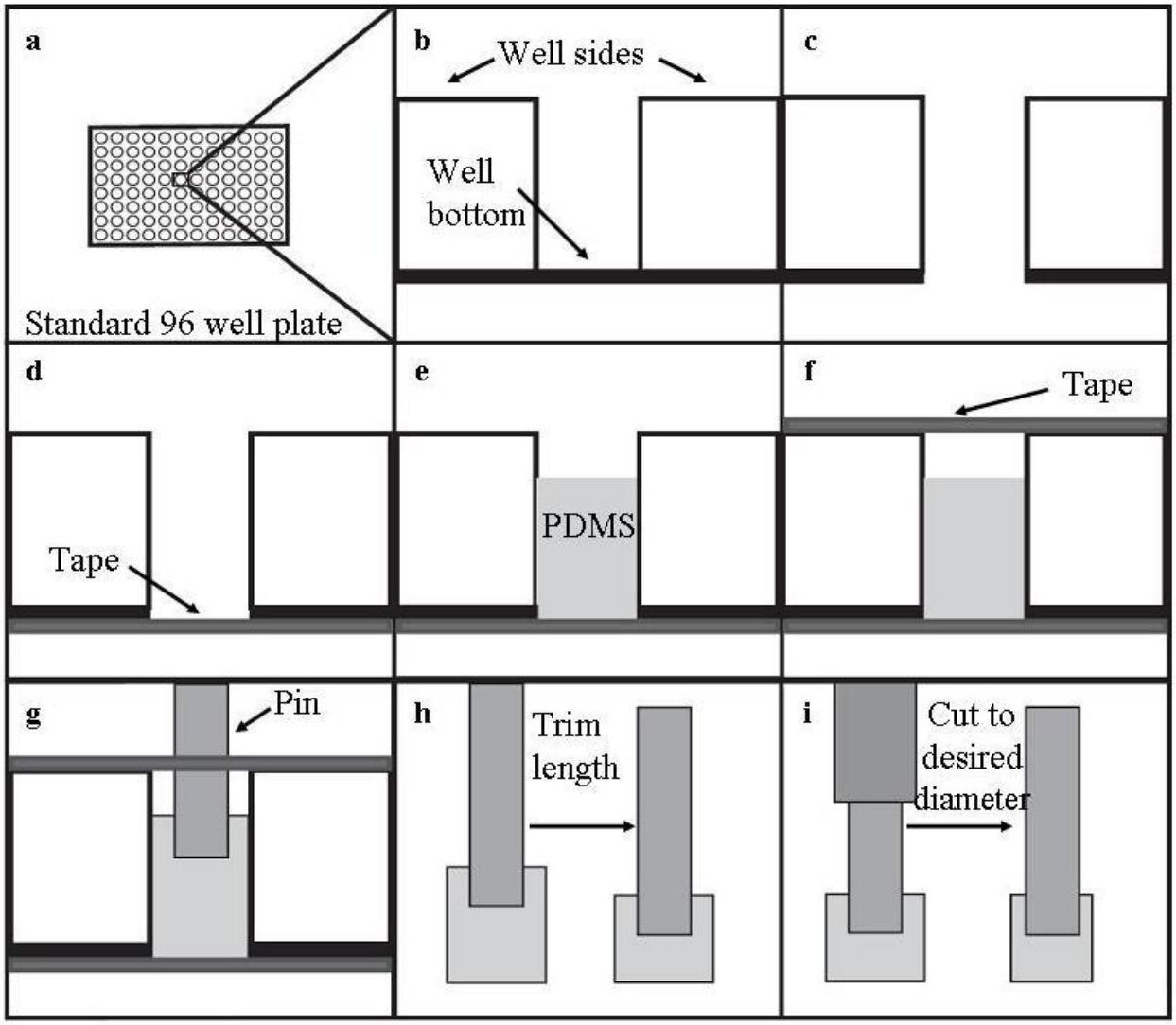

Figure 1.2: Pin valve fabrication. (a) A standard 96 well plate is used as the platform for fabrication. (b) Schematic of a single well. (c) The bottom of each well is removed. (d) Scotch tape is then used to cover the bottom on the 96 well plate. (e) PDMS is poured into wells and degassed. (f) The top of the 96 well plate is covered in Scotch tape and slits are cut above the wells for pin insertion. (g) Hollow stainless steel pins are pushed through the upper layer of Scotch tape and moved up and down vertically to fill the void within the pins with PDMS. The entire platform is then incubated at 75ºC for 2 hours and allowed to cool overnight. (h) The next day the pins are removed and trimmed. (i) A smaller gauge metal punch is then used to tailor the PDMS tip to a desired diameter.

1.3.2 Validation and Characterization of the Pin Valve

Pin valves were validated using a Y-channel device with inlet and outlet channels 4mm in length, and 1mm in width, which flowed into a channel of 10mm length and 1mm length, and an overall height of 375μm; in which a valve port was bored into one inlet channel as shown in Figure 1.1. The valve port was bored using a sharpened 12 gauge (2.05mm) needle (McMaster-Carr). Dye was injected via a syringe pump (Harvard Apparatus) and monitored with an in-line pressure transducer (PR Temp 1000, MadgeTech) in one inlet and water was injected into the other inlet. Both syringes were then attached to a single syringe pump (Harvard Apparatus) and set to a flow rate of 10μl/min. A schematic of the experimental set up can be seen in Figure 1.3. The valve was pushed down then released to block the channel containing dye, while the syringe pump continued pumping and building pressure on the valve. Pressure was recorded to determine the breakthrough pressure the valves could withstand. The breakthrough pressure is the measure of the highest pressure reached before there is complete failure of the valve. The device was imaged using either an inverted IX70 (Olympus) for FITC visualization or MVX10 with color camera (Olympus) for colored dye to visualize any leaking during these experiments; while simultaneously measuring the pressure in the channel leading to the valve. Pressure data was recorded using an IFC 200 data logger (MadgeTech) and information was exported to Sigma Plot (Systat) for analysis.

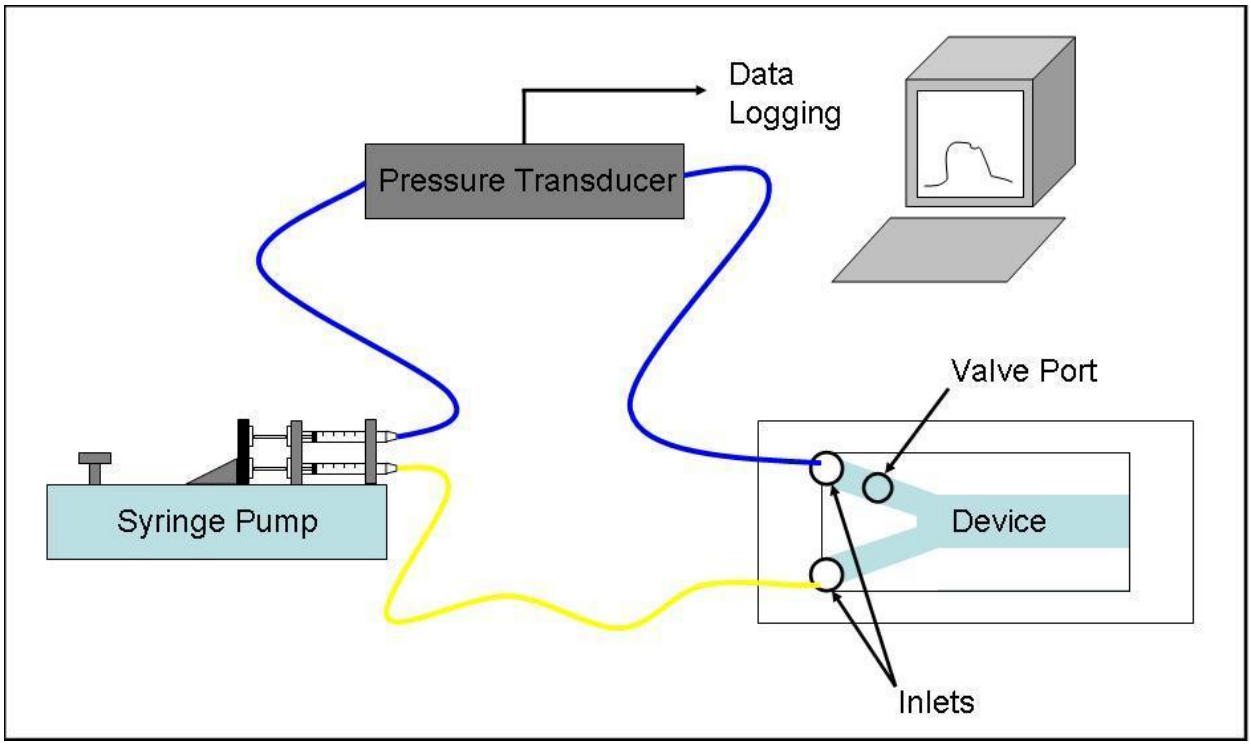

Figure 1.3: Diagram of Experimental Setup- Schematic of the pin valve test setup. As can be seen here a syringe pump is connected to a syringe containing water and an additional syringe containing dye. The syringe containing water is directly connected, via tubing, to one inlet of the Y-channel device. The syringe containing dye if first connected to a transducer and then to the second Y-channel, also by tubing. The dye moves from the syringe to the transducer, into a Y-channel inlet, and past the valve port to the 10mm in length portion of the channel.

1.4 Results and Discussion

To operate the pin valve, the valve is first inserted into the pre-bored valve port and then pushed to the bottom of the channel as shown in Figure 1.1. Since PDMS is self-sealing (i.e. forms reversible bonds with the PDMS of the device and the PDMS of the valve), the PDMS tip of the valve not only stops flow within the channels when pressed against the glass bottom, it also seals with the PDMS of the device, thus

preventing leaking up the side wall of the valve port. To release the valve and allow flow through the channel the pin is gently pulled up to become flush with the top of the channel. In fabricating this valve we used 14 gauge (1.6mm) tubing to create the metal pin and an 11 gauge (2.3mm) hollow metal needle to punch the diameter of the PDMS tip (Figure 1.2); however this technique could be modified to the dimensions of other microfluidic channels. Using a needle as a punch is necessary to reduce the diameter in the PDMS pad when molding in a 96 well plate. Attempts were made to mold a valve inside of a larger needle, but the PDMS of the valve ripped away from the pin upon valve removal. In the size valves tested in this chapter, the user can easily see when the valve has both reached the top and bottom of the channel. The user can also feel when the valve hits the bottom of the channel, as well as when the bottom of the PDMS pad is flush with the top of the channel. When this occurs, the resistance to pulling up the valve spikes and then increases exponentially. This should aid in reducing the introduction of dead volume in smaller valves as well, since although the user may not be able to see where the valve is vertically inside the channel, they should still feel the resistance increase. Currently the smallest valve that has been fabricated for this project is 16 gauge (1.29mm), it was successful in regulating flow.

Each valve was tested three times to determine the amount of pressure it would withstand over time. Figure 1.4 shows a representative time course pressure plot along with fluorescent images of the dye being blocked. This plot shows the general trend of pin valve behavior, although the amount of pressure each valve could withstand varied, the general profile was similar for all conditions. Figure 1.4 also depicts that there was no initial leaking and complete sealing was achieved

(represented in inset b). Once the valve reached its threshold, it began to leak and never returned to the highest pressure withstood, i.e. breakthrough value, again during that trial as seen in Figure 1.4c. This initial leak was usually slow and the valve recovered slightly on the pressure trace as shown in Figure 1.4d until the valve had a complete failure at which point there was a larger leak, displayed in Figure 1.4e. The single largest reason for valves to be excluded before testing, less than 10% per batch, was uneven cutting of the bottom of the PDMS pad which is easily inspected prior to use.

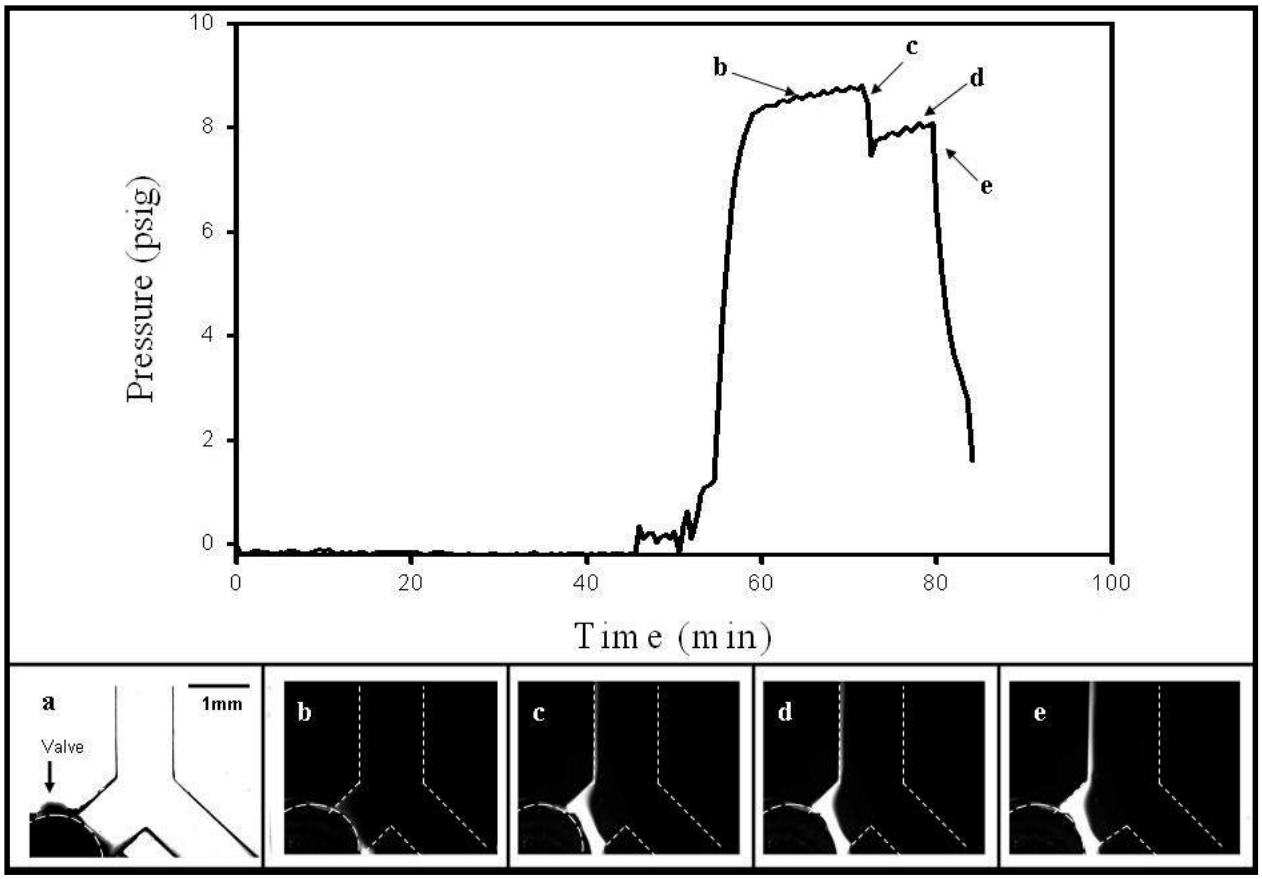

Figure 1.4: Pressure withstood by Valve over time. This figure takes a representative valve, V3 (trial 2), and shows its' ability to withstand pressure, while closed, without leaking until the pressure reaches a critical threshold, at which point the valve fails and begins to leak. (a) Brightfield image of valve in Y-channel. (b) FITC image of valve before the pressure reaches the critical threshold. (c) FITC image of valve at the point where it begins to leak. (d) FITC image of valve as it leaks but it still able to build up increased pressure. (e) FITC image of valve after failure.

The mean, range, and standard deviations for 10 valves are shown in the box plot of Figure 1.5. There is a large range of threshold values; however, each valve in the first trial of had a breakthrough pressure exceeding 2.7 psi and nine of the ten valves in the trial had a breakthrough pressure above 6.7 psi. Successive testing for each valve demonstrated there was a general trend of decreasing mean pressure with each usage. This is in part due to the fact that a few valves after one or two usages would no longer be able to stop flow as shown in Table 1.1. The valves in this case generally fell into two categories: either they were ripped or damaged upon removal from a device, or the amount of pressure they withstood in a previous trial was inordinately high. If the valves were just pulled up slightly between each valve cycle, the breakthrough pressures in successive cycles would likely be higher.

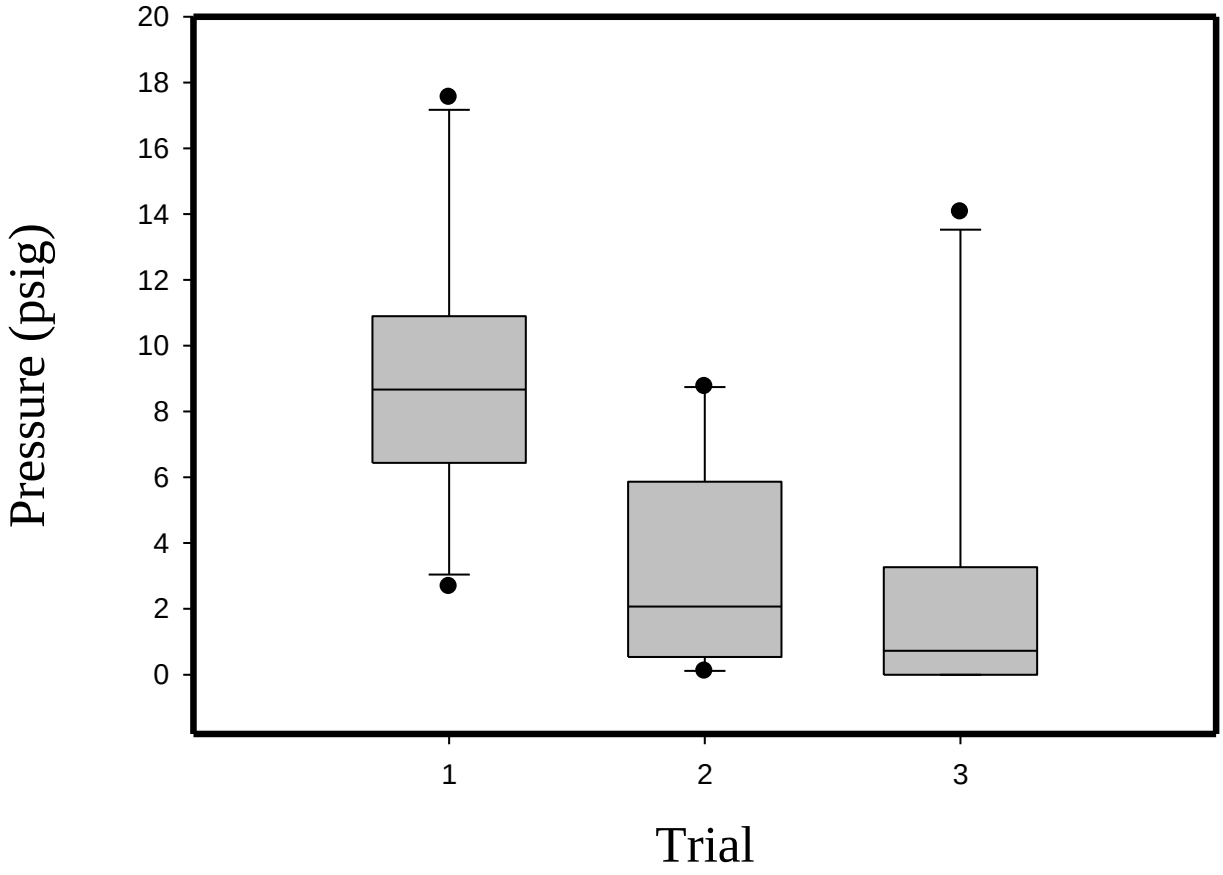

Figure 1.5: Pressure withstood by 10 tested valves. This figure represents data collected from 10 pin valves which each underwent three trials. Between each trial the pressure was released. Each of the gray colored boxes in the plot represent the middle 50% of the data for Trial one, two and three respectively. The lines that divide the boxes represent the median value for each trial. The whiskers or lines that extend above and below the boxes represent the entire data set and the small black circles represent statistical outliers.

Valve	Trial 1 (psi)	Trial 2 (psi)	Trial 3 (psi)
V1	2.7	0.3	0.3
V2	7.9	2.3	0
V3	14.1	8.6	6.4
V4	8.8	1.2	1.2
V5	13.9	1.9	1.5
V6	17.5	0.1	0
V7	9.1	0.6	0
V8	6.5	2.5	1.2
V9	9.9	5.0	0
V10	8.5	8.8	8.7

Table 1.1: Pressure withstood by 10 tested valves. This table contains data collected from 10 pin valves which each underwent three trials. Between each trial the pressure was released. Zero values represent a valves inability to be retested as they were either damaged upon removal from a device in the previous trial or withstood such a large amount of pressure in the previous trial that the valve was damaged.

Mean values were also inhibited because of the inlet connection with the device. In Figure 1.5, it can be seen that the mean pressure withstood is 8.8 psi for trial one, but there are also values that are nearly 18 psi. This confirms the valves worked quite well since tubing inserted directly into the PDMS inlet of our Y-channel device often began to leak around 9 psi. The valves that were able to overcome this value did so when the tubing and inlet of the device were cut perfectly and created a better seal. To allow more pressure to build behind the valve, fittings could be used at the tubing device interface in further applications.

To demonstrate the usefulness of the pin valve in a microfluidic device currently being used to study a biological phenomenon, we inserted 8 pin valves into an islet culture device as seen in Figure 1.6. Four of the pins inserted (pins 1-4) were used to control the amount of reagents that were perfused into the culture wells as seen in red. The other four valves (valves 5-8) were used to control the channels, in green, used for cell loading. The valves were successful and able to control flow with in their respective channels for the duration of the experiment. In this application, as well as in our experimental validation and characterization of the valves, we did not see a net vacuum introduced during the opening phase of the valve. This appears to be independent of whether the syringe pump is continuously pumping or if it has been stopped during the time at which the valve is closed.

Before the current valve design, there were two previous iterations.

When the fabrication of an On/Off, on-chip valve began it started with a metal pin filled with PDMS and with a notch cut out of the bottom. The idea was that this simple valve could control flow with in the channel through turning the valve, either

aligning the notch with the channel or doing a 180 degree turn to close flow. Unfortunately there were two major problems with this valve. First it leaked up the side walls of the valve port. Second it was too difficult to cut or mold a notch that would seal with the glass bottom of the device. To overcome the first issue of leaking up the side walls of the valve port grease was used to deter fluid from escaping up the side walls, which would hold off leaking for a period of time, but as pressure built, leaking would ensue. To remedy the second issue a second iteration of the valve was developed in which the first iteration would be placed in a larger metal pin with a notch cut for the channel width. This outer pin would not move but the inner pin would be rotated to align with the outer pins notch. The space between the two pins was filled with grease. Although leaking up the side walls of the valve port decreased, probably due to the fact that the outer pin was not twisting, the grease was sufficient to withstand the pressure that valve came under. This second iteration did not overcome the problem that the initial valve had making a seal with the bottom of the channel. When this was determined the grease was eliminated as the barrier and the PDMS pad that goes a bit beyond the diameter of the pin was added in order to stop leaking up the side walls. This PDMS pad also makes a good seal with the glass bottom of the device. This final iteration does have a fundamental difference as compared to previous iterations. Turning or twisting is eliminated. The push method does allow for On/Off control, but would not be able to be used to control the flow in a more complex way such as many of the aforementioned valves currently available.

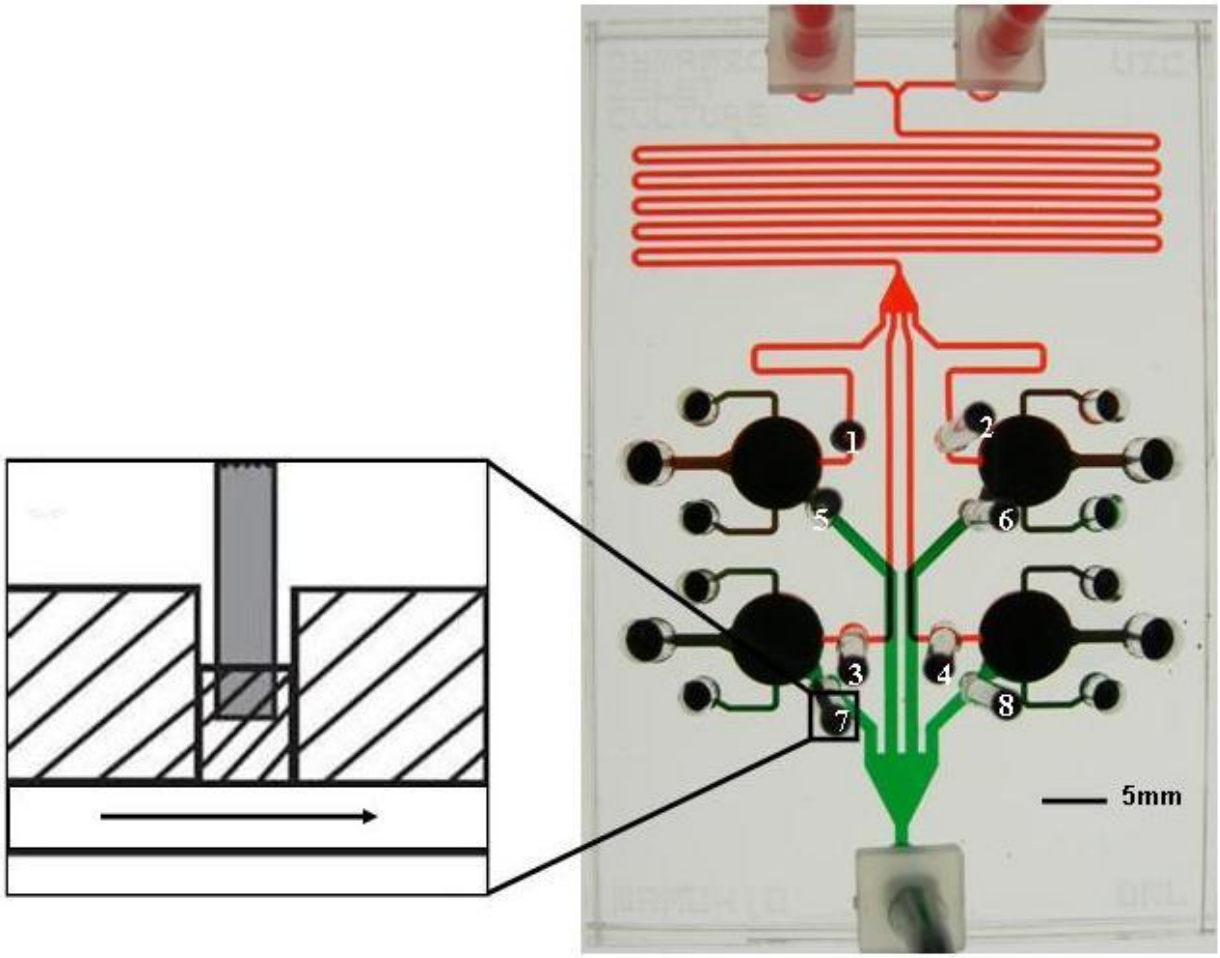

Figure 1.6: Islet Culture device. In this application, 8 pin valves were used to control flow. Valves 1-4 were used to control the flow of reagents into the culture wells, seen in red. Valves 5-8 were used to control the amount and timing of cell seeding in the culture wells by controlling the flow of cells through the cell seeding channels, seen in green.

There are several advantages of a valve with this design. First the valves are simple and inexpensive to construct. The components are readily available and are already used in most micro- and nano-systems laboratories. Second, the pin valve requires minimal training to operate. It can be used across disciplines and easily integrated into many microfluidic applications. The pin valve can also be produced in large numbers in a short amount of time (2 h). There are no moving parts within the valve, so as long as the stainless steel pin and PDMS pad remain intact the valve will function. Finally, this design not only prevents leakage due to the physical motion of the pin because of the self-sealing properties of PDMS, it likewise minimizes the possibility of introducing air bubbles into the system. Considering it costs very little to fabricate the pin valve and that the valve can successfully undergo three consecutive ON/OFF cycles, it should find use in standard microfluidic device applications.

1.5 Conclusions

In this investigation a simple two component valve was fabricated that is able to control the flow within a microfluidic channel. The valve was fabricated using simple techniques and readily available materials. Upon fabrication, the valves were tested using a simple Y-channel design. Each of the ten tested valves were tested three times. The resulting data showed that nine of the ten valves were able to hold over 6.7 psi as well as control the flow of fluid within the channel. These valves were also used to control the loading of cells as well as the dispersion of reagents in the islet culture device. These results support the idea that this simple valve can instantaneously stop flow and withstand a relatively large amount of pressure for a period on the scale of hours.

Chapter 2 Hypoxia

2.1 Abstract

Saphenous veins are commonly used in coronary artery bypass surgery (CABG) [9]. Unfortunately, many of the grafts fail due to vasoocclusion or constriction. Hypoxia is thought to be the cause of many of these negative outcomes. In this chapter, a six well hypoxic insert was fabricated and tested to determine if this device could be used to create a hypoxic environment for which to study saphenous vein hypoxia. The data garnered through the fabrication and testing of the six well hypoxic insert with a 3 mm gap showed that the device could be easily calibrated to determine the amount of oxygen present in the bottom of a standard six well culture dish. Upon calibration, the device could establish a desired concentration of oxygen, ranging from 0-21%, and these concentrations could be maintained over time.

2.2 Introduction

Hypoxia is a condition in a tissue or region of the body when the amount of oxygen falls below normal levels of oxygenation for that region of the body or tissue. There are three oxygenation states: hypoxia, when the partial pressure or percentage of oxygen is below normal; normoxia, partial pressure or percentage of oxygen typically found in a healthy tissue; and hyperoxia, excessive percentage of oxygen compared to physiological norm [36-38]. Normal oxygen levels are based on a relative scale depending on tissue type. For example, the amount of oxygen found in bone

marrow ranges from 4-7% [39-41], whereas the amount of oxygen found in healthy veins is approximately 5% [42], and the amount of oxygen found in cartilage tissue ranges from 6% in cartilage found in the superficial zone all the way down to less than 1% in the deep zone [43]. Unlike other scientific terminology normoxia is not always defined in the same manor in different contexts. In this chapter we will use normoxia to refer to the amount of oxygen, either percent or partial pressure, found within a healthy tissue. It should be noted however, that normoxia is also used to define the amount of oxygen found in sea level air, which is 21%.

Of the three oxygenation states that can be found in a region of the body or tissue, hypoxia is the most clinically relevant. Hypoxia can be continuous (CH) or oxygen levels can cycle between hypoxia and normoxia. In this later case, the cycling between hypoxia and normoxia is called intermittent hypoxia (IH). Intermittent hypoxia (IH) plays a role in tumor development [44], cardiac ischemia reperfusion injury [45], and vasodilation [46]. The role hypoxia plays in regulating cellular responses and affecting disease states is becoming increasingly important. Developing new tools to study hypoxia induced effects is critically important to the understanding of disease states. In this chapter, the development of a microfluidic insert for a 6 well plate is explored.

The amount of oxygen present in biological environments and *in vitro* tissue and cell cultures greatly affects the viability and behavior in these settings. The effects of oxygen concentration are most frequently mediated through the hypoxia-inducible factor (HIF) family of heterodimeric transcription factors [36-38]. The influence of HIF and the HIF-1α subunit is observed in metabolic processes ranging across many

biological areas including: angiogenesis [47, 48], development [49], migration [50], cell proliferation [51], apoptosis [52], metabolism [53, 54], cancer cell biology [48, 49, 53, 54], and islet transplantation [55]. For this study we will be developing a device to investigate the effects of hypoxia on veins.

In most coronary artery bypass surgeries saphenous veins are commonly used to replace blocked or damaged portions of the coronary arteries and restore blood flow to the heart [9]. Unfortunately, these veins often become occluded or constricted at the site of the graft. These graft failures are linked to many possible biochemical and mechanical factors including the disturbing of the natural tissue layers throughout the vein [9, 43], relief of pressure normally found within the vein during surgery [56], and the fact that the transplanted vein undergoes intermittent hypoxia [42, 43, 57-60]. The need for new tools to study the effects of IH on veins is great and the amount of tools that have been developed to further elucidate the link between intermittent hypoxia and vasoocclusion or vasoconstriction are few.

Currently, the hypoxic chamber is still viewed to be the gold standard in *in vitro* hypoxic studies [37]. The reasons for the hypoxic chamber's popularity are due in part to that fact that no specialized equipment is needed to operate the chamber and its relative ease of use [37, 61-63]. Although the hypoxic chamber is easy to use, it does not have the ability to create multiple conditions within the same chamber and the equilibration time is extensive. In recent years many devices have been developed to help overcome these limitations [64-69]. However, these devices are used to try to control the oxygen tensions experienced by cells placed in the hypoxic chamber.

These in chamber devices often need extensive electronic controls, specific operation parameters, and complex fluid handling [37]. To avoid these pitfalls of the oxygen tension regulation within the hypoxic chamber, a PDMS insert which nests into a multi-well plate has been devised [37, 38]. This new tool for hypoxic study is composed of a series of pillars, one for each well in the plate, see figure 2.1. The hypoxic insert has been used to induce the up regulation of HIF-1α in osteosarcoma cells (U2OS) [37] and has been modified to fit within a Boyden chamber insert to study the effects of hypoxia on cancer metastasis using MDA-MD-231, human breast cancer cells [38]. Ultimately the hypoxic insert has been shown to be able to spatially and temporally control the concentration of oxygen within a normal cell culture environment.

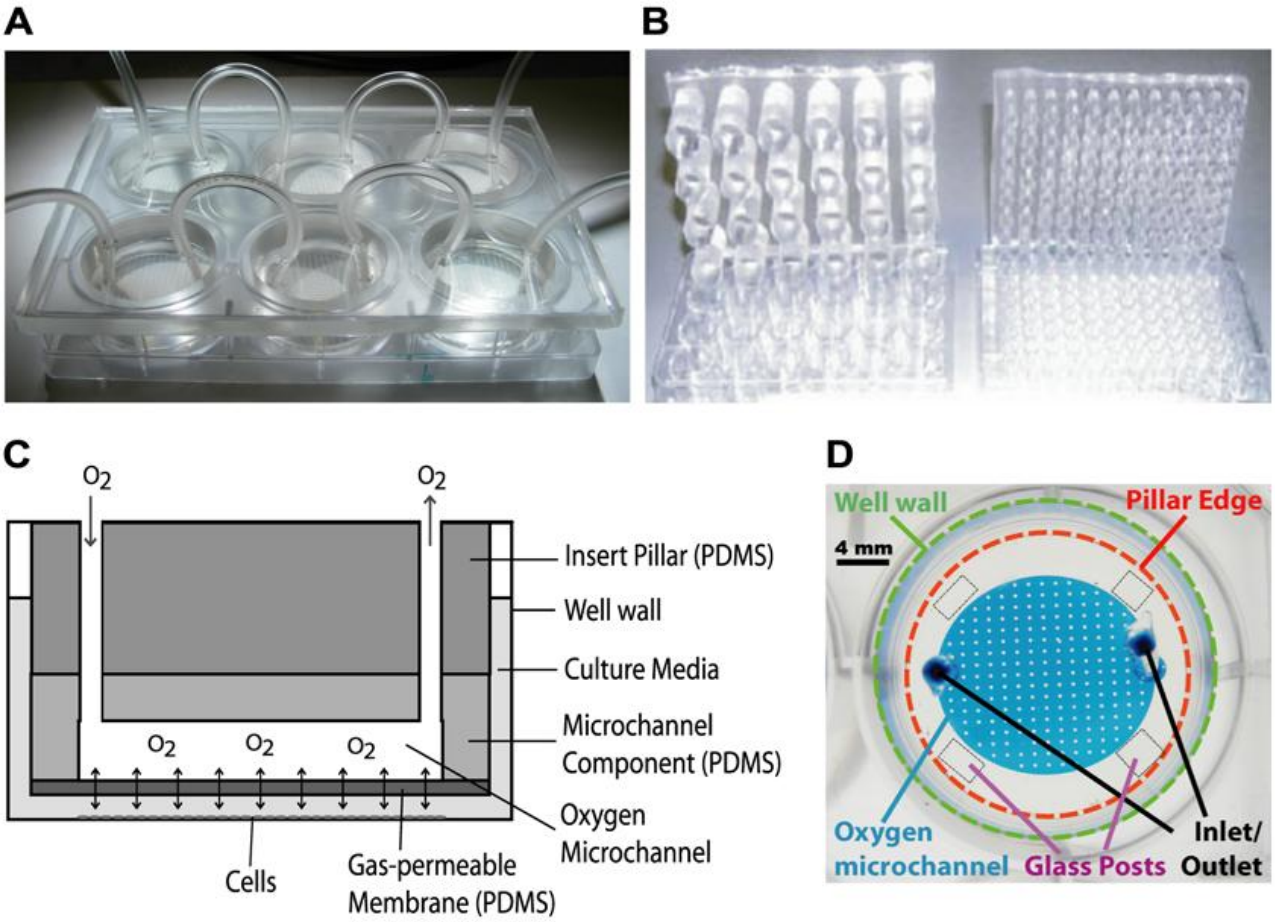

Figure 2.1: Schematic and diagrams illustrating device features. The oxygen insert device is fabricated by conventional photolithography (microfluidic network), replica molding (microfluidic network and insert scaffold), and defined spinning of PDMS (gas-permeable membrane). A) The oxygen device nested into a 6-well plate. B) Examples of 24 and 96-well pillar arrays. C) A cross-sectional schematic of a pillar. Oxygen flows into the device through the inlet and travels across a microfluidic network at the bottom of the pillar. Oxygen can freely diffuse across the gas-permeable PDMS membrane at the bottom of the pillar and dissolve into the culture media. D) A macroscope image showing the various features of a single channel pillar from above, with bonded glass posts for the equilibration studies. (Reprinted from: doi:10.1371/journal.pone.0006891.g001)

In this chapter we take this new tool and modify the depth of the culture area to accommodate the culture of veins. Previously the hypoxic insert was used to study monolayers of cells [37, 38] therefore the diffusion gap was 200 µm (figure 2.2). Until now the hypoxic insert has been characterized with up to a 1 mm diffusion gap as can be seen if figure 2.2. To use this device to spatially and temporally control the partial pressure of oxygen on a vein the fabrication and gap size were modified which is discussed in the material and methods section of this chapter. Ultimately a fully characterized device with the ability to house vein samples was fabricated. This device can be used to test the effects of both continuous and intermittent hypoxia on saphenous vein sections *in vitro*.

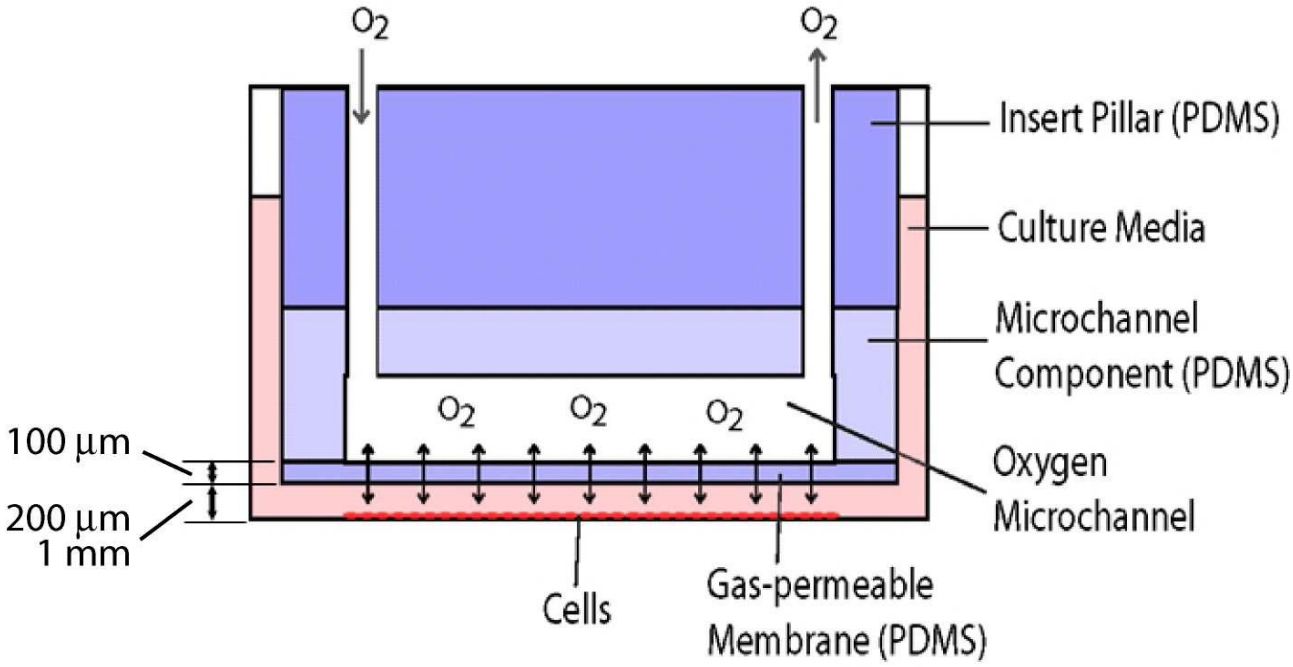

Figure 2.2: Cross-section illustration of a single pillar nested into the well of a multi-well plate. Gas is infused into the microfluidic network at the base of the pillar, which establishes a concentration gradient between the channel and media, driving equilibration towards a desired concentration. This figure depicts a single microchannel at the base of the pillar, but more complex spatial profiles can be established by incorporating different microchannel designs. Also, the diffusion gap is 0.2 mm in this case, but other diffusion gap distances can be used depending upon the requirements of the experiment. (Reprinted from Oppegard Thesis, UIC, Chicago, IL 2010)

2.3 Materials and Methods

2.3.1 Design of 6 well insert for study of intermittent hypoxia on veins

The gap between the bottom of the hypoxic insert and the bottom of the 6 well plate needs to be 3 mm in order to accommodate the diameter of the saphenous veins to be tested. To modify the 6 well plate hypoxic insert to utilize this device for these new studies, the length of each pillar of the 6 well insert was shortened using prefabricated oxygen microchannels (2 mm in height) that were placed in the pillar insert mold with tape to protect the microchannel design, in this case a pillar array, that would be bonded to the gas permeable membrane (figure 2.2). The depth of a standard 6 well plate is 18 mm and the depth of the Delran mold used to mold the 6 well pillars is 15mm in order to accommodate the microchannels being added after the hypoxic insert pillar array was fabricated (figure 2.3). The total desired height of each pillar of the 6 well hypoxic insert is 15 mm therefore, prebaking the microchannels and inserting them into each of the pillar molds eliminates the need to spacers or glass posts, figure 2.1d.

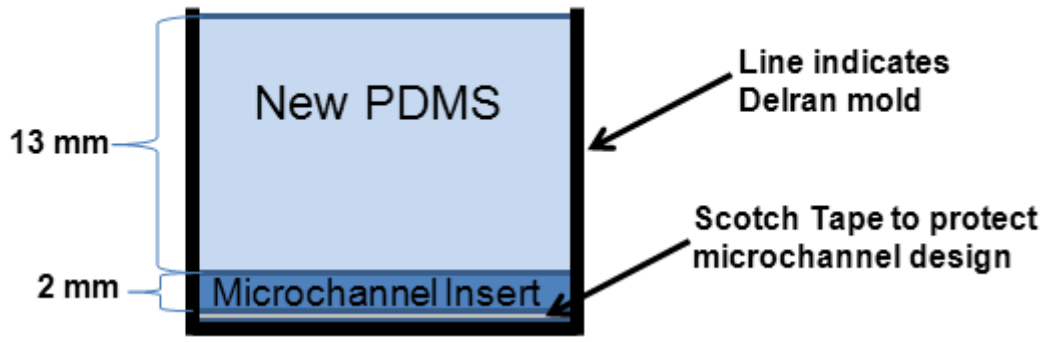

Figure 2.3: Hypoxic Insert Pillar Fabrication. During fabrication a microchannel 2 mm high is first fabricated using soft photolithograph. The side of the microchannel with the design is ten covered with Scotch tape (3M). This microchannel insert is then placed tape down into the Delran pillar mold. Once the microchannel insert is properly positioned uncured PDMS is poured into the mold for a resulting pillar height of 15 mm.

2.3.2 Fabrication of 6 well insert

To fabricate the 6 well hypoxic insert for saphenous vein culture, first microchannels were fabricated using standard soft photolithography methods of SU-8 2100 (Microchem) [70-73]. Here, SU-8 2100 was spun at 500 rpm for 10 seconds then 1200 rpm for 30 seconds. The photoresist covered wafer was then exposed with photomask containing design of microchannels (in this case and internal pillar array which can be seen in figure 2.1d) placed on top of SU-8 surface and a quartz dish used to keep the photomask in place. After hard bake and development the wafer containing 3 copies of the microchannel inserts deign was placed in a petri dish and 30 grams of degassed 10:1 PDMS to curing agent was poured on to the wafer. This was then degassed under vacuum until all bubbles were removed and baked at 75ºC

for 2 hours. After microchannel inserts cooled to room temperature, the PDMS was cut to reveal circular microchannel design. This is the microchannel insert seen in figure 2.3. The photomask contains the design for 3 insert channels, therefore PDMS casting of the wafer was repeated to fabricate the entire pillar insert.

To fabricate the 6 well pillar insert, first the Delran mold was put together. A transparency was cut to size and placed between the two halves of the mold that were subsequently screwed together. Pre-cut strips of hard plastic were then Superglued to the sides of the mold making sure to cover the area where the two halves come together and leave a 10 mm space at the top. Duct tape (3M) was then taped around the entire exterior of the mold and plastic strips so that the PDMS would not leak. One microchannel insert, tape side down was placed into each of the pillars in the Delran mold. Mixed and degassed 10:1 PDMS to curing agent was then used to fill the mold. The insert was then baked in an oven at 75ºC overnight and cooled to room temperature. Upon removal of the hypoxic insert from Delran mold tape from bottom of each pillar was removed and inlet and outlet channels were cut into each pillar with a sharpened 8 gauge metal needle.

To fabricate the gas permeable PDMS membrane, figure 2.2, a 3” Si wafer (Silicon Sense) was pretreated by pouring PDMS on top and baking for 2 hours at 75ºC. PDMS was peeled off wafers and this was repeated two more times. A quarter sized amount of 10:1 PDMS that was degassed for 2 hours was poured onto a pretreated wafer. The wafer was spun at 500 rpm for 10 seconds then 800 rpm for 30 seconds, and then baked at 75ºC for 2 hours. The PDMS membrane was cut into circles

using inside of pillar mold as the template and each circle was placed on its own small piece of transparency.

For final hypoxic insert assembly both the exposed side of the circular membranes and the end of each pillar / microchannel were treated with the hand held plasma gun, approximately 30 seconds for each membrane and 30 seconds for each pillar. Membranes were then rolled onto each pillar / microchannel and any remaining air bubbles were pushed out. The membranes were left overnight to bond, then the transparency was removed from each membrane. For a more detailed description of the fabrication process please see appendix A.1.

2.3.3 Characterization of 6 well insert

2.3.3.1 Oxygen Calibration and Sensing

To calibrate the setup used for the 6 well hypoxic insert ruthenium coated Foxy slides (FOXY-SGS, Ocean Optics) were cut to sized and glued to the bottom of each well in a 6 well plate. Ruthenium intensity is inversely proportional to the oxygen concentration because the ruthenium fluorophore is quenched by oxygen molecules. An experimental image of the intensity of one the ruthenium coating at one set point can be seen in figure 2.4. Each well was calibrated using 0, 10, and 21% oxygen balanced nitrogen gas mixtures. A 10x dry objective was focused on the top layer of the ruthenium slide. Three points in each well, under microchannel design, were set as positions for image capture. Each well was connected to a 0, 10, or 21% oxygen tank. The gas was allowed to equilibrate for 15 minutes. Images were then

captured at the predetermined set points. The gas concentration in the well was then switched and this was repeated until all wells received all concentrations. This data was then used to make a calibration curve, see figure 2.5.

2.3.3.2 Data collection and analysis

After calibration each well was characterized to determine what percentage of oxygen could be maintained within the well over time. First, 1/16" OD (Cole Palmer) tubing was connected to each well from a gas tank containing desired percent oxygen (between 0-21%) to well and turn on gas. Water was used as a media proxy in each well. The 6 well hypoxic insert was then nested into a standard 6 well culture plate containing ruthenium slides. Slidebook software (Intelligent Imaging Solutions, Inc.) was set to capture images at the set point determined during calibration at 5 minute intervals. Intensities were then analyzed using Excel (Microsoft) and the calibration curve was used to translate intensity to percent oxygen, see figure 2.6. For a more detailed description of this process please see appendix A.2.

2.4 Results and discussion

2.4.1 Calibration data

Each well was calibrated as described in section 2.3.3.1. In a typical experiment 3 wells of the 6 well plate were used. An example of the resultant data is shown in figure 2.4. Once each well was calibrated a linear regression was performed on the calibration data to determine the slope intercept form of the curve, figure 2.5. As can be seen in Figure 2.5, the calibration curves for each well analysed are very similar.

The data included in these curves are three individual intensity measurements for each well at each of the three oxygen concentrations used to calibrate the wells. The slope intercept equations from the calibration curves were then used to convert the intensity in the wells obtained during experiments to the percentage of oxygen in each well over time (Figure 2.6).

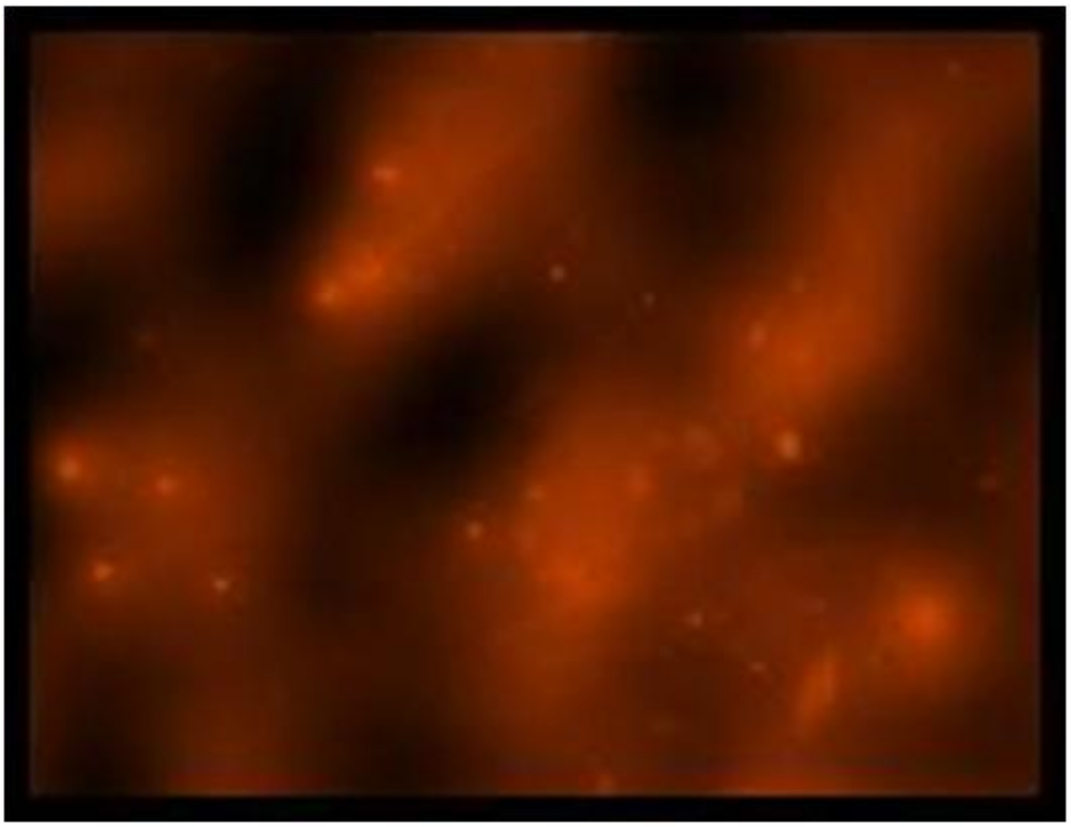

Figure 2.4: Intensity of ruthenium coating. Image of the florescent intensity on the surface of a FOXY slide in ambient air. This image captures the intensity of the ruthenium coating at one set point.

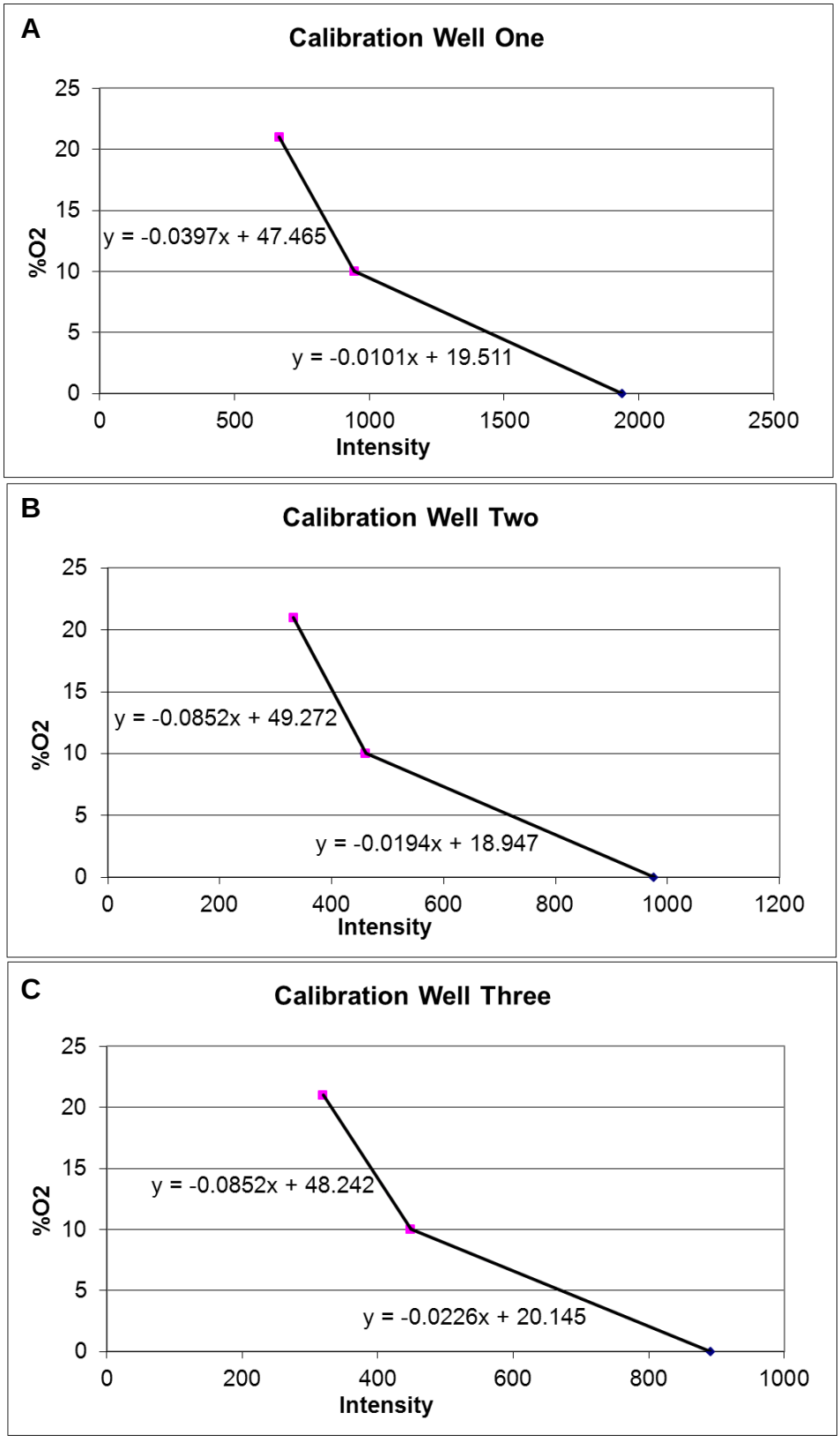

Figure 2.5: Calibration curves for 6 well hypoxic insert. Panels A, B, and C are representative calibration curves from the same experiment. Each of the curves represents one of three calibrated wells of the 6 well plate. Equations shown were determined using linear regression.

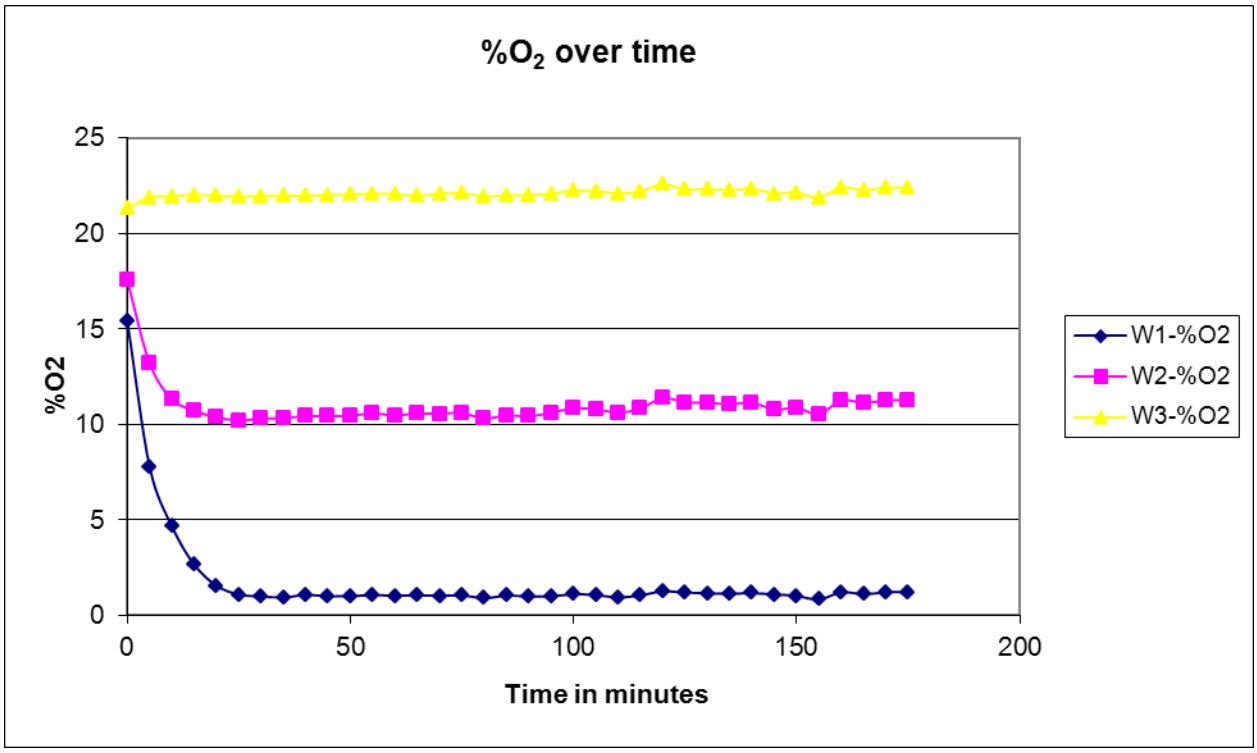

Figure 2.6: Percentage of oxygen over time. The three curves on this chart represent the amount of oxygen sensed by the FOXY slides placed at the bottom of each of three wells tested.

2.4.2 Hypoxic Insert data

After each well was calibrated, the desired percentage of oxygen was flowed into each well to determine how long and if it was possible to get this same oxygen percentage at the bottom of the well where the ruthenium oxygen sensor was located. As can be seen in figure 2.6, three wells of the 6 well plate were used to test 0, 10, and 21% oxygen concentrations. Well one was attached to a 0% oxygen, i.e. a nitrogen tank, and the data revealed that it took approximately 30 minutes for

the oxygen concentration to stabilize and that the lowest concentration that could be reached in this device was 1%. Although there was no oxygen flowed into the well, the water in the well that was used as a media proxy started off with an oxygen concentration of ambient air which is approximately 21%. The hypoxic insert was able to replace the majority of that oxygen with nitrogen. The fact that the insert is composed of PDMS, which is gas permeable, may be the reason for the inserts inability to attain a 0% oxygen concentration.

Well two was attached to a 10% oxygen balanced nitrogen tank and the data from this well shows that it took approximately 25 minutes for the oxygen concentration to stabilize and that the well was able to achieve the desired 10% oxygen concentration. This concentration was maintained for the first 100 minutes of the experiment and then there was a small fluctuation of the concentration between 10% and 11% oxygen. The reason for this fluctuation is unclear but it can be theorized that the pressure from the gas tank may have decreased as the tank was emptied.

In the remaining well, well three, balanced air (21% oxygen) was flowed into the well. The oxygen concentration was initially well maintained, as would be expected since the water in the well should already be approximately 21% oxygen. However, after 100 minutes the oxygen concentration in well three increased by about 1% and fluctuates, much like that seen in the other wells. This is an indication that there is an experimental artefact driving this change and that we can assume that the percent oxygen in the bottom of all three wells in nearly identical to that of the percent oxygen that is being delivered to the wells.

2.5 Conclusions

In this chapter, a 6 well hypoxic insert was fabricated and tested to determine if this device could be used to create a hypoxic environment for which to study saphenous vein hypoxia. The data garnered through the fabrication and testing of the 6 well hypoxic insert with a 3 mm gap showed that the device could be easily calibrated to determine the amount of oxygen present in the bottom of a 6 well plate. Upon calibration, the data shows that a desired concentration of oxygen, ranging from 0-21%, could be delivered and these concentrations could be maintained over time.

2.6 Future Work

Ultimately, the goal of this project is to subject saphenous veins to different concentrations of oxygen and measure the effects on the tissue. Initial vein hypoxia experiments should be first to determine if the vein culture is viable over an extended period of time in the device, which would be placed in a standard culture incubator set at 37ºC, 5% CO2 balance air. Once it is shown that the vein culture is viable, different oxygen concentrations can be perfused into the wells of the hypoxic insert placed in a standard culture incubator set at 37ºC, 5% CO2 balance nitrogen. The effects of vein hypoxia could be measured several ways including: the amount of HIF-1α up regulation; the extent of vasoocclusion and restriction.

Chapter 3 Yeast Chemotropism

3.1 Abstract

Chemotropism, or directed cell growth in response to a chemical gradient, is integral to many biological processes. The mating response of the budding yeast, *Saccharomyces cerevisiae*, is a well studied model chemotropic system. Yeast cells of opposite mating type signal their positions by secreting soluble mating pheromones. The mutual exchange of pheromones induces these cells to grow towards one another, resulting in “mating projections” or “shmoos.” Yeast cells exhibit a remarkable ability to orient their growth toward the nearest potential mating partner, and to reorient (i.e., bend their mating projections) in response to a change in the direction of the pheromone gradient. Although a number of microfluidic devices have been used to generate linear pheromone gradients and to measure initial orientation [17-19], none of them have the capability to change the direction of the gradient, other than to invert it. We have developed a microfluidic device that can produce stable pheromone gradients and rapidly rotate them in 90° increments, mimicking the dynamic gradients yeast are exposed to *in situ*, and allowing for the study of reorientation as well as initial orientation. The mean angle of orientation exhibited by gradient-stimulated yeast cells in this device was 56.9°. In control experiments, cells subjected to pheromone coming from all four directions showed no evidence of orientation. Switching the direction of the pheromone source by 90˚ induced 83.6% of the polarized cells to change their direction of growth. Of these,

85.2% bent their mating projections toward the second source, demonstrating the utility of this device in the study of reorientation with specifically controlled gradients.

3.2 Introduction

Haploid budding yeast exposed to mating pheromone produced by cells of the opposite mating type stop dividing and polarize their growth, thereby forming a mating project, or “shmoo.” Cells treated with pheromone under isotropic conditions form mating projections adjacent to their last bud site. This is called default shmooing. In contrast, mating cells interpret complex pheromone gradients and polarize their growth in the direction of the closest partner. This is called chemotropism, the directed growth of a cell in response to a chemical gradient. Chemotropism plays an important role in a broad range of biological phenomena, including metazoan development [12], pollen tube formation [13], and fungal infection. A well characterized example of chemotropism in mammals is axon growth cone guidance, which is essential for formation of proper neuronal connections during brain development [14]. It is notable that growing axons follow complex pathways as they track morphogenic gradients en route to their intended targets. The ability of budding yeast to change their direction of growth in dynamic pheromone gradients provides an opportunity to study reorientation in a genetically tractable, unicellular eukaryote. General principles are likely to emerge from the study of yeast chemotropism, as many fundamental signaling pathways are conserved between yeast and mammals [74, 75].

The yeast chemotropic response can be induced *in vitro*, as well as in mating mixtures. The first demonstration of yeast chemotropism in an artificially generated pheromone gradient was reported by Segall [15], who dispensed a continuous source of pheromone from a moving pipet. Unfortunately, the shape of the gradient cannot be controlled using this method and only cells closest to the pipet tip grew toward it [15, 16] Nevertheless, both orientation and reorientation were observed in this experiment. One other study of yeast chemotropism using Segall's apparatus was published [16], but due to the experimental difficulty of this method, the understanding of yeast gradient tracking has largely been left at the phenomenological level since its discovery in 1993. Recently, several groups have applied the precise microscale control afforded by microfluidic devices to study yeast chemotropism [17-20, 76]. However, most of these experiments were limited to stimulation from a single direction. In the exceptional cases, the gradient direction was rotated a full 180˚ by reversing the inputs of medium with and without pheromone. Here, a microfluidic device capable of generating stable linear pheromone gradients and rapidly changing their direction in 90° increments is designed, fabricated in PDMS, and tested as shown in Figure 3.1. This device is an important new tool for studying chemotropism, particularly reorientation, in *S. cerevisiae*. It enables the characterization of reorientation-defective mutants, which will ultimately lead to a mechanistic understanding of this phenomenon.

3.2.1 Non-porous substrate fabrication of the rotating gradient device

Previously, induction of orientation and reorientation in yeast cells has been presented in mating mixtures and microfluidic devices that have the ability to induce

orientation have not been able to systematically induce reorientation [17-19]. In the studies described above, a multilayer PDMS microfluidic device has been designed, characterized and tested. This PDMS-based device can systematically induce both orientation and reorientation in the same device. The characteristics of the rotating gradient device allow for quantitative data collection of the angle of orientation and reorientation as well as the visualization of the cells for future protein labeling capabilities. To improve the device design's ability to generate more robust data, the rotating gradient device design was fabricated in several non-porous substrates.

Initially, the gradient device design was fabricated in in glass through glass etching [77, 78]. Glass can be wet etched using a chromium based metal mask and hydrogen fluoride [77, 79-81]. For our purposes a 4" diameter piece of soda lime glass (Telic) coated first with a 1200 angstrom thick chrome layer, and then with AZ photoresist on the outer most layer was etched. A stepwise etching of each of the three layers was performed; first the U-shaped perfusion channels (Figure 3.1), then the layer containing the restriction channels, and finally the yeast trap area were etched. The etched glass can then be bonded to a cover slip by calcium-assisted bonding [82].

Hot embossing can be a high precision tool for rapid device fabrication. In this chapter a brass micromilled mold was used to hot emboss the rotating gradient device into polymethylmethacrylate (PMMA) [83, 84]. PMMA is a hard a hard non-porous material that can be used in hot embossing [85, 86]. A brass mold was fabricated through high precision micromilling (HPMM) using the rotating gradient device design, as described above [83, 84, 87]. The HPMM mold was inserted into a

hot press (Carver Inc.) which was used to hot emboss the yeast gradient device in 3” PMMA disks (KMAC Plastics). The PMMA substrate and brass mold were mounted on the heated platens and the embossing machine delivered the force needed for embossing [85].

A non-porous clear epoxy can be cast onto a PDMS substrate to create a non-porous version of the rotating gradient device [88]. A negative of the photomask used to create the yeast gradient device was printed (Fine-Line) and used to fabricate a master, described in materials and methods section, and ultimately a PDMS mold or substrate for casting the two part epoxy. A clear two part castable epoxy, Epoxy A Cast 690 (Smooth-On) was mixed and degassed and cured on a PDMS mold of the yeast gradient device.

In addition to glass etching, hot embossing, and epoxy casting, the rotating gradient device design was also fabricated in hard polydimethylsiloxane (h-PDMS). Soft photolithography like that performed to fabricate the rotating gradient device in PDMS has many advantages. These advantages include rapid iteration of design; gas permeability, and biocompatibility [37, 89, 90]. However, there is a major disadvantage, PDMS is hydrophobic and porous [87]. This means that small hydrophobic compounds are easily absorbed into the bulk of the PDMS used to fabricate ant device design. h-PDMS can be used to form a composite device with PDMS [4, 91]. This composite device retains the advantages of soft photolithography of PDMS, while limiting the absorption of small hydrophobic compounds. The fabrication of the device in a non-porous substrate will eliminate the need for a

polystyrene (PS) coating and allow for dissemination of identical devices to collaborators.

3.2.2 Analysis of mutant yeast

The PS coated rotating gradient device was used to subject GβP- mutant *S. cerevisiae* cells to a gradient. Mating yeast cells interpret complex pheromone gradients and polarize their growth in the direction of the closest partner. Chemotropic growth depends on both the pheromone receptor and its associated G protein. Upon activation by the receptor, Gα dissociates from Gβγ and Gβ is subsequently phosphorylated. Free Gβγ signals to the nucleus via a MAPK cascade and recruits Far1-Cdc24 to the incipient growth site. It is not clear how the cell establishes and stabilizes the axis of polarity, but this process is thought to require local amplification via the Gβγ-Far1-Cdc24 chemotropic complex, as well as communication between this complex and the activated receptor. The rotating gradient device, along with a multitude of other experiments, was used to show that a mutant form of Gβ that cannot be phosphorylated (GβP-) confers defects in directional sensing and chemotropic growth. This data suggest that phosphorylation of Gβ plays a role in localized signal amplification and in the dynamic communication between the receptor and the chemotropic complex, which underlie growth site selection and maintenance.

One explanation for the difference in orientation assay results between Gβ and GβP- cells is that GβP- confers a defect in directional sensing and/or chemotropic

shmooing. However, it is also possible that GβP- cells signal their positions less effectively than WT cells because their pheromone secretion is less focused. To distinguish these possibilities, we compared the ability of Gβ and GβP- cells to grow toward a source of pheromone in vitro, using a microfluidic device. As previously reported, the Gβ control cells formed normal mating projections in the artificial gradient (Appendix B, Fig. 6A) and oriented toward its source with an accuracy similar to that observed in other published microfluidic experiments [17-19]. Surprisingly, the GβP- cells were unable to sustain growth in a single direction. Rather, they formed multiple small protrusions, often without growing much in overall size; very much like the SMP cells found in GβP- bud1Δ cultures treated with isotropic pheromone (Appendix B, Fig. 1B). Moreover, the first protrusions formed by the gradient-stimulated GβP- cells were positioned randomly, virtually without detectable orientation toward the pheromone. These data strongly support the idea that Gβ phosphorylation plays a role in the positioning and maintenance of the chemotropic growth site. Under isotropic conditions, GβP- cells form normal mating projections at the presumptive default site, apparently unaffected by their inability to phosphorylate Gβ. When subjected to directional stimulation, however, the mutant cells appear to “realize” they are in a gradient, repeatedly trying and failing to stably grow towards the source. Remarkably, GβP- cells exposed to an artificial pheromone gradient were unable to stabilize their growth at the default shmoo site. Ultimately, this device will be used continue to test mutant strains with deficiencies in proteins along the chemotropic pathways for differences in phenotypic response.

3.2.3 Yeast cell positioning

Finally, in this chapter an attempt is made to microposition individual yeast cell through patterning [6, 92] and the use of the bio flip chip [93]. The reason for the desire to microposition is to gain the ability to test how differences in distance between cells or the addition of a confusing cell will affect the mating response in an *in vivo* assay. The ability to create a chemically induced pheromone gradient is then expanded to and agarose pad in a bath chamber of an automated chemical delivery device (ACDD). The ACDD used in this chapter consists of six pneumatically actuated valves used to control the dispersal of pheromone from the channel via into the agarose pad. The pneumatically actuated valves are regulated by six discrete solenoid valves that are switched between vacuum and air pressure using a LabVIEW graphic user interface (GUI). The pheromone gradient created in this device is first tested using wild type (wt) *S. cerevisiae* of MATa haploid type in order to determine if the cells can sense the gradient and orient in this device. The goal of this platform is to induce, orientation, reorientation, and ultimately be able to plate a mating mixture on the agarose pad and then subject this mixture to a chemically induced pheromone gradient to determine if the cells will still sense their closest mating partner.

3.3 Materials and Methods

3.3.1 Microfluidic Device Design for Rotating Gradient Device

A novel microfluidic device was developed that can generate stable and linear pheromone gradients, and rapidly change their direction in 90˚ increments. It utilizes

both perfusion and restriction of chemical species to achieve a stable gradient. Our design builds on an existing device that demonstrated rotating chemical gradients [94]. As shown in Figure 3.1, our device includes a central circular trapping region (5μm tall and 1.5mm in diameter) connected to four small restriction channels (50μm tall, 75 μm wide and 750μm long), which connect to four larger perfusion channels (375μm tall, 500μm wide and 2.5mm long) oriented 90˚ apart in the central trapping region. The device operates by pumping medium and medium containing pheromone into the perfusion channels. As the resistance of the restriction channels is much higher than that of the perfusion channels the flow down the restriction channels is limited and the limited flow allows the medium to reach the central trapping region where it diffuses across. By switching the inputs to the perfusion channels, the gradient can be rotated in 90˚ increments.

3.3.2 Fabrication of the gradient device

Each gradient device was fabricated using soft photolithography procedures similar to those previously described [70-73]. The three-layer device was constructed using three separate photo-masks (Fineline Imaging). Each layer was added in a stepwise fashion onto a 3” silicon wafer (Silicon Sense) using SU-8 photo-resist (Microchem) according to the manufacturer’s guidelines. Polydimethylsiloxane (PDMS) was then mixed in a 10:1 ratio of pre-polymer to curing agent, degassed, and cast onto the wafer containing the device design. Upon curing and removing the PDMS, 13 gauge holes were punched into each inlet and outlet of the perfusion channels to allow tubing to be directly inserted into the device. The PDMS microfluidic network was then spin coated with 0.05% polystyrene dissolved in toluene to block PDMS

absorption of the pheromone, as the pheromone is a small hydrophobic compound. The 0.05% polystyrene (PS) solution was added dropwise to the PDMS, which was then spun for 10 seconds at 500 rpm followed by a 30 second spin at 2800 rpm. The coated PDMS was air dried for 4 hours allowing the toluene to evaporate, after which the excess polystyrene was removed from outside the microfluidic network using Scotch Tape (3M). The coated PDMS was then bonded to a 75 mm x 38 mm glass slide using a corona plasma treater (Electro-Technic Products, Inc.). For a detailed description of these protocols please see Appendices A.5 and A.7. It should also be noted that the SU-8 master can be fabricated using a μPG (Heidleberg Instruments). This procedure is described in appendix A.6.

3.3.3 Cell culture

Yeast cells were cultured on the rich medium, YPD, as described previously [95]. *S. cerevisiae* strain DSY257, of genotype *MAT*a *bar1*Δ *ade1 his2 leu2-3,112 trp1-1a ura3*Δ (Stone Lab), was inoculated from a -80°C glycerol stock by streaking onto solid medium, and the plate was incubated at room temperature for 48 hours. Prior to each experiment, an inoculum from the plate was grown overnight in 5ml of liquid medium at 24°C and 200 rpm. Cells from the overnight culture were loaded into the device with pressure to force them through the perfusion and restriction channels into the yeast trapping area using a 3ml syringe.

3.3.4 Characterization of Sulforhodamine 101 gradients

To confirm formation of a chemical gradient in each trial, 0.05 mg/ml sulforhodamine

101 was added to the pheromone-containing medium. The diffusion coefficient of alpha factor was estimated to be 132μm^2/s using the Stokes-Einstein equation in mammalian cytoplasm with a viscosity of 2 Pa s [96]. In our experiments, alpha factor is diffusing through an aqueous environment with a viscosity of approximately 0.9 Pa s at 25°c. This would give an approximate diffusion coefficient for alpha factor of 293μm^2/s. Initially we used FITC, which has a diffusion coefficient of 640μm^2/s in an aqueous environment; ultimately we substituted sulforhodamine 101, which has a more physiologically relevant diffusion coefficient of approximately 400μm^2/s to track the gradient [97]. Characterizations of the sulforhodamine 101 gradients formed by the rotating gradient device are shown in Figure 3. 2.

The sulforhodamine 101 served as a proxy for pheromone, allowing real-time validation of a chemical gradient (Fig. 3.2). Fluorescent images were obtained at 3 hours in orientation experiments and at 3 hours and 7 hours during re-orientation experiments. To determine the time to establish the gradient and its stability, fluorescent images were captured every 5 minutes starting when sulforhodamine 101 was initially perfused into the device. Images were captured using Metamorph software (Metamorph Inc.) on an inverted microscope (Olympus X70). Images were analyzed using Image J.

3.3.5 Assay of PDMS absorption of hydrophobic compounds

To assess the effectiveness of PS coating the channels, the absorption of rhodamine B was measured as a proxy of a hydrophobic compound [98]. The devices were filled with rhodamine B (Sigma) dissolved in water at a concentration of

0.02 mg/ml, and imaged along the restriction channels for 7 hours. Image J was used to quantify the distance rhodamine B that travelled outside the channel wall (Fig. 3.3).

3.3.6 Orientation and reorientation assays

In orientation experiments, cells were loaded into the trapping area via a 3ml syringe containing overnight cell cultures. The syringe was placed in one inlet while pressure was applied by hand at the same time the corresponding outlet was blocked. Medium was perfused into three of the channels while medium containing 356nM pheromone (Multiple Peptide Systems) and 0.05mg/ml sulforhodamine 101 was perfused into the fourth channel as shown in Figure 3.1. This caused the pheromone and sulforhodamine 101 to slowly diffuse across the trapping resulting in a gradient of both. A single syringe pump (Harvard Apparatus) was used to inject these solutions at 3.5 µl/min for all four perfusion channels. Cells were stimulated for 7 hours and bright field images were taken hourly at three adjacent positions on a diagonal line starting at the pheromone source in the trapping region. Only cells that were visible at time zero were analyzed for their degree of orientation and reorientation. To determine how effectively the gradient induced oriented cell growth, the angle of orientation was quantified by drawing a line extending from the pheromone source to the midpoint of a cell's base, and a line extending from that point through the middle of the cell's mating projection (Fig. 3.4b). If a cell grows directly towards the pheromone source the angle of orientation would be 0˚, whereas growth directly away from the pheromone source corresponds to 180˚. Negative control experiments were performed and analyzed exactly as described above,

except that pheromone-containing medium (356nM) was perfused into all four channels (i.e., there was no gradient). Reorientation experiments were also conducted as described above with the exception that the pheromone input channel was switched halfway through the 7 hour time course, thereby rotating the pheromone source by 90˚. Bright field images were taken hourly at three adjacent positions on diagonal lines starting at both the primary and secondary pheromone sources. The angle of reorientation is formed by a line extending from the midpoint of the cell's base through the middle of its original shmoo tip, and a line extending from the end of the original shmoo tip at t = 3.5 hours through the end of the new shmoo tip at t = 7 hours (Fig. 3.5b). This results in a measure of how much a cell's mating projection bends relative to its initial direction following the gradient switch.

3.3.7 Statistical analysis of angle measurements

The mean, standard deviation, and standard error of mean were calculated for each set of orientation and reorientation angles. Orientation Data were subjected to both a two-tailed t-test and a Pearson's chi square test using GraphPad (GraphPad Software, Inc.).

3.3.8 Glass Etching

Soda lime glass pre-coated with 1200 angstrom of chromium and AZ photoresist (Telic Co.) was etched as previously described [80, 81]. Soda lime glass pre-coated with chromium and AZ photo resist (Telic) was placed into a maskless photolithography machine (Heidleberg Instruments). The AZ photoresist was

exposed using the maskless photolithography machine only where perfusion channels will be etched. The exposed glass was then immersed for 1 minute with constant agitation at room temperature in AZ 1500 developer (Haas), to remove resist from exposed areas. The glass was then thoroughly rinsed with deionized water. To remove chromium layer the glass was submerged in a chromium etchant 1020AC (Transeene) bath at room temperature for 15-60 seconds (Cr layer is 1200a thick); then rinsed with deionized water followed by Millipore water and dried with compressed nitrogen. The back of the soda lime glass was covered with PVC sealing tape (3M) and immersed in etching solution (1:0.5:0.75 mol/L of HF/NH4F/HNO3) heated to 40ºC For 5 hours 30 minutes. After etching the glass was rinsed with Millipore water followed by ethanol and dried with compressed air. Subsequent layers of the device design were etched by repeating this process. The etch time varied depending on desired height. The etch times for the restriction channels and yeast trapping were 38 minutes and 3 minutes respectively. For a more detailed description of the etching process see appendix A.8.

3.3.9 Hot Embossing

A brass mold was fabricated through high precision micromilling (HPMM) using the rotating gradient device design, as described above [83, 84, 87]. PMMA discs were rinsed with isopropanol followed by distilled water and placed in oven at 75ºC for 24 hours. To emboss, the HPMM mold was inserted into a hot press (Carver Inc.) and the 3” PMAA disk was placed on top. The PMMA disk was covered with a 4” Si wafter (Silicon Sense) and a force of 5 kN for 5 min at 155ºC was used to hot emboss the yeast gradient device in 3” PMMA disks (KMAC Plastics [85]. The

PMMA disk was removed from the brass mold and the excess PMMA form outside the channel area was removed using a Dremel (Multipro). 2 mm diameter holes were bored at the end of each channel and the PMMA embossed chip was sonicated in 0.5% Alconox solution for 20 minutes, and then rinsed in DI water. The PMMA embossed chip was then sonicated in DI water for 10 minutes and dried with compressed air. A 250 µm thin sheet was cut to size with an Exacto knife and the thin sheet, as well as the embossed PMMA disk, were plasma treated for 30 seconds. The embossed PMMA and thin PMMA sheet were sandwiched between two glass slides and clamped with binder clips. The sandwich was placed in convection oven set at 120ºC for 30 minutes. The device was allowed to cool to room temperature and fittings made from PDMS linked to double sided adhesive via nitro cellulous paper were attached. For a detailed description of this process please see appendix A.10.

3.3.10 Two Part Epoxy

To create a clear non-porous casting in two part epoxy (Smooth-ON) a negative of the photomask used to create the yeast gradient device was printed (Fine-Line). This photomask was used to fabricate a master, described above, and ultimately a PDMS mold for casting the two part epoxy. Epoxy was mixed in a 100A : 30B weight ratio of epoxy A to epoxy B. The mixture was stirred for at least 3 minutes. The mixture was the poured over the PDMS substrate to be molded and degassed until all bubbles were removed. The epoxy was the left to cure at room for 24 hours in a well-ventilated area. Upon curing the PDMS substrate was removed to reveal the yeast gradient design embedded in the epoxy.

3.3.11 h-PDMS fabrication

Soft photolithography like that performed to fabricate the rotating gradient device in PDMS was used to create an SU-8 master for h-PDMS casting. h-PDMS was mixed using 3.4 grams of vinyl-PDMS copolymer (VDT-731, Gelest Corp.); 18 µl of Platinum catalyst (SIP6837.2LC, Gelest Corp.); and 1 drop (2.2 wt %) of modulator, 2,4,6,8-tetramethyltetravinylcyclotetrasiloxane (Sigma). The mixture was then degassed for 1 to 2 minutes. 1 gram of hydrosilane copolymer (HMS-301, Gelest Corp.) was gently stirred into the mixture and the resultant combination was immediately (within 3 minutes) used to spin coat (30-40µl) of h-PDMS onto the Su-8 master (1000 rpm for 40seconds). The h-PDMS was then par-baked for 30 minutes at 60ºC. Degassed regular PDMS (10:1 ratio of PDMS to curing agent) was then poured on top of partially cured h-PDMS and baked for 1 hour at 60ºC. The composite was cooled to room temperature and then cut to remove design. 13 gauge holes were bored into each inlet and outlet and the h-PDMS composite was bonded to a glass slide using plasma treatment.

3.3.12 Mutant testing

The PS coated rotating gradient device was used to subject GβP- mutant *S. cerevisiae* cells to a gradient. To test the GβP- mutants, cells were loaded into the trapping area via a 3ml syringe containing overnight cell cultures. A syringe was placed in one inlet while pressure was applied by hand at the same time the corresponding outlet was blocked. YPD medium alone was perfused into three of the channels while medium containing 356nM pheromone (Multiple Peptide Systems) and 0.05mg/ml sulforhodamine 101 was perfused into the fourth channel as shown

in Figure 3.1. This caused the pheromone and sulforhodamine 101 to slowly diffuse across the trapping resulting in a gradient of both. A single syringe pump (Harvard Apparatus) was used to inject these solutions at 3.5 µl/min for all four perfusion channels. Cells were stimulated for 7 hours and bright field images were taken hourly at three adjacent positions on a diagonal line starting at the pheromone source in the trapping region. Only cells that were visible at time zero were analyzed for their degree of orientation. To determine how effectively the gradient induced oriented cell growth, the first projection of each GβP- mutant cell was measured for angle of orientation. The angle of orientation of these projections was quantified by drawing a line extending from the pheromone source to the midpoint of a cell's base, and a line extending from that point through the middle of the cell's mating projection (Fig. 3.4b). If a projection forms along the line connecting the pheromone point source to the midline base of the cell, the angle of orientation would be 0˚, whereas growth directly away from the pheromone source corresponds to 180˚. The data collected from GβP- mutant testing was analysed and compared to wt orientation and negative control data.

3.3.13 Stamping

PDMS stamps were fabricated using soft photolithography as described above. The stamp design consisted of circular pillars 25 µm in diameter spaced 700 µm apart. A YPD plate was cultured with wt MATa haploid type yeast cells via liquid culture spread by the hockey stick method. YPD plates were then allowed to absorb the liquid media for 4 hours and were then flipped upside down and grown at room temperature for 3 days. After a lawn was grown on the YPD plates, the PDMS

stamps were used to pick cells from the plates in a desired pattern and stamp the cells on to a glass slide. This procedure was also performed on diluted overnight yeast cultures.

3.3.14 Bio Flip Chip

Two SU-8 masters were fabricated containing alternating wells 25 μm in diameter and 75 μm apart. A 10:1 ratio of PDMS to curing agent was mixed, degassed and poured onto each of the flip chip masters. Flip chips were cured at 75ºC for two hours and cut to reveal wells. The ability of the wells to position yeast cells was tested two ways. First, each of the flip chips were plasma treated for 30 seconds using a hand held corona treater (Electro-technic, Inc.). After plasma treatment a colored dye solution was aliquoted onto the surface of the wells (ESCO). A different color was used on each of the chips. After 30 minutes excess dye was removed using a cell scraper. Chips were them imaged using and Olympus MVX10 macroscope with a color camera (Diagnostic Instruments, Inc.) on a light box. A YPD plate was then placed on each chip and was flipped. Chips remained on the plate for 30 minutes to allow the dye to be absorbed. The YPD plates were then imaged in the same manor to observe if the dye had been transferred.

Copies of each chip were also tested with 6 μm diameter FITC latex beads (Polysciences, Inc.). Beads were diluted to 2.3x10^4 particles/ml from a stock solution. Each of the flip chips was plasma treated for 30 seconds using a hand held corona treater (Electro-technic, Inc.). After plasma treatment a 50 μl aliquot of the FITC bead solution was pipetted onto the surface of the wells. After 30 minutes

excess solution was removed using a cell scraper. Florescent images were then taken of the chips were using and Olympus IX71 microscope with a Hamamatsu camera. A YPD plate was then placed on each chip and was flipped. Chips remained on the plate for 30 minutes to allow the solution surrounding the beads to be absorbed. The YPD plates were then imaged in the same manor to observe if the beads had been transferred.

3.3.15 ACDD fabrication

Standard photolithography techniques were used to create three SU-8 masters for each of the three patterned layers of the ACDD device. To fabricate the device, PDMS pre-polymer (Sylgard 184, Dow Corning) was mixed 10:1 (polymer to curing agent) and degassed. The PDMS was poured to a thickness of 2 mm onto the bottom valve layer master containing 150 µm tall features and baked at 85^{o}C for 90 minutes. To create the flexible membrane layer, a clean silicon wafer was dehydrated at 125^{o}C for 15 minutes. Once cooled, the wafer was silanized under a vacuum with a 30 µl aliquot of (Tridecafluoro 1, 2, 2-tetrahydroctyl)-1-trichlorosilane (United Chemical Technologies, PA) for 30 minutes to facilitate membrane removal. The membrane layer was created by spin coating a solution of PDMS and hexane (3:1) on a silicon wafer at 1000 rpm with an acceleration of 100 m/s^{2} for 30 seconds. The membrane was cured at 85^{o}C for 10 minutes. The channel layer was made by spin coating PDMS on a patterned SU-8 master for 30 seconds at 700 rpm. The PDMS used to fabricate this layer was mixed, degassed, and set aside at room temperature for 3 hours to produce a thicker membrane when spin coated. The

PDMS was removed from the top of the posts with a directed stream of compressed air to ensure the via were produced in the channels.

To construct the top channel layer, PDMS was poured onto an SU-8 master containing the pattern for this layer and cured for 90 minutes at 85^{o}C. Once cured, the PDMS was removed from the wafer and holes were bored for the inlets, outlet, and bath chamber. The bath chamber was cleaned with isopropanol (IPA), dried under compressed nitrogen, and cleaned with tape to remove any dust and debris. The channel layer, still on the Si wafer, was also cleaned with tape, and both layers were plasma bonded with a corona treater (BD-20AC, Electro-Technic, Inc.) and bonded. Bonded devices were placed on an 85^{o}C hotplate for 10 minutes with a 3 kg weight. While these layers bonded, the valve layer and membrane were bonded in same manner. In addition, the non-feature side of the valve layer was bonded to a glass slide and set aside. The combined chamber and channel layer was cut and removed from the wafer, and holes bored in the same positions where the inlets and outlets are located in the chamber layer. Transparency covered the valves and the corresponding area on the channel layer was also covered while plasma treated to prevent bonding between the valves and channels. Lastly, transparencies were removed and the two combined layers were aligned with under a microscope and bonded. The final device was place on the hot plate at 85^{o}C for 10 minutes. The device was removed, and an 18 gauge needle was used to puncture the membrane in the valve inlets to allow air and vacuum access. The valves were opened with a syringe to prevent any subsequent bonding from the heat of the hotplate.

3.3.16 ACDD testing

3.3.16.1 SR101 characterization for yeast chemotropism experiments

A series of experiments were conducted to determine which parameters produced a stable linear gradient on the surface of an agarose pad. The number of via used, puffing rates and duration, and the number of channels needed to produce a stable linear gradient over a 6 hour time period were tested to determine the most optimal settings. The optimal parameters used for the yeast studies are presented below.

SR101 was used to simulate the pheromone gradient in an agarose pad. Four of the six channels were utilized. Sterile water was flowed through the first and fourth channels and 0.0025 mg/mL and 0.00125 mg/mL concentrations of SR101 were placed in the second and third channels respectively. Gravity driven flow was used to push the fluids in each of the channels until they exited the via downstream. Four open syringes were prefilled with the desired contents for each of the four channels. The syringes were then hung above the device and allowed to flow freely through the channels to remove any bubbles. A 2% w/w concentration of agarose (BP1360-100, Fisher Scientific) in liquid yeast peptone dextrose (YPD) was autoclaved and poured into the bath chamber and cooled for two hours before experimentation. The valves for the water-filled channels (1 and 4) were programmed to open for 10 seconds and close for 240 seconds, and the valves for the SR101-filled channels (2 and 3) opened for 10 seconds and closed for 300 seconds for the duration of the 6 hour experiment. Valve opening and closing was controlled by LabVIEW GUI. Line-scans where drawn above the via to measure the intensity of SR101 on the agarose pad.

3.3.16.2 Yeast chemotropism experiments

To perform the yeast chemotropism experiments the ACDD was set up as described in the previous section. Four of the six channels were utilized. YPD media alone was placed in channels 1 and 4 and acted as a sink to flank the injected pheromone. YPD with 400 nM α factor and YPD with 200 nM α factor were placed in the second and third channels respectively. The channels were prefilled with their respective fluids until they exited the via downstream and all bubbles were removed from the channels and the tubing. A 2% w/w concentration of agarose in YPD was autoclaved and poured into the bath chamber and cooled for two hours before experimentation. The valves for the YPD alone channels (1 and 4) were programmed to open for 10s and close for 240 seconds, and the valves for the YPD with pheromone channels (2 and 3) opened for 10 seconds and closed for 300 seconds for 2 hours to establish a gradient at the surface of the agarose pad. A 28 mm coverslip was placed over the solidified agarose to prevent extensive drying and shrinkage. To culture the agarose pad with MATa haploid-type bar- cells, a PDMS stamp with 500 μm post 1.5 mm center to center spacing was dipped in overnight culture, excess liquid was removed and the stamp was aligned with the via. The yeast cells were positioned above the via in the device, and a 18 mm coverslip was placed on the yeast for 40X magnification imaging. The perfusion of the YPD and pheromone was continually cycling during yeast culture of the agarose pad and an image of the yeast was taken every hour for five hours.

3.3.17.3 Determination of yeast orientation to gradient

To determine if the established artificial gradient produced was able to induce directed cell growth, the angle of orientation was measured. The method for measurement is described in section 3.3.6. Briefly, the angle of orientation was determined by marking a line from the pheromone source through the midline of the cell, a second line starting at the end of this line was drawn through the middle of the cell's mating projection. The interior angle of this line, α, is the angle of orientation. The mean, standard deviation, and standard error of mean were calculated for each set of orientation angles and each experiment was conducted three times.

3.4 RESULTS

3.4.1 Rotating gradient device

To determine the mechanism of gradient formation, 1µm diameter fluorescein isothiocyanate (FITC) labeled latex beads (Polysciences, Inc.) were diluted to $4.55x10^6$particles/ml and perfused into the device at rate of 3.5µl/min. Bead velocity was limited to 51.5µm/min within the restriction channels. Beads then moved into the trap where they stopped progressing and displayed Brownian motion. The four restriction channels act as either a source or a sink for the pheromone, and a stable sulforhodamine 101 gradient was created across the central trapping region in less than 30 minutes (Fig. 3.2e). By switching perfusion channel inputs, the pheromone source can be rotated in 90° increments. An additional feature of the device is that the cells in the central trapping area are mechanically trapped by the 5µm height. This obviates the need for embedding the cells in a gel or coatings, such as agarose or Concanavalin A, that adhere to the cells and could potentially affect their chemotropic response.

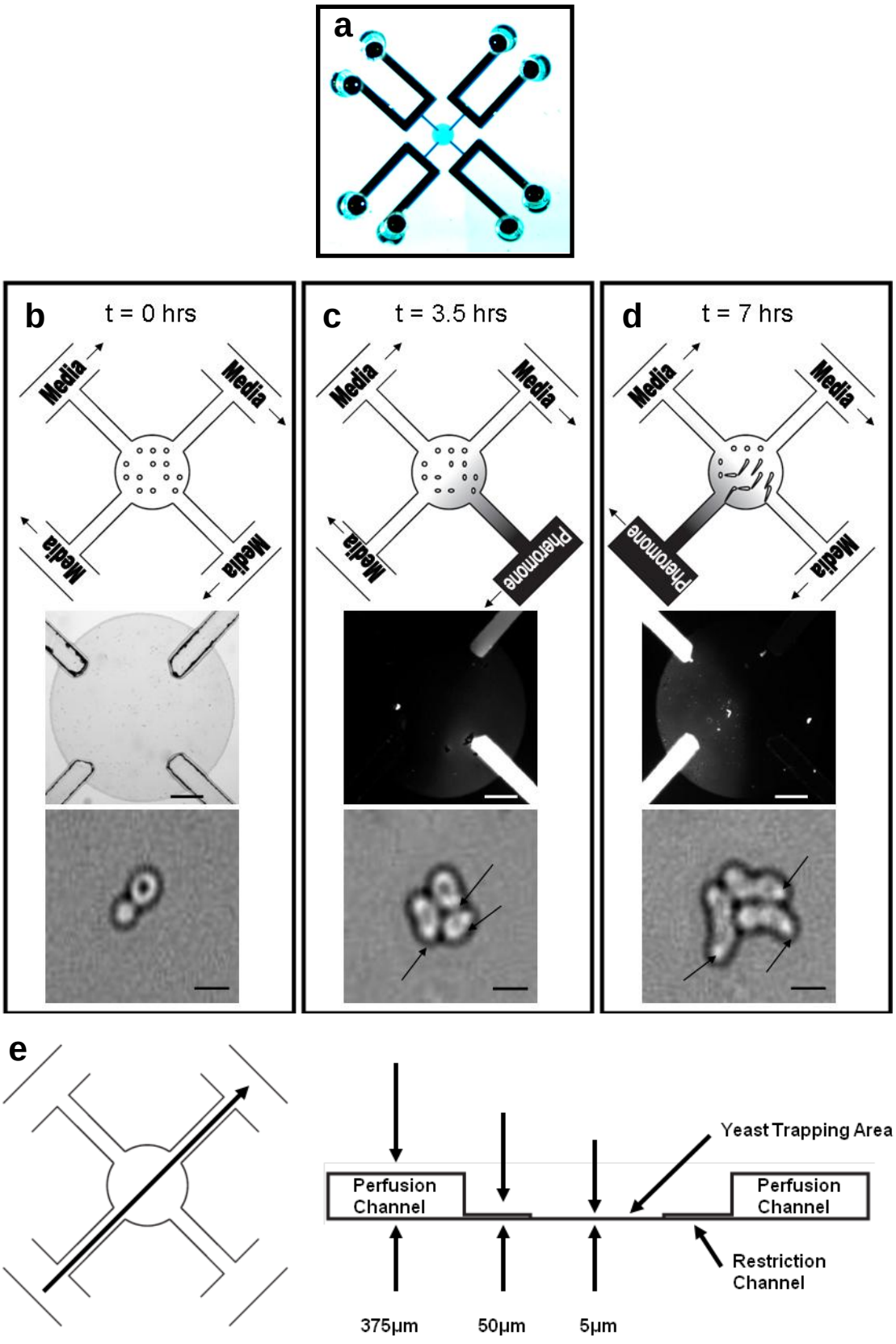
a
b
t = 0 hrs
Media
Media
Media
Media
c
t = 3.5 hrs
Media
Media
Media
Pheromone
d
t = 7 hrs
Media
Media
Pheromone
Media
e
Yeast Trapping Area
Perfusion Channel
Perfusion Channel
Restriction Channel
375µm
50µm
5µm

Figure 3.1: Rotating gradient device design and experimental set up. The device consists of four perfusion channels that are 500µm in diameter and 2.5mm across in the section closest to the restriction channels (75um in diameter and 750um length), which feed into a circular yeast trapping area that is 1.5mm in diameter and less than 5µm in height. a) Image of entire device filled with blue vegetable dye. b) Schematic of experimental process at t = 0. Bright field image of the yeast trapping area and a bright field image of cells in device at time t = 0. c) Schematic of experimental process at t = 3.5 hours. Fluorescent image of sulforhodamine 101 use to track the pheromone gradient. Bright field image of cells in device at time t = 3.5 hours, demonstrating shmooing in response to pheromone gradient in direction 1. d) Schematic of experimental process at t = 7 hours. Fluorescent image of sulforhodamine 101 use to track the pheromone gradient in direction 2. Bright field image of cells in device at time t = 7 hours demonstrating bending in response to pheromone gradient. e) Schematic of cross-section of microfluidic device. Schematic shows top view of device and arrow indicates where cross-section is taken. Scale bar on yeast trap images equals 200µm. Scale bar on lower three images of yeast equals 5µm.

The ability of the device to generate and rotate a chemical gradient was tested using sulforhodamine 101 as a tracer (Fig. 3.2). The intensity was measured across the trapping area in a diagonal line connecting the sulforhodamine 101/pheromone source to the opposite corner, and in a line perpendicular to the first. This measurement was taken at 3 hours, and again at 7 hours, 3.5 hours after the sulforhodamine 101/pheromone was rotated 90°. The data show that at t = 3 hours, there is a linear gradient of sulforhodamine 101 that begins at the end of the restriction channel of the initial source, declines over the next 600 µm, and becomes undetectable over the last 400 µm reaching to the end of the opposing restriction channel (Fig. 3.2c). At t = 7 hours, a very similar sulforhodamine 101 gradient emanated from the second source, whereas the original gradient was no longer detectable. Angles of orientation and reorientation were measured in the stable linear region of the sulforhodamine 101 gradient. The areas where the images for

these data were captured are labeled in schematic 3.4a. The data shown in figure panels 3.2c and 3.2d are an average of three trials and the noise seen in these panels can be attributed to the fact that dead cells and debris absorb the sulforhodamine 101 tracer. As expected, there is more noise at time t=7 hours than at t=3 hours. It is also important to note that, while the gradient was measured along the line connecting opposing restriction channels; the gradient extends radially from the restriction channel. Therefore, in reorientation experiments, cells measured from positions described in figure 3.4a are exposed to pheromone both before and after the 90° rotation. This is supported by the reorientation data described below where 83.6% of cells that shmooed in the first gradient reoriented when subjected to the rotated gradient. Together, these data demonstrate the ability of the device to form and rotate chemical gradients.

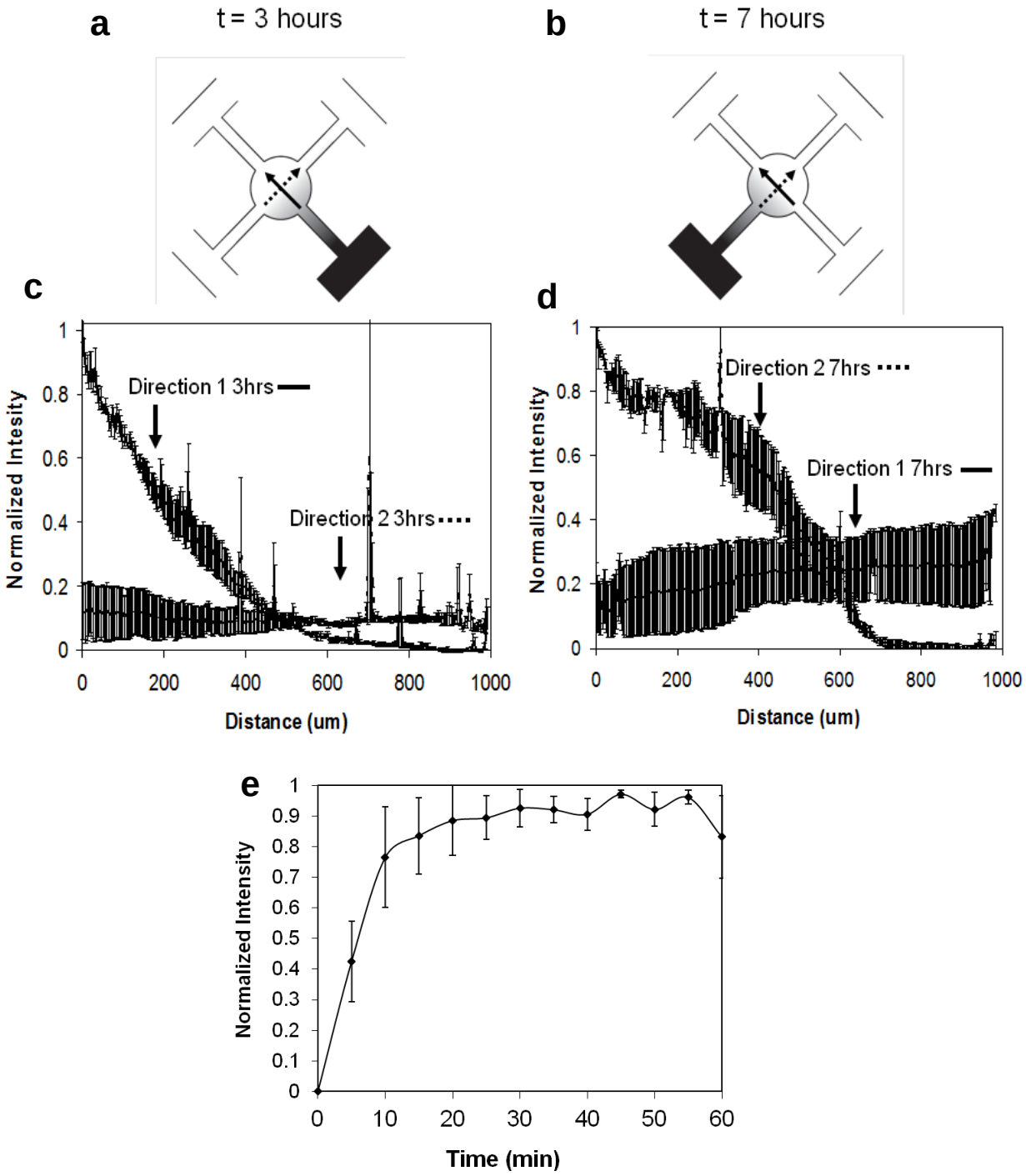

Figure 3.2: Schematic and Data from Sulforhodamine 101 gradient analysis. a) Schematic of pheromone in the device in the first direction. b) Schematic of pheromone in the device in the second direction. c) Sulforhodamine 101 gradient intensity across the trapping area in both directions at t = 3 hours. The spikes in intensity are from dead yeast cells and debris in the chamber. d) Sulforhodamine 101 gradient intensity across the trapping area in both directions at t = 7 hours. e) Sulforhodamine 101 Rate Data. Graph depicting the intensity of the sulforhodamine 101 gradient over time. Images were taken at positions 2 or 5 as described by figure 3.4a.

In initial tests of the device as a tool to study yeast chemotropism, cells exposed to a physiological dose of pheromone (356nM for a *BAR1* strain) did not shmoo (data not shown). Because α-Factor, the mating pheromone used in our orientation experiments, is a small hydrophobic molecule easily absorbed into PDMS, we spin-coated the device with a polystyrene solution to block this absorption. To test the efficacy of the coating at preventing absorption, the hydrophobic fluorescent dye, rhodamine B, was used as a model compound [98]. As shown in Figure 3.3, PS coated devices absorbed 3-fold less rhodamine B than uncoated devices over 7 hours. Although absorption of the model compound was not completely blocked, spin-coated devices delivered sufficient pheromone to induce the shmooing of cells in the trapping area.

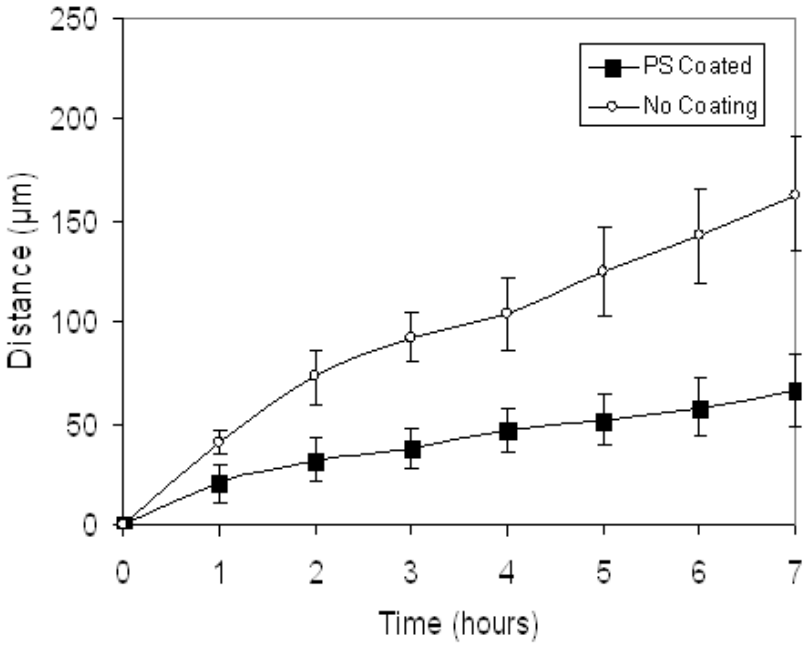

Figure 3.3: Analysis of polystyrene coating. Graph compares coated versus non-coated PMDS devices filled with Rhodamine B, fluorescent intensity measured over 7 hours. Distance refers to the distance outside the restriction channel that the Rhodamine B traveled.

Group	Orientation	Negative Control
Mean	56.9	89.9
SD	42.2	53.9
SEM	4.6	4.2
N	83	161

TABLE 3.1: Orientation Data. Orientation in response to a gradient of a single direction is compared to cells exposed to the same concentration without a gradient as a negative control.

Evidence that our device can generate a biologically active pheromone gradient is presented in Figure 3.4. Cells exposed to pheromone diffusing from a single channel exhibited clear chemotropism. The mean angle of orientation ± sem was 56.9 ± 4.6˚ (*n* = 83), which compares favorably with the results of analogous experiments [18] (Table 3.1). In contrast, cells exposed to pheromone diffusing from all four channels showed no systematic orientation. As expected, the negative control cells shmooed in response to isotropic pheromone treatment, but the direction of their growth was random. The mean angle of orientation ± sem relative to one input channel was 89.9 ± 4.2˚ (*n* = 161), where a value of 90˚ indicates unbiased growth in all directions. This result was not dependent on which source direction was chosen. A two-tailed t-test showed that the difference between the mean angles of orientation under gradient and isotropic conditions to be extremely significant ($p < 0.0001$). As an additional means of asking whether the device generated a pheromone gradient sufficiently potent to induce chemotropism, we used a yes/no scoring system. Cells were counted as having oriented toward the source of pheromone if they formed an angle of orientation < 90˚. Conversely, a shmoo was considered not to have oriented toward the source if this angle was ≥ 90˚. We used the chi-square test to determine whether the results were statistically significant. As expected for random orientation, the negative control cells were evenly split between values greater than and less than 90˚ ($p = 0.9372$). In the gradient experiments, on the other hand, more than three quarters of the shmoos formed angles of orientation < 90˚ ($p < 0.0001$).

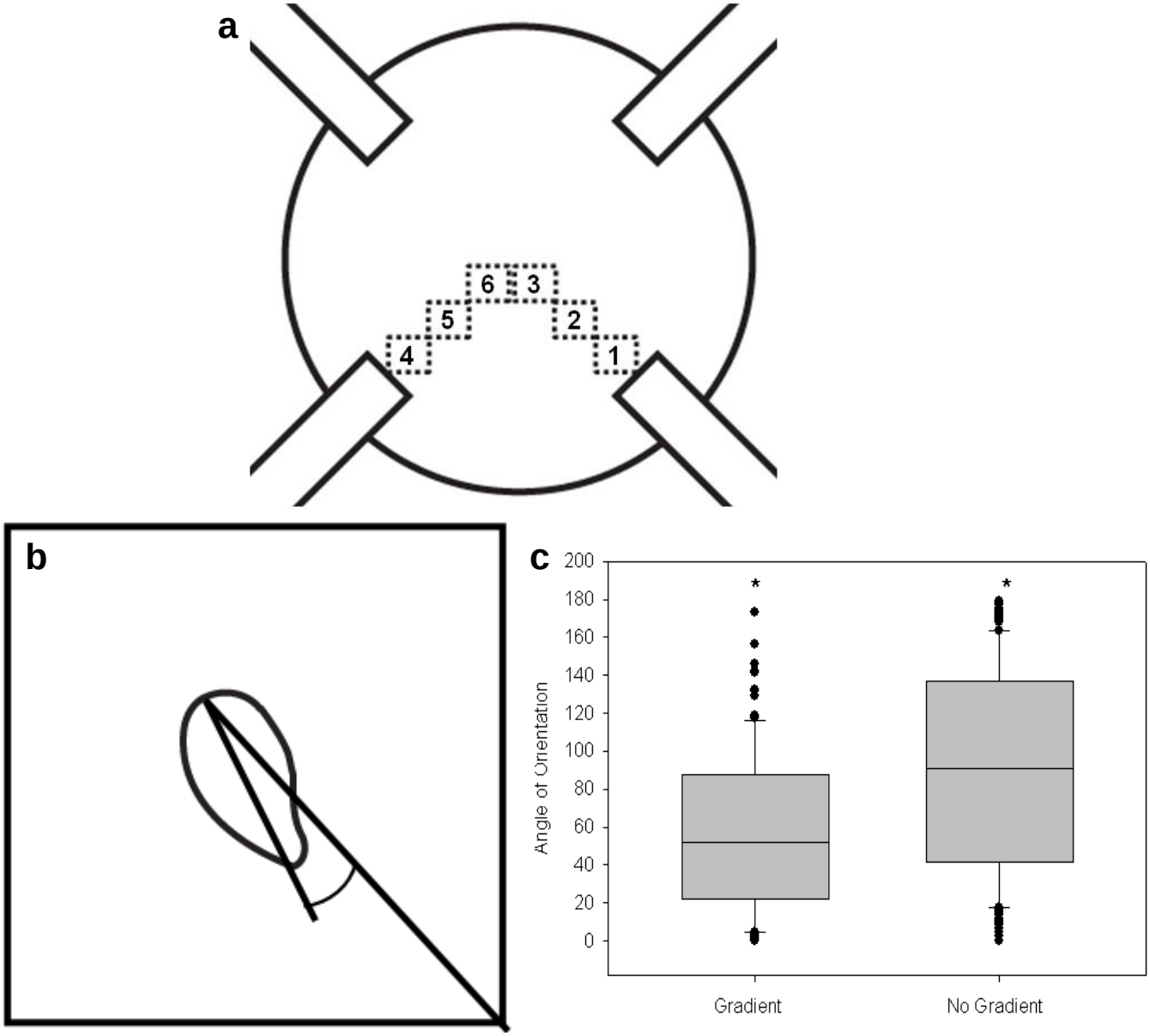

Figure 3.4: Angle of orientation. a) Schematic of data acquisition. Images were taken and analyzed as diagramed. For Orientation experiments images in rectangles 1-3 were analyzed to find angle of orientation as described in figure 4b. For reorientation experiments images 1-6 were analyzed at 3.5 hours to determine initial orientation and at 7 hours to determine the angle of reorientation as described by figure 5b. b) Angle of orientation, α, is determined by n=measuring the interior angle created with a line from the point source through the end of the cell and a line from this endpoint through the tip of the shmoo. c) Comparison of orientation and negative control data. This figure represents data collected from orientation and negative control experiments which each underwent three trials. Each of the gray colored boxes in the plot represent the middle 50% of the data for a one direction gradient and no gradient respectively. The lines that divide the boxes represent the median value for each type of experiment. The whiskers or lines that extend above and below the boxes represent the smallest and largest values in the data set that are not outliers and the small black circles represent statistical outliers. * P value less than 0.0001.

To fulfill its intended purpose, our device must be able to both form a stable pheromone gradient, and change its direction. In mating mixtures, cells sometimes bend their mating projections to align with the shmoo tip of the targeted mating partner (Fig. 3.5a). The bending of shmoo tips was also observed in Segall's classic study [15], but has not been systematically documented using microfluidic devices. To determine the capability of our device to mimic the dynamic gradients that elicit shmoo tip bending (i.e., reorientation), a series of experiments were performed in which the pheromone-containing medium was switched from its initial input to an adjacent port halfway through a 7 hour time course. Cells that shmooed during the first 3.5 hours were scored according to whether or not their projections bent after the presumptive gradient rotation, whether they bent toward or away from the second source, and the degree to which they changed direction (i.e., their angle of reorientation). In the many trials of the unidirectional gradient experiment, bending of mating projections was never observed. In the gradient-switch experiments, however, 71.54% of the cells that shmooed in the first gradient redirected their growth toward the second source, with a mean angle of reorientation ± sem equal to 36.4 ± 2.3 (n = 260) (Fig. 5). An additional 12.31% of the shmoos turned away from the second source, with a mean angle of reorientation ± sem equal to 32.0 ± 6.6, while the remaining 16.15% showed no detectable bending and their shmoos did not continue to elongate. To improve the device design's ability to generate more robust data, the rotating gradient device design was fabricated in several non-porous substrates

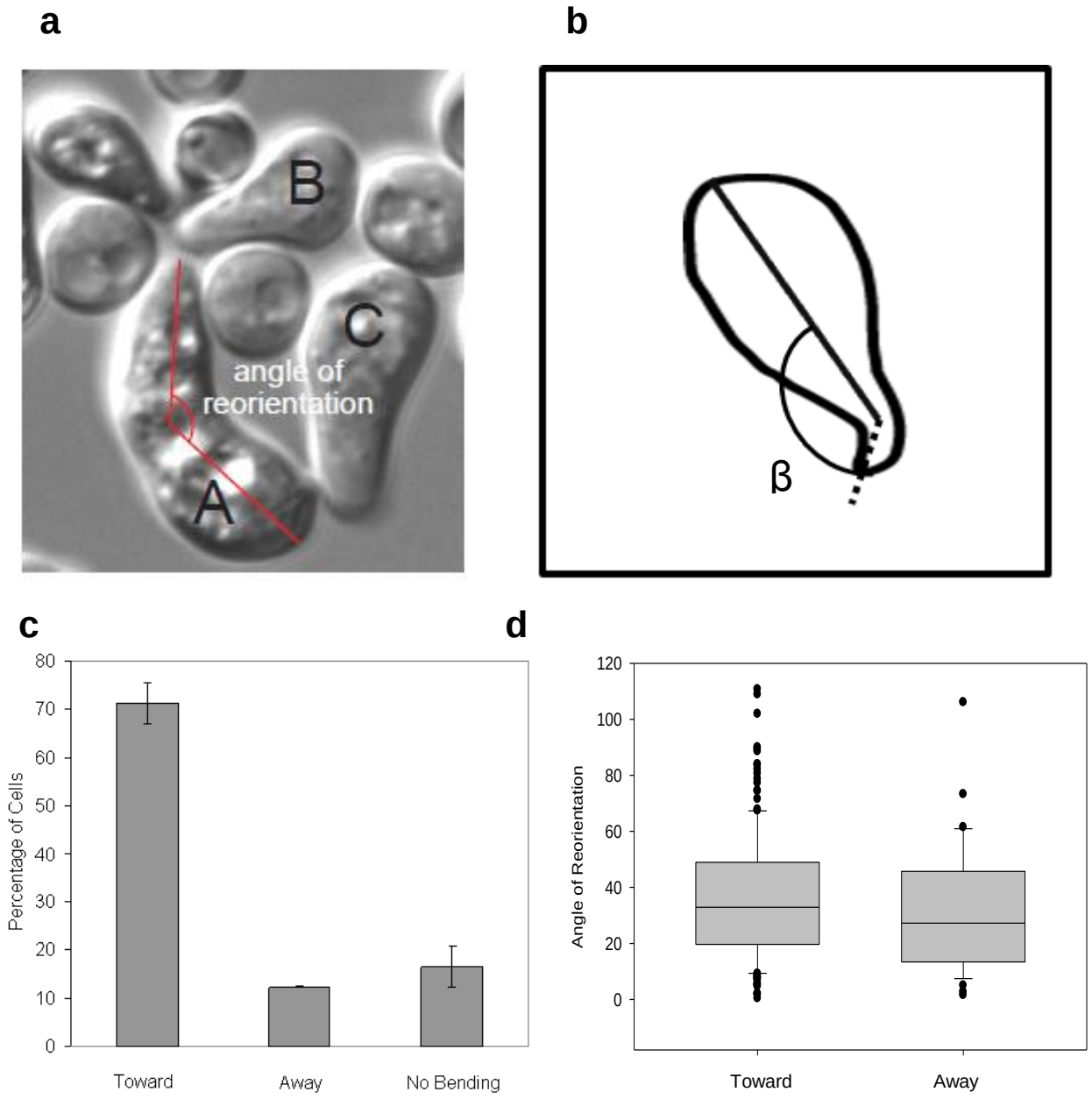

Figure 3.5: Angle of Reorientation. a) In vivo image of reorientation in a mating mixture. Angle of reorientation is determined by subtracting the interior angle shown here (red) from 180°. b) Angle of reorientation is determined using the line (solid) that bisected the cell in the orientation measurement and a new line (dashed) from the original shmoo tip to the newly formed shmoo tip. The interior angel, β, is the subtracted from 180° to determine the angle of reorientation c) Percentage of cell subjected to a 90° gradient switch that either bent toward the second pheromone source, away from the second pheromone source or did not bend. d) Comparison of reorientation data. This figure represents data collected from reorientation experiments over three trials, n = 260. Each of the gray colored boxes in the plot represent the middle 50% of the data for shmoos that bent toward and away from the

second pheromone source respectively. The lines that divide the boxes represent the median value for each subset of the data. The whiskers or lines that extend above and below the boxes represent the smallest and largest values in the data set that are not outliers and the small black circles represent statistical outliers.

3.4.2 Non-porous substrates

Initially the rotating gradient device design was etched in soda lime glass pre-coated with 1200 angstrom of chromium and AZ photoresist (Telic Co.) as described in section 3.3.8. Deep wet etching was performed on a 3" soda lime glass plate (Telic) like that pictured in figure 3.6. Unfortunately, even with special precautions taken to obscure any incidental UV irradiation of the AZ photoresist coating the plate the sensitivity of the photoresist was to great to overcome. As can been seen in figure 3.6, both pin holes and notch defects were present after only one exposure and etch cycle. This implies that the current etching conditions are not favorable for the three step etching needed to etch the three layer rotating gradient device in to soda lime glass.

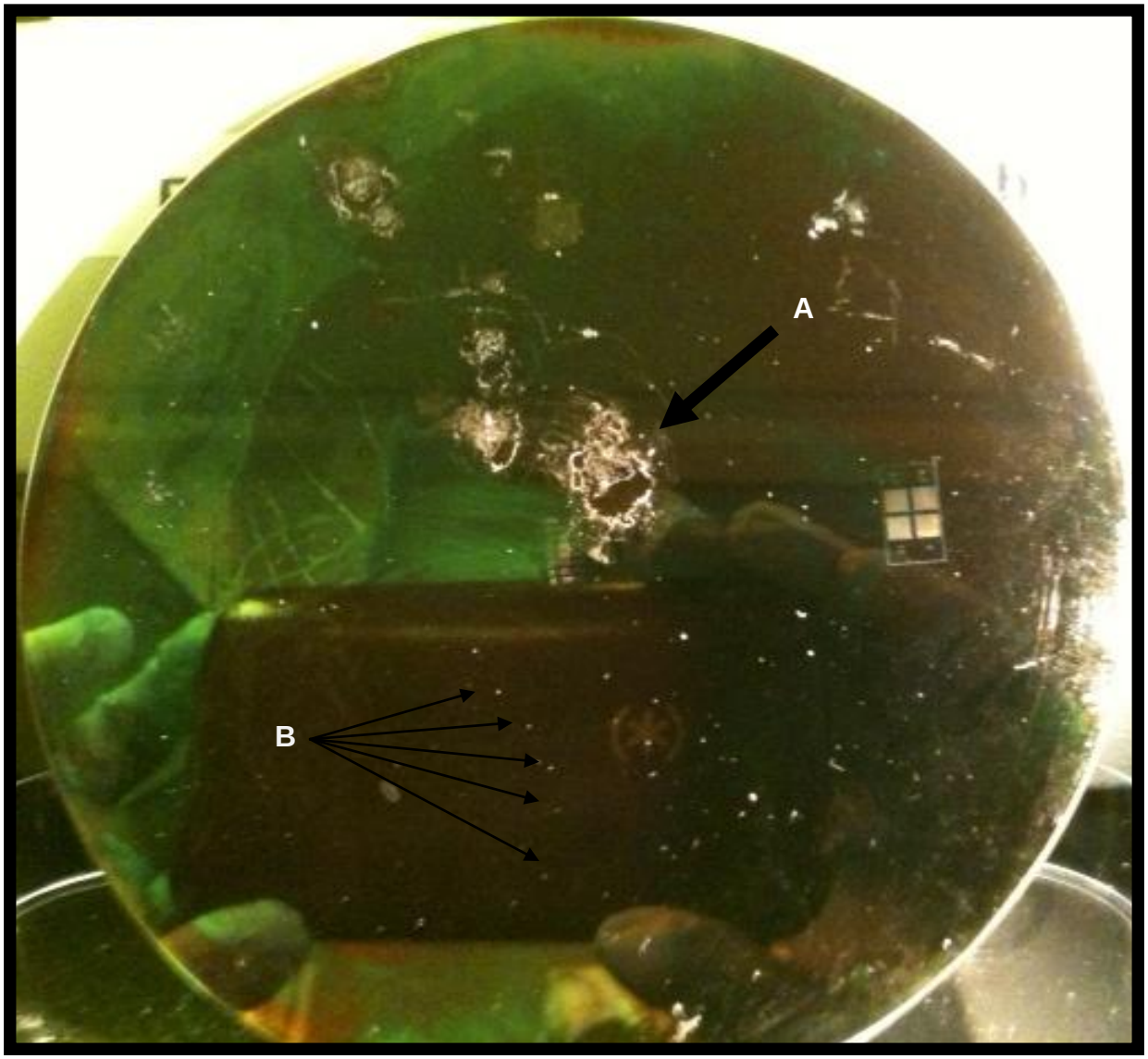

Figure 3.6: Soda lime glass coated with chrome and AZ photoresist. A) Notch defect. B) Pin holes.

After glass etching failed, several other methods were employed to replace the polystyrene coating used in the orientation and reorientation experiments. Hot Embossing, two part epoxy, and h-PDMS approaches were all developed in the search for a way to obviate the polystyrene coating. Three inch in diameter PMMA disks were hot embossed using a micromilled brass mold and a hot press (Carver Inc.). The resultant channel design was bonded to a thin sheet of PMMA (250 μm), see section 3.3.9.

To create a rotating gradient design of two part epoxy, a negative of the channel structure was fabricated in PDMS. This PDMS casting was then used a mold for the two part epoxy A Cast 690 (Smooth-On). After fabrication of the epoxy channels removal of the epoxy was difficult and led to cracks in the epoxy. Also, the epoxy did not bond well to glass. Because of these issues the two part epoxy method was eliminated from the list of potential non-porous substrates. Fabricating the channel in h-PDMS composite was also evaluated. h-PDMS was spun onto an SU-8 master fabricated in the μPG (Heidleberg Instruments), par-baked and a 10:1 ratio of PDMS to curing agent was poured onto the h-PDMS and cured. The h-PDMS composite was bonded to a glass slide using oxygen plasma. To compare the porosity of the successful methods to each other and to PDMS alone and with a PS coating the assay of PDMS absorption of hydrophobic compounds (section 3.3.5) was employed.

In figure 3.7 the absorption of rhodamine B, a small hydrophobic compound used as a proxy for pheromone absorption, is compared for all the substrates successfully used to fabricate the rotating gradient device. From this data it is clear that PDMS

absorbs the most rhodamine B into its bulk. The PS coating eliminates approximately two thirds of the rhodamine B absorption into the bulk of the PDMS substrate. However, the thickness of the coating and therefore its ability to block absorption varies. When this data is compared to the absorption in the h-PDMS composite, it is clear that this composite is far better than PDMS alone but is nearly indistinguishable from that of PS coated PDMS. The advantage of this substrate is that it can be fabricated more consistently that the PS coating. Ultimately, PMMA is the only substrate that blocks the absorption of small hydrophobic molecules. When comparing the data from the hot embossed device in PMMA to the other substrates, it is clear that PMMA does not absorb Rhodamine B, so it is unlikely it would absorb pheromone, and should be used going forward for rotating device fabrication.

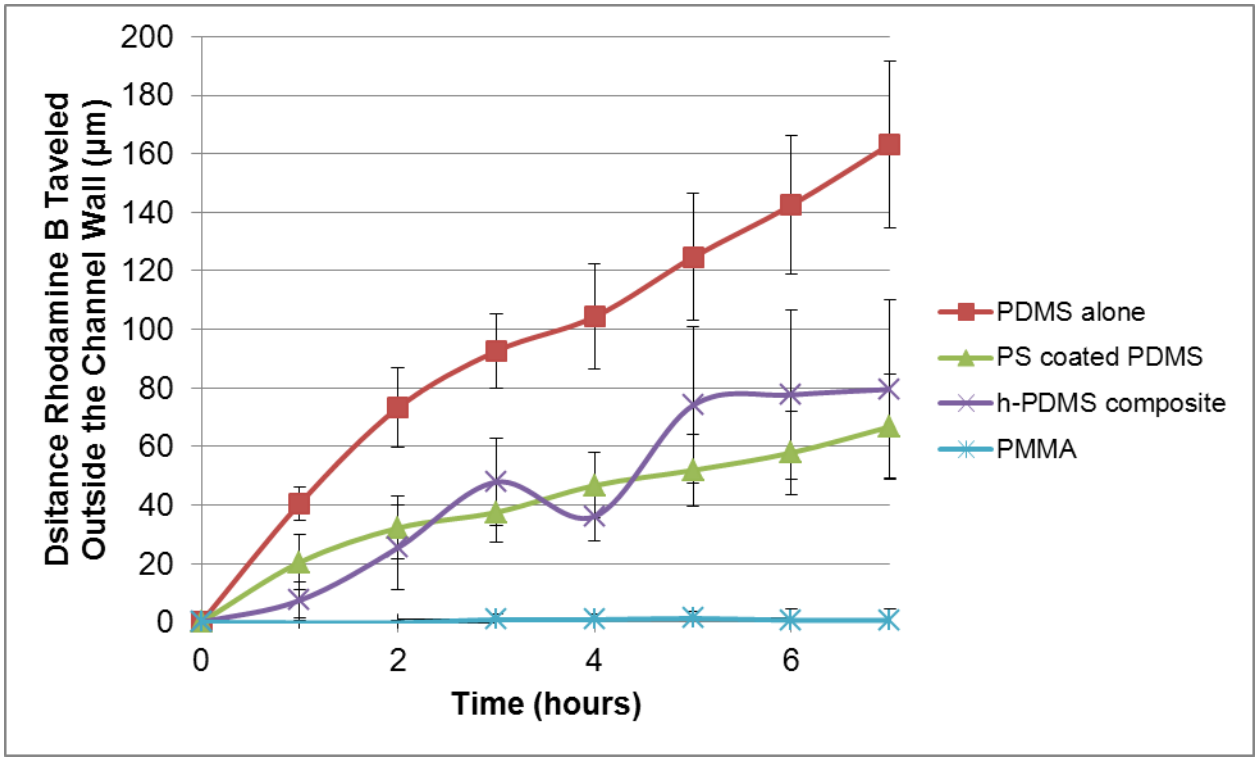

Figure 3.7: Assay of absorption of hydrophobic compounds. Comparison of rhodamine B absorption between PDMS, PS coated PDMS, h-PDMS, and PMMA subtrates.

3.4.3 Analysis of mutant yeast

$G\beta^{P-}$ were loaded into the PS coated rotating gradient device and subjected to a linear gradient, as described in section 3.3.6. To determine if the cells could form a shmoo or orient to the direction of the pheromone source images were captured every hour for a 7 hour time course, figure 3.8. The images were analyzed to determine the phenotypic response and the first projection of the $G\beta^{P-}$ cells was

measured to find the angle of orientation. As Gβ cannot be phosphorylated and thus is unable to recruits Far1-Cdc24 to the incipient growth site, it is expected that the data for the $G\beta^{P-}$ cells projections would have a mean angle of 90 degrees showing that the projections were random, inferring the mutants were unable to sense the gradient. The $G\beta^{P-}$ mutant did not orient and when compared to wild type data these was no significant difference in the angle of orientation in the $G\beta^{P-}$ cells and the negative control, figure 3.9. The rotating gradient device will be used to continue to test mutant strains with deficiencies in proteins along the chemotropic pathways for differences in phenotypic response.

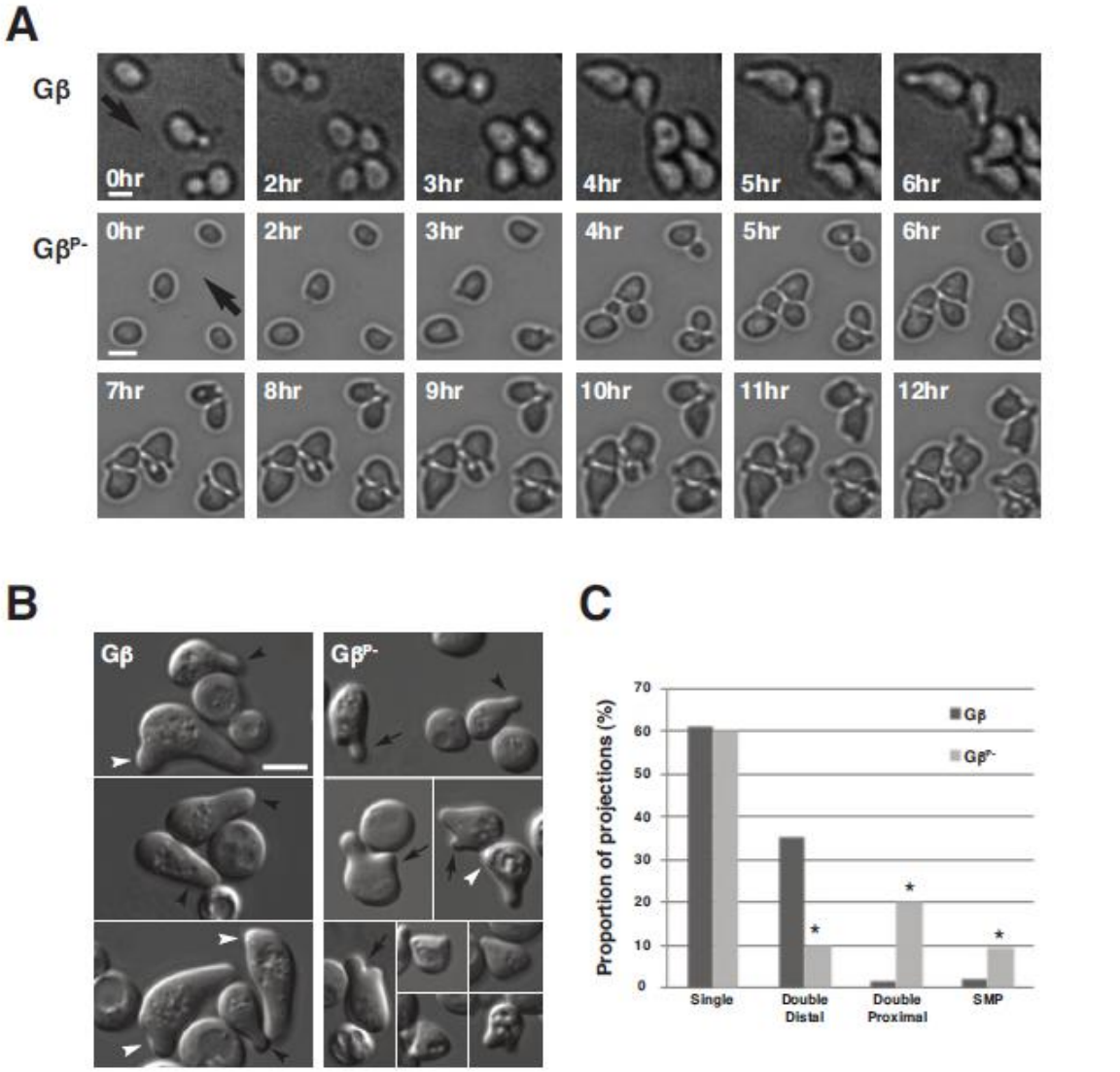

Figures 3.8: Gβ^{P-} confers chemotropic growth defects in both artificial and natural pheromone gradients. (A) Gβ^{P-} *BUD1* cells cannot properly orient and stabilize polarized growth in an artificial pheromone gradient. Representative time-lapse images of gradient-stimulated WT and Gβ^{P-} cells in a microfluidic device are shown. Arrows indicate the direction of the gradient. The mean orientation angle ± sem for the first protrusions formed by Gβ^{P-} cells was 89.9 ± 4.2˚(*n* = 314), as compared to 56.9 ± 4.6˚(*n* = 83) for WT shmoos, where 90˚ indicates random orientation. (B) Gβ^{P-} *BUD1* cells in mating mixtures exhibit shmoo defects similar to Gβ^{P-} *bud1*Δ cells exposed to isotropic pheromone. Representative images of cells from bilateral Gβ *BUD1* and Gβ^{P-} *BUD1* mating mixtures after 5 hr. Black arrowheads indicate cells scored as single shmoos; white arrowheads indicate distal double projections; black arrows indicate proximal double projections; small squares, are SMP cells. (C) Quantification of the shmoo types found in the WT and Gβ^{P-} bilateral mating mixtures. The percentages of shmooed cells in each class are shown in the bar graph. **p* < 0.0001 for the comparison Gβ vs. Gβ^{P-} in each class*; n* = 300 for both strains. Similar results were obtained in each of 3 trials.

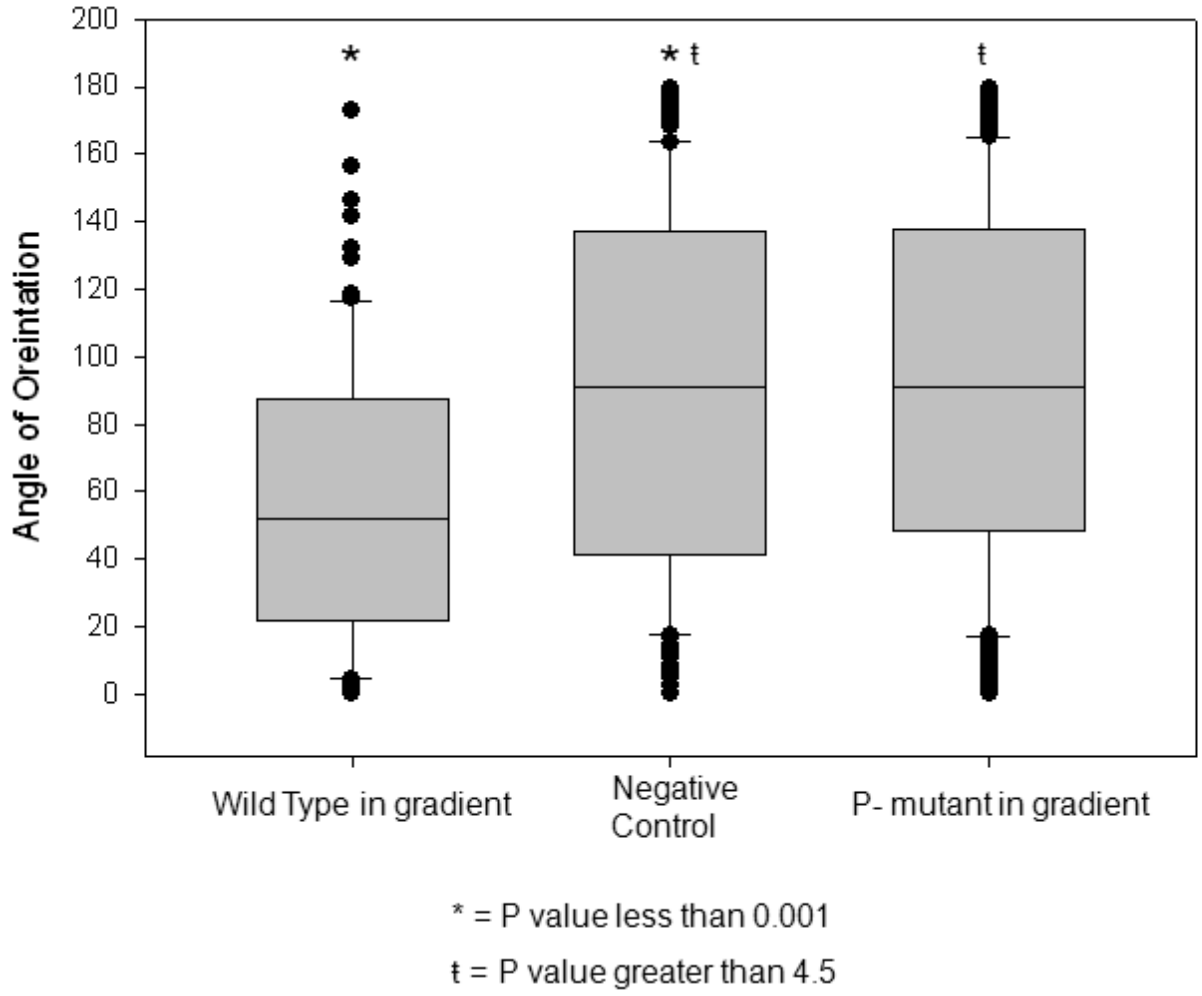

Figure 3.9: Comparison of angle of orientation of $G\beta^{P-}$ cells to wt cells in a gradient and in isotropic pheromone, the negative control. The $G\beta^{P-}$ mutant did not orient and when compared to wild type data these was no significant difference in the angle of orientation in the $G\beta^{P-}$ cells and the negative control.

3.4.4 Yeast cell positioning

PDMS stamps were fabricated using soft photolithography as described above. The stamp design consisted of circular pillars 25 μm in diameter spaced 700 μm apart. A YPD plate cultured with a lawn of wt MATa haploid type yeast cells, and PDMS stamps were used to pick cells from the plates in a desired pattern and stamp the cells on to a glass slide. This procedure was also performed on diluted overnight yeast cultures. Unfortunately the limits of soft photolithography do not allow for much more than a 1:1 aspect ratio. This was a problem in yeast stamping for two reasons. First, the width of the pillars was too large to pick up only one yeast cell. Secondly, if the diameter of the pillars on the stamp were decreased the height would also have to be decreased. This allowed liquid culture or cells from the YPD plate to get trapped next to the pillars and prohibited pattern formation.

A secondary method of yeast positioning was employed to achieve single cell patterning. This method was fabricating a set of two SU-8 masters containing alternating wells 25 μm in diameter and 75 μm apart to be used as a bio flip chip system. Upon flip chip fabrication, the chips were tested with either colored dye or 6 μm diameter FITC latex beads (Polysciences, Inc.), figure 3.10. Results from the colored dye experiments, as highlighted in figure 3.10 A and B, show that even with plasma treatment it was hard to fill the well with dye (figure 3.10A). After patterning this dye onto the YPD surface there are spots of excess dye and many wells that did not fill with dye at all (figure 3.10B). As a better proxy for yeast cells, 6 μm diameter FITC latex beads (Polysciences, Inc.) were similarly patterned on YPD plates. In figure 3.10C a brightfield image shows that even after solution removal, many of the

beads are on the flip chip but not in the wells. When the surface of the YPD was imaged, figure 3.10D, not only were many of the wells empty, but there was transfer of beads that were stuck on the flip chip but not in the well. This does not make this process a good candidate for micropositioning. Since none of the methods employed were able to pattern single cells for to be used for a confusion assay another route was taken all together. A confusion assay was to be implemented to test how differences in distance between cells or the addition of a confusing cell would affect the mating response in an *in vivo* assay.

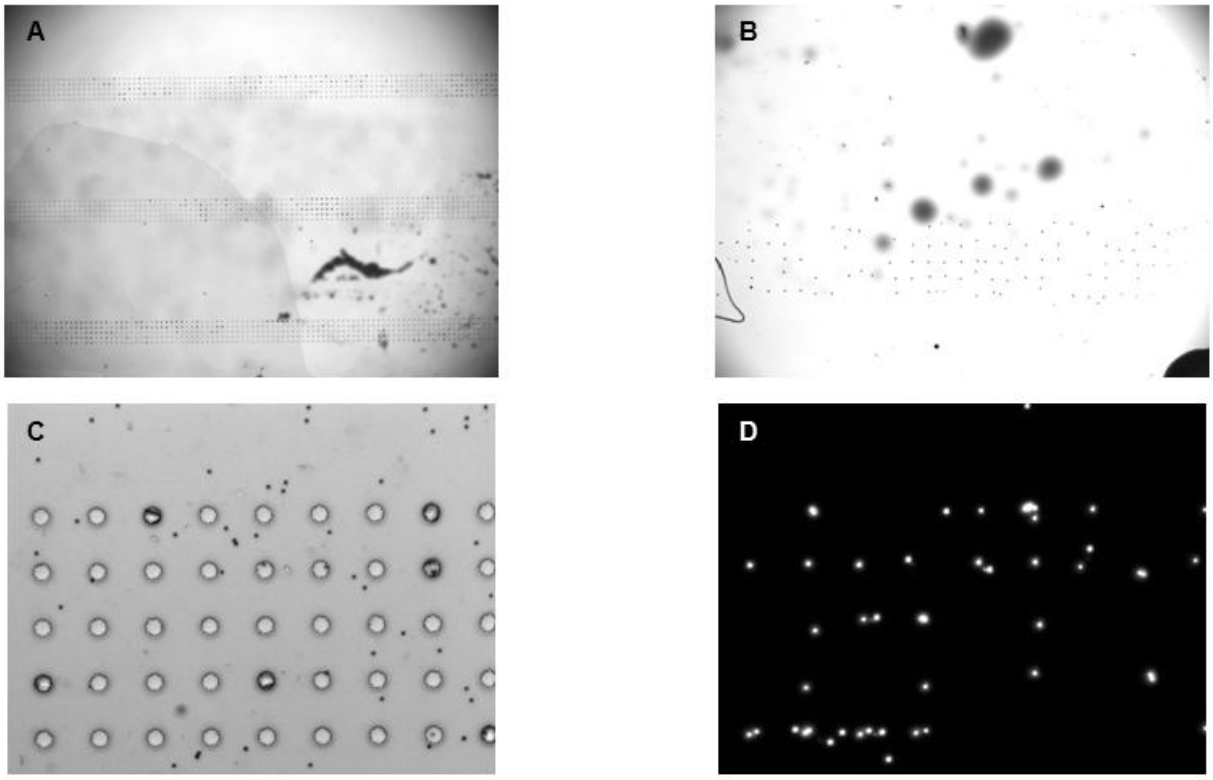

Figure 3.10: Flip Chip Patterning. A) Image of flip chip with dark blue dye after excess dye was removed. B) Image of agarose plate with flip chip patterned dye. C) Brightfield image of flip chip with 6 μm diameter FITC latex beads (Polysciences, Inc.) after excess solution was removed. D) Florescent image of YPD plate patterned with 6 μm diameter FITC latex beads (Polysciences, Inc.).

3.4.5 Automation Chemical Delivery Device

The ability to grease a stable linear gradient as shown in the rotating gradient device was conferred to an agarose pad. The reasoning behind this action is two fold. First, yeast biologists perform many assays on agarose pads in isotropic pheromone. This means a familiar platform can be used to repeat the same assays within a pheromone gradient, thus allowing for comparison with large sets of data. The second reason for ACDD is a confusion assay could be performed by plating a mating mixture on the agarose pad and then inducing a manufactured chemical gradient to see if this would confuse cells ways from their closest mating partner, thus eliminating the need for single cell positioning and allowing mutants along the chemotropic pathway to be tested.

The ACDD, figure 3.11, was used to manufacture a pheromone gradient by controlling the duration and timing of delivery of the four via used though a LabVIEW GUI, figure 3.12. To determine the pheromone gradient profile on the agarose surface, gradient characterization was performed with SR101, which has an excitation and emission of 585/605 nm. Sulforhodamine 101 dye was selected due to its comparable diffusion coefficient (4×10^{-6} cm2 s^{-1}) to alpha factor in water and commercial availability. The similarity of diffusion coefficients allowed for an estimation of gradient shape and concentration as a proxy for pheromone gradient used in the studies.

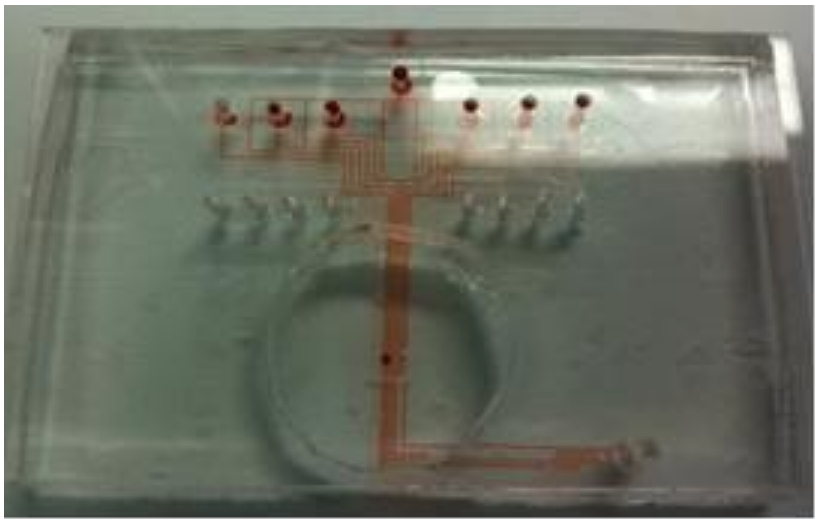

Figure 3.11: Image of ACDD. The ACDD was constructed through multi-layer soft photolithography of PDMS. Colored dye is used to highlight channels in red.

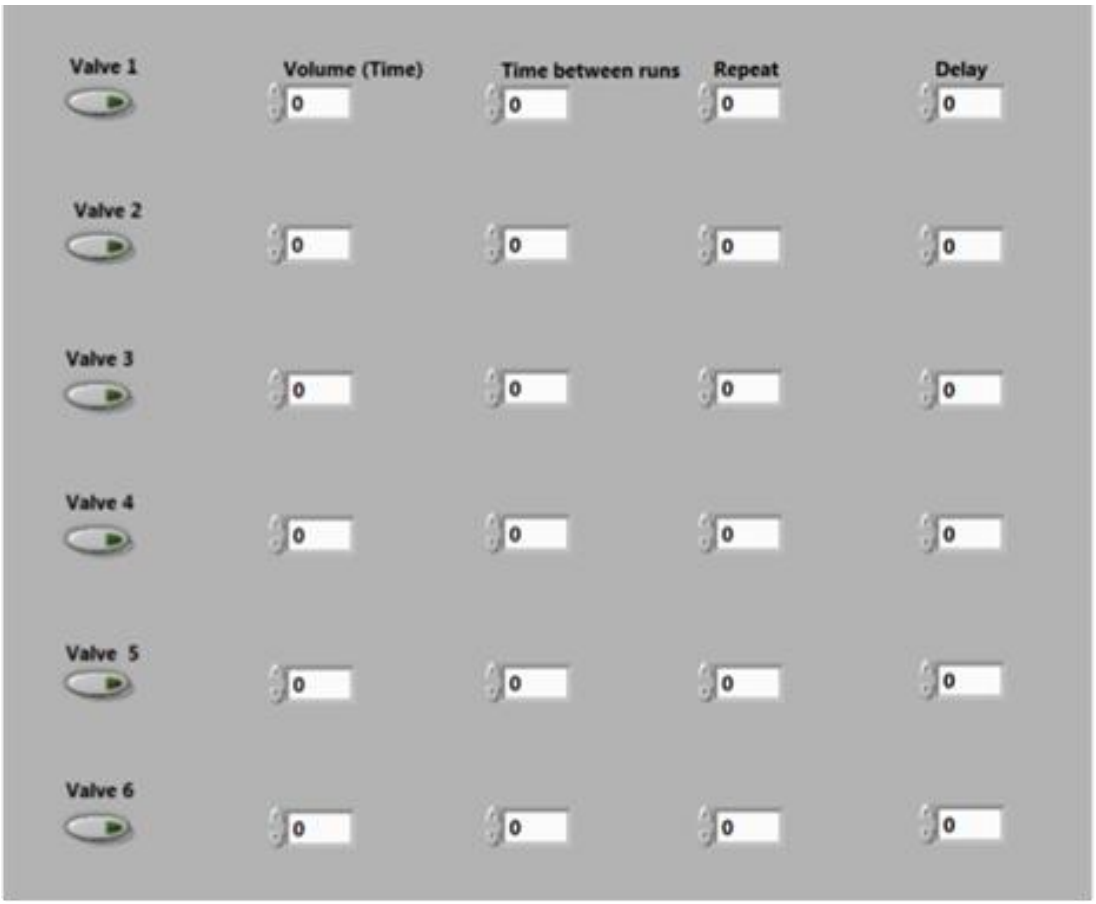

Figure 3.12: A screenshot of the LabVIEW based GUI to operate the PDMS valves in ACDD. Six different valves that can be independently controlled through the duration that the valves are open and close, the number of repetitions for a particular valve cycle, and the delay are controlled through this interface.

Establishing a linear and stable gradient in the agarose is essential to induce orientation. Dye was perfused into the channels and exited out the via where it diffused through the ~2 mm thick agarose pad to the surface where the yeast cells were seeded. To accomplish this, optimal timing of valve cycling was determined. To find a delivery cycle that did not overwhelm and saturate the agarose, but was capable of maintaining the stability of the gradient produced, several delivery cycles were tested, figure 3.13. Initially, one via was perfused with SR101 (0.01 mg/mL) with a delivery cycle of cycle of 5s on and 30 minutes off to determine the time it would take SR101 to reach the surface and the shape of the gradient profile produced. The results for this delivery cycle, figure 3.13a, show the gradient produced while linear was changed rapidly over time. As stability is an important factor for yeast chemotropic study, the amount of change was too large for this delivery cycle to be utilized. Several other combinations were tested but resulted in a widening profile. It was finally determined that a valving cycle of 10 seconds on and 5 minutes off produced a profile that was stable after 2 hours but did not flood the agarose pad, as shown in Figure 3.13b. Once the timing was determined, the focus became determine a delivery cycle that would create a sharp linear gradient over the via.

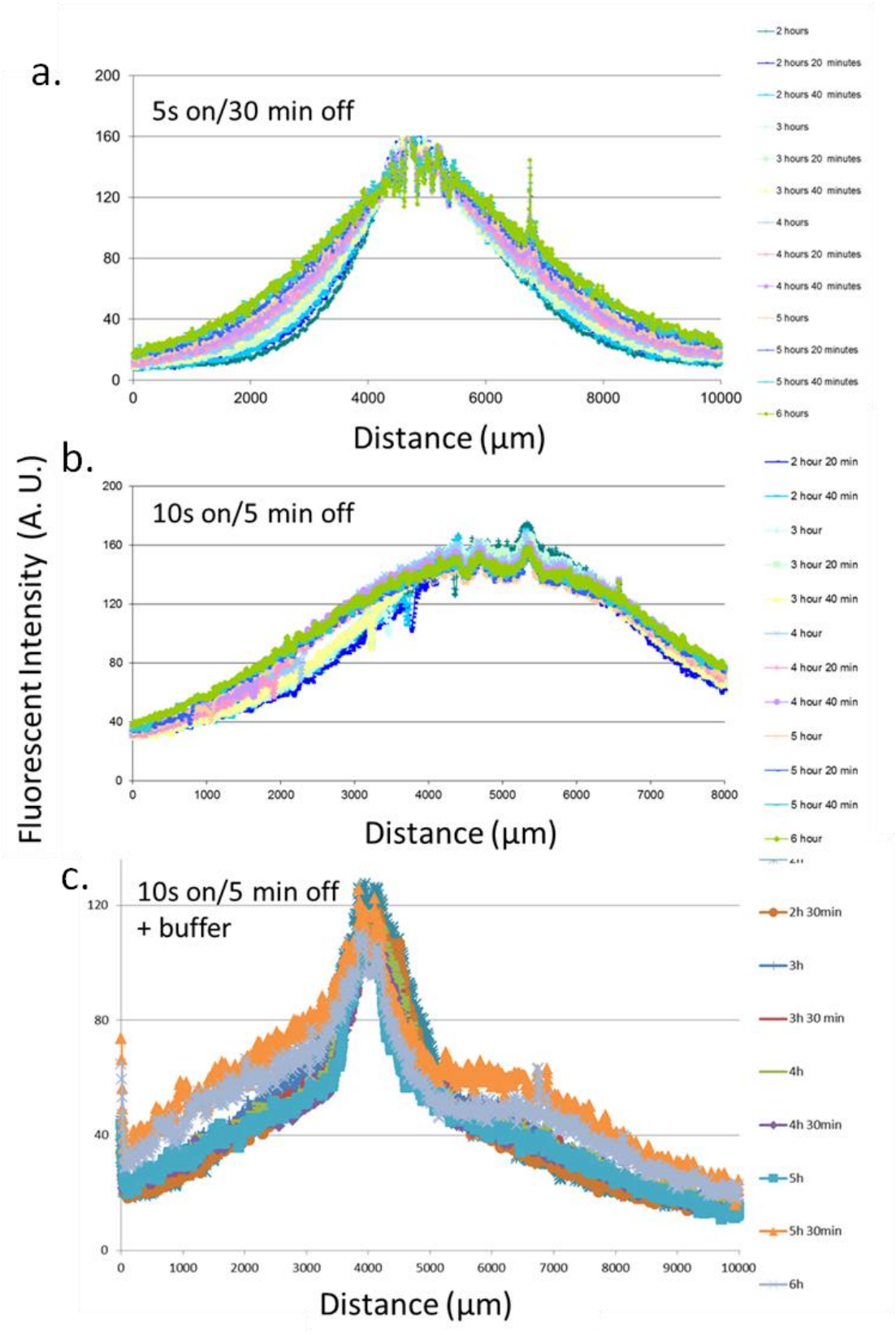

Figure 3.13: Line profiles of valve cycles (a) 5s on/30 minutes off, (b) 10s on/5 minutes off, and (c) 10s on/ 5 minutes off with buffer and pheromone were compared.

To produce a steep linear gradient over the via, a high concentration of SR101 (0.0025 mg/mL) was used in one channel (channel 2) and a low concentration of SR101 (0.00125mg/mL) (channel 3) to establish a steeper gradient difference. The concentration of SR101 was reduced from single via trials to decrease the incidence of oversaturation in the images. The slope of the linear portion of the gradient profile was sharper however spreading at the top of the profile and the edges were still apparent, 3.13b.

The final step to create a sharp linear profile was to flank the SR101 via with channels filled with buffer, in this case water. The delivery cycle of the buffer was also optimized. The time the valve remained open was held constant at 10 seconds. Only, the time the valves were off were changed. Initially, two delivery cycles of 2 or 3 minutes off were tested; unfortunately this disturbed the profile of the original gradient instead of sharpening it. When delivery cycle times were increased (5 and 6 minutes off) the profile did not exhibit a change. Ultimately, a buffer delivery cycle of 10 seconds on and 4 minutes off was determined to be fast enough to be a sink on either side of the SR101, but not so fast that it disturbed the profile or flooded the agarose surface, thus producing a sharp and stable gradient, figure 3.13c.

The final parameters used for the yeast studies are as follows. A linear gradient was established in the agarose pad by flowing a high concentration of SR101 (0.0025 mg/mL) in channel 2 and a low concentration of SR101 (0.00125 mg/mL) in channel 3. Channels 1 and 4, filled with sterile water, served as buffer channels to blunt the profile and created a sharper slope. In addition, the optimal valve cycling for a stable

gradient was determined to be 10 seconds open and 5 minutes closed for channels 2 and 3, and 10 seconds open and 4 minutes closed for channels 1 and 4. The outside channels were perfused faster to create a steeper slope in the gradient. Figure 3.14 shows the change in intensity of the agarose pad between 0 minutes (3.14a) and just after 30 minutes (3.14b) of perfusion, and the profile of SR101 in the agarose after two hours is shown Figure 3.14c.

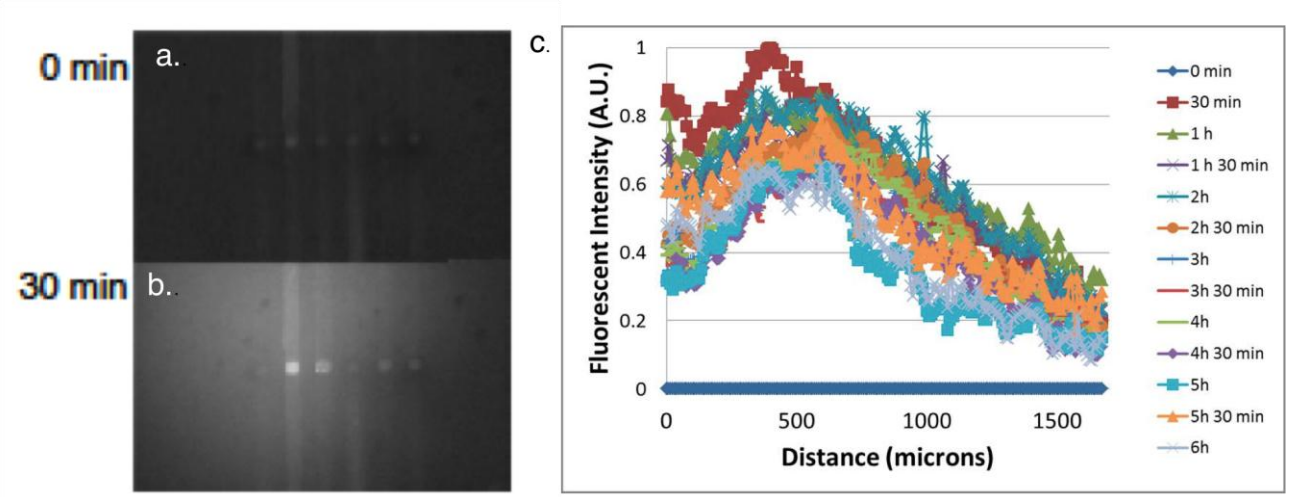

Figure 3.14 SR101 visualization of the gradient profile in the agarose before perfusion (a) and 30 minutes after perfusion of SR101 dye (b). After 30 minutes, a noticeable increase in intensity was observed. (c). An intensity profile was collected after 2 hours of perfusion and it exhibited a stable and linear profile.

The SR101 studies gradient experiments provide an approximation of the pheromone gradients produced to be used in orientation assays. A linear pheromone gradient was established similarly to the SR101gradient in the agarose by flowing a high concentration of pheromone (400 nM) + YPD in channel 2 and a low concentration of pheromone (200 nM) + YPD in channel 3. Channels 1 and 4, filled with YPD without pheromone, served as buffer channels. Since the gradient stabilized after 2 hours, the yeast cells were placed onto the agarose pad with a PDMS stamp after this time point (figure 3.15). The stamp ensured that a small number of yeasts and more importantly single yeast cells were deposited onto the agarose. Stamping was performed using a PDMS stamp with 400 μm diameter posts positioned 1mm apart. The stamp was dipped in overnight liquid culture of wt MATa cells and excess sample was removed. The stamp was then placed on the agarose pad over the via, figure 3.15. The yeast cells were imaged every hour for 5 hours to track the chemotropic response to the artificial gradient. Using the same criteria as in the rotating gradient device, the angle of orientation, α, was measured for single yeast cells. Table 3.2 shows the results from the studies. Out of 62 eligible cells, 36 cells shmooed, and the average angle of orientation was 62.2 degrees with an SEM of 6.8 degrees. This confirmed that the cells were able to recognize the gradient and orient preferentially towards it. It is important to note that the cells oriented with a similar orientation to the gradients as in other microfluidics devices.

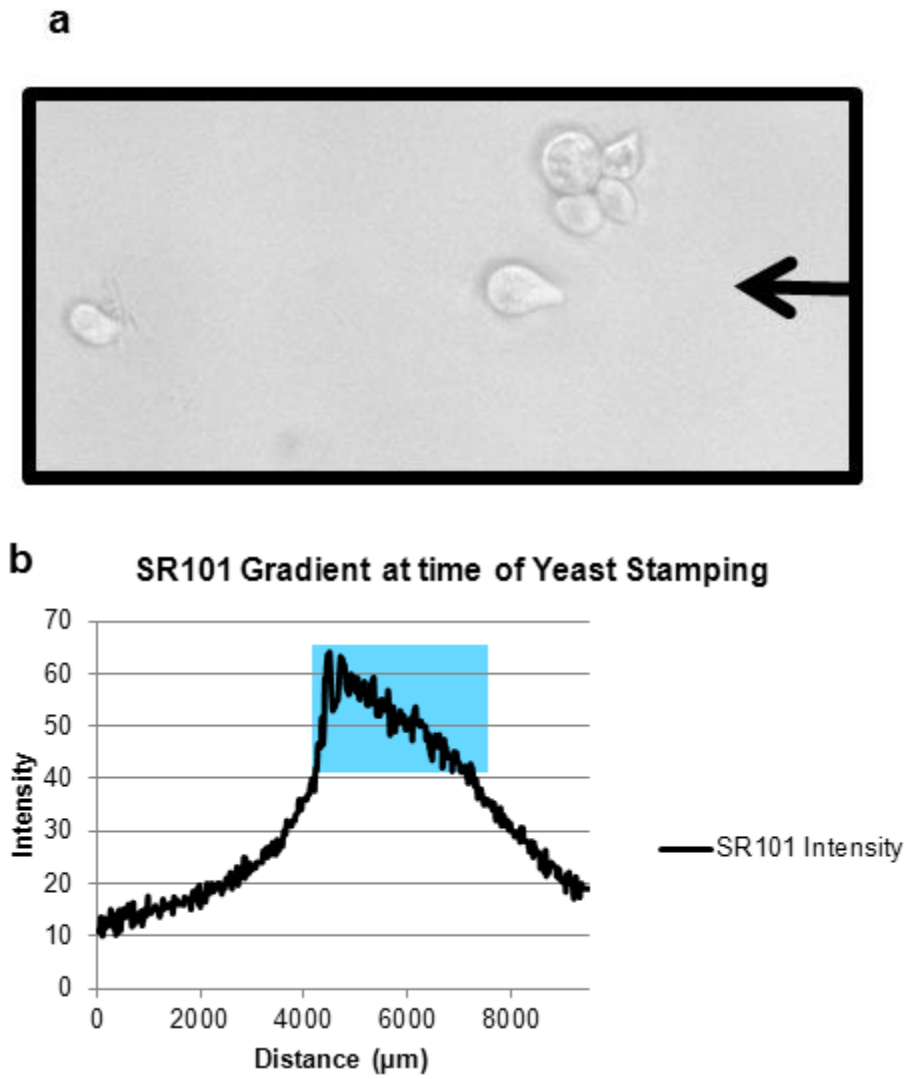

Figure 3.15: Orientation in the ACDD. a) wt MATa cells on the surface of the agarose pad, arrow indicates the direction of the pheromone gradients. b) SR101 gradient at time of yeast stamping. Blue represents area over via where cells were positioned.

# of eligible cells	64
# of shmooing cells	36
Average angle of orientation	62.2 degrees
Standard Deviation	40.8 degrees
SEM	6.8 degrees

TABLE 3.2: ACDD orientation data. Data derived from ACDD orientation assays.

3.5 Discussion

There are several examples of microfluidic devices that are able to generate microscale gradients [20, 94, 99-102], including some that have been used to apply a pheromone gradient to the budding yeast, *S. cerevisiae* [17-20, 76, 103]. However, none of the devices designed to study yeast chemotropism can mimic the dynamic gradients that yeast cells experience in bona fide mating mixtures. Although these devices have been used to completely reverse gradients, a 180˚ change of this magnitude is likely to induce the formation of a second mating projection rather than the bending of the initial projection, and may be of limited physiological relevance in the study of gradient tracking. To remedy this, a novel microfluidic device has been developed for the study of yeast chemotropism that has the standard ability to form stable, linear pheromone gradients, and the unique ability to rapidly change the direction of the applied gradients in 90˚ increments. The data in this chapter demonstrate these capabilities in two ways. First, the capabilities of the rotating gradient device were directly imaged and quantified to measure the formation and redirection of chemical gradients in the device using sulforhodamine 101 (Fig. 3.2). Second, the yeast cells themselves were used as sensors of the putative pheromone gradients. The orientation and reorientation data shown in Figures 3.4 and 3.5 clearly indicate that the cells detect and respond to both the initial gradient and the change in its direction suggesting this is a dynamic process. An additional advantage of our device is that the cells are held in place by mechanical trapping rather than being chemically coupled to the substrate, thus eliminating the concern that their chemotropic growth could be influenced by membrane protein signaling pathways.

Although not documented here, the rotating gradient device, like those that have been published, can be used to create pheromone gradients of variable concentration and shape. To decrease the slope of the applied gradient, for example, medium containing a 0.25X concentration of pheromone can be diffused into the three channels while 1X pheromone is diffused into the fourth.

In summary, the ability to control the rotation of a pheromone gradient provides a powerful new tool to investigate chemotropism in a model eukaryote. This device will be used to characterize the phenomenology of gradient tracking, and ultimately, by taking advantage of the genetic tools available in yeast, to dissect the mechanisms underlying this important cellular function. In the next section this tool is used to further elucidate the chemotropic pathway through the study of a chemotropic mutant, GβP-.

3.5.1 Mutant yeast cells

GβP- mutant cells were subjected to standard orientation and reorientation assays as described in Appendix B and seen in figure 3.8. One explanation for the results of the orientation and reorientation assays is that GβP- confers a defect in directional sensing and/or chemotropic shmooing. However, it is also possible that GβP- cells signal their positions less effectively than WT cells because their pheromone secretion is less focused. To distinguish these possibilities, the ability of Gβ and GβP- cells to grow toward a source of pheromone in vitro was compared using the rotating gradient device. As previously reported, the Gβ control cells formed normal mating projections in the artificial gradient (Appendix B, Fig. 6A) and oriented toward

its source with an accuracy similar to that observed in other published microfluidic experiments [17, 18, 76]. Surprisingly, the GβP- cells were unable to sustain growth in a single direction. Rather, they formed multiple small protrusions, often without growing much in overall size, very much like the SMP cells found in GβP- bud1Δ cultures treated with isotropic pheromone (Appendix B, Fig. 1B). Moreover, the first protrusions formed by the gradient-stimulated GβP- cells were positioned randomly, virtually without detectable orientation toward the pheromone. This was confirmed when the GβP- orientation angles were compared to that of wt cells in a gradient and in isotropic solution conferred in the negative control, figure 3.9.

These data strongly support the idea that Gβ phosphorylation plays a role in the positioning and maintenance of the chemotropic growth site. Under isotropic conditions, GβP- cells form normal mating projections at the presumptive default site, apparently unaffected by their inability to phosphorylate Gβ. When subjected to directional stimulation, however, the mutant cells appear to “realize” they are in a gradient, repeatedly trying and failing to stably grow towards the source. Remarkably, GβP- cells exposed to an artificial pheromone gradient were unable to stabilize their growth at the default shmoo site. This device will continue to be used test mutant strains with deficiencies in proteins along the chemotropic pathways for differences in phenotypic response.

3.5.2 Non-porous substrates

Initially the rotating gradient device design was etched in soda lime glass as described in section 3.3.8. Unfortunately, even with special precautions taken to obscure any incidental UV irradiation of the AZ photoresist coating the plate, the sensitivity of the photoresist was too great to overcome. As can been seen in figure 3.6, both pin holes and notch defects were present after only one exposure and etch cycle [79, 104]. This implies that the current etching conditions are not favorable for the three step etching needed to etch the three layer rotating gradient device design into soda lime glass.

After glass etching failed, several other methods were employed to replace the polystyrene coating used in the orientation and reorientation experiments. Hot Embossing, two part epoxy, and h-PDMS approaches were all developed in the search for a way to obviate the polystyrene coating. After fabrication of the epoxy channels, removal of the epoxy was difficult and lead to cracks in the epoxy. Also, the epoxy did not bond well to glass. Because of these issues the two part epoxy method was eliminated from the list of potential non-porous substrates. To compare the porosity of the successful methods to each other and to PDMS alone and with a PS coating, the assay of PDMS absorption of hydrophobic compounds (section 3.3.5) was employed.

In figure 3.7 the absorption of Rhodamine B, a small hydrophobic compound used as a proxy for pheromone absorption, is compared for all the substrates successfully used to fabricate the rotating gradient device. From this data it is clear that PDMS

absorbs the most rhodamine B into its bulk. The PS coating eliminates approximately two thirds of the rhodamine B absorption into the bulk of the PDMS substrate. However, the thickness of the coating and therefore its ability to block absorption varies. When this data is compared to the absorption in the h-PDMS composite, it is clear that this composite is far better than PDMS alone but is nearly indistinguishable from that of PS coated PDMS. The advantage of this substrate is that it can be fabricated more consistently that the PS coating. Ultimately, PMMA is the only substrate that blocks the absorption of small hydrophobic molecules. When comparing the data from the hot embossed device in PMMA to the other substrates, it is clear that PMMA does not absorb rhodamine B, so it is unlikely it would absorb pheromone, and should be used going forward for rotating gradient device fabrication.

3.5.3 Automated Chemical Delivery Device

The automated chemical delivery device is a platform that can establish gradients in tissues and other constructs. Here, a pheromone gradient was produced on an agarose pad for the study of yeast chemotropism. While the construction of the device and its corresponding setup require many components, the device was not difficult to operate after assembly and the end user is simply required to use gravity perfusion and the LabVIEW GUI for operation. An advantage of this device is the ability to seed cells on agarose. This means a familiar platform can be used to repeat the same assays within a pheromone gradient, thus allowing for comparison with large sets of data already available. The second reason for employing the ACDD is that a confusion assay could be performed by plating a mating mixture on the

agarose pad and then inducing a manufactured chemical gradient to see if the influx of an external gradient would confuse cells ways from their closest mating partner, thus eliminating the need for single cell positioning and allowing mutants along the chemotropic pathway to be tested.

The gradient profile produced by the ACDD can be adjusted to fit experimental needs. For the chemotropism experiments, the optimal valve cycle and pheromone concentrations created a profile suitable for orientation studies. However, these parameters are flexible and can be altered for other studies. For example, to create a steeper gradient, a larger difference between the pheromone concentrations (400 nM and 200 nM to 400 nM to 50 nM) or faster perfusion of the buffer channels could be implemented.

The orientation experiments performed in the ACDD confirmed that wt yeast sensed a gradient and preferentially shmooed in the direction of the gradient. There were initial concerns over the ability of the yeast to shmoo since the gradient was essentially underneath the cells and although the yeast cannot burrow in the agarose, it was unknown if they would be able to sense a planar gradient below them. However, the angle of orientation of 62.2^{o} measured in the orientation experiments is comparable to other microfluidic devices [17, 18, 76, 87]. One issue that arose was the number of cells that were shmooing in the gradient. In liquid yeast culture with an α factor concentration of 200 nM or 400 nM approximately 80% of cells shmoo. The results from the ACDD reveal a much lower portion of cells, approximately 56%, shmooed. Several factors could contribute to the discrepancy. Although a PDMS stamp was used to place cells onto the agarose pad, a large

number of cells were aggregated together. These cells, although many of them shmooed, did not meet the criteria to be scored in the orientation assay. In addition, it is possible that the concentrations used (400 and 200 nM) do not produce a gradient steep enough to trigger shmooing in a high percentage of cells. As stated before, cells respond to a very steep gradient, so increasing the slope may increase the number of cells that shmoo. Future experiments, detailed in the future direction section, will explore the limits of the gradient production to improve both angle of orientation and the number of cells shmooing.

It is important to note that the success of both the rotating gradient device and the ACDD is relative. When compared with previous microfluidic devices, the rotating gradient device out performs other microfluidic devices by inducing orientation with a mean angle nearly 15 percent lower than previously published reports [17-19, 76]. The ACDD also has shown the ability to induce orientation similar to previously published microfluidic devices. The ability of these devices to induce a chemotropic response in wild type and mutant cells has allowed for the generation of robust data that can be systematically quantified and has permitted the measurement of biological phenomena, such as reorientation, that were only able to be anecdotally observed by other researchers. Microfluidic techniques harbor the ability to devise devices that allow the study of biological processes previously unable to be elucidated by other technologies. However, these devices are not always able to exactly replicate what nature provides. In the case of yeast chemotropism, in a true mating mixture of MATa and MATα haploid cells, the degree to which cells will orient to form a diploid is on the scale of 0 to 10 degrees. This highlights the fact that while microfluidic tools allow for the generation of new types of data and quantification of

phenomena that other technologies do not, there is still room to improve in order to truly replicate the microenvironment found in nature.

3.6 CONCLUSION

In this chapter the design, fabricate, and characterize a microfluidic device that creates and rotates a chemical gradient by 90° was accomplished through soft photolithography techniques. After characterizing the gradient created by the device and testing the polystyrene coating, the validity of the device was tested through the induction of orientation in wild type *S. cerevisiae* and compared the angle of orientation to a negative control. The device was able to induce orientation, with an angle of 56.9°, compared to the negative control which showed no discernible orientation. Ultimately the goal of this work is to induce reorientation. The rotating gradient device was able to induce reorientation in 83.6% of cells in a systematic and measurable fashion. The advantage of this device is its ease of use and ability to create and rotate chemical gradient to further study *S. cerevisiae* and its mutants to further elucidate the chemotropic mechanisms involved in mating projection growth.

The rotating gradient device was then used to test the ability of GβP- cells to orient in a chemically manufactured α factor gradient. The comparison of the angle of orientation measured in GβP- cells versus wt cells in a gradient or treated with isotropic pheromone highlighted the GβP- cells inability to sense the direction of a gradient. To obviate the need for the PS coating several non-porous substrates were tested to determine if the rotating gradient design could be replicated in a substrate that would not absorb small hydrophobic compounds into its bulk. Through

this testing it became clear that hot embossing of PMMA is a good solution to replace the PS coating.

Finally, the ability to induce a manufactured α factor gradient was conferred to an agarose pad using the ACDD. Preliminary results from orientation studies in this device suggest that the ACDD can be used to induce orientation. Ultimately, this device will be used to subject mating mixtures to a manufactured α factor gradient in the hopes that a confusion assay can be developed to further elucidate the chemotropic pathway.

3.7 Future direction

To completely eliminate the PS coating from the rotating chemical device design the PMMA embossed substrate needs to be fully characterized. As the assay for absorption of small hydrophobic molecules has already been completed, the next step is to use SR101 as in section 3.3.4 to characterize the rate and shape of the gradient formation in the PMMA device. Upon characterization of the gradient orientation and reorientation assay should be performed to insure that cells can be loaded and subjected to a pheromone gradient. The concentration of pheromone may need to be altered as it will be blocked from absorption in to the bulk of the PMMA. Finally, this new fabrication of the rotating gradient device can be used to test mutants along the chemotropic pathway.

While a 60^{o} angle of orientation measured in the ACDD device coincides with the angles stated in literature [17, 18, 76, 87], to determine if this phenomenon is

significant negative control experiments must be performed in this device. Negative controls will be performed by replacing the varying concentration of pheromone in YPD and YPD alone in the channels with the same concentration of pheromone in YPD to induce the formation of an isotropic solution of pheromone on the agarose surface. This isotropic pheromone solution on the agarose surface will also be characterized with SR101 to determine uniformity.

To eliminate the clusters of cells found in current ACDD orientation experiments, a velvet-PDMS stamp will be fabricated. Velvet is commonly used to replicate yeast plates and the fibers of the velvet surface only transfer a single cell layer. The use of this stamp to introduce yeast to the agarose pad should allow for a higher number of cells to meet the criteria of orientation measurement. After orientation experiments, the ACDD can be modified to add via for the induction of reorientation in yeast. The ACDD could also be used to subject mating mixtures to a manufactured α factor gradient in the hopes that a confusion assay can be developed to further elucidate the chemotropic pathway.

3.8 AKNOWLEDGEMENTS

This work was supported by NSF grant: Heterotrimeric G Protein Regulation of Chemotropism in Yeast; Award number: MCB-1024718. Also a special thanks to Elizabeth Ferraz for her fabrication contributions.

Chapter 4 *Ex Vivo* Culture of Mouse Embryos

4.1 Abstract

The development of mammalian embryos occurs in utero, making it impossible to achieve high resolution imaging of most stages of mammalian development in its native environment. As such, one shortcoming of mammalian developmental biology is the inability to combine genetic analyses with real-time imaging to provide an understanding of the dynamics associated with many developmental processes. This shortcoming is especially evident for gastrulation in mouse embryos, where the kinetics of cellular behavior are not understood with respect to rapidly changing patterning signals. To address this problem, a novel method for culturing gastrulating mouse embryos in a microfluidic device was designed. This new platform improved *in vitro* development of embryos relative to commonly used culture techniques. This device is adaptable to a variety of microscopy systems and has the potential to be modified for potentially powerful future applications bringing together the genetics of the mouse with methods of assessing rapidly changing dynamics of cellular defects.

4.2 Introduction

The study of gastrulation in mouse embryos is important to elucidate the pathway of early development in mammalian embryos. This process requires expansive cell movements that must occur in the correct spatial and temporal pattern to set up the basic body plan of the embryo [23]. Currently, the study of whole embryos is limited

to collecting data at static time points and inferring development between these periods [21, 22]. The dependency of embryos on the support of the uterine environment has been a challenge in culturing embryos *ex vivo*. Roller-bottle culture, described below, allows for the *ex vivo* culture of embryos, but not continuous visualization or imaging of embryos [22], leaving the problem of taking data at static time points. Jones *et al*. devised a way to culture mouse embryos under continuous monitoring but were unable to culture embryos less that 8.5 days postcoitum (dpc) [21], thus eliminating the possibility to study gastrulation.

Mouse gastrulation is a dynamic process through which cell lineage specification is coordinated with elaboration of the basic body plan. Embryos change significantly between embryonic day 6.5 (e6.5) to e7.5, progressing through up to eight distinct morphogenetic stages. The small size of gastrulating embryos requires examination at the resolution of a dissecting microscope for staging [105]. Cells in gastrulating embryos exhibit extremely rapid proliferation, as embryos expand from ~660 cells at e6.5 to ~15,000 cells at e7.5 [106]. Labeling epiblast cells and subjecting embryos to *in vitro* culture reveals extensive cell movements after a 24 hour culture period [107, 108]. Remarkably, these cellular and embryonic dynamics occur concomitantly with the specification of the three primary germ layers from epiblast progenitor cells.

Although the dynamic nature of gastrulation may indicate spatiotemporal coordination between cellular movements and lineage specification, how these cellular processes may be coordinated remains unclear. Despite years of research progress that have genetically defined factors (BMP, Wnt, Nodal) necessary for gastrulation [109], the relatively poor understanding of cellular behaviors in embryos

at this stage has held back the understanding of how the signals work together. One issue is that developmental biologists have almost exclusively used static measurements to (i.e. gene expression or morphology of fixed embryos) to examine this dynamic process. Consequently, no consensus has been reached as to how the activity of three pathways is coordinated to direct cell lineage specification at the primitive streak (PS) at the true time.

New methods of manipulating embryos and pluripotent cells are needed to understand the cellular dynamics associated with gastrulation. Real-time imaging of cellular activities during gastrulation would provide a powerful complement to mouse genetics. Currently, *in vitro* embryo culture techniques are ill-fit for combining live imaging with normal developmental progression from e6.5 to e7.5. Traditionally, roller culture systems have been utilized for *ex utero* development of these stages [22, 110-112]. These systems allow “in utero”-like development of gastrulating embryos for approximately 24 hours in a nutrient rich media with high concentrations of rat serum [22]. However, this technique is incompatible with live imaging due to the constant motion of the embryo. The alternative to roller culture systems is to allow the embryo to develop in a static environment, sitting atop a glass coverslip or in a petri dish [22, 111-113]. While static culture is amenable to live imaging, it is not clear how well the embryo progresses through normal development. For instance, a recent report utilizing static culture showed a surprisingly lack of cell movement in the embryo at the onset of gastrulation [114]; a finding incongruent with previous observations of extensive cell movement during gastrulation [108]. It is thought that roller culture systems allow normal embryonic development because the constant

agitation of media accommodates a need for embryos to replenish energy/nutrient sources and exhaust waste products [22, 112, 113].

Recently, the parameters determining how embryos can be cultured have been transformed by microfluidic devices that can manipulate the flow of fluids at the micrometer scale [115, 116]. Several groups have designed culture systems utilizing microfluidic-based culture chambers for culture of *D. melanogaster*, Zebra fish, and pre-implantation mouse embryos [117-120]. The flexibility and ease of designing and fabricating such microfluidic devices presented unique possibilities for the generation of a new culture system for post-implantation mouse embryos that could combine the positive features of both roller and static culture systems. In this chapter, methods for the development of new methods enabling live culturing of gastrulation-staged mouse embryos are described. These new methods utilize novel microfluidic devices that perfuse media over a stationary mouse embryo. The microfluidic device culture methods accommodated normal developmental progression through gastrulation. The optical clarity of the device and static position of the embryo within the device provides an ideal methodology for live-imaging of cellular activity during mammalian gastrulation.

4.3 Materials and Methods:

4.3.1 Fabrication of the microfluidic embryo culture chamber

Standard soft photolithography techniques were used to fabricate mouse embryo culture devices from PDMS (Figure 4.1). The device geometries were designed in Adobe Illustrator and printed onto a Mylar transparency at 1600 dpi (Fineline Imaging). To create the device master, SU-8 photo-resist 2150 (Microchem) was spun onto a 3 inch silicon wafer at 500 rpm for 10 seconds followed by 1000 rpm for 30 seconds. The photoresist covered wafer was soft baked at 65ºC for 15 minutes and then 95ºC for 75 minutes. Following the soft bake, the photo-mask was placed on top of the wafer and both were exposed to UV radiation at an intensity of 100 mJ for 75 seconds. The exposed wafer was baked at 65ºC for 7 minutes and then 95ºC for 60 minutes. The unexposed SU-8 photo-resist was removed using SU-8 developer solution (Microchem) revealing only the exposed SU-8 photo-resist containing the pattern of the device on the wafer, which serves as a master to fabricate the device in PDMS. PDMS was mixed at a 10:1 ratio of PDMS pre-polymer to curing agent (Sylgard 184, Dow Chemical), degassed under vacuum, and cast onto the master wafer in a petri dish. The polymer was cured by baking at 75ºC for 2 hours and removed from the master by cutting out the area containing the device design. 13 gauge holes were punched into each inlet and outlet channel using a hollow metal needle (McMaster-Carr). The PDMS device was then bonded to a 75 mm x 38 mm glass slide using a corona plasma treater (Electro-Technic Products, Inc.). The transparency of the PDMS device allows for imaging of embryos from either the top through the device or bottom through the slide. Alternatively, the device could be bonded to a glass coverslip to allow for confocal microscopy. Thus,

the device can be utilized for simultaneous culture and live imaging of three embryos with various microscopy systems.

4.3.2 Fabrication of bench-top device

The bench-top mouse culture device consists of four layers. First, 1/8" od Tygon tubing (Cole Palmer) is cast in a 120mmx120mm square Petri dish (Fisher) using PDMS. Once the PDMS is cured the casting is removed and cut into sixths with each piece including Tygon tubing cast in the center. A 13mm diameter hole is then punched into the center of each piece, this forms layer one of the device. Layer one is then plasma bonded to a 75 mm x 38 mm glass slide using a corona plasma treater (Electro-Technic Products, Inc.). Layer two is an 18mm x 18mm coverslip (Fisher) which is plasma bonded to layer one, covering the hole punched in layer one. This will be the layer the embryos rest on. Layer three is the same PDMS casting used in the incubator device, see above, this layer is bonded to layer two using plasma treatment as well as a thin bead of PDMS around the outside of the third layer. The partially fabricated device is then inverted, placed on a 75°C hot plate; a 300 gram weight is placed on top, and baked for 2 hours. The final layer is a 375 µm in height hexagonal warming channel which is positioned over the embryo platforms in the third layer and plasma bonded.

4.3.3 DSML device fabrication

A micro-scale embryo culture device containing a single U-shaped channel with one embryo barrier was fabricated to be used in a custom built Digital Scanned Laser

Light Sheet Fluorescence Microscope (DSML) (University of Chicago). The entire size of the PDMS portion of the device measures 4x8 mm and contains an internal culture channel with an embryo barrier, like that seen in both the incubator and bench-top devices. Devices were fabricated in varying diameters ranging from 150 µm to 250 µm to accommodate the variation in size of 6.5 dpc embryos. First, a 3" silicon wafer was dehydrated for 15 minutes at 115ºC and spin coated with SU-8 2150 for 10 seconds at 500 rpm followed by 1200 rpm for 30 seconds. The wafer was then baked for 7 minutes at 65ºC followed by 50 minutes at 95ºC. The wafer was the exposed to ultraviolet light for 50 seconds (100 mJ) with a photomask containing an array of U of C embryo chambers placed on top of the SU-8 surface and a quartz plate covering the photomask which is used to keep the photomask in place. The wafer was then baked for 5 minutes at 65ºC followed by 18 minutes at 95ºC. Unexposed SU-8 photo-resist was removed using SU-8 developer by placing the wafer in glass dish on orbital shaker and covering it with old SU-8 developer solution, then agitating this solution for 10 minutes at 2000 rpm on an orbital shaker. The old developer was poured into waste container and the wafer was covered in new developer, and agitated for 10 minutes at 2000 rpm on an orbital shaker. The wafer was then removed from the solution and rinsed with isopropyl alcohol and dried with compressed nitrogen. The height of microchannel design was measured and the wafer was baked at 75ºC for 10-15 minutes.

The developed wafer was placed in a petri dish and 25 grams of degassed 10:1 PDMS to curing agent was poured on to the wafer and degassed. The PDMS was then cured by baking for 2 hours at 75ºC and cut to reveal design. A 20 gauge needle was sharpened and used to bore holes for inlet and outlet ports. 18x18 mm

coverslips were cut in thirds and bonded to the PDMS casting using hand held plasma treater for 30 seconds on the coverslip and 30 seconds on the channel side of the PDMS. The devices were then baked for 1 hour at 85ºC, Finally, uncured PDMS was spread along the left side of the device to cover any cut marks that may refract light and the device was baked for 2 hours at 85ºC.

4.3.4 Characterization of the bench-top device

To determine the temperature and Co2 concentration within the bench-top device over a 24 hour period two sets of characterization studies were performed. First, a sheet of liquid temperature crystals was cut to size and sandwiched between the glass cover slip and the PDMS layer containing the embryo culture chamber to measure the temperature at the location of the embryo barriers. Colorimetric measurements were then taken every 30 minute for 24 hours. After three trials were performed in three different devices, RT water was perfused into the embryo chamber, as a proxy for media and colorimetric measurements were taken every 30 minutes for 24 hours.

To measure the concentration of CO2 at the embryo barriers, 1% phenol red was perfused into the embryo chamber at the experimental flow rate of 1.3 µl/min. Two fiber optic probes were inserted in to channels in the device adjacent to the embryo barriers. One probe was then connected to a light source, while the second probe was connected to a spectrophotometer (Ocean Optics). The absorption at 555 nm was measured and logged every 15 minutes. Calibration of the measurement was performed using 0, 5, and 10% CO2 and a calibration curve was calculated through

linear regression. The regression equation was then used to calculate the amount of CO_2 in the device over a 24 hour period.

4.3.5 Experimental set-up of incubator device

The incubator device was attached to two 5ml syringes filled with embryo culture media in the inlet ports and flushed to remove bubbles. The device was then placed in a standard incubator (NuAire), the 5ml syringes were then attached to a syringe pump (Harvard Apparatus), and media was perfused into the device at a flow rate of 1.3 µl/min. 6.5 day mouse embryos were loaded into the device and then cultured over night in a standard culture incubator, 37°C and 5% CO_2.

4.3.6 Experimental Set-Up for Bench top device

The bench-top device was first attached to a Tygon tube from a water bath (NuAire) set at 50°C, which was attached to the large warming area in layer one. Warm water flowed from the water bath through an 18” piece of Tygon tubing, through the Tygon tubing inside layer one and into the large warming channel. From here the water flowed through another embedded piece of Tygon tubing that starts at the opposite end of the large warming channel and is attached to one end of the small warming channel. The water then goes though the small warming channel and is then recycled into the water bath. Once the warming channels have been occupied, 5ml syringes are filled with embryo culture media and attached to a syringe pump at one end and the inlet ports of the x-shaped embryo channels of the third layer of the device. Media is then pushed through the embryo channels to remove bubbles, and

the syringe pump is set to perfuse the media at a rate of 1.3 µl/min. 6.5 day embryos are then loaded into the embryo channels through one of the media inlet ports. The embryos can remain on the bench-top or on a microscope for continual visualization.

4.3.7 DSML device setup and culture

DSML devices were fabricated as described in section 4.3.3. These devices were filled with embryo culture media using a gel loading tip (fisher). Once the devices were filled with media, a 6.5 dpc embryo was loaded into the inlet using the same gel loading tip. 19 gauge metal connectors were placed inside 0.04”inner diameter Tygon tubing (Cole Palmer), the tubing connected to the inlet was then connected to a syringe containing media on the other end. The metal connectors were placed in the inlet and outlet of the DSML device and media was perfused at 1.3 µl/min. The device was then placed in the slit of a stainless steel metal pin, cut to 23x2.5 mm with a 2.5 mm slit at one end, using double sided tape to adhere the device to the pin. The pin was then inserted into the stage platform of the DSML and the embryo was allowed to develop normally while images were taken.

4.3.8 Mouse mating and embryo dissection

The age of embryos at harvesting was determined by assuming at noon on the day a vaginal plug was discovered corresponded to e0.5. To collect pre-streak stage embryos, pregnant females were sacrificed between e6.25-e6.5. Decidua were dissected from uteri in 1X phosphate buffered saline (PBS) and transferred to a petri dish containing warm culture media. Embryos were dissected from decidua using

Dumont #5 fine forceps and previously described techniques [110]. The ectoplacental cone was left intact for embryo culture, but Reichert's membrane was removed using fine dissection needles (Ernest Fullam Inc). Prior to initiating embryo cultures, embryos were staged according to current criteria first outlined by Downs and Davies [105, 111]. Cultures were started with embryos classified as pre-streak/pre-PS stage based upon the absence of any visible mesoderm formation, an embryonic length : extraembryonic length ratio of ~1.25 or less [105], the positioning of the anterior visceral endoderm (AVE) at the anterior of the epiblast, and the transverse anteroposterior axis of the epiblast being longer than the transverse left-right axis of the epiblast [111].

4.3.9 Embryo Culture

Serum-free embryo culture media consisted of GMEM (Invitrogen) supplemented with 15% Knockout Serum Replacement (KSR, Invitrogen), 0.1 mM NEAA, 1 mM sodium pyruvate, 0.1 mM 2- mercaptoethanol, 100 U/ml penicillin, 100 µg/ml streptomycin and 2 mM L-glutamine [121]. Prior to culturing embryos the device was prepared by attaching two 5 ml syringes filled with media via Tygon tubing to the inlet ports, the syringes were attached to a syringe pump (Harvard Apparatus Compact Infusion Pump 975). Media was perfused at a rate 10 times faster than the rate used to culture embryos in order to remove any bubbles in the embryo channels. Once all the bubbles were removed the flow rate was lowered to 1.3µl/min into each inlet and media was perfused through the device while embryos were dissected. The device was then placed in a standard cell culture incubator at 37C and 5% CO2. Embryos were loaded into the device by collecting them into a gel loading pipet tip attached to

a positive-pressure pipetman device, detaching tubing from an inlet port, and inserting the pipet tip into the inlet ports. After injecting embryos through the port, embryos were positioned at the barriers of individual channels by tilting the device in a fashion in which each embryo tumbles into its own channel. The orientation of the embryo (whether the epiblast or ectoplacental cone rested on the barrier) had no apparent effect on the development of the embryos in culture. When reattaching tubing to the inlet port, the tubing and input port were brimming over with media so that air bubbles would not enter the device after injecting the embryos. The process of loading and positioning embryos into the device took about five minutes. Embryos were cultured for 24 hours at a media flow rate of 2.6 µl/min. This was the fastest flow rate that allowed embryos to remain at the barriers for the duration of culture without deforming the embryos and forcing them past the barriers (data not shown). At this flow rate, assuming a total embryo length of approximately 1 mm, the media covering the embryo would be completely replaced every 7.2 seconds. Following a 24 hour culture period, embryos were recovered from the culture device by removing the media tubing, tilting the device to allow the embryos to fall toward the inlet ports, and collecting the embryos with a pipetman.

4.3.10 Whole mount *in situ* hybridization and staging of embryos after in vitro culture

Whole mount *in situ* hybridization was performed essentially as previously described [122]. Briefly, embryos were fixed for 1 hour at 4C in 4% PFA and dehydrated through a methanol/PBS series. Embryos were then rehydrated, bleached in 4:1 methanol/30% hydrogen peroxide, treated with proteinase K (3-5 minutes), post fixed

in 4% PFA/0.2% glutaraldehyde, and hybridized with a digoxigenin-labeled antisense cRNA probe against Brachyury. Hybridized cRNA probe was detected with sheep anti-DIG AP FAB antibody (Roche) and BCIP/NBT (Roche) reaction. Finally, embryos were dehydrated and rehydrated through a methanol/PBST series to improve color, and transferred to 75% glycerol for microscopy.

4.4 Results and Discussion:

4.4.1 Design of the microfluidic embryo culture chamber

The goal of this work was to create a method of culturing gastrulation stage mouse embryos that would allow normal, in vivo-like, development of a visible, stationary embryo. To provide a new method of examining cellular characteristics involved in induction of the primitive streak, experimentation was focused on culturing embryos starting from the pre-streak stage. By continuously flowing fresh media past a stationary embryo, an embryo's need to draw nutrients and release waste could be accommodated. Therefore, experimental design focused on the engineering of a microfluidic device, figure 4.1, to satisfy two criteria: maintaining a stationary embryo and supplying a sufficient replenishment of fresh media.

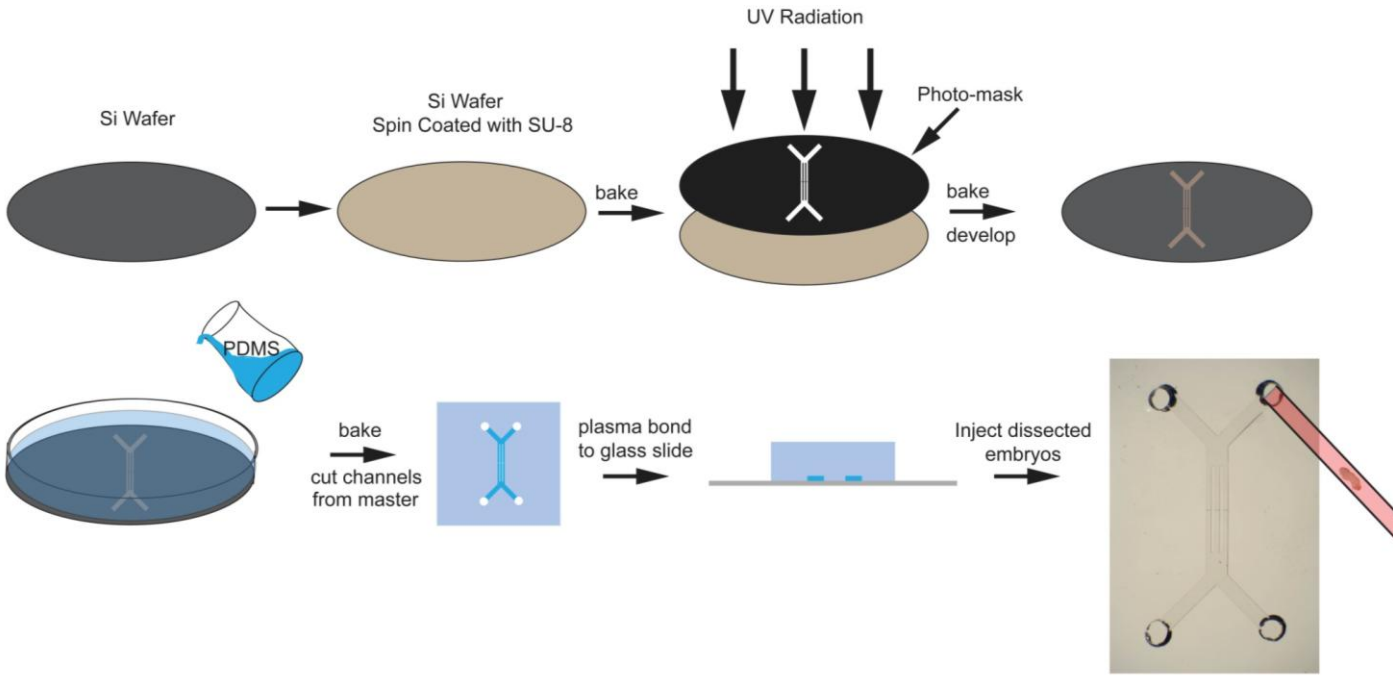

Figure 4.1: Step-by-step schematic of embryo culture device fabrication. This schematic chronicles the soft photolithography process from Si wafer to finished incubator culture device.

The device was fabricated using standard soft lithography techniques of polydimethylsiloxane (PDMS), because of its optical clarity, chemical resistance, and gas permeability properties, figure 4.1. Both the incubator and bench-top devices include an embryo chamber consisting of a channel through which media flowed and a partial barrier upon which the embryo rested (Figure 4.2). The diameter of a late-streak stage mouse embryo is approximately 300 um (emouseatlas.org), so the height of the channels was set to 315 um. This basic “stage within a channel” design was modified to allow simultaneous culture of three embryos by making 1.5 mm wide

channel with two evenly spaced 250 um wide dividers to create three 333 um wide incubation chambers. To position embryos at the midpoint of the incubation chamber, 250 um wide stages were placed in the center of each sub-channel (Figure 4.2). Thus, media could pass through the chamber and perfuse the embryo as it remained at the barrier under constant media flow. The chamber system requires positive pressure from the continuous flow of media to keep embryos at the barrier. Other design elements were incorporated to enable expanded use in the future. Notably, two input/output channels were placed on either end of the single culture channel. This “X”-shaped design allows future experiments to utilize the microfluidic property of laminar flow. In the small volumes of the culture device, liquids will not mix turbulently. Rather, they will flow as laminar sheets. The “X”-shaped design allows media containing different signaling factors, chemical inhibitors, or dyes to be injected into each input and flow unmixed through the channel; therefore, individual embryos can be simultaneously subjected to different media/factors within the same device.

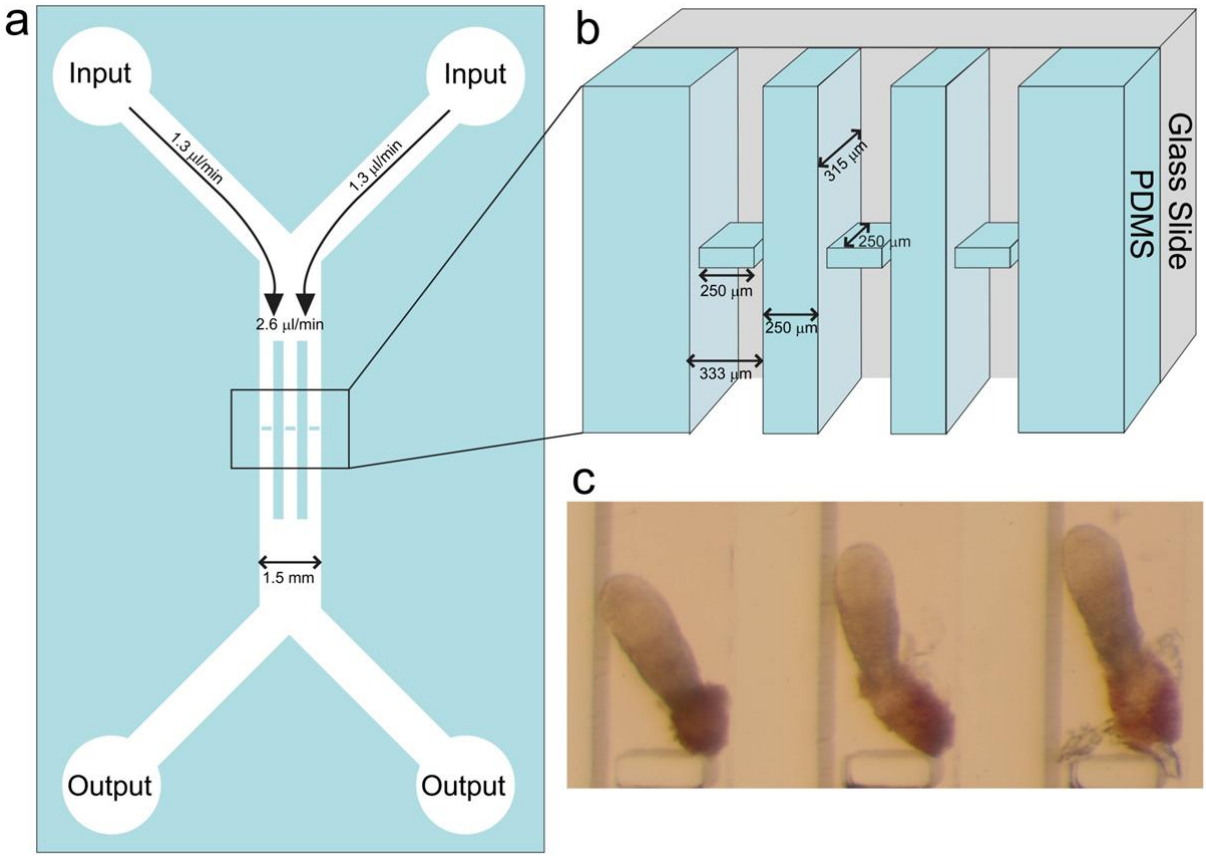

Figure 4.2: Microfluidic culture device schematics. a) Diagram of the full microfluidic culture device. Boxed in area of the device is enlarged in b. b) Diagram of the center of the culture device detailing the dimensions of the barriers at which cultured embryos rest. c) Micrograph image of pre-streak mouse embryos positioned at the culture device barriers.

4.4.2 Embryo culture – Media formulations

Existing embryo culture techniques commonly employ high concentrations (50% to 100%) of rat serum to recapitulate the nutrient-rich environment present in the deciduum that surrounds the embryo following implantation into the uterine wall [22, 111, 113]. Isolation of rat serum by individual labs and in small batches introduces potential for significant variability between studies; therefore, ways to eliminate the use of small batches of rat serum were investigated. Commercially-available rat serum (Atlanta Biologicals) was used to culture pre-streak embryos in either DMEM, DMEM supplemented with 25%, 50%, or 75% rat serum, or undiluted 100% rat serum. Embryos were cultured statically in a petri dish for 24 hours at 37ºC and 5% CO_2. Embryos cultured in any concentration of rat serum for 24 hours did not appear to have developed normally, were opaque, and appeared to be shedding dead cells (Figure 4.3). In contrast, embryos cultured in DMEM alone for 24 hours did not display the substantial defects caused by commercially-available rat serum (Figure 4.3). Due to the substantial deleterious effects of the purchased rat serum in static culture, it was not further tested for embryo culture in microfluidic devices.

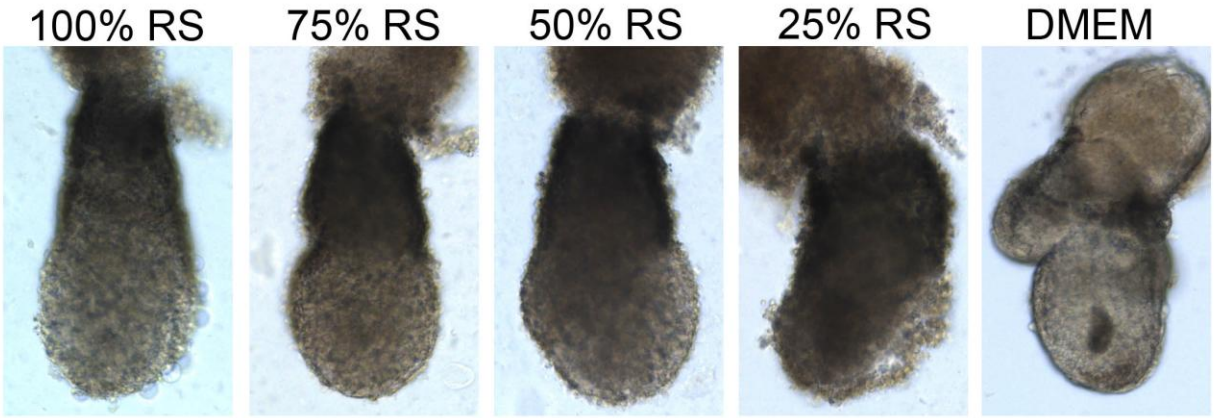

Figure 4.3: Effects of Rat serum on the in vitro static culture of pre-streak mouse embryos. Pre-streak embryos cultured in the presence of any concentration of commercial rat serum failed to undergo gastrulation and exhibited massive cell death and shedding after 24 hours of static culture. Embryos cultured in DMEM alone exhibited abnormal development, but did not exhibit any apparent cell death during 24 hours of static culture.

Serum-free embryo culture media that had been previously used to culture post implantation embryos [121] was examined. Embryos cultured in this serum-free media formulation did not display the cell death observed in rat serum, and progressed to express Brachyury in the PS region (Figure 4.4). Thus, the serum-free culture supported viability and partial development through gastrulation in a static culture setting. Furthermore, the serum-free media provides substantial benefits over rat serum in terms of availability, ease of use, cost, variability among individual preparations, and variability among different labs. Therefore, this serum-free media formulation was used to test microfluidic devices for culturing embryos.

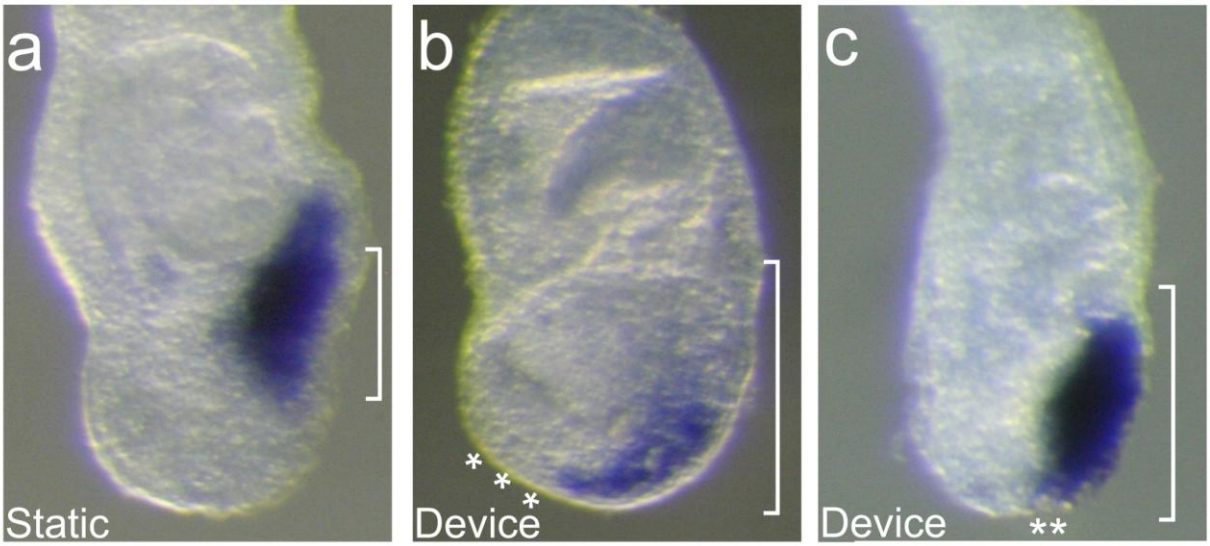

Figure 4.4: Comparison of morphology and Brachyury mRNA expression in 24 hour static culture vs. device culture. a) Representative embryo following 24 hour static culture. Note that the domain of Brachyury expression (purple staining, marked by bracket) extends only ~50% of the length of the epiblast. b-c) Representative embryos following 24 hour device culture. Note that the domain of Brachyury expression (purple staining, marked by brackets) extends to the tip of the embryo, where advanced morphological structures such as the head process (triple asterisks in b) and node (double asterisks in c) have formed.

4.4.3 Embryo Culture – Using the incubator device

To test the incubator device, embryonic development following a 24 hour culture period for pre-streak embryos in static culture in a petri dish versus embryos loaded into the microfluidic device and subjected to flowing media was assessed. After 24 hours of culture, all embryos were moved to a petri dish, where they were staged using morphological landmarks (Figure 4.4) prior to being used for whole mount in situ hybridization detection of Brachyury mRNA expression. Nearly all (6 of 8) pre-streak embryos subjected to static culture for 24 hours developed to specify mesoderm and express Brachyury in a PS like structure (Figure 4.4). The static culture embryos and their PS-like structure never appeared normal, as Brachyury expressing cells reached only 50% the length of the posterior of the epiblast. All static cultured embryos formed a peri-amniotic fold, an extraembryonic structure indicative of mid-streak stage embryos (Figure 4.4, Table4.1). None of the static cultured embryos advanced sufficiently through gastrulation to form a node, head process or an extraembryonic ectocoelomic cavity (Table 4.1). It is not known if progression through gastrulation was slow throughout the 24 hour culture period, if embryos progressed to a mid-streak stage and abnormalities halted further progression, or if a combination of effects limited progression through gastrulation in static culture conditions. Regardless, the abnormal structure of the embryos indicates abnormal cellular dynamics occurred in static culture conditions.

Embryo	PS/Mesoderm	Presence of Morphological Landmarks			
		PAF	Node	HP	XC/Bud
Static 1	++	+	-	-	-
Static 2	++	+	-	-	-
Static 3	+	+	-	-	-
Static 4	+	+	-	-	-
Static 5	+	+	-	-	-
Static 6	+	+	-	-	-
Static 7	+	+	-	-	-
Static 8	+	+	-	-	-
Device 1	++		+	+	+
Device 2	++		+	+	+
Device 3	++		+	+	+
Device 4	++	+	+	-	-
Device 5	++	+	+	-	-
Device 6	++	+	+	-	-
Device 7	++	+	+	-	-
Device 8	++	+	+	-	-
Device 9	++	+	+	-	-
Device 10	++	+	+	-	-
Device 11	+	+	+	-	-
Device 12	+	+	-	-	-
Device 13	+	+	-	-	-
Device 14	+	+	-	-	-
Device 15	-	-	-	-	-
Device 16	-	-	-	-	-
Device 17	-	-	-	-	-
Device 18	-	-	-	-	-

TABLE 4.1: Staging of embryos following 24 hours in either static or perfusion device culture. PS/Mesoderm denotes the extent of primitive streak and mesoderm formation along the total proximal-distal length of the epiblast as judged by morphology and Brachyury in situ hybridization. “++” denotes PS/mesoderm covering >50% of the epiblast length, “+” denotes <50%, and “-“ denotes no PS/mesoderm formation. Presence of morphological landmarks denote the presence (+) or absence (-) of the node, posterior amniotic fold (PAF), head process (HP) and exocoelomic cavity/bud (XC/Bud).

In contrast to static culture conditions, most (10 of 18) pre-streak embryos cultured in the microfluidic device for 24 hours developed to the late-streak or early bud stage. All ten of these embryos formed a PS that reached the entire proximodistal length of the epiblast, and exhibited advanced developmental landmarks such as the node (7/18), head process (3/18), and the ectocoelomic cavity (3/18) (Figure 4.3, table4.1). Four of 18 device culture embryos developed to a midstreak- like stage, similar to static-culture embryos. Finally, four of 18 device cultured embryos failed to progress through gastrulation. Considering the extra manipulation of loading embryos into the device, it is likely the embryos that did not progress through gastrulation were critically damaged during processing. Taken together, these results support a significant benefit of culturing embryos in the microfluidic device and show a significant improvement over static culture methods in terms of stimulating normal embryonic development.

The incubator device is relatively simple to use; however, it requires an external incubation system to control the temperature and gas levels within the culture chamber. Therefore embryos must be cultured within a standard tissue culture incubator, as performed here, or using microscope systems equipped with a stage that provides environmental control of temperature and gas. Although many groups who may be interested in spatiotemporally tracking events during mouse gastrulation have access to a microscope specialized for live imaging, such microscope systems are usually expensive, are not always available, and are frequently in high demand. As such, obviating the need for specialized microscopes would substantially increase

the number of groups that could feasibly examine cellular dynamics in the mouse gastrula.

4.4.4 Embryo Culture – Using the bench-top device

To overcome this obstacle the embryo chamber from the incubator device was sandwiched in between to warming chambers as can be seen in figure 4.5. The warming chambers were then connected to a standard water bath, found in most biology labs. Gravity driven flow forced water, warmed to 37ºC, into the bottom warming chamber via 1/8" od Tygon tubing (Cole Palmer). An additional piece in the same tubing was connected from this warming chamber to a warming chamber located directly above the embryo barriers, figure 4.5. The water exiting the second warming chamber was then recycled into the water bath.

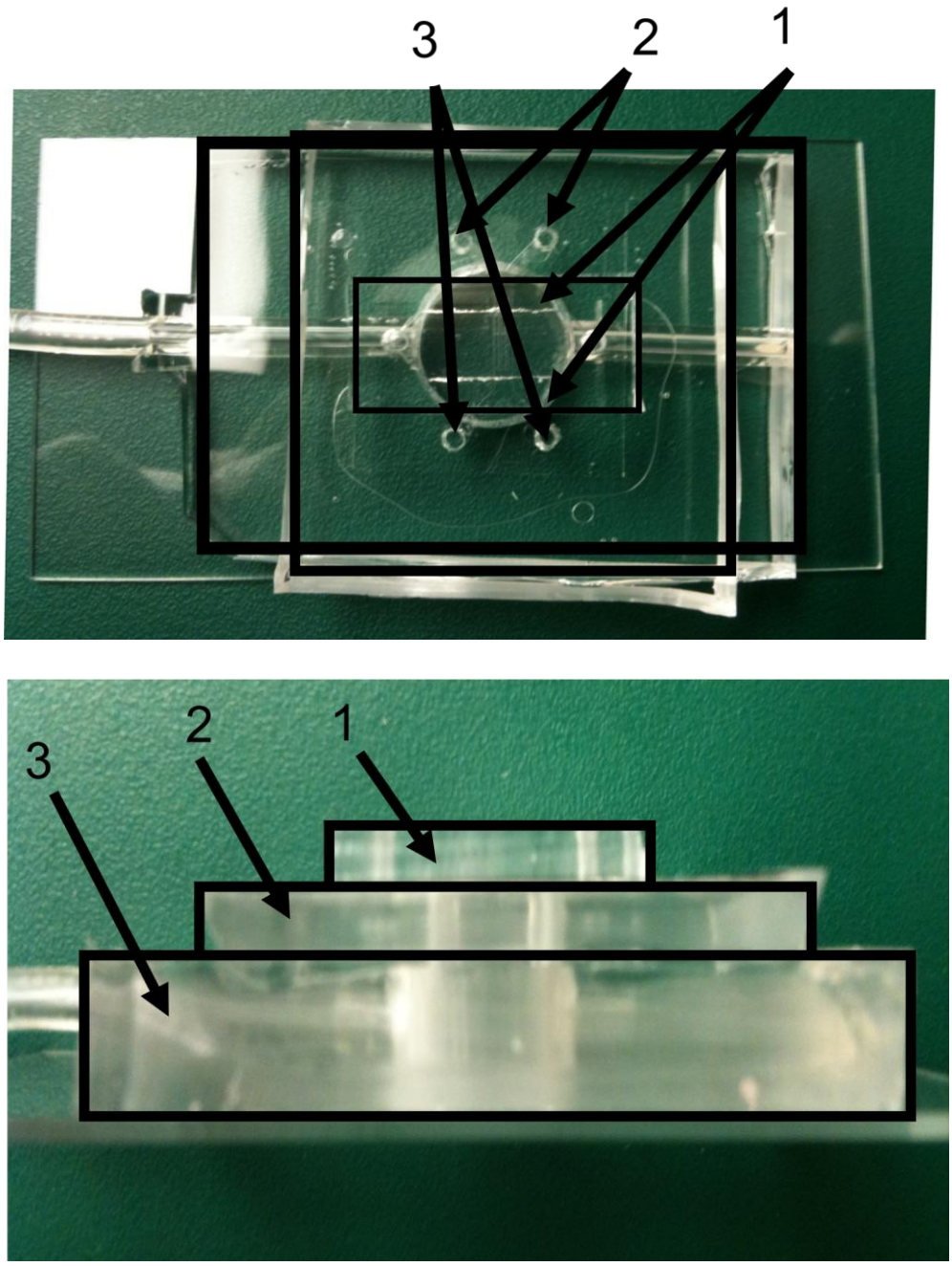

Figure 4.5: Bench-top Culture device. A) Top View. 1. Circular warming channel from layer 3, and top warming channel. 2. Inlets in which embryos are loaded and media is perfused over 24 hours. 3. Outlets, media exits the device.B) Side View. This view shows that the device contains three distinct layers of PDMS each housing a functional aspect of the design. Layer 1 houses the top warming channel in which 40ºC water flows from the waterbath to heat the embryos from the top. This is directly bonded to layer 2 which houses the X-shaped channels that contain the embryos. Between layer 2 and 3 is a glass coverslip that the embryos rest on. Under the glass coverslip, in layer 3 there is a circular warming channel. Layer three is directly bonded to a glass slide.

To measure the temperature at the embryo barriers over a 24 hour period, a sheet of liquid temperature crystals was cut to size and sandwiched between the glass cover slip and the PDMS layer containing the embryo culture platform, figure 4.6a. Colorimetric measurements were then taken every 30 minute for 24 hours. After three trials were performed in three different devices, RT water was perfused into the embryo chamber, as a proxy for media and colorimetric measurements were taken every 30 minute for 24 hours. As can be seen in the graph on figure 4.6b, the temperature at the embryo barriers remained stable at 37ºC over a 24 hour period; with and without room temperature water being perfused through the embryo chamber.

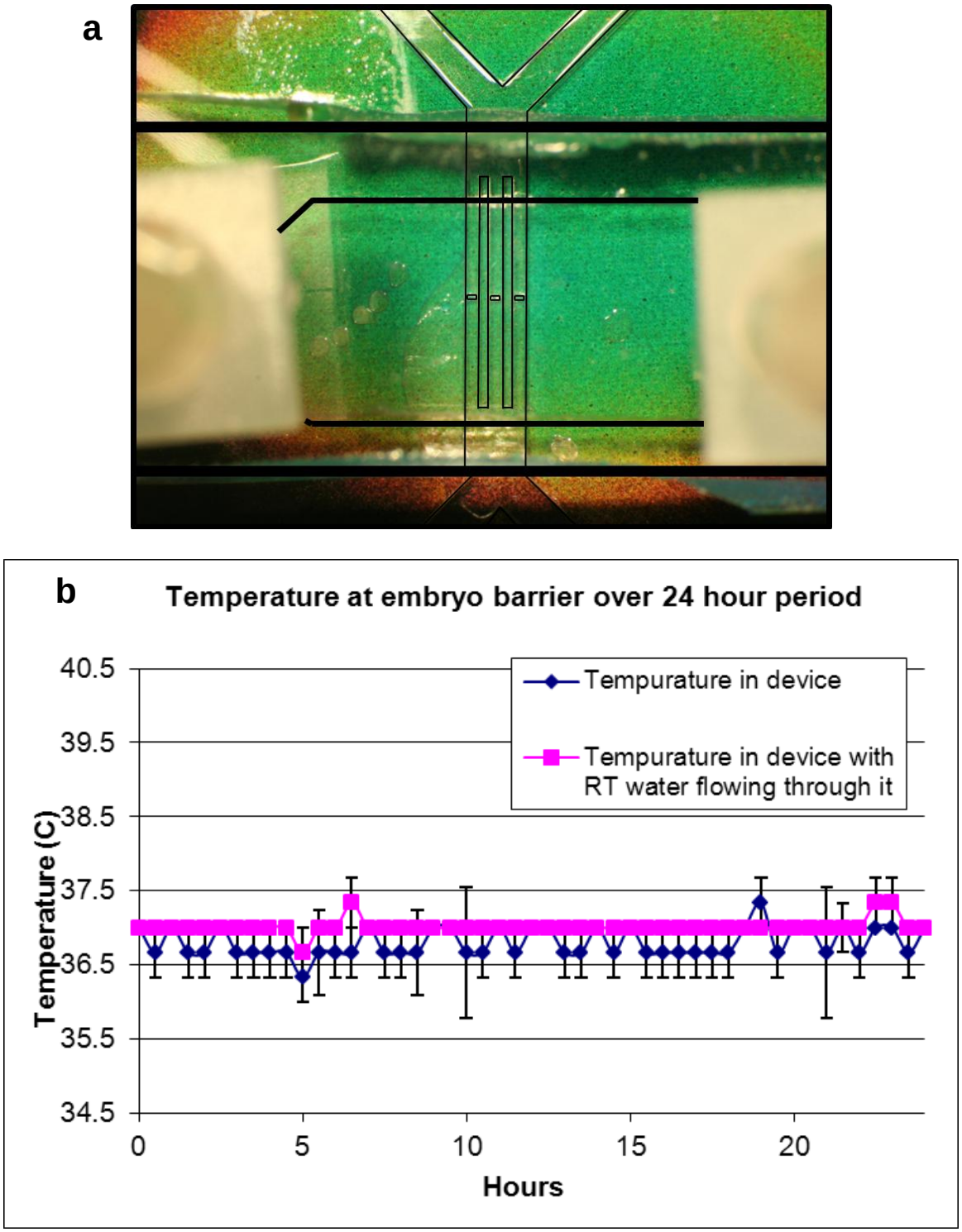

Figure 4.6: Liquid crystal temperature measurement. a) Image of liquid temperature crystals in device with 37ºC water flowing through warming chambers. b) Graph containing colorimetric temperature data measure over 24 hours with and without room temperature water flowing through the embryo chamber.

To measure the concentration of CO_2 at the embryo barriers, 1% phenol red was perfused into the embryo chamber at the experimental flow rate of 1.3 µl/min. Two fiber optic probes were inserted in to channels in the device adjacent to the embryo barriers. One probe was then connected to a light source, while the second probe was connected to a spectrophotometer (Ocean Optics). A diagram of this experimental set up can be seen in figure 4.7. The absorption at 555 nm was measured and logged every 15 minutes. In figure 4.8, images show that after the first 15 minutes of 5% CO_2 perfusion into the gas chambers the color of the phenol red indicates that there is 5% CO_2 at the embryo barrier.

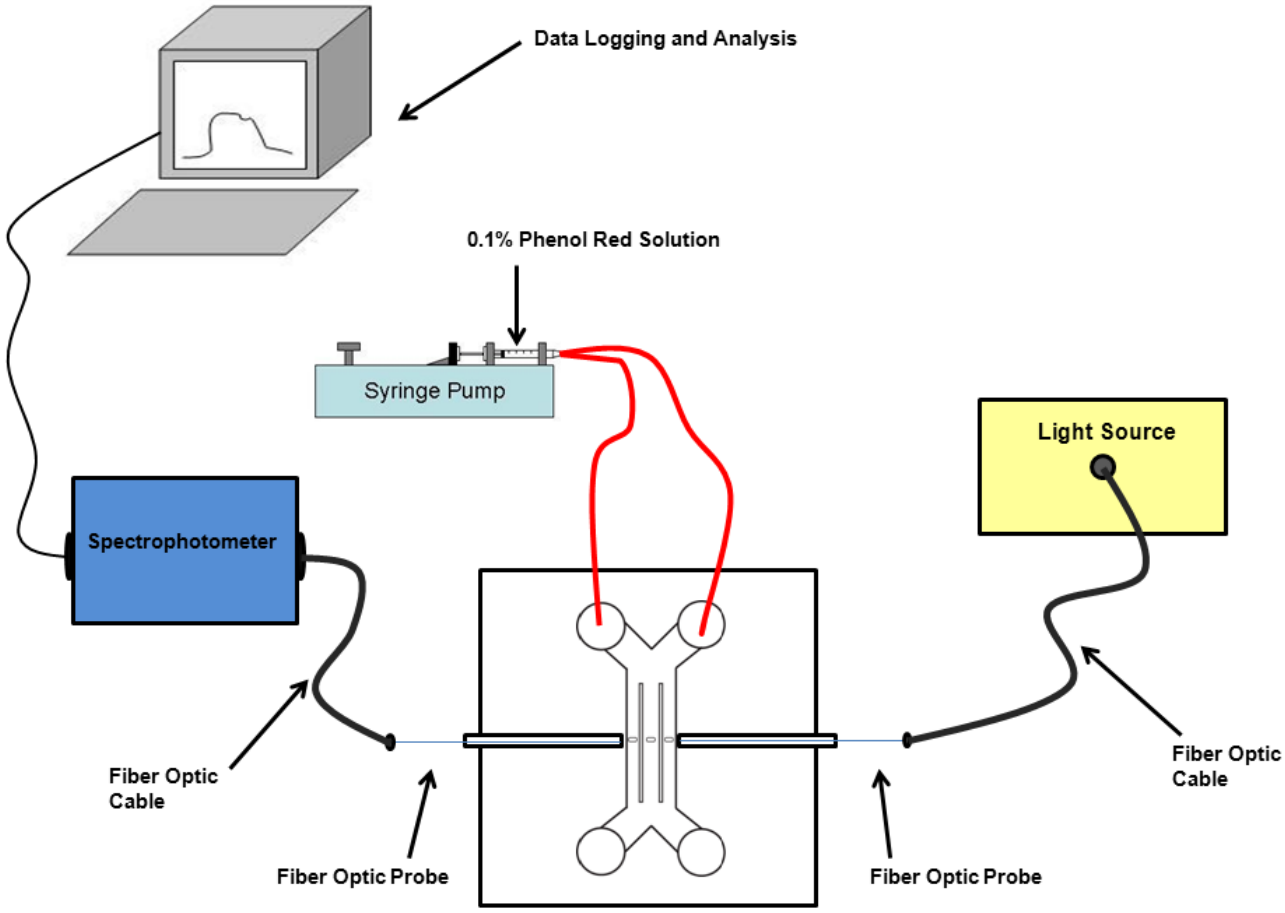

Figure 4.7: Schematic of CO_2 measurement set up. Fiber optic probes (light blue) were placed in the channels adjacent to the embryo barriers. The fiber optic probe on the right side was connected to a light source, while the fiber optic probe on the left side was connected to a spectrophotometer. The spectrophotometer was then attached to a computer containing data logging software to collect measurements. A syringe pump was used to perfuse 1% phenol red through the CO2 calibration device.

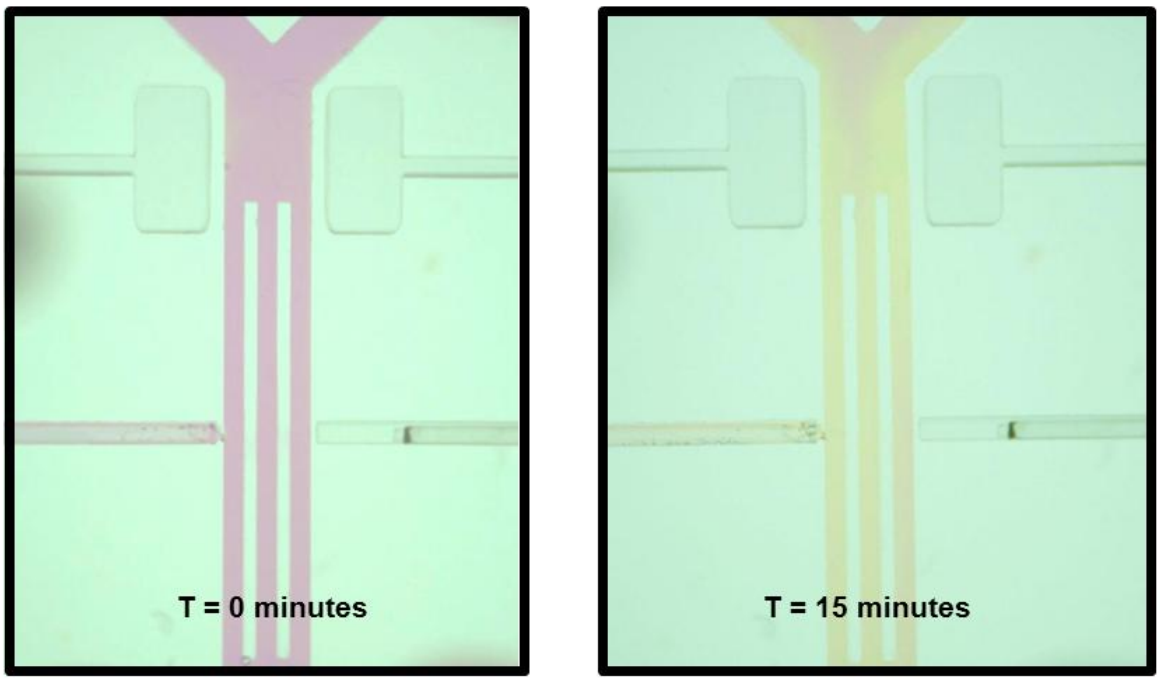

Figure 4.8: Carbon Dioxide Calibration. Images of 1% phenol red in the CO_2 calibration device at t = 0 minutes and t = 15 minutes. The images display that there is a complete color change of the phenol red within 15 minutes. This correlates to a change in CO_2 concentration from 0.039 % (CO_2 in air) to 5% CO_2.

Calibration of the measurement was performed using 0, 5, and 10% CO_2 and a calibration curve was used to calculate a slope-intercept equation through linear regression, figure 4.9a. The regression equation was then used to calculate the amount of CO_2 in the device over a 24 hour period. As can be seen in figure 4.9b, the concentration of CO_2 can take an hour to stabilize in the device and that this concentration fluctuates over time. However, after 3 hours the concentration never dips below 4.5% CO_2. If it is determined in the future that embryos need a height CO_2 concentration it is easily to increase the amount of CO_2 added to the gas chambers.

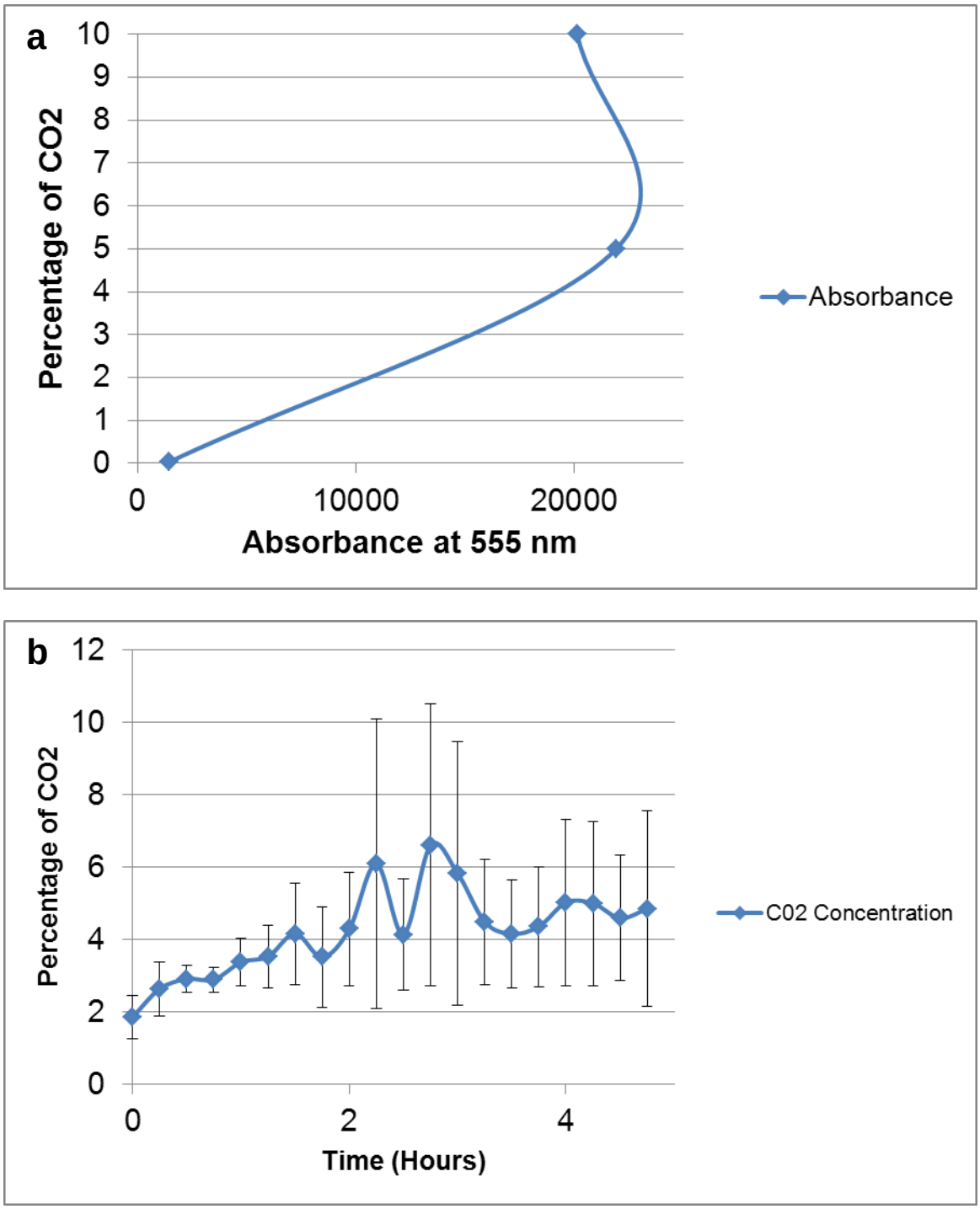

Figure 4.9: Calculatuion of CO_2 concentration in bench-top device. a) Calibration curve used to translate absorbane to the amount of CO_2 in phenol red. b) Concentration of CO_2 at barrier chambers over time.

Currently the bench-top device is being used to culture 6.5e embryos over a 24 hour time period. If these embryos develop normally in the device, this platform could revolutionize the study of mammalian development. The gas permeability and heat transfer properties of PDMS are well suited for the flow of hot water and compressed carbon dioxide adjacent to the central embryo incubation chamber [36, 37]. These modifications will enable *ex vivo* culture to be performed with only a tank of compressed gas and a water bath need to be near a microscope. Together with the use of serum-free media, development of these microfluidic embryo culture devices provides researchers new means of addressing questions concerning dynamic cellular properties during mammalian gastrulation, a problem that had been intractable until now.

4.4.5 DSML device culture

DSML devices were fabricated as described in section 4.3.3. These devices, figure 4.10a, were filled with embryo culture media using a gel loading tip (fisher). Once the devices were filled with media, a 6.5 dpc embryo was loaded into the inlet using the same gel loading tip. The device was then placed in the slit of the stainless steel metal pin, figure 4.10b, left, using double sided tape to adhere the device to the pin. The pin was then inserted into the stage platform of the DSML, figure 4.10c and d. The embryo was allowed to develop normally while images were being taken. Initial results show that the embryo can be imaged using this device. To maintain normal culture conditions warmed water and CO_2 will need to be added to the DSML stage platform.

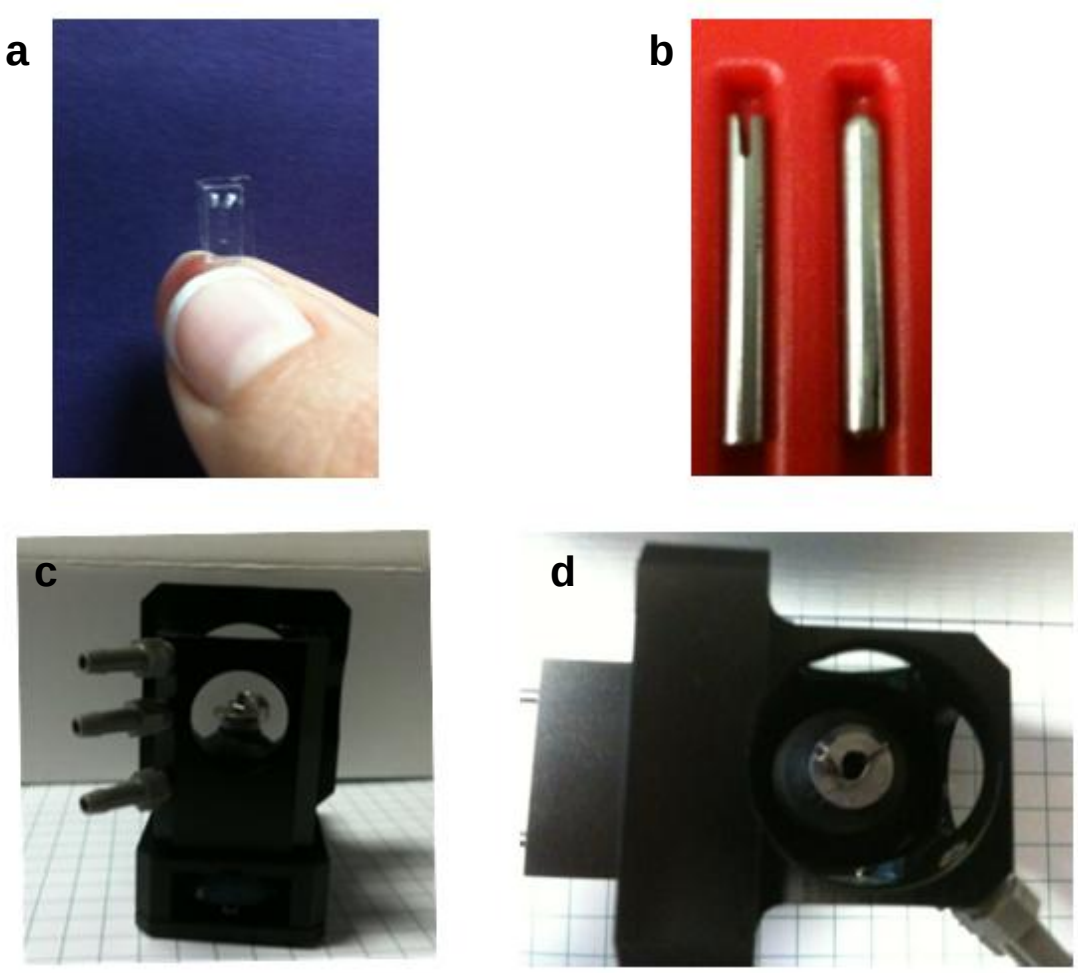

Figure 4.10: DSML device and setup. a) DSML device containing 20 gauge inlet and outlet and a U-shaped channel with one embryo barrier for culture. b) Pins for stage platform; 23x2.5 mm stainless steel pin with slit (2.5 mm long), left, and 23x2.5 mm stainless steel pin used in original DSML set up, right. c) Side view of DSML stage platform. d) Top down view of DSML stage platform.

4.5 Conclusions

The primary, immediate application of the devices described here is to enable live imaging of cellular events during gastrulation in mice. These devices were specifically tested for the ability to support embryogenesis at the stage of PS induction, when cell lineage decisions are coordinated with elaboration of a basic body plan. With the ability to mount these devices on either a full thickness glass slide or a coverslip, they are amenable for imaging with a wide range of microscopy systems. The embryo culture methods described here can be combined with low magnification stereomicroscope systems to elucidate the spatiotemporal dynamics of the morphogenesis of structures that define stages of gastrulation. Combined with more powerful microscopes and fluorescent labels, the device now enables real time tracking of cell movements, shape changes, and proliferation through gastrulation.

Although these devices are better at replicating the microenvironment found during mouse embryo gastrulation than other culture platforms, it is important to realize that not all of the cultured embryos were able to develop through each of the eight stages of gastrulation. For some of the embryos tested this difference can be attributed to damaged incurred during the dissection processes, but other variances, such a 90% PS streak formation, can be attributed to the fact that microfluidic technologies can not exactly mimic the native environment of embryo development. There are steps that can be taken to close the gap between the *ex vivo* culture platform and the innate microenvironment, including perfecting embryo culture media, but as with most other technologies it is extremely difficult the exactly replicate the native environment. Microfluidic technologies allow us to mimic the microenvironment

better than other experimental techniques and hold much promise for improvement in the future.

4.6 Future work

Once it is determined that embryos develop normally in the bench top device, experimentation will be performed to further elucidate the mammalian developmental pathway. The unique characteristics of the microfluidic platform will be used to subject embryos to chemical factors thought to influence development. Laminar flow will allow researchers to treat different portions of the embryo in varying conditions by manipulating the flow rates in the embryo chamber. Factors that may be used could include chemical activators of wnt or bmp signaling that would inhibit neuroectoderm (NE) formation and promote extra mesoectoderm (ME) formation. Eventually, a side port or deflectable membrane will be added to the embryo device so that embryos can be subjected to different mechanical forces while they undergo development. In order to visual symmetry breaking cell movements in the three dimensional space over time, the DSML device will be used for *ex vivo* culture in the custom built DSML. The device will need to be submerged in warmed water and 5% CO_2 to maintain normal culture conditions, therefore warmed water and CO_2 will need to be added to the DSML stage platform.

4.7 Acknowledgements:

This work was supported in part by NSF grant DBI-0852416 (D.T.E) and awards from UIC Chancellor's Supplemental Graduate Research Fellowship (J.A.H.) and the UIC Chancellor's Discovery Fund for Multidisciplinary Research (B.J.M and D.T.E).

Chapter 5 Conclusions

Microfluidic techniques improve the manner in which biological data is harvested and allow for new types of data to be collected. Here, soft photolithography along with several other microfluidic tools enabled the precise control over the microenvironment of cells and tissues that most other techniques cannot attain. The microfluidic technologies employed were instrumental in the data collected in all four chapters of this manuscript, allowing new biological phenomena to be uncovered.

In chapter one, a small foot print valve, the “pin valve”, was created using microfluidic tools and tested for its ability to control flow within the channels of a microfluidic network. The pin valve design can attain on/off control of fluid flow without an external power source using readily-available, low-cost materials. The valve is simply constructed from a section of 14 gauge (1.6mm) metal tubing and contains a PDMS pad at the tip to achieve a fluidic seal when pressed against a microfluidic channel’s substrate. The pin valve is manually actuated allowing for fully on-chip control. The valve was validated using a pressure transducer and fluorescent dye to determine the breakthrough pressure the valve can withstand over multiple cycles. In the first cycle, the median value for pressure withstood by the valve was 8.8 psi with a range of 17.5 - 2.7 psi. The pressure the valves were able to withstand during each successive trial was lower suggesting they may be most valuable as a method to control the initial introduction of fluids into a microfluidic device. These valves can achieve flow regulation within microfluidic devices, have a small dead volume, and are simple to fabricate and use, making this technique widely suitable for a range of applications.

Microfluidic techniques are not limited to exerting control over liquid solutions. In chapter two, soft photolithography was used to create a six well insert for a standard culture dish that can exert spatial and temporal control of the oxygen concentration within a 3 mm high region. This insert was fabricated and tested to determine if this device could be used to create a hypoxic environment in which to study saphenous vein hypoxia. The data garnered through the fabrication and testing of the six well hypoxic insert indicated that the device could be easily calibrated to determine the amount of oxygen present in the bottom of a six well plate. Upon calibration, the device established a desired concentration of oxygen, ranging from 0-21%, and these concentrations could be maintained over time. The use of this device will allow new types of data to be generated. This data can be used to find the link between hypoxic conditions and undesired outcomes, such as vasoocclusion or constriction, commonly seen in saphenous vein transplantation.

Microfluidic techniques have a wide range of applications, and in chapter three these techniques are employed to vary the microenvironment in order to subject subpopulations of cells in the same device to different conditions. This was first done using the rotating chemical gradient device to study yeast chemotropism. As previously mentioned, haploid budding yeast exposed to mating pheromone produced by cells of the opposite mating type stop dividing and polarize their growth, thereby forming a mating projection, or “shmoo.” Cells treated with pheromone under isotropic conditions form mating projections adjacent to their last bud site. This is called default shmooing. In contrast, mating cells interpret complex pheromone gradients and polarize their growth in the direction of the closest partner [10, 11].

This is called chemotropism, the directed growth of a cell in response to a chemical gradient.

Here, microfluidic techniques were employed to design, fabricate, and characterize a microfluidic device that creates and rotates a chemical gradient by 90°. After characterizing the gradient created by the device and testing the polystyrene coating, the validity of the device was tested through the induction of orientation in wild type *S. cerevisiae* and compared the angle of orientation to a negative control. The device was able to induce orientation, with an angle of 56.9°, compared to the negative control which showed no discernible orientation. Ultimately the goal of this work is to induce reorientation. The rotating gradient device was able to induce reorientation in 83.6% of cells in a systematic and measurable fashion. The advantage of this device is its ease of use and ability to create and rotate chemical gradient to further study *S. cerevisiae* and its mutants to further elucidate the chemotropic mechanisms involved in mating projection growth.

The rotating gradient device was then used to test the ability of GβP- cells to orient in a chemically manufactured α factor gradient. The comparison of the angle of orientation measured in GβP- cells versus wt cells in a gradient or treated with isotropic pheromone highlighted the GβP- cells inability to sense the direction of a gradient. To obviate the need for the PS coating several non-porous substrates were tested to determine if the rotating gradient design could be replicated in a substrate that would not absorb small hydrophobic compounds into its bulk. Through

this testing it became clear that hot embossing of PMMA is a good solution to replace the PS coating.

Finally, the ability to induce a manufactured α factor gradient was conferred to an agarose pad using the automated chemical delivery device (ACDD). Preliminary results from orientation studies in this device suggest that the ACDD can be used to induce orientation. Ultimately, this device will be used to subject mating mixtures to a manufactured α factor gradient in the hopes that a confusion assay can be developed to further elucidate the chemotropic pathway.

Lastly, the ability to use microfluidic techniques to generate new types of data or study previously unreachable phenomenon was moved from the study of single cells in yeast chemotropism to the whole tissue of the mouse embryo. In chapter four, microfluidic techniques were employed to culture 6.5 day embryos *ex vivo* for 24 hours through the gastrulation phase of mammalian development. The study of gastrulation in mouse embryos is important to elucidate the pathway of early development in mammalian embryos. Currently, the study of whole embryos is limited to collecting data at static time points and inferring development between these periods [21, 22]. The dependency of embryos on the support of the uterine environment has been a challenge in culturing embryos *ex vivo*. At the present time, a roller-bottle method allows for the *ex vivo* culture of embryos, but not continuous visualization or imaging of embryos [22], leaving the problem of taking data at static time points. Jones *et al*. devised a way to culture mouse embryos under continuous monitoring but were unable to culture embryos less that 8.5 days postcoitum (dpc) [21].

Two devices, one for incubator culture and one for bench-top culture, were designed, fabricated and characterized for the *ex vivo* culture of gastrulation stage embryos. The primary, immediate application of these devices, described in chapter four, is to enable live imaging of cellular events during gastrulation in mice. Devices were tested for the ability to support embryogenesis at the stage of primitive streak (PS) induction, when cell lineage decisions are coordinated with elaboration of a basic body plan. The ability to mount the device on either a full thickness glass slide or a coverslip, make the embryo culture devices amenable for imaging with a wide range of microscopy systems. The embryo culture methods described here can be combined with low magnification stereomicroscope systems to elucidate the spatiotemporal dynamics of the morphogenesis of structures that define stages of gastrulation. Combined with more powerful microscopes and fluorescent labels, the device now enables real time tracking of cell movements, shape changes, and proliferation through gastrulation.

It is important to note that the success of the platforms developed here is relative. Microfluidic techniques harbor the ability to devise devices that allow the study of biological processes previously unable to be elucidated by other technologies. However, these devices are not always able to exactly replicate what nature provides. In the case of yeast chemotropism, in a true mating mixture of MATa and MATα haploid cells, the degree to which cells will orient to form a diploid is on the scale of 0 to 10 degrees, compared to 60 degrees in most microfluidic devices. In embryo culture, not all of the cultured embryos were able to develop through each of the eight stages of gastrulation. For some of the embryos tested this difference can be attributed to damaged incurred during the dissection processes, but other

variances, such a 90% PS streak formation, can be attributed to the fact that microfluidic technologies can not exactly mimic the native environment of embryo development. There are steps that can be taken to close the gap between the *ex vivo* culture platform and the innate microenvironment, including perfecting embryo culture media. These examples highlight the fact that while microfluidic tools allow for the generation of new types of data and quantification of phenomena that other technologies do not, there is still room to improve in order to truly replicate the microenvironment found in nature.

Microfluidic technologies can be used create a variety of tools to study many biological phenomena. Here, four vastly different platforms were developed using microfluidic tools. Each of these platforms fills a unique niche that can only be filled using microfluidic technologies. Although these technologies enable the collection of new types of data, the real significance of this research lies in the ability to advance understanding of biological elements. Microfluidics enables the creation of platforms that enhance the ability to generate robust data and explore areas that are unable to be reached with larger scale technologies.

Appendices

Appendix A Protocols

A.1Pin Valve Fabrication

Pin Valve Fabrication

1) Measure and Mark 1” sections of 14 gauge (1.6mm) stainless steel tubing
2) Cut in one inch sections using Drummel
3) Buff ends of the metal sections to remove any unevenness or roughness from the edges
4) Bore holes through bottoms of well in 96 well plate using Drummel
5) Cover bottom of wells with Scotch tape
6) Fill wells with degassed PDMS mixed at a 10:1 ratio of pre-polymer to curing agent
7) Degass again under vacuum pressure
8) Place on the top surface of the 96 well plate
9) Use a dental probe (McMaster-Carr) to form a hole above each well
10) Place metal pins vertically in individual wells and moved up and down to fill the lumen of the pin with PDMS
11) Bake entire setup at 75°C for 2 hours and allow to cool to room temperature overnight
12) Remove pins with cured PDMS from each well of the 96 well plate
13) Trim excess PDMS from above the pad area

14) Cut PDMS plug to 1 mm beyond the length of the metal portion of the pin
15) Reduce the diameter of the PDMS plug using an 11 gauge (2.30mm) punch as shown in Figure 1.2.

A.2 Pin Valve Testing

Pin Valve Testing

1) Bore valve port into desired channel, in this case using a sharpened 12 gauge (2.05mm) needle (McMaster-Carr)
2) Fill a syringe with colored dye of florescent dye, then fill a second syringe with either a different colored dye or water depending of weather you are testing in color of the macroscope or with fluorescent dye on MR. Roboto
3) Pump dye via a syringe pump (Harvard Apparatus) and monitor with an in-line pressure transducer (PR Temp 1000, MadgeTech) in one inlet and pump water into the other inlet
4) Attach both syringes to a single syringe pump (Harvard Apparatus) and set to a flow rate of 10µl/min. A schematic of the experimental set up can be seen in Figure 1.3
5) Push valve down until it meets the glass at the bottom of the channel to block the channel containing dye
6) Continue pumping via the syringe
7) Record Pressure of pressure transducer via data logger

A.3 Hypoxic Insert Fabrication

Hypoxic Insert Fabrication

Microchannel Fabrication:

1) Plasma treat 3” Si wafer for 35 seconds in plasma microwave
2) Spin SU-8 2100 at 500 rpm for 10 seconds then 1200 rpm for 30 seconds
3) Bake for 5 minutes at 65ºC then 40 minutes at 95ºC
4) Cool wafer at 65ºC for 5 minutes
5) Expose wafer with photomask containing design of micro channels (in this case and internal pillar array which can be seen in figure 2.1d) placed on top of SU-8 surface and a quartz dish used to keep the photomask in place
6) Bake for 5 minutes at 65ºC then 40 minutes at 95ºC, let cool to room tempurature
7) Place wafer in glass dish on orbital shaker and cover with old SU-8 developer solution, shake for 10 minutes at 2000 rpm
8) Pour old developer into waste container and cover wafer in new developer, shake for 10 minutes at 2000 rpm
9) Pour developer into used developer container and rinse wafer with IPA
10) N_2 blow dry and measure height of microchannel design
11) Place developed wafer in a petri dish and pour 30 grams of degassed 10:1 PDMS to curing agent on to the wafer
12) Degass under vacuum until all bubbles are removed
13) Bake at 75ºC for 2 hours, let cool to room temperature
14) Cut to remove circular microchannel design
15) This will be the microchannel insert seen in figure 2.3
16) The photomask contains the designs for 3 insert channels, so PDMS casting of the wafer should be repeated

6 well pillar fabrication

1) Put Delran mold together
2) Place a transparency cut to size between the two halves of the mold
3) Screw both halves of the mold together
4) Superglue precut strips of thin hard plastic to the sides of the mold making sure to cover the area where the two halves come together and leave a 10 mm space at the top
5) Put duct tape around the entire exterior of the mold and plastic strips so that the PDMS will not leak
6) Thoroughly mix 130 grams of PDMS and 13 grams of curing agent in a plastic weigh boat; degass under vacuum

7) Cover the microchannel design of each of the 6 microchannel inserts completely with Scotch tape (3M)
8) Cut excess tape from the edge of the microchannel inserts
9) Place one microchannel insert, tape side down into each of the pillars in the Delran mold
10) Pour degassed PDMS into the mold
11) Bake in oven at 75ºC overnight
12) Let cool to room temperature
13) Remove hypoxic insert from Delran mold
14) Remove tape from bottom of each pillar
15) Cut inlet and outlet channels into each pillar with sharpened 8 gauge metal needle

Membrane fabrication

1) Pretreat 3” Si wafers by pouring PDMS on them and baking for 2 hours at 75ºC
2) Peel PDMS off wafers
3) Repeat steps 1 and 2 two more times
4) Wafers should now be able to release membranes
5) Mix 20 grams of PDMS and 13 grams of curing agent in a plastic weigh boat; degass under vacuum
6) Leave under vacuum for 2 hours
7) Pour a quarter sized amount of degassed PDMS onto pretreated wafer
8) Spin at 500 rpm for 10 seconds then 800 rpm for 30 seconds
9) Place wafer on hot plate and bake for 2 hours at 75ºC
10) Cut circles out of membrane using inside of pillar mold as the template
11) Place each circle on its own small piece of transparency

Final hypoxic insert assembly

1) Treat both the exposed side of the circular membranes and the end of each pillar / microchannel with the hand held plasma gun, approximately 30 seconds for each membrane and 30 seconds for each pillar
2) Roll membrane onto pillar / microchannel
3) Push out any remaining air bubbles
4) Let bond overnight
5) Remove transparency from each membrane

A.4 Oxygen Calibration and sensing

Oxygen Calibration and Sensing

Calibration

1) Glue ruthenium coated Foxy slide to the bottom of each well in a 6 well plate
2) Calibrate each well to be used at 0, 10, and 21% Oxygen using % Oxygen balanced nitrogen gas mixtures
3) For a 3 mm gap make sure the gas pressure on the tank you are using is at least 100 psi
4) Setup:
    a. use 10x dry objective
    b. Focus on top layer of ruthenium slide
5) Set points:
    a. Go to X,Y marker / tab
    b. Set 3 points in each well, make sure they are under microchannel design
    c. Intensity for 0% O_2 should be between 2000-3000
    d. Intensity for 21% O_2 should be between 100-500
6) Connect 1/16” OD (Cole Palmer) tubing from gas tank to well and turn on gas
7) Wait 15 minutes for gas to equilibrate if gap is 3mm
8) Take images at set points
9) Switch gas concentration in well
10) Repeat until all wells received all concentrations
11) Use data to make calibration curve

Data collection

1) Calibrate each well to be used as described in the section above
2) Connect 1/16” OD (Cole Palmer) tubing from gas tank containing desired percent oxygen (between 0-12%) to well and turn on gas
3) Put water, as a media proxy, into each well
4) Nest 6 well hypoxic insert into 6 well plate containing ruthenium slides
5) Set software to capture images at set point determined during calibration at 5 minute intervals
6) Analyze INTENSITIES and use calibration curve to determine percentage of oxygen over time

To get intensity from images using Slidebook software

1) Double click on first image in stack to open
2) Go to mask Tab
    a. Select create

    b. In pop up check box that says “in all images in same channel” (last choice)
3) Go to View tab
    a. Click select all i.e. 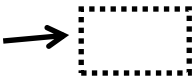
4) Go to Mask tab
    a. Click “mark selection” should turn image purple
5) Go to Mask tab
    a. Click “copy to all image in slide”
    b. Click “yes” on pop us
6) Go to Mask tab
    a. Click “Mask Statistics”
    b. Check box that says “ all images in slide with same mask name”
    c. Open intensity tab
    d. Select mean intensity
    e. Click “export”
7) Save statistical data to your folder (will be text file)

Once data has been collected you can remove excess text from text file to make it easier to analyze by:

1) Open text file containing desired data in excel
2) Delete column A (Select, Edit, Delete)
3) Select what has become the new column A (REMOVE TEXT)
    a. Hit F5
    b. Choose “Special”
    c. Click box next to “constants” and uncheck box next to “numbers”
    d. Choose “delete”
4) Select what has become the new column A again (REMOVE BLANKS)
    a. Hit F5
    b. Choose “Special”
    c. Click box next to “blanks”
    d. Choose “edit”
    e. Choose “delete”
    f. Choose “shift cells up”
5) Now data can be easily analyzed

A.5 Multilayer SU-8 Lithography for Yeast Gradient Device

Multilayer SU-8 lithography for Yeast Gradient Device Protocol

Layer 1

1) Dehydrate 3” Si wafer for 15 minutes at 115ºC
2) Spin SU-8 2002 for 5 seconds at 500 rpm then 30 seconds at 1000 rpm
3) Bake for 1 minute at 65ºC followed by 3 minutes at 95ºC
4) Expose wafer to UV for 25 seconds with photomask containing design of layer one (in this case the layer one photomask containing the yeast trapping area) placed on top of SU-8 surface and a quartz plate covering the photomask which is used to keep the photomask in place
5) Bake for 3 minutes at 95ºC
6) Put tape over alignment marks and measure height

Layer 2

1) Spin SU-8 2050 for 10seconds @ 500 rpm flowed by 30 seconds @ 2000 rpm
2) Bake for 6 min at 65ºC followed by 20 minutes at 95ºC
3) Remove tape from alignment marks
4) Align photomask for layer 2
5) Expose wafer to UV for 50 seconds with photomask containing design of layer two
6) Bake 15 min at 95 C
7) Check to see if layer 1 and layer 2 are aligned and measure height of layer 2

Layer 3

1) Spin SU-8 2150 for 10seconds @ 500 rpm flowed by 30 seconds @ 900 rpm
2) Bake for 7 minutes @ 65ºC followed by 60 minutes at 95ºC
3) Align photomask for layer 3
4) Expose wafer to UV for 50 seconds with photomask containing design of layer two
5) Bake 20 min @ 95ºC, let cool to room temperature and measure height
6) Place wafer in glass dish on orbital shaker and cover with old SU-8 developer solution, shake for 15 minutes at 2000 rpm
7) Pour old developer into waste container and cover wafer in new developer, shake for 15 minutes at 2000 rpm
8) Pour developer into used developer container and rinse wafer with IPA
9) N_2 blow dry and measure height of microchannel design
10) Bake wafer @ 75ºC for 10-15 minutes
11) Place developed wafer in a petri dish and pour 25 grams of degassed 10:1 PDMS to curing agent on to the wafer
12) Degass and bake for 2 hours @ 75ºC
13) Cut PDMS to reveal design

A.6 µPG Protocol for SU-8 Fabrication of Yeast Gradient Device

µPG for Yeast Protocol

Layer 1

1) Dehydrate 3” Si wafer for 15 minutes at 115ºC
2) Spin SU-8 2002 for 5 seconds at 500 rpm then 30 seconds at 1000 rpm
3) Bake for 1 minute at 65ºC followed by 3 minutes at 95ºC
4) Put in µPG and expose at 18 mW, 50% power, Fx2 ~ 5 hours
5) Bake for 3 minutes at 95ºC
6) Put tape over alignment marks and measure height

Layer 2

1) Spin SU-8 2050 for 10 s at 500 rpm - 30 s at 3000 rpm
2) Bake for 6 min at 65ºC followed by 20 minutes at 95ºC
3) Remove tape from alignment marks
4) Put in µPG at exposure 18 mW, 100% power, Fx4 ~ 9 hours
5) Bake 15 min at 95ºC
6) Check to see if layer 1 and layer 2 are aligned; measure height of layer 2

Layer 3

1) Spin SU-8 2150 for 10seconds @ 500 rpm followed by 30 seconds @ 2000 rpm
2) Bake for 7 minutes @ 65ºC followed by 50 minutes at 95ºC
3) Put in µPG at exposure 18 mW, 100% power, Fx4 ~ 9 hours
4) Bake 20 min @ 95ºC, let cool to room temperature and measure height

5) Spin SU-8 2150 for 10 seconds @ 500 rpm flowed by 30 seconds @ 1500 rpm
6) Bake 7 min @ 65ºC followed by 60 minutes at 95ºC
7) UV expose w/ hand aligned photomask for layer 3 for 75 seconds
8) Bake 30 minutes @ 95ºC, let cool to room temperature
9) Place wafer in glass dish on orbital shaker and cover with old SU-8 developer solution, shake for 10 minutes at 2000 rpm
10) Pour old developer into waste container and cover wafer in new developer, shake for 10 minutes at 2000 rpm
11) Pour developer into used developer container and rinse wafer with IPA
12) N2 blow dry and measure height of microchannel design
13) Bake wafer @ 75ºC for 10-15 minutes
14) Place developed wafer in a petri dish and pour 25 grams of degassed 10:1 PDMS to curing agent on to the wafer
15) Degass and bake for 2 hours @ 75ºC
16) Cut PDMS to reveal design

A.7 Polystyrene Coating for Yeast Gradient Device

Polystyrene Coating Protocol

1) Clean the chuck of the spinner with IPA, DO NOT SQUIRT IPA DIRECTLY ONTO THE CHUCK! Squirt IPA onto a Kim wipe then wipe down the chuck
2) Place PDMS casting with inlets and outlets already bored channel side up onto the chuck and apply vacuum pressure
3) Add 0.05% polystyrene dissolved in toluene drop wise to each of the channels using a toothpick
4) Spin for 5 seconds at 500 rpm then 30 seconds at 2800 rpm
5) Allow to air dry for at least 4 hours
6) Remove excess polystyrene form outside the channel walls using Scotch tape
7) Use hand held plasma gun to bond normally to glass slide

A.8 Glass Etching for Yeast Gradient Device

Glass Etching Protocol for Yeast Device:

Etch of Perfusion Channel Layer (max height/depth 500 µm)

1. Place soda lime glass pre-coated with chromium and AZ photo resist (Telic) into maskless photolithography machine
2. AZ photoresist is exposed using the maskless photolithography machine only where perfusion channels will be etched
3. Immerse the exposed glass for 1 min with constant agitation at room temperature in AZ 1500 developer (Haas), to remove resist from exposed areas. Rinse with deionized water.
4. Remove chromium layer using chromium etchant 1020AC (transesne) at room temperature for 15-60 seconds (Cr layer is 1200a thick). Rinse with deionized water.
5. Rinse glass with Millipore water then dry with N2.
6. Cover back of glass PVC sealing tape.
7. Immerse glass in etching solution (1:0.5:0.75 mol/L of HF/NH4F/HNO3) heated to 40ºC For 5 hours 30 minutes.
8. Rinse with Millipore water.
9. Rinse with Ethanol.
10. N2 blow dry.

Etch of Diffusion Channel Layer (max height/depth 50µm)

11. Place soda lime glass pre-coated with chromium and AZ photo resist (Telic) into maskless photolithography machine

12. AZ photoresist is exposed using the maskless photolithography machine only where perfusion channels will be etched
13. Immerse the exposed glass for 1 min with constant agitation at room temperature in AZ 1500 developer (Haas), to remove resist from exposed areas. Rinse with deionized water.
14. Remove chromium layer using chromium etchant 1020AC (transesne) at room temperature for 15-60 seconds (Ask Telic how thick Cr layer is). Rinse with deionized water.
15. Rinse glass with Millipore water then dry with N2.
16. Cover back of glass PVC sealing tape.
17. Immerse glass in etching solution (1:0.5:0.75 mol/L of HF/NH4F/HNO3) heated to 40ºC For 38 minutes.
18. Rinse with Millipore water.
19. Rinse with Ethanol.
20. N2 blow dry.

Etch of Yeast Trap Area (max height/depth 5 µm)

21. Place soda lime glass pre-coated with chromium and AZ photo resist (Telic) into maskless photolithography machine
22. AZ photoresist is exposed using the maskless photolithography machine only where perfusion channels will be etched
23. Immerse the exposed glass for 1 min with constant agitation at room temperature in AZ 1500 developer (Haas), to remove resist from exposed areas. Rinse with deionized water.

24. Remove chromium layer using chromium etchant 1020AC (transesne) at room temperature for 15-60 seconds (Ask Telic how thick Cr layer is). Rinse with deionized water.
25. Rinse glass with Millipore water then dry with N2.
26. Cover back of glass PVC sealing tape.
27. Immerse glass in etching solution (1:0.5:0.75 mol/L of HF/NH4F/HNO3) heated to 40ºC For 3minutes.
28. Rinse with Millipore water.
29. Rinse with Ethanol.
30. N2 blow dry.

A.9 h-PDMS Protocol

h - PDMS Protocol

1) Mix 3.4g of vinyl-PDMS copolymer (VDT-731); 18 µl of Pt catalyst (SIP6837.2LC); and 1 drop of modulator = 2,4,6,8-tmtvcts (2.2 wt%)
2) Degass mixture for 1 -2 minutes
3) Gently stir in 1 gram of hydrosilane copolymer (HMS-301)
4) Immediately (within 3 minutes) spin coat (30-40µl) of h-PDMS onto Si Master (1000 rpm for 40seconds)
5) Bake for 30 minutes at 60ºC
6) While h-PDMS is baking mix and degass 25 g of regular PDMS (10:1 ratio of PDMS to curing agent)
7) Pour degassed PDMS on top of partially cured h-PDMS
8) Bake for 1 hour at 60ºC
9) Allow to cool to room temperature
10) Cut to remove design

A.10 Hot Embossing with Micro-milled Brass Mold

PMMA Hot Embossing Protocol

1) Rinse PMMA discs w/ isopropanol followed by distilled water
2) Place in oven at 75ºC for at least 24 hours
3) Emboss PMMA with brass mold at force = 5 kN for 5 min at 155ºC
4) Remove excess PMMA form outside the channel area using Drummel
5) Drill 2 mm diameter holes at the end of each channel

6) Sonicate PMMA embossed chip in 0.5% Alconox solution for 20 minutes

7) Rinse in DI water

8) Sonicate PMMA embossed chip in DI water for 10 min

9) Dry with compressed air

10) Cut 250 µm thin sheet to size with Exacto knife

11) Plasma treat both the embossed PMMA and PMMA thin sheet for 30 seconds

11) Sandwich embossed PMMA w/ thin PMMA sheet between 2 glass slides and clamp with binder clips

12) Place sandwich in convection oven set e 120ºC for 30 minutes

13) Allow to cool to room temperature

14) Device is now ready for fittings to be attached

A.11 Epoxy

Smooth - On Protocol

1) Mix epoxy in a 100A : 30B weight ratio of epoxy A to epoxy B
2) Stir for at least 3 minutes
3) Pour over substrate to be molded
4) Degass until all bubbles are removed
5) Let cure at room for 24 hours in a well-ventilated area

A.12 Fabrication of incubator Device

Mouse incubator device fabrication

1) Dehydrate 3” Si wafer for 15 minutes at 115ºC
2) Spin SU-8 2150 for 10 seconds at 500 rpm followed by 1000 rpm for 30 seconds
3) Bake for 15 minutes at 65ºC followed by 75 minutes at 95ºC
4) Expose wafer to UV for 75 seconds (100 mJ) with photomask containing design of embryo chamber layer placed on top of SU-8 surface and a quartz plate covering the photomask which is used to keep the photomask in place
5) Bake for 7 minutes at 65ºC followed by 60 minutes at 95ºC
6) Remove unexposed SU-8 photo-resist was removed using SU-8 developer Place wafer in glass dish on orbital shaker and cover with old SU-8 developer solution, shake for 15 minutes at 2000 rpm
7) Pour old developer into waste container and cover wafer in new developer, shake for 15 minutes at 2000 rpm
8) Pour developer into used developer container and rinse wafer with IPA
9) N_2 blow dry and measure height of microchannel design
10) Bake wafer @ 75ºC for 10-15 minutes
11) Place developed wafer in a petri dish and pour 25 grams of degassed 10:1 PDMS to curing agent on to the wafer
12) Degass and bake for 2 hours @ 75ºC
13) Cut PDMS to reveal design
14) Bond PDMS casting to glass slide using hand held plasma treater for 30 seconds on the slide and 30 seconds on the channel side of the PDMS

A.1 Fabrication of Bench-Top Device

Bench-Top device fabrication

1) cast 1/8” od Tygon tubing (Cole Palmer) is cast in a 120mmx120mm square Petri dish (Fisher) using PDMS
2) Once the PDMS is cured remove casting and cut into 6ths with each piece including Tygon tubing cast in the center
3) Punch a 13mm diameter hole into the center of each piece, this forms layer one of the device
4) Plasma bond Layer one is then plasma bonded to a 75 mm x 38 mm glass slide using a corona plasma treater (Electro-Technic Products, Inc) for 30 seconds on the slide and 30 seconds on layer one
5) plasma bond an 18mm x 18mm coverslip (layer 2) (Fisher) to layer one, covering the hole punched in layer one
6) Bond layer three (the same PDMS casting used in the incubator device) to layer two using plasma treatment as well as a thin bead of PDMS around the outside of the third layer
7) Invert the partially fabricated device and place on a 75°C hot plate, place a 300 gram weight on top, and baked for 2 hours
8) Position a 375 µm in height hexagonal warming channel over the embryo platforms in the third layer and plasma bond

A.15 Temperature Characterisation

Liquid crystal temperature measurement

1) Cut a portion of a sheet of liquid temperature crystals into a 1”x1” square
2) Put a bead of uncured PDMS around the bottom and top of the liquid crystal sheet
3) Sandwich this sheet of liquid temperature crystals between the glass cover slip and the PDMS layer containing the embryo culture platform to measure the temperature at the location of the embryo barriers
4) Bake at 75ºC inverted for 2 hours
5) Add top warming layer as described in section A.13
6) Set up device as normal with water recycling through warming channels
7) Take color photos every 30 minute for 24 hours
8) After three trials are performed in three different devices, perfuse RT water into the embryo chamber, as a proxy for media and Take color photos were taken every 30 minute for 24 hours
9) Use colorimetric chart to determine temperature in each image

A.16 Fabrication of Embryo CO2 Calibration Device

Calibration device fabrication

1) Dehydrate 3” Si wafer for 15 minutes at 115ºC
2) Spin SU-8 2150 for 10 seconds at 500 rpm followed by 800 rpm for 30 seconds
3) Bake for 15 minutes at 65ºC followed by 90 minutes at 95ºC

4) Expose wafer to UV for 100 seconds (100 mJ) with photomask containing design of embryo chamber layer with channels for fiber optic probes placed on top of SU-8 surface and a quartz plate covering the photomask which is used to keep the photomask in place
5) Bake for 7 minutes at 65ºC followed by 60 minutes at 95ºC
6) Remove unexposed SU-8 photo-resist was removed using SU-8 developer Place wafer in glass dish on orbital shaker and cover with old SU-8 developer solution, shake for 15 minutes at 2000 rpm
7) Pour old developer into waste container and cover wafer in new developer, shake for 15 minutes at 2000 rpm
8) Pour developer into used developer container and rinse wafer with IPA
9) N_2 blow dry and measure height of microchannel design
10) Bake wafer @ 75ºC for 10-15 minutes
11) Place developed wafer in a petri dish and pour 25 grams of degassed 10:1 PDMS to curing agent on to the wafer
12) Degass and bake for 2 hours @ 75ºC
13) Cut PDMS to reveal design
14) Bond PDMS casting to glass slide using hand held plasma treater for 30 seconds on the slide and 30 seconds on the channel side of the PDMS

A.17 CO2 Characterization

CO2 measurement for bench-top device

1) Dilute phenol red stock solution to 1%
2) Perfuse 1% phenol red into the inlets of the embryo chamber in the CO2 calibration device at the experimental flow rate of 1.3 µl/min
3) Insert each of the two fiber optic probes into the channels in the device adjacent to the embryo barriers
4) Connect one probe to a light source
5) Connect the second probe the spectrophotometer (Ocean Optics)
6) Use ocean optics software to measure the absorption at 555 nm
7) Calibrate the probes using 0, 5, and 10% CO2 and taking measurement every 5 minutes for 30 minutes
8) Use these measurements to formulate a calibration curve
9) Calculate y- intercept equation through linear regression, use this equation to calculate the amount of CO_2 in the device over a 24 hour period.
10) Use ocean optics software to measure the absorption at 555 nm and log every 15 minutes

A.18 Fabrication of U of C device

U of C device fabrication

1) Dehydrate 3” Si wafer for 15 minutes at 115ºC
2) Spin SU-8 2150 for 10 seconds at 500 rpm followed by 1200 rpm for 30 seconds

3) Bake for 7 minutes at 65ºC followed by 50 minutes at 95ºC
4) Expose wafer to UV for 50 seconds (100 mJ) with photomask containing array of U of C embryo chambers placed on top of SU-8 surface and a quartz plate covering the photomask which is used to keep the photomask in place
5) Bake for 5 minutes at 65ºC followed by 18 minutes at 95ºC
6) Remove unexposed SU-8 photo-resist was removed using SU-8 developer Place wafer in glass dish on orbital shaker and cover with old SU-8 developer solution, shake for 10 minutes at 2000 rpm
7) Pour old developer into waste container and cover wafer in new developer, shake for 10 minutes at 2000 rpm
8) Pour developer into used developer container and rinse wafer with IPA
9) N_2 blow dry and measure height of microchannel design
10) Bake wafer @ 75ºC for 10-15 minutes
11) Place developed wafer in a petri dish and pour 25 grams of degassed 10:1 PDMS to curing agent on to the wafer
12) Degass and bake for 2 hours @ 75ºC
13) Cut PDMS to reveal design
14) Cut 18x18 mm coverslips in thirds
15) Bond PDMS casting to a piece using hand held plasma treater for 30 seconds on the slide and 30 seconds on the channel side of the PDMS
16) Bake for 1 hour at 85ºC
17) Spread uncured PDMS along the left side of the device to cover any cut marks that may refract light
18) Bake 2 hours at 85ºC

Appendix B Gβ phosphorylation is critical for efficient chemotropism in yeast

Gβ phosphorylation is critical for efficient chemotropism in yeast

Reagan DeFlorio[*,†], Elisabetta Apollinari[*,Σ], Marie-Elena Brett[#,Σ], Metodi Metodiev[*,✎], Oleksii Dubrovskyi[*,¶], David Eddington[#], Robert A. Arkowitz[†] and David E. Stone[*,@]

[*]Laboratory for Molecular Biology, Department of Biological Sciences, University of Illinois at Chicago, Chicago, IL 60607, USA

[#]Department of Bioengineerning, University of Illinois at Chicago, Chicago, IL 60607

[†]CNRS UMR7277 / INSERM UMR1091 / Université de Nice - Sophia Antipolis, Institute of Biology Valrose, Nice, France

[✎]Current address: School of Biological Sciences, University of Essex, Essex, UK

[¶]Current address: College of Medicine, University of Chicago, Chicago, IL 60637

[Σ]These authors contributed equally to this work.

[@]Correspondence should be addressed to D. S. at the Laboratory for Molecular Biology, Department of Biological Sciences, University of Illinois at Chicago, 900

South Ashland Avenue, Chicago, IL 60607, USA; e-mail: dstone@uic.edu; phone: 312-996-5710; fax: 312-413-2691

Running Title: Effect of Gβ phosphorylation on yeast mating

SUMMARY

Mating yeast cells interpret complex pheromone gradients and polarize their growth in the direction of the closest partner. Chemotropic growth depends on both the pheromone receptor and its associated G protein. Upon activation by the receptor, Gα dissociates from Gβγ and Gβ is subsequently phosphorylated. Free Gβγ signals to the nucleus via a MAPK cascade and recruits Far1-Cdc24 to the incipient growth site. It is not clear how the cell establishes and stabilizes the axis of polarity, but this process is thought to require local amplification via the Gβγ-Far1-Cdc24 chemotropic complex, as well as communication between this complex and the activated receptor. Here we show that a mutant form of Gβ that cannot be phosphorylated confers defects in directional sensing and chemotropic growth. Our data suggest that phosphorylation of Gβ plays a role in localized signal amplification and in the dynamic communication between the receptor and the chemotropic complex, which underlie growth site selection and maintenance.

INTRODUCTION

In metazoans, directed cell movement in response to a chemical gradient (chemotaxis), plays a vital role in embryogenesis, postnatal development and homeostasis, and immunity. Moreover, the survival of many single-celled organisms depends on their ability to detect and move in response to chemical stimuli. The related phenomenon, directed cell growth in response to a chemical gradient (chemotropism), is also essential in many species. For example, in mammals, chemotropism is integral to axon guidance (Hong and Nishiyama, 2010; Tojima et al., 2011) and angiogenesis (English et al., 2001; Basile et al., 2004). Pollen tube guidance is also a chemotropic process (Palanivelu and Preuss, 2000; Kim et al., 2004), and there is an increasing appreciation for the role of chemotropism in the life cycles of fungal species, including plant and human pathogens (Snetselaar et al., 1996; Daniels et al., 2006).

To direct movement or growth up a chemical gradient, chemotactic and chemotropic cells must solve a set of common challenges. They must be able to detect the presence of the extracellular signaling molecule and determine the direction of its source. Many chemosensing cells express G-protein coupled receptors (GPCRs) for this purpose (Weiner, 2002). Using the spatial information encoded in the distribution of activated receptors, the cell must establish a site or landmark for polarization. Actin and/or microtubule cytoskeletal elements are then assembled at, or recruited to, this site to promote directional movement or growth. Finally, the cell must be able to stabilize the axis of polarity over time, while retaining the plasticity to change its orientation in response to changes in the direction of the gradient.

Because physiological gradients of chemoattractant are typically very shallow, 1-10% across the cell's length (Mato et al., 1975; Tranquillo et al., 1988; Segall, 1993), establishment of the polarity site requires the conversion of small differences in receptor occupancy into a substantially steeper intracellular signaling gradient. This is thought to depend on feedback loops such as those first discovered in *Dictyostelium* and neutrophils. Exposure of these cells to chemoattractant gradients leads to a gradient of receptor occupancy such that

slightly more receptors are activated on the surface of the cell closest to the signaling source (Hoeller and Kay, 2007). This results in a similar gradient of activated heterotrimic G protein subunits, Gα-GTP and free Gβγ (Jin et al., 2000). Gβγ then recruits and activates the lipid kinase, PI3K, which generates PIP_3. In addition, Gβγ activates the Rho GTPases, Rac and Cdc42, and Rac-GTP enhances PIP_3 accumulation (Takeda et al., 2007). PIP_3, in turn, promotes further Rac activation. Together, these actions generate a "local excitation" that enhances signaling at the cell's leading edge. Key to generating the steep gradient of PIP_3 is a second pathway that causes a graded inhibition of PIP_3 accumulation across the cell. This depends on the localization of the PIP_3 phosphatase, PTEN, to the lagging edge. Although other signaling pathways are now known to be essential for chemotaxis (Chen et al., 2007; Kamimura et al., 2008; Veltman et al., 2008), feedback loops that generate and couple local excitation with global inhibition (LEGI) have emerged as a generally accepted mechanism underlying directional sensing (Iijima et al., 2002; Weiner, 2002; Devreotes and Janetopoulos, 2003).

In comparison to chemotactic models, the amplification mechanisms that underlie directional sensing in chemotropic systems are less well understood. To date, the best characterized example of eukaryotic chemotropism occurs during the mating response of the budding yeast, *Saccharomyces cerevisiae*. In the haploid phase of its life cycle, budding yeast exist as two mating types, *MAT***a** and *MAT*α. Each mating type constitutively secretes a specific peptide mating pheromone that binds to GPCRs on cells of the opposite type. When occupied by ligand, the pheromone receptors activate the mating-specific Gα protein, Gpa1 (henceforth Gα), *via* guanine nucleotide exchange and the subsequent dissociation of Gα-GTP from the Gβγ dimer, Ste4/Ste18. The signal is then transmitted by Gβγ via the Fus3 MAP kinase (MAPK) cascade that ultimately induces arrest in the G1 phase of the cell cycle, broad changes in gene expression, and morphogenesis (Dohlman and Thorner, 2001; Bardwell, 2005). Cells polarize their growth and form pear-shaped cells called shmoos, in response to both uniform (isotropic) pheromone and pheromone gradients. In mating mixtures, cells find and then contact the closest potential mating partner by determining the

direction of the most potent pheromone source and growing toward it (Jackson and Hartwell, 1990).

Polarized growth in *S. cerevisiae*, like that in higher eukaryotes, requires the marking of a growth site at the cell cortex and alignment of the actin cytoskeleton towards it. Cargo bound for the polarized structures is transported by myosin motors along the actin cables (Pruyne and Bretscher, 2000a; Pruyne and Bretscher, 2000b). Actin polarization depends on Cdc42, which is thought to activate a formin protein, Bni1, that nucleates and tethers actin cables to the polarization site (Evangelista et al., 2002; Sagot et al., 2002). Bni1 is part of the "polarisome" complex, together with Spa2, Bud6, and Pea2 (Pruyne and Bretscher, 2000a). Cdc42 is activated by the guanine nucleotide exchange factor, Cdc24, which itself undergoes localized activation by positional cues during both vegetative budding and mating. In vegetative cells, cortical tags promote localized activation of the Ras-related GTPase, Bud1/Rsr1 (hereafter Bud1), which binds directly to Cdc24 (Park et al., 1997) and Cdc42 (Kang et al., 2010). In cells exposed to pheromone, $G\beta\gamma$ interacts with the Far1-Cdc24 complex (Butty et al., 1998; Nern and Arkowitz, 1998; Nern and Arkowitz, 1999). Interaction of $G\beta\gamma$ with Far1 is thought to activate Cdc24 (Wiget et al., 2004), leading to localized GTP-loading of Cdc42, recruitment of Bni1, nucleation of actin cables, and polarized growth to form the mating projection. Under physiological conditions, the $G\beta\gamma$-Far1-Cdc24 complex is presumed to assemble in the region of the cell surface that experiences the highest concentration of pheromone, and to mark this area for growth in preference to the predetermined bud site — *i.e.*, formation of the $G\beta\gamma$-Far1-Cdc24 chemotropic complex competitively inhibits formation of the Bud1-Cdc24 budding complex (Nern and Arkowitz, 2000). In this way, the cell is thought to orient its growth toward the source of pheromone, although the feedback loops that amplify the directional signal have not been well studied. When cells are unable to sense a gradient of pheromone, on the other hand, they form a mating projection at the site that would have been used for the next bud — the site marked by Bud1 (Dorer et al., 1995; Nern and Arkowitz, 1999). This is called the default mating projection site.

Like chemotaxing cells, yeast exhibit a remarkable ability to interpret chemical gradients. It has been estimated that a 1% difference in receptor occupancy across the 5μm length of a yeast cell in a pheromone gradient is sufficient to elicit robust orientation toward the pheromone source (Segall, 1993), and recent microfluidic studies suggest an even greater acuity (Moore et al., 2008). How is this very slight asymmetry in activated receptor and G protein amplified internally to establish a unique shmoo site, and how is this positional information continually communicated to the polarisome to ensure properly oriented growth over time?

Since it was first reported that pheromone induces the phosphorylation of Gβ on multiple sites (Cole and Reed, 1991), the function of this modification has been elusive. In the initial attempt to assess the pheromone response of cells unable to phosphorylate Gβ, a deletion allele of STE4 lacking 40 codons was used. The resulting defect in adaptation to pheromone was most likely due to the internal Gβ deletion rather than to a lack of phosphorylation because, subsequently, a double point mutant form of Gβ that cannot be phosphorylated was found to have no measurable effect on signal transmission to the nucleus, adaptation, or diploid formation (Li et al., 1998a). More recently, we discovered that the activated forms of the mating-specific Gα protein and the Fus3 MAPK interact directly. A mutant form of Gα that is severely defective in binding Fus3, GαDSD1, confers a defect in partner discrimination, indicating a problem in directional sensing and/or directed growth (Metodiev et al., 2002; Strickfaden and Pryciak, 2008; Yu et al., 2008). GαDSD also results in hypo-phosphorylation and reduced levels of Gβ, as does fus3Δ. These observations raised the possibility that the phosphorylation of Gβ plays a role in chemotropism. Here we show that Gβ phosphorylation is critical for this process. Specifically, this modification of Gβ appears to promote communication between activated receptors and downstream components essential for polarized growth. Cells unable to phosphorylate Gβ exhibit specific defects in pheromone-induced morphogenesis, orientation towards mating partners, and the ability to reorient in response to a

[1] Gα-docking site disrupted; previously $G\alpha^{K21E\ R22E}$

vectorial change in the gradient. We propose a model in which Gβ phosphorylation provides a means to amplify the spatial signal and the Gβ phosphorylation/dephosphorylation cycle constitutes an updating mechanism that conveys the status of the receptor to the chemotropic complex and downstream cell polarity proteins.

Gα plays an essential role in the chemotropic shmoo pathway

The findings that $G\alpha^{DSD}$ confers partial defects in partner discrimination and mating efficiency (Metodiev et al., 2002), as well as in shmooing and actin polarization (Matheos et al., 2004), suggest that the Gα-Fus3 interaction plays a role in chemotropism. Moroever, Gα has been implicated in chemotropism by two other studies (Strickfaden and Pryciak, 2008; Yu et al., 2008). To further test this possibility, we asked whether $G\alpha^{DSD}$ *bud1*Δ cells can shmoo. Cells can form mating projections if either the default or chemotropic shmoo pathways are inactivated, but are unable to polarize their growth in response to pheromone if neither pathway is functional (Nern and Arkowitz, 2000). Therefore, components required for chemotropic growth can be uncovered by examining mutations in a *bud1*Δ background. For example, *cdc24-m1 bud1*Δ and *far1-H7 bud1*Δ cells cannot shmoo (Nern and Arkowitz, 2000) because Cdc24 and Far1 are essential chemotropic elements (Valtz et al., 1995; Nern and Arkowitz, 1998). Similarly, $G\alpha^{DSD}$ *bud1*Δ cells were unable to form mating projections (Fig. 1A). Whereas the Gα *bud1*Δ cells and $G\alpha^{DSD}$ *BUD1* cells (not shown) formed normally shaped shmoos, the $G\alpha^{DSD}$ *bud1*Δ cells either enlarged uniformly, or exhibited highly aberrant morphologies, consistent with the idea that the Gα-Fus3 interaction is required for chemotropic growth.

$G\beta^{P-}$ *bud1*Δ cells exhibit a range of defects in pheromone-induced polarized growth

Gβ phosphorylation and level are greatly reduced in pheromone-treated $G\alpha^{DSD}$ and *fus3*Δ cells, raising the possibility that Gβ is a target of Gα-Fus3. Because $G\alpha^{DSD}$ also confers defects in partner discrimination and in the genetic assay for “chemotropic” shmooing described above, we wondered whether the phosphorylation of Gβ plays a role in the chemotropic response. As a first test of this idea, we again used the genetic assay of “chemotropic” shmooing. The T320A/S335A allele of *STE4* encodes a mutant form of Gβ that is not phosphorylated in vivo (Li et al., 1998a). Strains were created in which the native *STE4* was replaced with $ste4^{T320A/S335A}$ (henceforth $G\beta^{P-}$) in *BUD1* and *bud1*Δ

backgrounds. The Gβ^{P-} *bud1*Δ, Gβ *bud1*Δ, Gβ^{P-} *BUD1*, and Gβ *BUD1* (henceforth WT, for wild type) cells were treated with a range of pheromone concentrations in liquid medium and examined at 60 min intervals for five hours. When stimulated with isotropic pheromone, the morphological response of Gβ^{P-} *BUD1* cells was indistinguishable from that of WT cells. In contrast, the Gβ^{P-} *bud1*Δ cells exhibited a variety of shmoo abnormalities at all doses and time points. Representative images of the phenotypes are shown in Fig. 1B.

A high proportion of the Gβ^{P-} *bud1*Δ shmoos were significantly shorter and broader than those formed by the Gβ *bud1*Δ control cells, as if their growth was less well focused. Their mean lengths were 0.89 and 0.84 that of the Gβ *bud1*Δ cells 4 and 5 hours after treatment, respectively ($p < 0.0001$; $n = 300$ for each time point), and most were abnormally shaped. Instead of narrowing smoothly to a pointed tip, Gβ^{P-} *bud1*Δ mating projections often extended almost straight out from the cell body and terminated in a bulbous curve, forming a shape reminiscent of a light bulb. Although aberrant shmoo morphologies were also seen in the Gβ *bud1*Δ culture, likely due to the absence of Bud1, their occurrence was greatly increased by Gβ^{P-} (80.7% as compared to 16.7%; $n \geq 260$; $p < 0.0001$).

Wild type yeast cells treated with high pheromone concentrations form successive mating projections with regular periodicity such that the growth of the first projection ends as the second begins (Bidlingmaier and Snyder, 2004). Under isotropic pheromone conditions, the second growth site is usually established far from the first one, so that the two projections ultimately form a wide angle (distal projections). Another striking phenotype of the Gβ^{P-} *bud1*Δ cells was their tendency to form second and third mating projections earlier than the control cells and in abnormal positions (Fig. 1C). In the *bud1*Δ control strain, we observed a small fraction of cells with two or more projections adjacent to one another (proximal projections). However, the occurrence of such cells was dramatically increased in the Gβ^{P-} *bud1*Δ strain, with the ratio of proximal to distal shmoos more than 10-fold greater in Gβ^{P-} as compared to control cells. Similar results were observed at all pheromone concentrations and incubation times. Interestingly, the Spa2-GFP marker of polarized growth simultaneously localized to more than one shmoo tip in a high

proportion of Gβ^{P-} *bud1*Δ cells (Fig. 1D), suggesting that Gβ phosphorylation is involved in the switching of growth from one site to another.

Although none of the Gβ^{P-} *bud1*Δ cells were completely incapable of polarized growth in isotropic pheromone, as are Gα^{DSD} *bud1*Δ and *cdc24-m*1 *bud1*Δ cells, a significant fraction were apparently unable to sustain unidirectional growth long enough to form a projection even after prolonged treatment. Such cells were usually quite small and formed multiple protrusions that, on the basis of morphological criteria, could not be considered true mating projections. In Fig. 1C, these cells are counted in the "multiple proximal" category; we refer to them as small multiple protrusion (SMP) cells. (The percentages of SMP cells ± s.e.m. were 16.2 ± 1.4 and 4.0 ± 0.5 for the Gβ^{P-} *bud1*Δ and Gβ *bud1*Δ cultures, respectively; $n \geq 200$; $p < 0.0001$.) Together, the results presented in Fig. 1B-D suggest that, in cells unable to shmoo *via* the Bud1-dependent default pathway, phosphorylation of Gβ is critical for the stabilization of the axis of polarity and hence the focused growth of mating projections, as well as for proper growth site switching.

The growth site of pheromone-treated Gβ^{P-} *bud1*Δ cells wanders where the receptor is concentrated

As discussed above, cells in which both the default and chemotropic pathways have been inactivated are unable to form mating projections. Surprisingly, this phenotype arises not from a failure to establish polarity, but from an inability to maintain it. This was first demonstrated by Nern and Arkowitz, who found that in pheromone-treated *cdc24-m1 bud1*Δ cells, the Cdc42 guanine nucleotide exchange factor Cdc24 and the polarisome component Spa2 localized to discrete sites. The cell grows uniformly, however, because its axis of polarity wanders (Nern and Arkowitz, 2000). Indeed, markers for secretion, new cell wall incorporation, and the Ste2 pheromone receptor were spread out over approximately half the cell after several hours of pheromone treatment. More recently, it has been found that another polarity marker, Bem1-GFP, wanders rapidly around the membrane of pheromone-treated *cdc24-m1 bud1*Δ cells (D. Lew, personal communication). This supports the earlier conclusion that chemotropic/default shmoo pathway double mutants are unable to shmoo because they cannot stabilize their axis of polarity long enough to polarize their growth.

Could the blunt shmoo and SMP phenotypes be the result of a less severe wandering-axis phenotype as observed in *cdc24-m1 bud1*Δ cells? To test this possibility, we mixed *MAT***a** Gβ^{P-} *bud1*Δ and *MAT***a** Gβ *bud1*Δ cells expressing Spa2-GFP with WT *MAT*α cells, and assayed the localization of the reporter over time (Fig. 2A). In the Gβ *bud1*Δ control cells, Spa2-GFP typically localized tightly and invariantly to the tip of the growing mating projection, moving steadily outward along the axis of polarity. In the Gβ^{P-} *bud1*Δ cells, Spa2-GFP moved more than twice as fast and twice as far, even though the mutant shmoos did not elongate more than the control cells. Rather, the increased mobility of Spa2-GFP correlated with a significantly increased tendency to change direction (Table 1). Multiple Spa2-GFP spots were also commonly observed in the mutant, but rarely in control cells. Thus, the axis of polarity exhibited confined wandering within the broad mating projections formed by Gβ^{P-} *bud1*Δ cells during mating.

It is well established that essential regulators of actin cable polymerization (e.g., Cdc24, Cdc42, Bem1, and Spa2) cluster tightly in a patch at the tips of shmooing cells (Pruyne and Bretscher, 2000a; Arkowitz, 2009). A recent study concluded that in pheromone-treated WT cells, this “polarity patch” wanders along the cell cortex, becoming restricted in its movement around the incipient growth site (D. Lew, personal communication). Polarity patch movement is thought to be retarded by free G$\beta\gamma$, which is ultimately determined by the local density of activated receptor. A supporting observation is that the role of the receptor and G$\beta\gamma$ in stabilizing the polarity patch can be bypassed by a chimeric protein consisting of Bem1 and the transmembrane domain of the v-SNARE, Snc2. Expression of Bem1-GFP-Snc2 dramatically slowed movement of the polarity patch, focusing the growth of WT cells and restoring the ability of *cdc24-m1 bud1*Δ cells to shmoo (D. Lew, personal communication). If the shmoo morphology and maintenance defects displayed by Gβ^{P-} *bud1*Δ cells are also due to a wandering axis of polarity stemming from a weakened link between the receptor and polarity patch, we would expect these phenotypes to be suppressed by Bem1-GFP-Snc2 as well. This proved to be the case: The shmoos formed by Gβ *bud1*Δ and Gβ^{P-} *bud1*Δ cells transformed with the Bem1-GFP-Snc2 construct were indistinguishable (Fig. 2B).

In cells responding to pheromone, the receptor and G protein polarize to the mating projection (Suchkov et al., 2010) — the same area within which the growth site wanders in pheromone-treated Gβ^{P-} bud1Δ cells. This confined wandering might underlie the formation of proximal projections. To determine whether receptor polarity influences the tendency of Gβ^{P-}bud1Δ cells to form proximal mating projections, we constructed Gβ^{P-} bud1Δ and Gβ bud1Δ strains expressing the Ste2$^{7XR/GPAAD}$ mutant form of the receptor. Ste2$^{7XR/GPAAD}$ cannot be internalized (Ballon et al., 2006) and therefore, does not polarize in response to pheromone (Suchkov et al., 2010). Although cells expressing Ste2$^{7XR/GPAAD}$ also form blunt shmoos, preventing internalization and polarization of the receptor completely suppressed the increased formation of proximal projections by Gβ^{P-} bud1Δ cells (Fig. 2C), consistent with our hypothesis.

Together, the data shown in Fig. 2 indicate that, although the axis of polarity wanders in Gβ^{P-} *bud1*Δ cells, the movement of the growth site is limited to the region of highest receptor density. This implies that phosphorylation of Gβ helps to link the position of the polarity proteins to that of the receptor.

The effect of Gβ phosphorylation on Gβ localization

One way that the cell's inability to phosphorylate Gβ could result in the phenotypes we observe in Gβ^{P-} *bud1*Δ cells is if the mutant form of Gβ is not properly localized. To test this possibility, we tagged the N-termini of WT Gβ and Gβ^{P-} with GFP in situ. In cells subjected to isotropic pheromone treatment, the WT Gβ polarized to the incipient shmoo site significantly earlier than did GFP-Gβ^{P-} (Table 2; Fig. 3A). Moreover, GFP-Gβ^{P-} failed to stably polarize in a significantly higher proportion of cells. Similar but more pronounced defects were observed in mating mixtures (Table 2; Fig. 3B). Notably, a substantial fraction of mating GFP-Gβ cells switched from one polarization site to another, perhaps due to orientation away from the default site or to changes in the direction of the strongest ambient gradient. In contrast, mating GFP-Gβ^{P-} cells were significantly defective in site switching, as well as in consolidating Gβ in a single region of the membrane and in maintaining a single axis of polarized growth. These data suggest that Gβ phosphorylation plays

an important role in the pheromone-induced redistribution of Gβ, particularly in gradient-stimulated cells.

The effect of Gβ^{P-} on Gβ-Far1 interaction and Spa2 and Cdc42 dynamics

Another way that inability to phosphorylate Gβ could impact the cell is if the phosphorylation of Gβ affects the strength of its interactions. For example, Ste5 interacts preferentially with the phosphorylated form of Gβ in yeast (Feng et al., 1998), and phosphorylation affects the activity of a mammalian Gβ (Chakrabarti and Gintzler, 2003). Given the phenotypes conferred by Gβ^{P-}, the interaction of Gβ with the Far1-Cdc24 chemotropic complex is a good candidate to be regulated by Gβ phosphorylation. To test of this possibility, we used a well-established genetic assay (Whiteway et al., 1990; Cole et al., 1990; Bar et al., 2003; Draper et al., 2009) to ask whether Far1 can discriminate between Gβ and Gβ^{P-}. The assay is based on the observation that by triggering the pheromone-responsive MAPK pathway, overexpression of Gβ blocks cell cycle progression, and therefore, cell proliferation. Co-overexpression of a protein that binds Gβ can prevent pathway induction, and thereby rescue the vegetative growth of cells expressing excess Gβ. At the level of transcriptional induction, cell cycle arrest, and shmooing, Gβ and Gβ^{P-} appear to be equally potent (Li et al., 1998a; see also Fig. 1B). Nevertheless, overexpression of Far1 specifically rescued the cell growth defect due to the overexpression of Gβ^{P-}, and not that of Gβ (Fig. 4A), suggesting that Far1 has a greater affinity for the unphosphorylated form of Gβ.

To further investigate the possibility that the phosphorylation of Gβ affects the dynamic interactions of the chemotropic complex, we used in vivo fluorescence photobleaching approaches. First, we compared recovery times of the Spa2-GFP signal after photobleaching the shmoo tips of Gβ^{P-} *bud1*Δ and Gβ *bud1*Δ cells. We chose to study Spa2 because, as a component of the polarisome, its positional stability is likely linked to that of the chemotropic complex. In FRAP (Fluorescence Recovery After Photobleaching) analysis, the recovery time is a function of the protein's dynamics — i.e., the slower the exchange into and out of a complex, the longer the signal will take to recover. As shown in Fig. 4B, the signal recovered in bleached Gβ *bud1*Δ shmoo tips significantly faster and to a greater degree than in

bleached Gβ^{P-} *bud1*Δ shmoo tips. This suggests that the stability of Spa2 interactions at the shmoo tip, and hence their duration, is increased when Gβ cannot be phosphorylated.

To assess the effect of Gβ^{P-} on the stability of the chemotropic complex itself, we performed iFRAP (Inverse Fluorescence Recovery After Photobleaching) analysis of GFP-Cdc42 at the shmoo tips of Gβ^{P-} *bud1*Δ and Gβ *bud1*Δ cells. In this technique, the area that serves as a source of molecules bound for the complex of interest is photobleached, and the rate at which the signal intensity decreases at the site of complex formation is measured. The rate of signal loss is inversely related to the stability of the complex. In our experiment, the back two thirds of cells were bleached, and the rate of GFP-Cdc42 signal loss at the shmoo tip was determined. As shown in Fig. 4C, the Cdc42-GFP signal decreased faster in Gβ *bud1*Δ shmoo tips than in the Gβ^{P-} *bud1*Δ shmoo tips. Consistent with the Spa2-GFP FRAP results, this suggests that the duration of Cdc42 interactions at the shmoo tip are increased when Gβ cannot be phosphorylated. Together, these data suggest that the unphosphorylated form of Gβ binds more tightly than the phosphorylated form to components of the chemotropic complex and/or polarisome. In other words, Gβ phosphorylation may negatively affect the stability of the chemotropic complex and/or polarisome.

Gβ^{P-} confers a defect in chemotropism

In cells lacking Bud1, mating projection formation in isotropic pheromone depends on chemotropic components (Nern and Arkowitz, 2000). Therefore, the observation that Gβ^{P-} *bud1*Δ cells but not Gβ^{P-} *BUD1* cells shmoo aberrantly in isotropic pheromone implicates Gβ phosphorylation in chemotropism. To test this, we set up dilute bilateral mating mixtures in which the cells best able to form stable, chemotropic mating projections were most likely to find and fuse with a partner, and analyzed images of newly formed zygotes (Fig. 5A). How precisely a cell orients towards a potential mating partner can be inferred by measuring the angle created when two cells fuse. When orientation is optimal, the two cells of a mating pair grow directly toward one another, and consequently, their angle of fusion is ~ 0˚. In contrast, large fusion angles are indicative of poor orientation. In the zygote

formation assay Gβ^{P-} cells exhibited a clear orientation defect, forming significantly greater fusion angles (Fig. 5C).

In addition to their well studied ability to orient growth toward a pheromone source, budding yeast are also adept at changing the direction of their growth in response to a vectorial change in the gradient (Segall, 1993; Moore et al., 2008). Cells respond to a change in the direction of a pheromone gradient in one of two ways: They either initiate a second projection oriented toward the new source, or, the existing projection bends in the direction of the new source (Moore et al., 2008). These phenomena are collectively referred to as *reorientation*. Although there are, as yet, no published insights into how cells reorient, the mechanisms underlying this process are likely to overlap and/or interact with those involved in initial orientation and maintenance. As our data suggest a role for Gβ phosphorylation in initial orientation and stable chemotropic growth, we asked whether it is involved in reorientation as well. WT and Gβ^{P-} bilateral mating mixtures were shaken vigorously to induce non-directional (default) shmooing while preventing cell fusion, then allowed to produce and respond to pheromone gradients on solid medium. As shown in Fig. 5B,C, Gβ^{P-} conferred a clear reorientation defect. Whereas pre-stimulated WT cells often bent dramatically to contact a mating partner, Gβ^{P-} cells formed zygotes that were predominantly the result of “collision matings” — i.e., two shmoos appeared to have simply grown into one another without having significantly changed their direction of growth.

One explanation for the results of the orientation and reorientation assays is that Gβ^{P-} confers a defect in directional sensing and/or chemotropic shmooing. However, it is also possible that Gβ^{P-} cells signal their positions less effectively than WT cells because their pheromone secretion is less focused. To distinguish these possibilities, we compared the ability of Gβ and Gβ^{P-} cells to grow toward a source of pheromone in vitro, using a microfluidic device (Brett et al., 2012). As previously reported, the Gβ control cells formed normal mating projections in the artificial gradient (Fig. 6A) and oriented toward its source with an accuracy similar to that observed in other published microfluidic experiments (Brett et al., 2012). Surprisingly, the Gβ^{P-} cells were unable to sustain growth in a single direction.

Rather, they formed multiple small protrusions, often without growing much in overall size — very much like the SMP cells found in Gβ^{P-} *bud1*Δ cultures treated with isotropic pheromone (Fig. 1B). Moreover, the first protrusions formed by the gradient-stimulated Gβ^{P-} cells were positioned randomly, virtually without detectable orientation toward the pheromone. These data strongly support the idea that Gβ phosphorylation plays a role in the positioning and maintenance of the chemotropic growth site. Under isotropic conditions, Gβ^{P-} cells form normal mating projections at the presumptive default site, apparently unaffected by their inability to phosphorylate Gβ. When subjected to directional stimulation, however, the mutant cells appear to "realize" they are in a gradient, repeatedly trying and failing to stably grow towards the source. Remarkably, Gβ^{P-} cells exposed to an artificial pheromone gradient were unable to stabilize their growth at the default shmoo site.

The inability of Gβ^{P-} cells to maintain a single axis of polarity in an artificial gradient combined with their ability to form normal mating projections in isotropic pheromone provides the first example, to our knowledge, of a gradient-specific shmoo phenotype. We therefore wished to confirm this observation using natural gradients. To look for gradient-dependent destabilization of polarized growth under physiological conditions, we compared WT and Gβ^{P-} shmoos formed in liquid culture (isotropic treatment) with those formed in bilateral crosses. Although the Gβ^{P-} cells in mating mixtures were not as severely compromised in chemotropic shmooing as the Gβ^{P-} cells in the microfluidic device, they exhibited a number of obvious shmoo defects (Fig. 6B,C). In fact, the response of Gβ^{P-} *BUD1* cells exposed to natural pheromone gradients was essentially the same as that of Gβ^{P-} *bud1*Δ cells exposed to isotropic pheromone: Gβ^{P-} mating mixtures accumulated fewer shmoos, shorter shmoos (their mean length was 0.852 of the control cells after 5 hours of mating; $n \geq 105$; $p < 0.0001$), and a significantly higher proportion of aberrant shmoos (compare Fig. 6C to Fig. 1C). In contrast, the Gβ^{P-} and WT shmoos induced by isotropic treatment were indistinguishable at all concentrations and time points (Fig. 1B). These data suggest that the phosphorylation of Gβ plays a critical role in chemotropic, but not default, shmooing.

DISCUSSION

The rapid phosphorylation of Gβ in yeast cells responding to mating pheromone was observed over 20 years ago (Cole and Reed, 1991), and yet, its function has remained enigmatic. Two early studies failed to elucidate its role (Cole and Reed, 1991; Li et al., 1998a). We were impelled to revisit this issue by the discovery that the activated forms of Gα and Fus3 interact, and that a double mutation that uncouples them, $G\alpha^{DSD}$, conferred defects in mating and partner discrimination (Metodiev et al., 2002). Indeed, we show here that $G\alpha^{DSD}$ *bud1*Δ cells cannot form mating projections, which identifies $G\alpha^{DSD}$ as a chemotropic-defective allele (Fig.1A), in the same class as *cdc24-m1* and *far1-H7* (Nern and Arkowitz, 2000). This suggests that the Gα-Fus3 interaction, like the Cdc24-Far1 interaction, is critical for chemotropism. Because $G\alpha^{DSD}$ also results in reduced Gβ phosphorylation and protein levels in stimulated cells, we hypothesized that Gβ phosphorylation plays a role in chemotropism. Our results demonstrate that this is the case.

Aberrant shmoo morphology and proximal projections: wandering limited by high receptor and Gβγ density

When combined with mutations that inactivate the default shmoo pathway (e.g. *bud1*Δ), mutations that inactivate the chemotropic shmoo pathway result in the inability to form mating projections (Dorer et al., 1995; Nern and Arkowitz, 1999). We therefore examined the morphological response of $G\beta^{P-}$ *bud1*Δ cells in isotropic pheromone conditions. Although not completely defective for mating projection formation, $G\beta^{P-}$ *bud1*Δ cells exhibited a variety of shmoo morphologies (Fig. 1B,C), including short and blunt shmoos, cells that formed multiple projections proximal to the first, and very small cells with multiple protrusions (SMP cells). Time-lapse imaging of Spa2-GFP in these cells indicated that the axis of polarity wandered, albeit in a confined area (Fig. 2A). This broader region of Spa2 movement correlated with the generation of proximal projections that, as noted above, were formed in the region in which receptor density is expected to be highest. It is therefore of significance that preventing receptor polarization in $G\beta^{P-}$ *bud1*Δ cells dramatically suppressed the proximal-projection phenotype, and that expression of Bem1-GFP-Snc2, which slows polarity site wandering by a mechanism independent

of the receptor and G protein, restored their ability to shmoo normally (Fig. 2B,C). Together, these observations suggest that although the axis of polarity is destabilized in pheromone-treated Gβ^{P-} *bud1*Δ cells, its wandering is limited by the high concentration of receptor and G$\beta\gamma$ (Suchkov et al., 2010) in the nascent mating projection. This confined wandering likely underlies the formation of short, blunt shmoos, and in combination with the apparent defect in regulating growth-site switching (Fig. 1D; Table 2), may result in the emergence of multiple projections proximal to the first. The occurrence of ≥ 2 Spa2-GFP spots in Gβ^{P-} *bud1*Δ shmoos also correlates with the eventual formation of proximal projections (Table 1).

The role of Gβ phosphorylation in receptor communication to actin cables

What causes confined wandering? In essence, chemotropism is the translation of an extracellular pheromone gradient into a gradient of activated receptors across the cell surface, and the communication of this spatial information to the actin cytoskeleton. The receptor does not communicate with actin directly, but rather via its G$\beta\gamma$, which recruits Far1-Cdc24. Along with the polarisome, Cdc42, and Bem1, the G$\beta\gamma$-Far1-Cdc24 chemotropic complex ultimately nucleates actin cables at the incipient mating projection site. In *cdc24-m1* and *far1-H7* cells, the link between the receptor and chemotropic complex is completely severed. Polarization sites are established in such cells (Nern and Arkowitz, 2000), but according to a recently proposed model (D. Lew, personal communication), they lack the constraint provided by interaction with receptor-activated G$\beta\gamma$. Hence, their position is not sufficiently stable to sustain polarized growth in one direction. Gβ^{P-} *bud1*Δ cells exhibit a similar, although less severe, phenotype. Instead of global wandering and uniform growth, wandering is confined to the area of most concentrated receptor. This implies that the link between the receptor and chemotropic complex is weakened, but not broken.

We explored the effect of Gβ phosphorylation on the stability of the chemotropic complex and polarisome. Surprisingly, the results of a genetic assay suggested that phosphorylation of Gβ reduces its affinity for Far1 (Fig. 4A). This conclusion was supported by the results of the Spa2-GFP FRAP and GFP-Cdc42 iFRAP analyses (Fig. 4B,C). Both Spa2 and Cdc42 exhibited a substantially

decreased mobility in $G\beta^{P-}$ cells as compared to $G\beta$ cells, consistent with longer-lived associations at the shmoo tips. This suggests that the phosphorylation of $G\beta$ decreases its affinity for the chemotropic complex and destabilizes the association of Spa2 with the polarisome. We can explain the confined wandering observed in $G\beta^{P-}$ *bud1*Δ cells as follows.

Immediately after exposure to pheromone, the activated receptor and G protein are distributed almost uniformly on the plasma membrane, as are the first chemotropic and polarisome complexes to be assembled. As the receptor polarizes, however, so do $G\alpha$ and $G\beta\gamma$, leading to the eventual concentration of the signaling proteins at the incipient shmoo site. The high density of free $G\beta\gamma$ in this area biases the recruitment of Far1-Cdc24, and thus the localized formation of the chemotropic complex. Moreover, as chemotropic complexes dissociate, they are much more likely to reassemble where free $G\beta\gamma$ is concentrated. The half-life of the chemotropic complex is critical. If it is too short, the cell will not be able to initiate polarized growth. If it is too long, the complex will wander out of the region of high-density receptor and G protein before the axis of polarity is established. In WT cells, phosphorylation of $G\beta$ decreases the half-life of the complex, thereby limiting the distance it can move before dissociating. This increases the chance that the complex components will reassemble within the active growth area, where receptor and G protein concentration are highest. In $G\beta^{P-}$ cells, on the other hand, the half-life of the complex is longer — long enough to allow movement across the entire region of high-density receptor and G protein. Additionally, the zone of $G\beta$ appears to be less well consolidated in $G\beta^{P-}$ cells (Table 2; Fig. 3). A key aspect in this scenario is the recycling of the G protein — i.e., the re-association of the heterotrimer with the receptor. $G\beta\gamma$ cannot report the position of active receptor until it releases from the chemotropic complex and binds inactive $G\alpha$. Conversely, the chemotropic complexes can move away from the growth site, blind to local $G\beta\gamma$ density, as long as they remain intact. Interestingly, mutations that disrupt the interaction of $G\beta$ with the N-terminal interface of $G\alpha$ (Strickfaden and Pryciak, 2008), and mutations that slow or prevent inactivation of $G\alpha$, *sst2*Δ and $G\alpha^{Q323L}$ (D. Lew, personal communication; Strickfaden and Pryciak, 2008), also implicate G protein cycling in

chemotropic shmooing. We infer that by increasing the rate at which the position of the activated receptor is reported, the Gα-GDP/GTP and the Gβ-phosphorylation/dephosphorylation cycles strengthen the indirect link between the receptor and the chemotropic complex, and consequently, influence the position of the polarity proteins. Posttranslational modification of Gβ may therefore extend the well-established paradigm that cycling is central to the function of G proteins.

Polarization of Gβ

The results shown in Table 2 and Fig. 3 suggest that Gβ phosphorylation is critical for pheromone-induced Gβ polarization. Although the GFP-$G\beta^{P-}$ polarization defect could result simply from the drifting axis of polarity discussed above, a number of observations raise a more interesting possibility: Gβ phosphorylation could play a key role in the genesis of pheromone-induced intracellular signaling gradients. Given that full pheromone-induced phosphorylation of Gβ depends on Fus3 and on Gα-Fus3 interaction (Metodiev et al., 2002), and that gradients of active Fus3 emanate from the tips of shmooing cells (Maeder et al., 2007), we propose that Gα recruits Fus3 to phosphorylate Gβ at the incipient shmoo site. As it is also known that pheromone-induced polarization of Gα and Gβ requires their co-internalization with the receptor (Suchkov et al., 2010), it will be interesting to determine whether unphosphorylated Gβ is preferentially internalized along with Gα and the receptor while phosphorylated Gβ is left on the membrane. A synergistic combination of these two mechanisms — localized Gβ phosphorylation at the shmoo site and preferential internalization of unphosphorylated Gβ at the back of the cell — would be expected to rapidly generate a steep gradient of phosphorylated Gβ via what is essentially a LEGI-type mechanism. An intracellular gradient of phosphorylated Gβ underlying yeast chemotropism would provide an interesting analogy to the intracellular gradient of the phosphorylated lipid, PIP_3, found in numerous chemotactic systems (Jin et al., 2000; Servant et al., 2000; Comer and Parent, 2002).

The role of Gβ phosphorylation in chemotropism

If Gβ phosphorylation contributes to chemotropic growth, and not just to the growth of stable mating projections, we would expect $G\beta^{P-}$ to compromise oriented growth towards a pheromone source. To test this, we examined how the inability to

phosphorylate Gβ affects chemotropism in both natural and artificial pheromone gradients. These experiments were performed with *BUD1* strains, as we wished to determine how well the chemotropic shmoo pathway would override the default shmoo pathway to orient and sustain growth up a gradient. In mating mixtures, $G\beta^{P-}$ conferred significant defects in initial orientation (Fig. 5A) and polarized growth (Fig. 6B). Similar but more pronounced defects were observed in artificial pheromone gradients (Fig. 6A). Remarkably, the polarized growth defects were gradient-specific. $G\beta^{P-}$ cells formed mating projections when treated with isotropic pheromone, but could not maintain polarized growth in either artificial or natural gradients. It is noteworthy that the types and proportions of aberrant shmoos formed by $G\beta^{P-}$ *BUD1* cells in mating mixtures were very similar to those formed by $G\beta^{P-}$ *bud1*Δ cells in isotropic pheromone (compare Fig. 6B,C and 1B-C). In both cases, the cells were forced to use the chemotropic pathway without being able to phosphorylate Gβ. The resulting defects reveal that the cells attempt to shmoo chemotropically, but cannot maintain a stable axis of polarity. These data strongly suggest that Gβ phosphorylation is critical for the initial positioning and maintenance of the chemotropic growth site.

In addition to mechanisms that establish and stabilize directional growth, chemotroping cells must have a means to alter their direction and track dynamic gradients in mating mixtures. To successfully fuse with the shmoo tip of a partner, a yeast cell must not only determine the direction of the strongest source of pheromone and orient its growth accordingly, it must continually reassess the position of the target cell while ignoring weaker signals. The shape of the gradient and concentration of pheromone most likely change as the two cells grow towards each other, and as zygotes form in the mating mixture. Although the mechanisms underlying reorientation are unknown, it is easy to appreciate that the establishment of a chemotropic growth site and ongoing adjustments to its position pose distinct challenges. To date, only one mutation that specifically affects reorientation has been reported, $ste2^{T236}$ (Vallier et al., 2002). It is therefore of considerable interest that $G\beta^{P-}$ confers a dramatic defect in reorientation. This suggests that Gβ phosphorylation plays a critical role in gradient tracking.

In summary, we propose that the phosphorylation of Gβ contributes to chemotropism in two ways: (1) Gβ modification is used to rapidly generate a signaling gradient in which phosphorylated Gβ is concentrated at the incipient shmoo site. This may facilitate the amplification of other intracellular signaling gradients; (2) Phosphorylation of Gβ decreases its affinity for Far1 and perhaps other chemotropic components, thereby shortening the cycle time between the receptor and polarisome. More frequent updating of receptor status increases sensitivity to changes in the pheromone gradient.

MATERIALS AND METHODS

Molecular and microbiological techniques

Standard methods were used for microbial and molecular manipulation (Sherman, 1986; Ausubel et al., 1994; Guthrie and Fink, 2002). All strains used in this study were derived from strain 15Dau (*MAT***a** *bar1*D *ade1 his2 leu2-3*, *-112 trp1 ura3*D), which is congenic with strain BF264-15D (Reed et al. 1985), and are listed in Table S1. RDY114 was generated by in situ transplacement of *ste4*Δ::*URA3* in strain ELY104 (Li et al., 1998b) with *ste4*$^{T320A\ S335A}$, excised as an *Eco*RI-*Sph*I fragment from the plasmid YCplac33/ *ste4*$^{T320A\ S335A}$ (Li et al., 1998a). Recombinants were selected on 5´FOA and confirmed by sequencing. The *BUD1/RSR1* locus was deleted in strains 15Dau *bar1*Δ and RDY114 to create strains RDY103 and RDY120, respectively, using a *bud1*Δ*::KANMX4* cassette which was PCR-amplified from pFA6a-Kan (Wach, 1996) using the oligomers 5´- GCGCATTCATCCTCGACATTCTCAAACGCGAAATATCGTCGAACGTACGCTG CAGGTCGACGG - 3´ and 5´- GTTGTGAAGTAGCGCTAATTCCTGTCCTGTTGCTAGAACCAGATATCGATGA ATTCGAGCTCG - 3´. GFP-tagging was performed in situ by transplacement of an excised *Eco*RI-*Sma*I fragment from pRS316/*STE4*p-*GFP-STE4* (Kim et al., 2000) or pRS316/*STE4*p-*GFP-ste4*$^{T320A\ S335A}$ (RDB122, see construction below) into strain ELY104 to create strains RDY126 and RDY139, respectively. The *BUD1/RSR1* locus was deleted as described above in strains RDY126 and RDY139 to create strains RDY130 and RDY132, respectively. RDY114 was transformed with pGAL-HO and the mating type was switched to generate RDY217 as described (Guthrie and Fink, 2002). Strains EAY106 and EAY107 were created by transforming pRS304/STE2$^{7XR/GPAAD}$ cut with BsmI into strains RDY103 and RDY120, respectively, and confirmed by sequencing.

Plasmid construction. The plasmids used in this study are listed in Table S2. RDB122 was created by sequential site-directed mutagenesis of pRS316/*STE4*p-*GFP-STE4* (Kim et al., 2000), and YCplac111/GAL1- STE4$^{T320A\ S335A}$ was created by sequential site-directed mutagenesis of YCplac111/GAL1- STE4, using QuikChange II XL kit (Qiagen, Valencia, CA, USA). The oligomers used to create the T320A mutation were 5´-

CGAGGTTATGAAGAACGTACCCCTGCCCCTACTTATATGGCAGC - 3´and 5´- GCTGCCATATAAGTAGGGGCAGGGGTACGTTCTTCATAACCTCG - 3´. The oligomers used to create the sequential S335A mutation were 5´ - GGAGTACAATACCGCGCAAGCGCCACAAACTTTAAAATCAAC -3´ and 5´ - GTTGATTTTAAAGTTTGTGGCGCTTGCGCGGTATTGTACTCC - 3´. To create pEB15.1 (pESC/GAL10-FLAG-FAR1), *FAR1* was PCR-amplified from strain15Dau genomic DNA and the product was cloned into pESC-URA as a PacI-BglII fragment, thereby placing *FAR1* under *GAL10* promoter control. The priming oligonucleotides were: 5´ - CCTTAATTAAGCGTAGTATAGACGTGGAG - 3´ and 5´ - GAAGATCTTGAAGACACCAACAAGAGTTTCG - 3´.

Spa2-GFP localization in isotropic pheromone. RDY246 and RDY247 (*MAT***a** *bud1*Δ Gβ or $G\beta^{P-}$ cells expressing *SPA2-GFP*) were incubated together at 30°C on SD complete agar pads containing 150 nM α-factor. The strains were distinguished by labeling one or the other with ConA-Alexa Fluor 594 (Molecular Probes, Eugene, Oregon, USA) in alternate experiments. Cells were first imaged 15 min after exposure to pheromone and at 15 min intervals thereafter. Six fields were imaged at each time point with 6 Differential Interference Contrast (DIC) and 6 GFP z-stacks collected in 0.5 µm slices using a DeltaVision deconvolution microscopy system (Applied Precision, Issaquah, WA, USA) on an Olympus IX-70 microscope with an NA 1.4 X 60 objective. The images were then deconvolved using Huygens Deconvolution Software V. 3.7 (Scientific Volume Imaging, Hilversum, The Netherlands), sum projected (GFP) or average projected (DIC), and converted into 8-bit TIF files using ImageJ software. The scale bar equals 5 µm in all images.

Spa2-GFP time-lapse microscopy in mating mixtures. Wild type BF264-15D *MAT*α cells were stained with 10 µg/ml ConA-Alexa Fluor 594 (Molecular Probes, Grand Island, NY, USA) for 1 hr and then washed 3X with water prior to mixing with strains RDY246 and RDY247 (*MAT***a** *bud1*Δ Gβ or $G\beta^{P-}$ cells expressing *SPA2-GFP*). Mating mixtures were incubated at 30˚C on SD complete agar pads. Images were acquired 25 min after mixing and at 15 min intervals thereafter. Six fields were imaged at each time point. Image acquisition and analysis was identical to that described above for isotropic pheromone conditions. Tracking analysis was

performed using the ImageJ Manual Tracking plugin (developed by Fabrice Cordelières, Institut Curie, Orsay FR).

GFP-Gβ time-lapse microscopy in isotropic pheromone conditions. Strains RDY130 (*MAT***a** *bud1*Δ GFP-Gβ) and RDY132 (*MAT***a** *bud1*Δ GFP-Gβ^{P-}) were incubated together at 30°C on SD complete agar pads containing 150 nM α-factor. The strains were distinguished by labeling one or the other with ConA-Alexa Fluor 594 in alternate experiments. Cells were first imaged 15 min after exposure to pheromone and at 10 min intervals thereafter. Six fields were imaged at each time point with 15 DIC and 15 GFP z-stacks in 0.3 μm sections using an ANDOR Revolution XD spinning disk laser confocal microscopy system with a fully motorized Olympus IX-81 inverted microscope, a Yokogawa CSU-X1 confocal spinning disk unit, motorized XYZ control (piezo) and two iXon897 EMCCD cameras all controlled by Andor iQ2 software. A UplanSApo NA 1.4 X 100 objective was used with 488-nm laser excitation. Voxel size was 133 nm x 133 nm x 280 nm. An Okolab chamber was used to maintain cells at 30ºC. The images were then sum projected and converted into 8-bit TIF files using ImageJ and false colored. Data analysis was carried out using the program, BudPolarity, which is a semi-automated Matlab program that quantifies the intensity profile along the major axis of yeast cells, and is described elsewhere (Vernay et al., submitted). In Table 2, cells were scored as exhibiting polarized Gβ if they met all of the following criteria: peak signal intensity ≥ 2X the baseline value over less than one half the cell surface for at least 3 consecutive time points. Cells were scored as exhibiting polarized growth when they were judged to be elongating predominantly along one axis at the center of the DIC z-stack (slices 6-8). The ImageJ ellipse tool was used to help make this determination.

GFP-Gβ time-lapse microscopy in mating mixtures. Wild type BF264-15D *MAT*α cells were mixed 1:1 with strains RDY130 (*MAT***a** *bud1*Δ GFP-Gβ) or RDY132 (*MAT***a** *bud1*Δ GFP-Gβ^{P-}). Mating mixtures were incubated at 30°C on SD complete agar pads and images were acquired 15min after mixing and at 15min intervals thereafter. Image acquisition and analysis was identical to that described above for isotropic pheromone conditions. In Table 2, cells were scored as exhibiting polarized Gβ if they met all of the following criteria: peak signal intensity ≥ 1.5X the baseline

value over less than one half the cell surface for at least 3 consecutive time points. Cells were scored as exhibiting polarized growth as described above. For cells that did not maintain a single axis of polarity for the duration of the experiment, the first time point at which non-uniform growth could be measured was taken to reflect the initiation of polarized growth.

Gβ overexpression genetic assay. 15Dau *bar1*Δ cultures co-transformed with pESC/GAL1-FAR1 and either YCplac111/GAL1-STE4 or YCplac111/GAL1-STE4$^{T320A\ S335A}$ were grown to mid-log phase (~10^7 cells/ml) in selective sucrose medium. 10-fold serial dilutions from 10^5 to 1 were then spotted on selective galactose and selective glucose media and incubated at 30˚C for 48 hr. Ten transformants of each strain were tested.

FRAP analysis of Spa2-GFP. *MAT***a** *bud1*Δ Gβ or Gβ^{P-} cells expressing *SPA2-GFP* (RDY246 and RDY247) were grown to mid-log phase at 30°C in YEPD containing 550 mg/L adenine and then exposed to 30 nM α-factor at 30°C for 1 hr. FRAP analysis was carried out on a Zeiss LSM 510 META confocal Axiovert 200M microscope (Carl Zeiss, Thornwood, NY, USA) using an NA 1.4 X 63 Plan-Apo objective and 488-nm LASER excitation. Images were captured every 1s at 2–5% maximum laser intensity and 10 x 0.5 ms photo-bleaching scans at 100% laser intensity were performed on a circular area of 1 μm^2 at the shmoo tip. Data analysis was carried out essentially as described (Bassilana and Arkowitz, 2006).

iFRAP analysis of GFP-Cdc42. *MAT***a** *bud1*Δ Gβ or Gβ^{P-} cells expressing *GFP-CDC42* (RDY259 and RDY260) were grown to mid-log phase at 30°C in YEPD containing 550 mg/L adenine and exposed to 30 nM α-factor at 30°C for 1 hr. iFRAP analysis was carried out on a Zeiss LSM 510 META confocal on an Axiovert 200M microscope using an NA 1.4 X 63 Plan-Apo objective and 488-nm LASER excitation. Images were captured every 1s at 2–5% maximum laser intensity and 10 x 0.5 ms photo-bleaching scans at 100% laser intensity were performed on the cell with the exception of the area in which GFP-Cdc42 was polarized at the shmoo tip. The average intensity of the bleached or unbleached area was normalized for photo-bleaching during image acquisition, using the average intensity of the cell with MatLab. Loss of fluorescence intensity was then fitted to an exponential curve.

Mating projection assays. To study mating projection formation and maintenance under isotropic pheromone conditions, cells were grown to mid-log phase at 30°C in YEPD media, and exposed to α-factor at the concentrations and times indicated. DIC images for experiments carried out in liquid cultures were acquired using a Zeiss Axioskop 2 microscope fitted with an NA 1.4 X 63 Plan-Apo oil immersion objective and a Zeiss AxioCam digital camera, and processed with Zeiss AxioVision software. To study mating projection formation and maintenance in physiological pheromone gradients, cultures were grown to mid-log phase at 30°C in YEPD. Dilute bilateral Gβ and $G\beta^{P-}$ mating mixtures containing ~10^7 *MAT*α cells and ~10^7 *MAT***a** cells were then spread on YEPD agar and incubated at 30˚C. Time points were taken at 1 hr intervals for 5 hr, fixed with 3.7% formaldehyde, and 630X DIC images of shmoos were acquired using the Zeiss Axioskop 2 microscope and Zeiss camera described above. Mating projection lengths were measured using ImageJ. Percentages in each shmoo class were scored on a haemocytometer using a Leitz Laborlutz S phase-contrast microscope fitted with an NA 0.65 X 40 Plan objective.

Orientation assays. To measure the ability of cells to orient their growth in physiological pheromone gradients, cultures were grown to mid-log phase at 30°C in YEPD. Dilute bilateral Gβ and $G\beta^{P-}$ mating mixtures containing ~$5x10^6$ *MAT*α cells and ~$5x10^6$ *MAT***a** cells were then incubated at 30°C for 3 hr on filters (0.45 µm Millipore) placed on YEPD agar. Matings were between either wild type *MAT*α (DSY246) and wild type *MAT***a** (DSY257) cells or *MAT*α $G\beta^{P-}$ (RDY217) and *MAT***a** $G\beta^{P-}$ (RDY114) cells. Filters were washed in 1 ml sterile H_2O to harvest cells. 630X DIC images of zygotes were acquired using the Zeiss Axioskop 2 microscope and Zeiss camera described above. Zygote angles were measured using ImageJ. The response of cells to artificial pheromone gradients was assayed using a microfluidic device, as described (Brett et al., 2012).

Reorientation assay. Cells were grown to mid-log phase at 30°C in YEPD. Liquid cultures containing ~10^7 *MAT*α cells and ~10^7 *MAT***a** cells were shaken at 250 rpm at 30°C for 3 hr to induce shmooing prior to mating. Cultures of either wild type *MAT*α (DSY246) and wild type *MAT***a** (DSY257) cells or *MAT*α $G\beta^{P-}$ (RDY217) and *MAT***a** $G\beta^{P-}$ (RDY114) cells were then spread onto YEPD agar and incubated at 30°C for 3

hr. Images of zygotes were collected using an Olympus BH-2 inverted microscope fitted with a CDPlan 40 objective and an Olympus digital camera (magnification = 400X). Zygote angles were measured using ImageJ.

Statistics. The *p* values for the comparisons of length, angle, and time measurements were determined using unpaired, two-tailed t-tests (Graphpad). The *p* values for the comparisons of percentages were determined using the chi-square test (Graphpad).

ACKNOWLEDGMENTS

The authors would like to thank Jayme Johnson and Daniel Lew for yeast strains and plasmids, for helpful discussions, and for communicating results prior to publication, Jill Eskara for technical assistance, and the PRISM microscopy facility at Institute of Valrose Biology CNRS UMR7277 / INSERM U1091 University of Nice. This work was supported by National Science Foundation grants #MCB-0453964 and #MCB1024718 (DES). RD was supported in part by EMBO (ASTF 196.00-2009) and Eiffel (690570F) fellowships and work in RA's lab was supported by the CNRS, FRM-BNP-Paribas, an ANR-09-BLAN-0299-01, and an ARC 4979 grant.

REFERENCES

Arkowitz, R. A. (2009). Chemical gradients and chemotropism in yeast. *Cold Spring Harb Perspect Biol* **1**, a001958.

Arkowitz, R. A. and Lowe, N. (1997). A small conserved domain in the yeast Spa2p is necessary and sufficient for its polarized localization. *J Cell Biol* **138**, 17-36.

Ausubel, F. M., Brent, R., Kingston, R. E., Moore, D. D., Seidman, J. G., Smith, J. A. and Struhl, K. (1994). Current Protocols in Molecular Biology: John Wiley and Sons, Inc.

Ballon, D. R., Flanary, P. L., Gladue, D. P., Konopka, J. B., Dohlman, H. G. and Thorner, J. (2006). DEP-domain-mediated regulation of GPCR signaling responses. *Cell* **126**, 1079-93.

Bar, E. E., Ellicott, A. T. and Stone, D. E. (2003). Gbetagamma recruits Rho1 to the site of polarized growth during mating in budding yeast. *J Biol Chem* **278**, 21798-804.

Barale, S., McCusker, D. and Arkowitz, R. A. (2006). Cdc42p GDP/GTP cycling is necessary for efficient cell fusion during yeast mating. *Mol Biol Cell* **17**, 2824-38.

Bardwell, L. (2005). A walk-through of the yeast mating pheromone response pathway. *Peptides* **26**, 339-50.

Basile, J. R., Barac, A., Zhu, T., Guan, K. L. and Gutkind, J. S. (2004). Class IV semaphorins promote angiogenesis by stimulating Rho-initiated pathways through plexin-B. *Cancer Res* **64**, 5212-24.

Bassilana, M. and Arkowitz, R. A. (2006). Rac1 and Cdc42 have different roles in Candida albicans development. *Eukaryot Cell* **5**, 321-9.

Bidlingmaier, S. and Snyder, M. (2004). Regulation of polarized growth initiation and termination cycles by the polarisome and Cdc42 regulators. *J Cell Biol* **164**, 207-18.

Brett, M.-E., DeFlorio, R., Stone, D. E. and Eddington, D. (2012). A microfluidic device that forms and redirects pheromone gradients to study chemotropism in yeast. *Lab Chip* **12,** 3127-3134.

Butty, A. C., Pryciak, P. M., Huang, L. S., Herskowitz, I. and Peter, M. (1998). The role of Far1p in linking the heterotrimeric G protein to polarity establishment proteins during yeast mating. *Science* **282**, 1511-1516.

Chakrabarti, S. and Gintzler, A. R. (2003). Phosphorylation of Gbeta is augmented by chronic morphine and enhances Gbetagamma stimulation of adenylyl cyclase activity. *Brain Res Mol Brain Res* **119**, 144-51.

Chen, L., Iijima, M., Tang, M., Landree, M. A., Huang, Y. E., Xiong, Y., Iglesias, P. A. and Devreotes, P. N. (2007). PLA2 and PI3K/PTEN pathways act in parallel to mediate chemotaxis. *Dev Cell* **12**, 603-14.

Cismowski, M. J., Metodiev, M. V., Draper, E. M. and Stone, D. E. (2001). Biochemical analysis of yeast Gα mutants that enhance adaptation to pheromone. *Biochem. Biophys. Res. Comm.* **284**, 247-254.

Cole, G. M. and Reed, S. I. (1991). Pheromone-induced phosphorylation of a G protein ß subunit in S. cerevisiae is associated with an adaptive response to mating pheromone. *Cell* **64**, 703-716.

Cole, G. M., Stone, D. E. and Reed, S. I. (1990). Stoichiometry of G protein subunits affects the Saccharomyces cerevisiae mating pheromone signal transduction pathway. *Mol. Cell. Biol.* **10**, 510-517.

Comer, F. I. and Parent, C. A. (2002). PI 3-kinases and PTEN: how opposites chemoattract. *Cell* **109**, 541-4.

Daniels, K. J., Srikantha, T., Lockhart, S. R., Pujol, C. and Soll, D. R. (2006). Opaque cells signal white cells to form biofilms in Candida albicans. *Embo J* **25**, 2240-52.

Devreotes, P. and Janetopoulos, C. (2003). Eukaryotic chemotaxis: distinctions between directional sensing and polarization. *J Biol Chem* **278**, 20445-8.

Dohlman, H. G. and Thorner, J. W. (2001). Regulation of G protein-initiated signal transduction in yeast: paradigms and principles. *Annu. Rev. Biochem.* **70**, 703-754.

Dorer, R., Pryciak, P. M. and Hartwell, L. H. (1995). Saccharomyces cerevisiae cells execute a default pathway to select a mate in the absence of pheromone gradients. *J. Cell Biol.* **131**, 854-861.

Draper, E., Dubrovskyi, O., Bar, E. E. and Stone, D. E. (2009). Dse1 may control cross talk between the pheromone and filamentation pathways in yeast. *Curr Genet* **55**, 611-621.

English, D., Garcia, J. G. and Brindley, D. N. (2001). Platelet-released phospholipids link haemostasis and angiogenesis. *Cardiovasc Res* **49**, 588-99.

Evangelista, M., Pruyne, D., Amberg, D. C., Boone, C. and Bretscher, A. (2002). Formins direct Arp2/3-independent actin filament assembly to polarize cell growth in yeast. *Nat Cell Biol* **4**, 260-9.

Feng, Y., Song, L. Y., Kincaid, E., Mahanty, S. K. and Elion, E. A. (1998). Functional binding between Gbeta and the LIM domain of Ste5 is required to activate the MEKK Ste11. *Curr Biol* **8**, 267-78.

Guthrie, C. and Fink, G. R. (2002). Guide to Yeast Genetics and Molecular Biology. San Diego, CA.: Academic Press.

Hoeller, O. and Kay, R. R. (2007). Chemotaxis in the absence of PIP3 gradients. *Curr Biol* **17**, 813-7.

Hong, K. and Nishiyama, M. (2010). From guidance signals to movement: signaling molecules governing growth cone turning. *Neuroscientist* **16**, 65-78.

Howell, A. S., Savage, N. S., Johnson, S. A., Bose, I., Wagner, A. W., Zyla, T. R., Nijhout, H. F., Reed, M. C., Goryachev, A. B. and Lew, D. J. (2009). Singularity in polarization: rewiring yeast cells to make two buds. *Cell* **139**, 731-43.

Iijima, M., Huang, Y. E. and Devreotes, P. (2002). Temporal and spatial regulation of chemotaxis. *Dev Cell* **3**, 469-78.

Jackson, C. L. and Hartwell, L. H. (1990). Courtship in S. cerevisiae: both cell types choose mating partners by responding to the strongest pheromone signal. *Cell* **63**, 1039-51.

Jin, T., Zhang, N., Long, Y., Parent, C. A. and Devreotes, P. N. (2000). Localization of the G protein betagamma complex in living cells during chemotaxis. *Science* **287**, 1034-6.

Kamimura, Y., Xiong, Y., Iglesias, P. A., Hoeller, O., Bolourani, P. and Devreotes, P. N. (2008). PIP3-independent activation of TorC2 and PKB at the cell's leading edge mediates chemotaxis. *Curr Biol* **18**, 1034-43.

Kang, P. J., Beven, L., Hariharan, S. and Park, H. O. (2010). The Rsr1/Bud1 GTPase interacts with itself and the Cdc42 GTPase during bud-site selection and polarity establishment in budding yeast. *Mol Biol Cell* **21**, 3007-16.

Kim, J., Bortz, E., Zhong, H., Leeuw, T., Leberer, E., Vershon, A. K. and Hirsch, J. P. (2000). Localization and signaling of Gβ subunit Ste4p are controlled by a-Factor receptor and the a-specific protein Asg7p. *Mol. Cell. Biol.* **20**, 8826-8835.

Kim, S., Dong, J. and Lord, E. M. (2004). Pollen tube guidance: the role of adhesion and chemotropic molecules. *Curr Top Dev Biol* **61**, 61-79.

Li, E., Cismowski, M. J. and Stone, D. E. (1998a). Phosphorylation of the pheromone-responsive Gbeta protein of Saccharomyces cerevisiae does not affect its mating-specific signaling function. *Mol Gen Genet* **258**, 608-18.

Li, E., Meldrum, E., Stratton, H. and Stone, D. E. (1998b). Substitutions in the pheromone responsive Gβ protein of Saccharomyces cerevisiae confer a defect in recovery from pheromone treatment. *Genetics* **148**, 947-961.

Maeder, C. I., Hink, M. A., Kinkhabwala, A., Mayr, R., Bastiaens, P. I. and Knop, M. (2007). Spatial regulation of Fus3 MAP kinase activity through a reaction-diffusion mechanism in yeast pheromone signalling. *Nat Cell Biol* **9**, 1319-26.

Matheos, D., Metodiev, M., Muller, E., Stone, D. and Rose, M. D. (2004). Pheromone-induced polarization is dependent on the Fus3p MAPK acting through the formin Bni1p. *J Cell Biol* **165**, 99-109.

Mato, J. M., Losada, A., Nanjundiah, V. and Konijn, T. M. (1975). Signal input for a chemotactic response in the cellular slime mold Dictyostelium discoideum. *Proc Natl Acad Sci U S A* **72**, 4991-3.

Metodiev, M. V., Matheos, D., Rose, M. D. and Stone, D. E. (2002). Regulation of MAPK function by direct interaction with the mating-specific Galpha in yeast. *Science* **296**, 1483-6.

Moore, T. I., Chou, C. S., Nie, Q., Jeon, N. L. and Yi, T. M. (2008). Robust spatial sensing of mating pheromone gradients by yeast cells. *PLoS One* **3**, e3865.

Nern, A. and Arkowitz, R. A. (1998). A GTP-exchange factor required for cell orientation. *Nature* **391**, 195-8.

Nern, A. and Arkowitz, R. A. (1999). A Cdc24p-Far1p-Gbetagamma protein complex required for yeast orientation during mating. *J Cell Biol* **144**, 1187-202.

Nern, A. and Arkowitz, R. A. (2000). G proteins mediate changes in cell shape by stabilizing the axis of polarity. *Mol. Cell* **5**, 853-864.

Palanivelu, R. and Preuss, D. (2000). Pollen tube targeting and axon guidance: parallels in tip growth mechanisms. *Trends Cell Biol* **10**, 517-24.

Park, H. O., Bi, E., Pringle, J. R. and Herskowitz, I. (1997). Two active states of the Ras-related Bud1/Rsr1 protein bind to different effectors to determine yeast cell polarity. *Proc Natl Acad Sci U S A* **94**, 4463-8.

Pruyne, D. and Bretscher, A. (2000a). Polarization of cell growth in yeast. *J Cell Sci* **113 (Pt 4)**, 571-85.

Pruyne, D. and Bretscher, A. (2000b). Polarization of cell growth in yeast. I. Establishment and maintenance of polarity states. *J Cell Sci* **113 (Pt 3)**, 365-75.

Sagot, I., Klee, S. K. and Pellman, D. (2002). Yeast formins regulate cell polarity by controlling the assembly of actin cables. *Nat Cell Biol* **4**, 42-50.

Segall, J. E. (1993). Polarization of yeast cells in spatial gradients of alpha mating factor. *Proc Natl Acad Sci U S A* **90**, 8332-6.

Servant, G., Weiner, O. D., Herzmark, P., Balla, T., Sedat, J. W. and Bourne, H. R. (2000). Polarization of chemoattractant receptor signaling during neutrophil chemotaxis. *Science* **287**, 1037-40.

Sherman, F., G. R. Fink, J. B. Hicks, Eds. (1986). *Laboratory Course Manual For Methods in Yeast Genetics*. (Cold Spring Harbor Laboratory Press, Cold Spring Harbor, New York, 1986).

Snetselaar, K. M., Bolker, M. and Kahmann, R. (1996). Ustilago maydis Mating Hyphae Orient Their Growth toward Pheromone Sources. *Fungal Genet Biol* **20**, 299-312.

Stratton, H. F., Zhou, J., Reed, S. I. and Stone, D. E. (1996). The mating-specific Gα protein of Saccharomyces cerevisiae downregulates the mating signal by a mechanism that is dependent on pheromone and independent of Gβγ sequestration. *Mol. Cell. Biol.* **16**, 6325-6337.

Strickfaden, S. C. and Pryciak, P. M. (2008). Distinct roles for two Galpha-Gbeta interfaces in cell polarity control by a yeast heterotrimeric G protein. *Mol Biol Cell* **19**, 181-97.

Suchkov, D. V., DeFlorio, R., Draper, E., Ismael, A., Sukumar, M., Arkowitz, R. and Stone, D. E. (2010). Polarization of the yeast pheromone receptor requires its internalization but not actin-dependent secretion. *Mol Biol Cell* **21**, 1737-52.

Takeda, K., Sasaki, A. T., Ha, H., Seung, H. A. and Firtel, R. A. (2007). Role of phosphatidylinositol 3-kinases in chemotaxis in Dictyostelium. *J Biol Chem* **282**, 11874-84.

Tojima, T., Hines, J. H., Henley, J. R. and Kamiguchi, H. (2011). Second messengers and membrane trafficking direct and organize growth cone steering. *Nat Rev Neurosci* **12**, 191-203.

Tranquillo, R. T., Lauffenburger, D. A. and Zigmond, S. H. (1988). A stochastic model for leukocyte random motility and chemotaxis based on receptor binding fluctuations. *J Cell Biol* **106**, 303-9.

Vallier, L. G., Segall, J. E. and Snyder, M. (2002). The alpha-factor receptor C-terminus is important for mating projection formation and orientation in Saccharomyces cerevisiae. *Cell Motil Cytoskeleton* **53**, 251-66.

Valtz, N., Peter, M. and Herskowitz, I. (1995). FAR1 is required for oriented polarization of yeast cells in response to mating pheromones. *J. Cell Biol.* **131**, 863-873.

Veltman, D. M., Keizer-Gunnik, I. and Van Haastert, P. J. (2008). Four key signaling pathways mediating chemotaxis in Dictyostelium discoideum. *J Cell Biol* **180**, 747-53.

Vernay, A., Schaub, S., Guillas, I., Bassilana, M. and Arkowitz, R. A. A Steep phosphoinositide-bis-phosphate gradient is critical for fungal filamentous growth, *submitted*.

Wach, A. (1996). PCR-synthesis of marker cassettes with long flanking homology regions for gene disruptions in S. cerevisiae. *Yeast* **12**, 259-265.

Weiner, O. D. (2002). Regulation of cell polarity during eukaryotic chemotaxis: the chemotactic compass. *Curr Opin Cell Biol* **14**, 196-202.

Whiteway, M., Hougan, I. and Thomas, D. Y. (1990). Overexpression of the STE4 gene leads to mating response in haploid Saccharomyces cerevisiae. *Mol. Cell. Biol.* **10**, 217-222.

Wiget, P., Shimada, Y., Butty, A. C., Bi, E. and Peter, M. (2004). Site-specific regulation of the GEF Cdc24p by the scaffold protein Far1p during yeast mating. *Embo J* **23**, 1063-74.

Yu, L., Qi, M., Sheff, M. A. and Elion, E. A. (2008). Counteractive control of polarized morphogenesis during mating by mitogen-activated protein kinase Fus3 and G1 cyclin-dependent kinase. *Mol Biol Cell* **19**, 1739-52.

FIGURES and FIGURE LEDGENDS

Figure 1

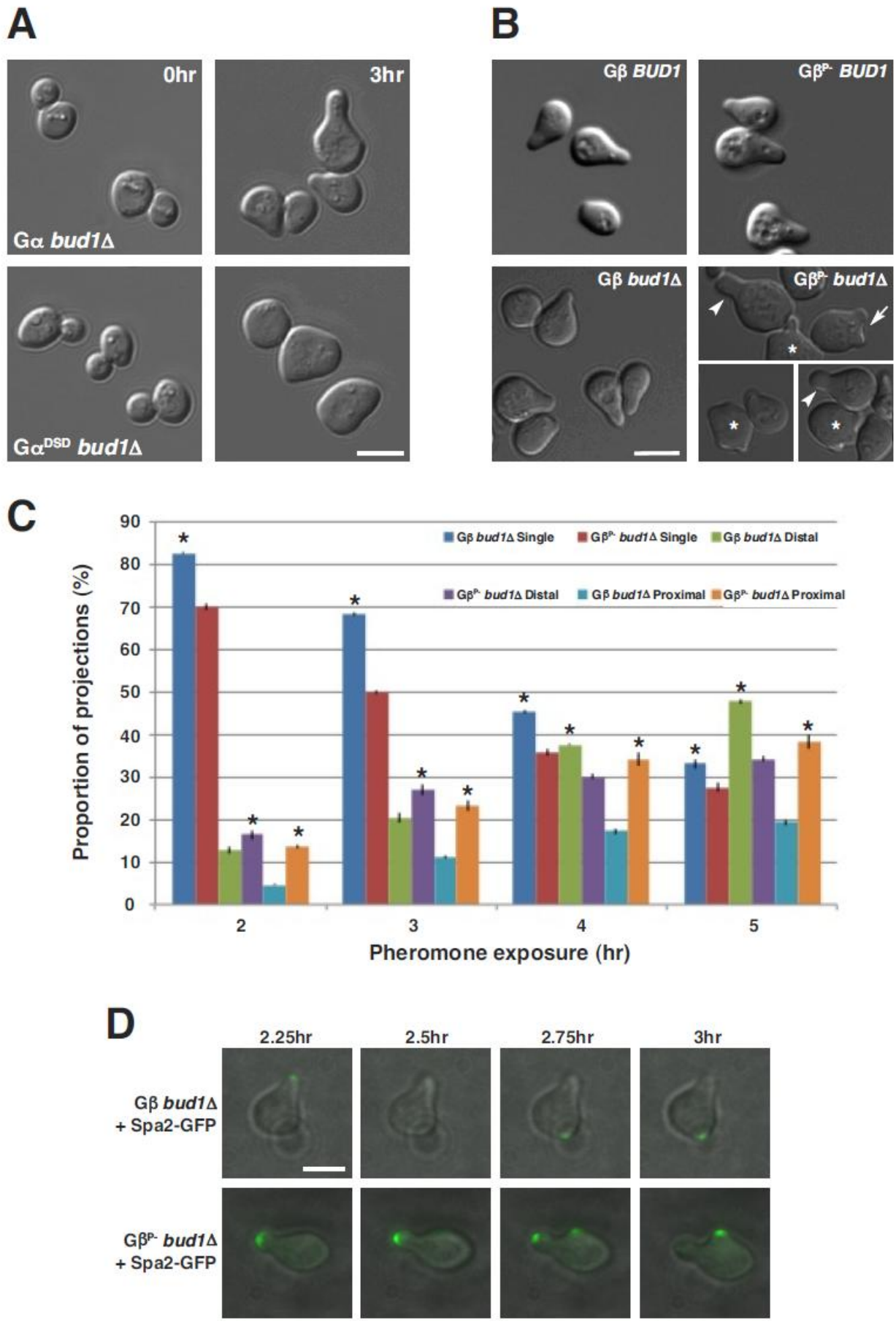

Figure 1. Effect of $G\alpha^{DSD}$ and $G\beta^{P-}$ on the chemotropic shmoo pathway. (A) $G\alpha^{DSD}$ *bud1*Δ cells are unable to form mating projections. *MAT***a** *gpa1*Δ *bud1*Δ cells expressing either Gα or $G\alpha^{DSD}$ were exposed to 150 nM pheromone for 3 hr. (B) $G\beta^{P-}$ *bud1*Δ cells exhibit a variety of mating projection abnormalities. *MAT***a** Gβ *bud1*Δ, $G\beta^{P-}$ *bud1*Δ, Gβ *BUD1*, and $G\beta^{P-}$ *BUD1* cells were exposed to 30 nM pheromone for 3 hr. Representative images are shown. Lower right is a composite. White arrowheads indicate cells scored as bulbous shmoos, white arrows indicate proximal double shmoos, and white asterisks mark examples of SMP cells. (C) $G\beta^{P-}$ *bud1*Δ cells form projections proximal to the initial growth site. *MAT***a** Gβ *bud1*Δ and $G\beta^{P-}$ *bud1*Δ cells were exposed to 30 nM pheromone and the percentages of cells with a single projection, multiple distal projections, and multiple proximal projections were determined at each time point. Averages of 3 independent experiments with s.e.m. are shown ($n \geq 200$ for each strain/time); $^*p < 0.0001$ for comparing the higher to lower percentage of a given projection type. (D) Simultaneous localization of Spa2-GFP to multiple projection tips. *MAT***a** Gβ *bud1*Δ and $G\beta^{P-}$ *bud1*Δ cells expressing *SPA2-GFP* were exposed to 150 nM pheromone for 3 hr. In 3 trials, the mean percentage ± s.e.m. of cells in which Spa2-GFP was concentrated at > 1 site was 17.4 ± 0.33 and 4.4 ± 0.56 for the $G\beta^{P-}$ and Gβ cells, respectively ($n < 120$; $p < 0.0001$)**.**

Figure 2

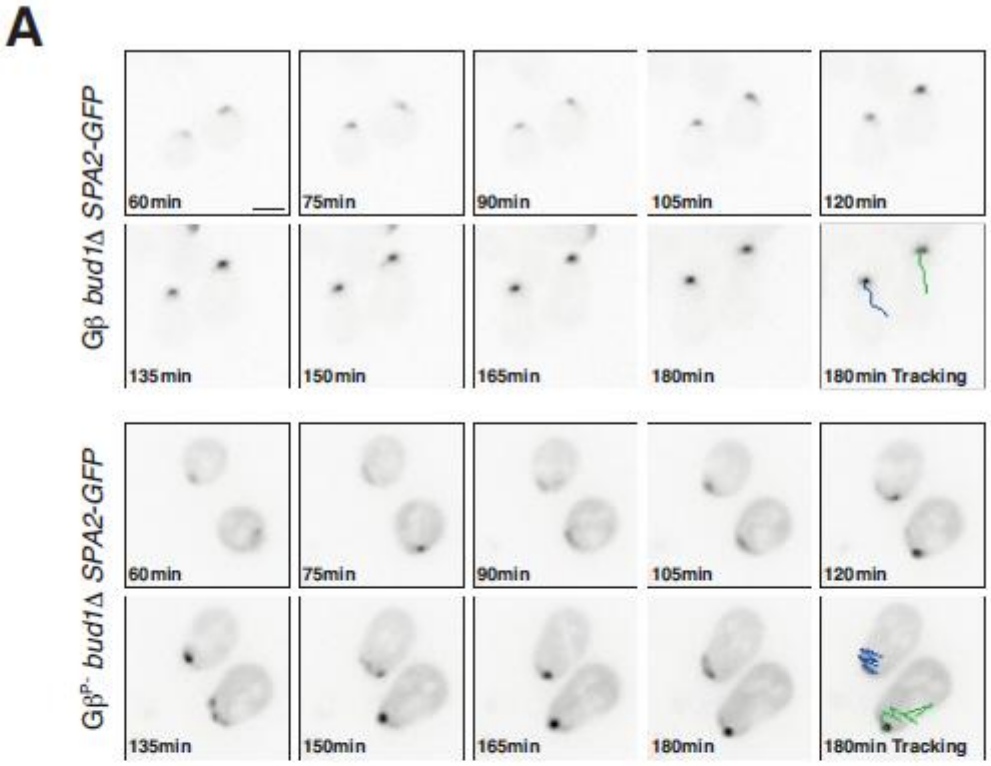
A
Gβ bud1Δ SPA2-GFP
60min
75min
90min
105min
120min
135min
150min
165min
180min
180min Tracking
Gβ^P- bud1Δ SPA2-GFP
60min
75min
90min
105min
120min
135min
150min
165min
180min
180min Tracking

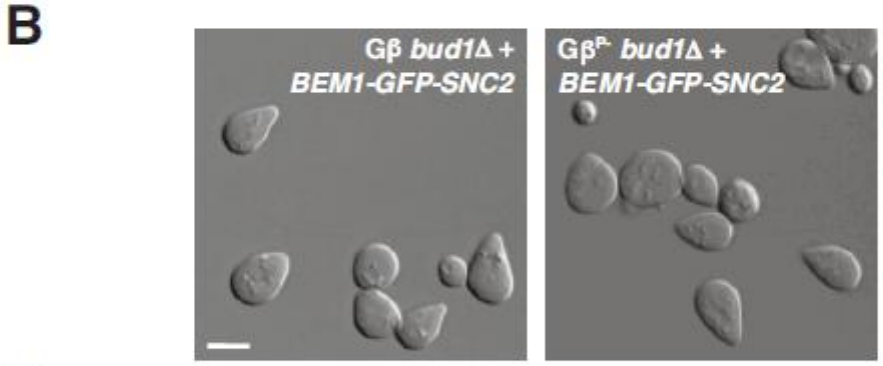
B
Gβ bud1Δ +
BEM1-GFP-SNC2
Gβ^P- bud1Δ +
BEM1-GFP-SNC2

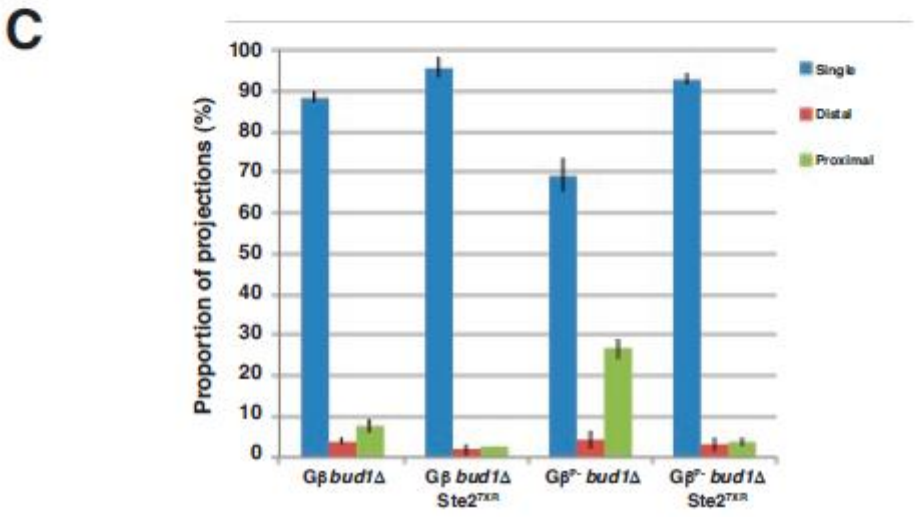
C
Proportion of projections (%)
100
90
80
70
60
50
40
30
20
10
0
Single
Distal
Proximal
Gβbud1Δ
Gβ bud1Δ Ste2^TKR
Gβ^P- bud1Δ
Gβ^P- bud1Δ Ste2^TKR

Figure 2. The growth site of pheromone-treated Gβ^{P-} *bud1*Δ cells wanders where the receptor is concentrated. (A) Time-lapse images of Spa2-GFP in mating cells. *MAT***a** Gβ *bud1*Δ or Gβ^{P-} *bud1*Δ cells expressing *SPA2-GFP* were mixed with congenic *MAT*α cells and incubated for the indicated times. Final images show an overlay of Spa2-GFP movement from 60-180 min. (B) Bem1-GFP-Snc2 rescues the Gβ^{P-} *bud1*Δ shmoo abnormalities. *MAT***a** Gβ *bud1*Δ or Gβ^{P-} *bud1*Δ cells expressing *BEM1-GFP-SNC2* were exposed to 30 nM pheromone for 3 hr. Representative images are shown. (C) Gβ^{P-} *bud1*Δ cells don't form proximal projections when receptor internalization is blocked. *MAT***a** Gβ *bud1*Δ, Gβ *bud1*Δ *ste2*$^{7XR/GPAAD}$, Gβ^{P-} *bud1*Δ, and Gβ^{P-} *bud1*Δ *ste2*$^{7XR/GPAAD}$ cells were exposed to 25 nM pheromone for 4 hr. The percentages of cells with a single projection, multiple distal projections, and multiple proximal projections were determined. The means of three independent experiments ± s.e.m. are shown (n = 300 for each strain and trial). $p < 0.0001$ for the % single projections and % proximal projections formed by the Gβ^{P-} *bud1*Δ strain as compared to the other three strains.

Figure 3

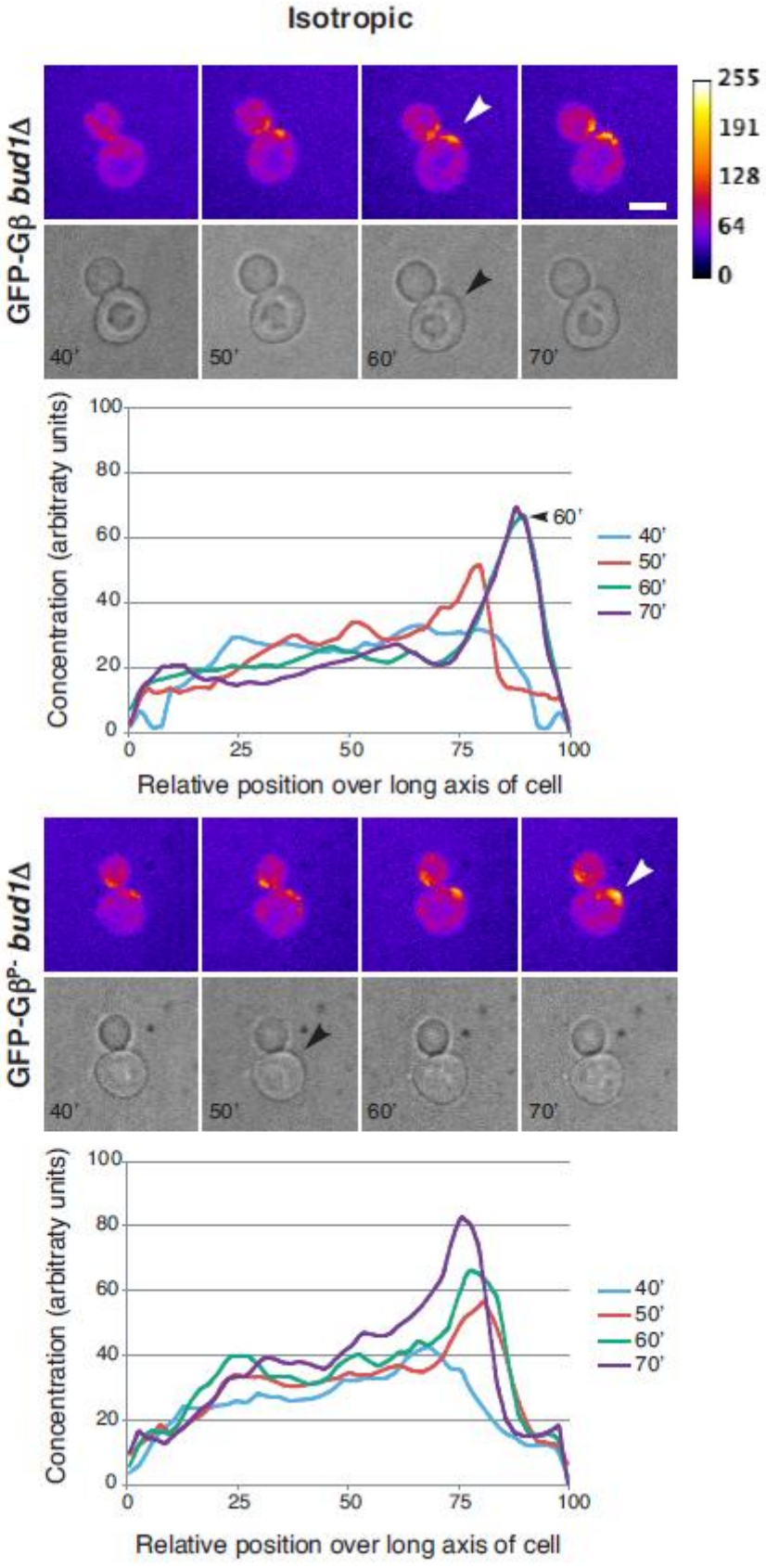
A
Isotropic
GFP-Gβ bud1Δ
255
191
128
64
0
40'
50'
60'
70'
Concentration (arbitraty units)
100
80
60
40
20
0
0
25
50
75
100
Relative position over long axis of cell
40'
50'
60'
70'
GFP-Gβ^P- bud1Δ
40'
50'
60'
70'
Concentration (arbitraty units)
Relative position over long axis of cell
40'
50'
60'
70'

Figure 3

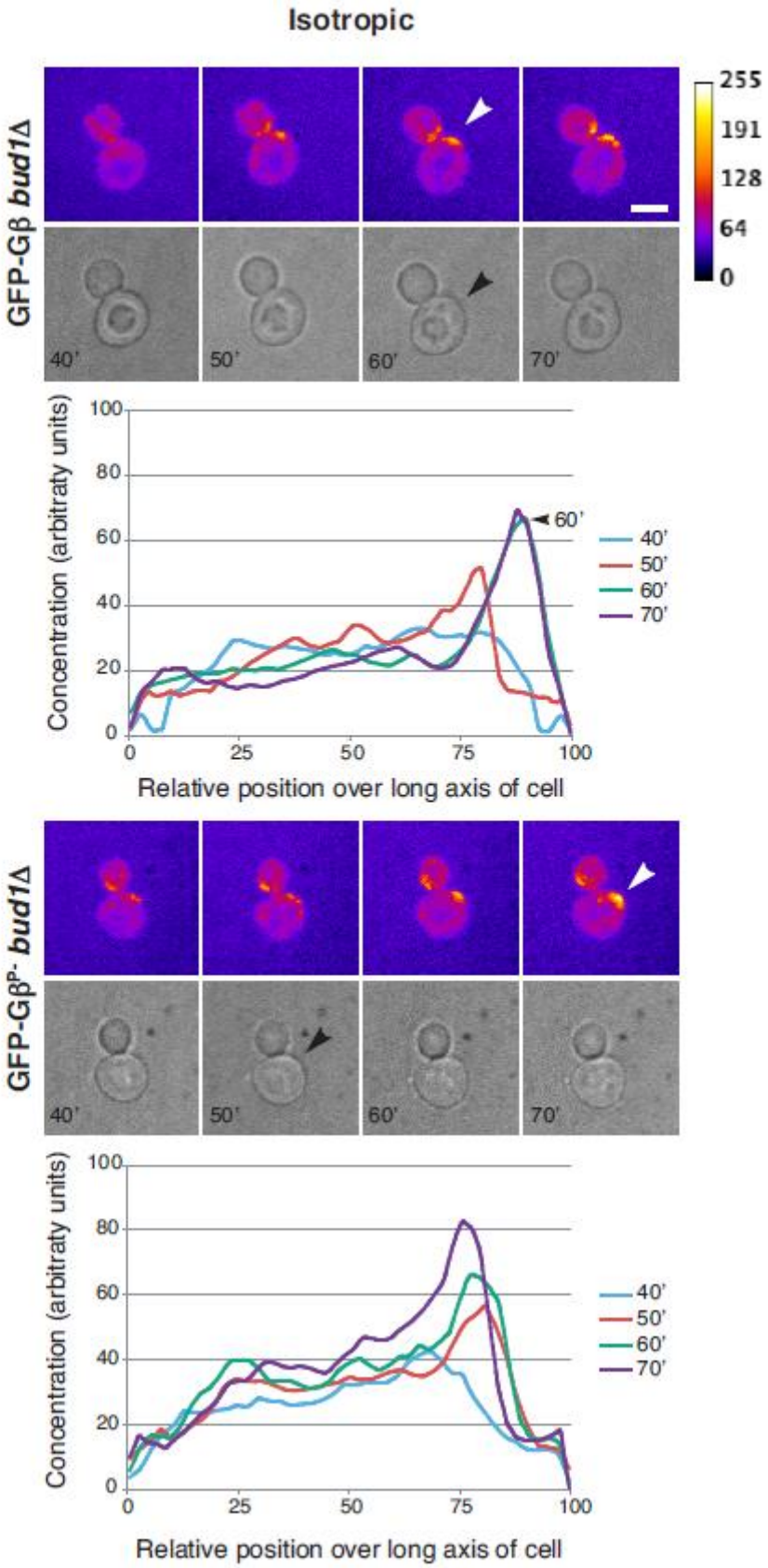
A
Isotropic
GFP-Gβ bud1Δ
255
191
128
64
0
40'
50'
60'
70'
Concentration (arbitraty units)
100
80
60
40
20
0
0
25
50
75
100
Relative position over long axis of cell
60'
40'
50'
60'
70'
GFP-Gβ^P- bud1Δ
40'
50'
60'
70'
Concentration (arbitraty units)
Relative position over long axis of cell
40'
50'
60'
70'

Figure 3

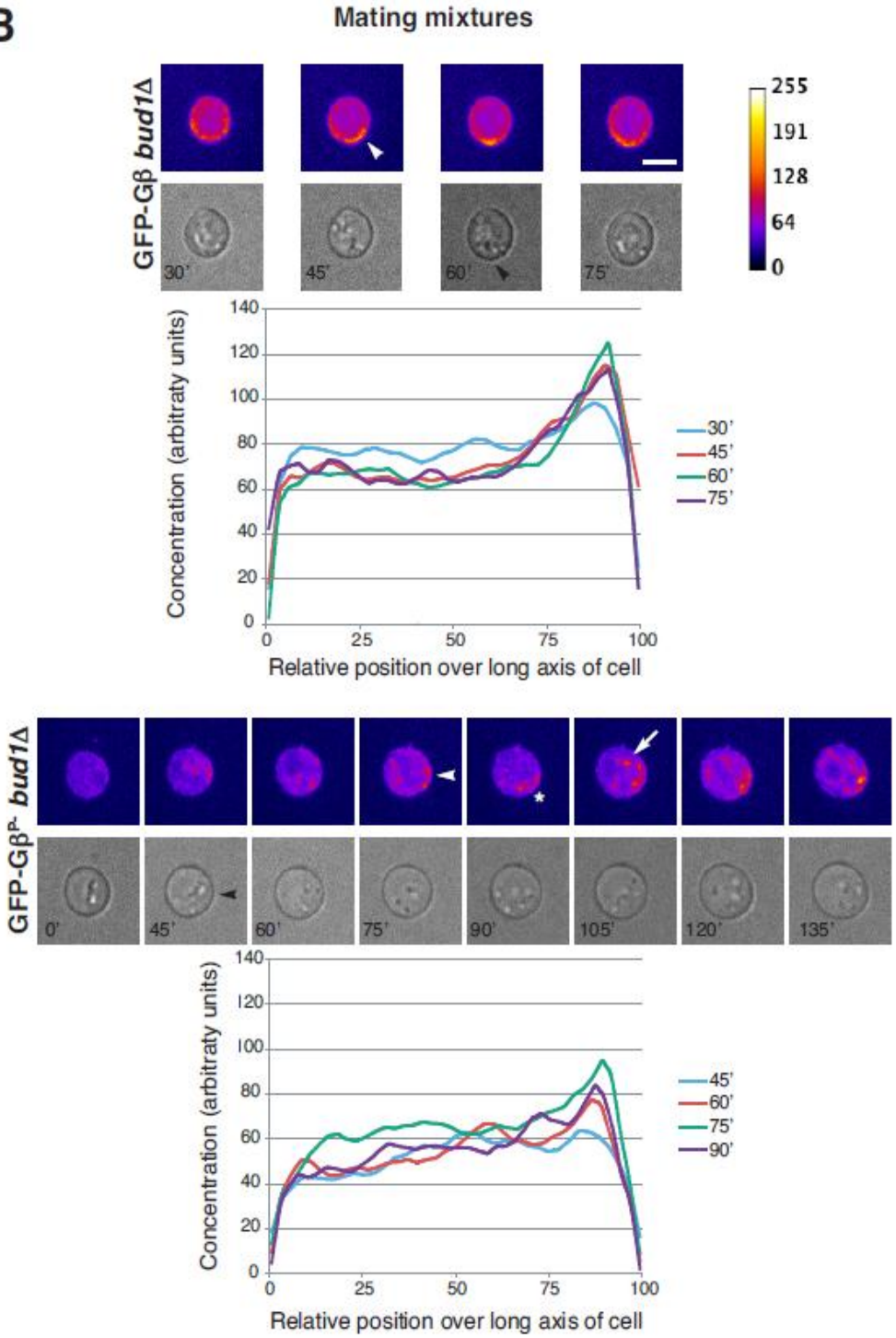

Figure 3. GFP-Gβ^{P-} polarizes later and less stably than GFP-Gβ in both isotropic and gradient conditions. (A) Isotropic treatment. *MAT***a** GFP-Gβ *bud1*Δ and GFP-Gβ^{P-} *bud1*Δ cells were exposed to 150 nM pheromone for the indicated times. (B) Mating mixtures. *MAT***a** GFP-Gβ *bud1*Δ and GFP-Gβ^{P-} *bud1*Δ cells were mixed with congenic *MAT*α cells, and incubated for the indicated times. For A and B, GFP-Gβ concentration in arbitrary units was quantified (line graphs); black arrowheads mark polarized growth and white arrowheads mark polarity. For B, white arrows mark spots and the white asterisk marks non-consolidated polarization. The Gβ polarization data are summarized in Table 2.

Figure 4

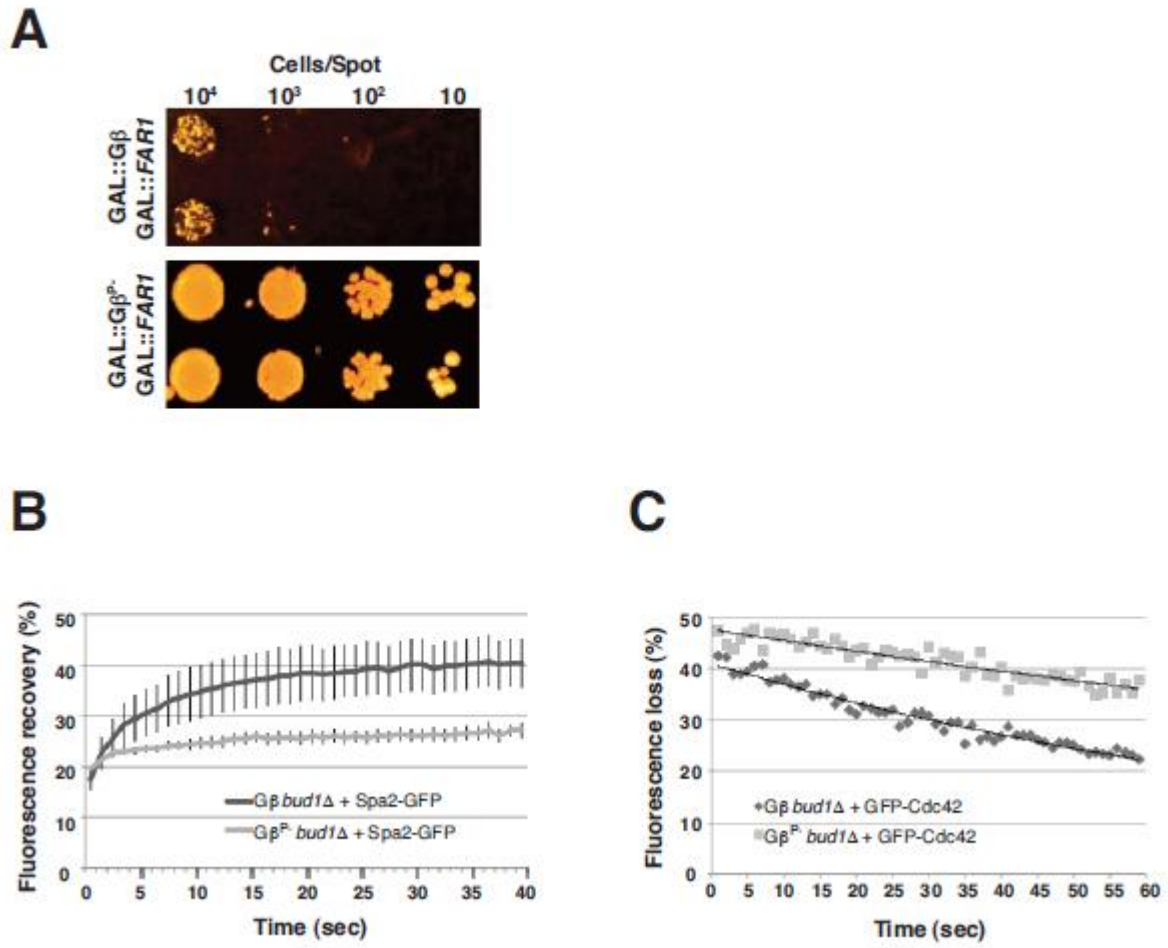

Figure 4. The effect of Gβ^{P-} on Gβ-Far1 interaction and positional stability of Spa2 and Cdc42. (A) Far1 overexpression rescues overexpression of Gβ^{P-} but not of Gβ. Strains carrying the indicated plasmids were spotted on galactose-containing medium to induce the overexpression of Far1, and Gβ or Gβ^{P-}. Results for two representative strains of each type are shown. All strains grew similarly on glucose-containing medium. (B) FRAP analysis of Spa2-GFP. *MAT***a** Gβ *bud1*Δ and Gβ^{P-} *bud1*Δ cells expressing *SPA2-GFP* were exposed to 30 nM pheromone for 1 hr prior to photobleaching. The data represent the means of two independent experiments ± s.e.m. The FRAP $t_{1/2}$ in seconds and % recovery were 9.7 ± 1.87 and 40.3 ± 3.43, respectively, in Gβ *bud1*Δ cells (n = 18), as compared to 19.3 ± 2.32 (p = 0.003) and 24.6 ± 1.73 (p = 0.0002) in Gβ^{P-} *bud1*Δ cells (n = 20). (C) iFRAP analysis of GFP-Cdc42. *MAT***a** Gβ *bud1*Δ and Gβ^{P-} *bud1*Δ cells expressing *GFP-CDC42* were exposed to pheromone as above. Representative scatter plots of fluorescence loss and corresponding trend lines are shown. The iFRAP $t_{1/2}$ in seconds and % loss were 41.9 ± 3.25 and 22.9 ± 1.48, respectively, in Gβ *bud1*Δ cells (n = 27), as compared to 54.3 ± 3.55 (p = 0.01) and 21.1 ± 3.05 in Gβ^{P-} *bud1*Δ cells (n = 28).

Figure 5

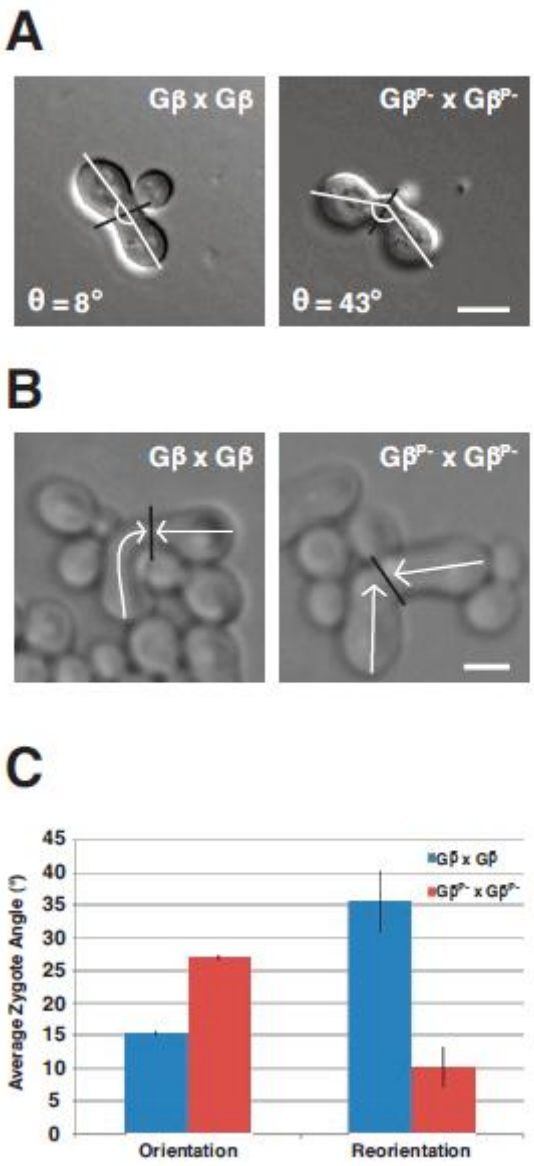

Figures 5. Gβ^{P-} confers a defect in directional sensing. (A) Representative straight and angled zygotes from the orientation assays. Zygotes were analyzed from WT and Gβ^{P-} bilateral matings. The angle of orientation was measured by drawing a line from the base of each shmooing cell (white) to the zone of fusion (black). (B) Representative zygotes from the reorientation assays. Pre-stimulated *MAT***a** and *MAT*α cells were allowed to mate on agar media and scored for their ability to reorient growth of an existing mating projection. Zygotes were analyzed from WT and *MAT***a** Gβ^{P-} bilateral matings. Reorientation was defined as a change in direction in a line drawn from the base of a shmoo to the zone of fusion. The angle of reorientation for a given shmoo was measured by drawing a line from the original axis of polarity (white) to the zone of fusion (black). (C) Mean angles of orientation and reorientation ± s.e.m. For orientation, the total *n* for each strain in 3 trials > 200; $p < 0.0001$. For reorientation, $n = 58$ for both strains; $p < 0.0001$.

Figure 6

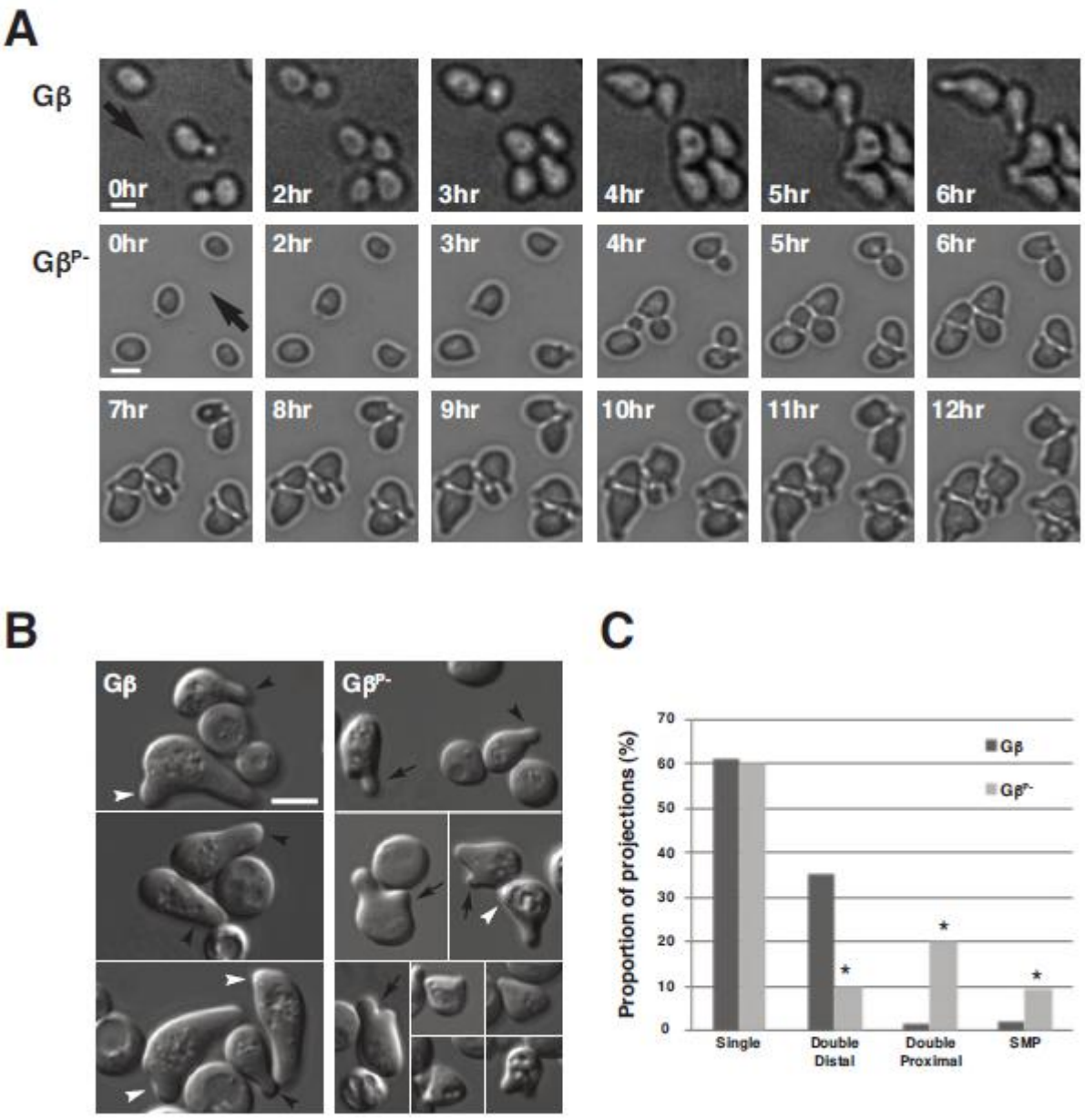

Figures 6. Gβ^{P-} confers chemotropic growth defects in both artificial and natural pheromone gradients. (A) Gβ^{P-} *BUD1* cells cannot properly orient and stabilize polarized growth in an artificial pheromone gradient. Representative time-lapse images of gradient-stimulated WT and Gβ^{P-} cells in a microfluidic device are shown. Black arrows indicate the direction of the gradient. The mean orientation angle ± s.e.m. for the first protrusions formed by Gβ^{P-} cells was 89.9 ± 4.2˚(*n* = 314), as compared to 56.9 ± 4.6˚(*n* = 83) for WT shmoos (Brett et al., 2012), where 90˚ indicates random orientation. (B) Gβ^{P-} *BUD1* cells in mating mixtures exhibit shmoo defects similar to Gβ^{P-} *bud1*Δ cells exposed to isotropic pheromone. Representative images of cells from bilateral Gβ *BUD1* and Gβ^{P-} *BUD1* mating mixtures after 5 hr. Black arrowheads indicate cells scored as single shmoos, white arrowheads indicate distal double projections, and black arrows indicate proximal double projections. Small squares, examples of SMP cells. (C) Quantification of the shmoo types found in the WT and Gβ^{P-} bilateral mating mixtures. The percentages of shmooed cells in each class are shown in

the bar graph. *$p < 0.0001$ for the comparison Gβ vs. $G\beta^{P-}$ in each class; $n = 300$ for both strains. Similar results were obtained in each of 3

trials.

Table 1. Spa2-GFP Mobility

Strain	Movement/15' (μm)	Velocity (μm/hr)	ΔDirection (%)[a]	Final length (μm)	≥ 2 spots	*n*
$G\beta^{WT}$ *bud1*Δ	0.54 ± 0.15	2.15 ± 0.61	19± 13	8.07 ± 0.97	1	89
$G\beta^{P-}$ *bud1*Δ	1.13 ± 0.24	4.51 ± 0.96	52± 15	7.39 ± 1.10	18	38

[a] ΔDirection (%) is the number of direction changes divided by the number of steps observed for each cell.

Table 2. Pheromone-induced polarization of Gβ

	Isotropic			*Mating*		
	GFP-Gβ	GFP-Gβ^{P-}	*p* value	GFP-Gβ	GFP-Gβ^{P-}	*p* value
Polarized *n*/Total *n*	47/49	39/52		33/36	25/43	
% Polarized Gβ	95.9	75	< 0.0001	91.7	58.1	< 0.0001
Mean time of Gβ polarization (min)[a]	1. 8 ± 0.4	17.3 ± 1.73	< 0.0001	-8.8 ± 2.4	16.8 ± 4.2	< 0.0001
% Polarized Gβ pre-polarized growth[b]	55.3	38.4	0.034	84.8	28.0	0.0001
% Switch[c]	NA	NA		39.4	12.0	0.005
% Wandering[d]	ND	ND		9.1	36.0	0.0001
% Not consolidated[e]	ND	ND		34.4	92.0	< 0.0001
% Spots[f]	ND	ND		21.2	72.0	< 0.0001

[a]For the cells that polarized Gβ, the mean times of polarization ± s.e.m. relative to the onset of polarized growth are indicated; [b]The percentages of Gβ-polarized cells in which polarization occurred at or before morphogenesis; [c]The percentage of Gβ-polarized cells that clearly switched polarization sites during the time-course; [d]The percentage of Gβ-polarized cells in which the region of concentrated Gβ appeared to wander; [e]The percentage of Gβ-polarized cells in which the region of concentrated Gβ was composed of two or more discreet spots; [f]The percentage of Gβ-polarized cells in which high-intensity spots were observed well apart from the region of concentrated Gβ.

Supplementary Table 1. Yeast strains used in this study

Strain	Genotype	Source
	*MAT***a** *bar1*Δ *ade1 his2 leu2-3, 112 trp1-1a ura3*Δ	Stone lab
DSY257	*MAT***a** *bar1*Δ *ade1 his2 leu2-3, 112 trp1-1a ura3*Δ *ste4::URA3*	Stone lab
ELY104		
RDY114	*MAT***a** *ste4*$^{T320A\ S335A}$ *bar1*Δ *ade1 his2 leu2-3, 112 trp1-1a ura3*Δ	This study
RDY103	*MAT***a** *bud1***Δ**::*KAN bar1*Δ *ade1 his2 leu2-3, 112 trp1-1a ura3*Δ	This study
RDY120	*MAT***a** *ste4*$^{T320A\ S335A}$ *bud1***Δ**::*KAN bar1*Δ *ade1 his2 leu2-3, 112 trp1-1a ura3*Δ	This study
MMY110	*MAT***a** *gpa1*Δ::*URA3 bud1***Δ**::*KAN bar1*Δ *ade1 his2 leu2-3, 112 trp1-1a ura3*Δ YCplac22/*gpa1*$^{K21E\ R22E}$	This study
MMY111	*MAT***a** *gpa1*Δ::*URA3 bud1***Δ**::*KAN bar1*Δ *ade1 his2 leu2-3, 112 trp1-1a ura3*Δ YCplac22/*GPA1*	This study
	*MAT***a** *gpa1*Δ::*URA3 bar1*Δ *ade1 his2 leu2-3, 112 trp1-1a ura3*Δ YCplac22/*gpa1*$^{K21E\ R22E}$	This study
RDY130	*MAT***a** *ste4::URA3 GFP-STE4::ura3 bud1***Δ**::*KAN bar1***Δ** *ade1 his2 leu2-3, 112 trp1 ura3*	This study
RDY132	*MAT***a** *ste4::URA3 GFP- ste4*$^{T320A\ S335A}$*::ura3 bud1***Δ**::*KAN bar1***Δ** *ade1 his2 leu2-3, 112 trp1 ura3*Δ	This study
RDY126	*MAT***a** *ste4::URA3 GFP-STE4::ura3 bar1***Δ** *ade1 his2 leu2-3, 112 trp1 ura3*	This study
RDY139	*MAT***a** *ste4::URA3 GFP- ste4*$^{T320A\ S335A}$*::ura3 bar1***Δ** *ade1 his2 leu2-3, 112 trp1 ura3*Δ	This study
DSY246	*MAT*α *bar1*Δ *ade1 his2 leu2-3, 112 trp1-1a ura3*Δ	Stone lab
RDY217	*MAT*α *ste4*$^{T320A\ S335A}$ *bar1*Δ *ade1 his2 leu2-3, 112 trp1-1a*	This study
RDY246	*ura3*Δ	This study
	*MAT***a** *bud1***Δ**::*KAN bar1*Δ *ade1 his2 leu2-3, 112 trp1-1a*	
RDY247	*ura3*Δ pRS406/SPA2-GFP	This study
	*MAT***a** *ste4*$^{T320A\ S335A}$ *bud1***Δ**::*KAN bar1*Δ *ade1 his2 leu2-3,*	

RDY259	*112 trp1-1a ura3*Δ pRS406/SPA2-GFP	This study
RDY260	*MAT***a** *bud1*Δ::*KAN bar1*Δ *ade1 his2 leu2-3, 112 trp1-1a ura3*Δ pRS424/GFP-CDC42	This study
EAY106	*MAT***a** *ste4*$^{T320A\ S335A}$ *bud1*Δ::*KAN bar1*Δ *ade1 his2 leu2-3, 112 trp1-1a ura3*Δ pRS424/GFP-CDC42	This study
EAY107	*MAT***a** *bud1*Δ::*KAN bar1*Δ *ade1 his2 leu2-3, 112 trp1-1a ura3*Δ pRS304/STE2$^{7XR/GPAAD}$	This study
	*MAT***a** *ste4*$^{T320A\ S335A}$ *bud1*Δ::*KAN bar1*Δ *ade1 his2 leu2-3, 112 trp1-1a ura3*Δ pRS304/STE2$^{7XR/GPAAD}$	

Supplementary Table 2. Plasmids used in this study

Plasmid no.	Plasmid name	Marker/Type	Source
DSB159	YCplac22/GPA1	TRP1/CEN	(Stratton et al., 1996)
MMB104	YCplac22/gpa1$^{K21E\ R22E}$	TRP1/CEN	(Metodiev et al., 2002)
RDB116	YCplac33/ste4$^{T320A\ S335A}$	URA3/CEN	(Li et al., 1998a)
BLT49	pRS316/GFP-Ste4	URA3/CEN	(Kim et al., 2000)
RDB122	pRS316/GFP- ste4$^{T320A\ S335A}$	URA3/CEN	This study
RDB151	pRS406/Spa2-GFP	URA3/INT	(Arkowitz and Lowe, 1997)
DLB2823	pRS305/Bem1-GFP-Snc2	LEU2/INT	(Howell et al., 2009)
	pRS424/GFP-Cdc42	URA3/2μm	(Barale et al., 2006)
DLB3217	pRS304/STE2$^{7XR/GPAAD}$	TRP1/INT	Lew lab
MCB26	YCplac111/GAL1-Ste4	LEU2/CEN	(Cismowski et al., 2001)
RDB131	YCplac111/GAL1-ste4$^{T320A\ S335A}$	LEU2/CEN	This study
pEB15.1	pESC /GAL10-FLAG-Far1	URA3/2μm	This study

Appendix C ACC Approval for Mouse Work

UIC UNIVERSITY OF ILLINOIS AT CHICAGO

Office of Animal Care and
Institutional Biosafety Committees (MC 672)
Office of the Vice Chancellor for Research
206 Administrative Office Building
1737 West Polk Street
Chicago, Illinois 60612-7227

August 5, 2010

Bradley Merrill
Biochemistry & Molecular Genetics
M/C 669

Dear Dr. Merrill:

The protocol indicated below was reviewed at a convened ACC meeting in accordance with the Animal Care Policies of the University of Illinois at Chicago on **7/20/2010**. *The protocol was not initiated until final clarifications were reviewed and approved on* **8/4/2010**. *The protocol is approved for a period of 3* years with annual continuation.

Title of Application: Embryonic Stem Cell Properties in Cancer

ACC Number: 10-139

Initial Approval Period: 8/4/2010 to 7/20/2011

Current Funding: ***Portions of this protocol are supported by the funding sources indicated in the table below.***

Number of funding sources: 2

Funding Agency	**Grant Title**			**Portion of Grant Matched**
ACS- American Cancer Society	*Role Of Tcf Proteins In Stem Cell Self Renewal And Cell Cycle Progression*			*Matched*
Grant Number	**Current Status**	**UIC PAF NO.**	**Performance Site**	**Grant PI**
RSG-07-146-01-CCG	*Funded*	*2007-01608*	*UIC*	*Brad Merrill*
Funding Agency	**Grant Title**			**Portion of Grant Matched**
NIH	*Embryonic Stem Cell Properties In Cancer*			*Matched*
Grant Number	**Current Status**	**UIC PAF NO.**	**Performance Site**	**Grant PI**
RO1 CA128571 (A2 version)	*Funded*	*2008-02116*	*UIC*	*Brad Merrill*

This institution has Animal Welfare Assurance Number A3460.01 on file with the Office of Laboratory Animal Welfare, NIH. **This letter may only be provided as proof of IACUC**

Phone (312) 996-1972 • Fax (312) 996-9088 • www.research.uic.edu

approval for those specific funding sources listed above in which all portions of the grant are matched to this ACC protocol.

Thank you for complying with the Animal Care Policies and Procedures of UIC.

Sincerely yours,

Richard D. Minshall, PhD
Chair, Animal Care Committee

RDM/*ss*
cc: BRL, ACC File, JD Churchill, **PAF # 2007-01608, PAF # 2008-02116**

Appendix D Curriculum Vitae

Marie-Elena Brett

OBJECTIVE

To obtain a postdoctoral research position with a focus on microfluidics and cell or tissue engineering.

EDUCATION

The University of Illinois at Chicago
Doctoral Candidate - expected 2012 graduation
GPA: 3.9

The University of New Hampshire
Bachelors of Science in Biochemistry (Honors) May 1998
Advisory minor: Pre-Med.; Concentration: French
GPA: 3.25
Honors: Graduated with Dean's list Honors (Major);
1997 and 1998 Honors convocation;
1997 most active in improving student life from The Inter-Residence Organization;
Alpha Zeta Honor Society.

RESEARCH EXPERIENCE

The University of Illinois at Chicago August 2008 – Present
Doctoral Candidate - Dr. David Eddington

Thesis research in the Biological Microsystems Laboratory. Research project includes microfluidics, photolithography, micropatterning, hot embossing, glass etching, device and material characterization, as well as all techniques for all biological elements employed. Training of new students. Teaching assistant in Biomaterials and Cell and Tissue Engineering Laboratory.

The University of Illinois at Chicago December 1998 – June 2002
Research Specialist in the Health Sciences - Dr.Bin He Ph.D.

Participated in independent research projects and group research projects utilizing various techniques including cell culture; creation of new cell lines; cloning; protein expression and purification; cDNA library screenings; yeast two hybrid assays; virus creation, propagation and titration; agarose and SDS-PAGE gel electrophoresis; PCR and RT-PCR; and general bacterial work. Managed the laboratory including all purchasing, interviewing of lab assistants and training of new students.

ID Biomedical Inc. San Diego, CA September 1998-October 1998

Research Assistant – Dr.Ram S. Bhatt Ph.D.

Responsible for assay development including Hydroxylapitite and size exclusion chromatography, DNA hybridizations, PAGE gel electrophoresis and radioactive labeling of oligonucleotides.

The University of Cincinnati May 1997 - August 1997

Research Assistant - Dr. Andrew Norman Ph.D.

Responsibilities: Performed drug addiction behavioral experiments on rats. Assisted in microsurgery to implant subcutaneous pumps and self-administration apparatus in these test animals.

The University of New Hampshire July 1996-May 1997

Research Assistant - Dr. Charles Walker Ph.D.

Responsibilities: Mounting tissue samples in paraffin and other plastics, sectioning tissue samples using a microtome, creating slides for histological examination.

The University of New Hampshire August 1997-May 1998

Senior Thesis - Dr. Charles Walker Ph.D.

Designed and executed an independent project using the techniques of transforming bacterial cell lines; plasmid preps; enzyme digests; ethidium bromide agarose gel electrophoresis; RNA extraction and purification; PCR and RT-PCR; Northern blot analysis; creating a cDNA library; and DNA sequencing.

The University of New Hampshire August 1997-December 1997

Cell Culture - Dr. Thomas Foxall Ph.D.

Responsibilities: A survey of all areas of cell culture including aseptic techniques of passaging; mixed primary cultures; selective primary cultures of both plant and animal cells, several methods of cloning, cell fusions using HAT media for selection; ELISA plating; and cryopreservation.

The University of New Hampshire January 1997- May 1997

Laboratory in Biochemistry - Dr. Thomas Laue Ph.D.

Responsibilities: Enzyme purification involving: SDS-PAGE and ethidium bromide agarose gel electrophoresis; ion exchange and gel filtration chromatography. Fusion protein creation and column chromatography; and Western blot analysis; as well as DNA extraction, purification, and sequencing.

LABORATORY SKILLS

Soft Photolithography; hot embossing; glass etching; micropatterning; microfluidic device and material characterization; yeast culture; embryo extraction from mice; mammalian cell culture; cloning; protein expression and purification; cDNA library screening; yeast two hybrid assay; ELISA; PCR and RT-PCR; agarose and SDS-PAGE gel electrophoresis; general bacteria work; live virus handling including: creation, propagation and tittering; chromatography.

OTHER EXPERIENCE

UIC Early Outreach Program

HSEPS Teacher – Joy Valentine July 2012

Taught high school students scientific writing, medical terminology, and ethics. Wrote lesson plans, taught 40 students, organized research projects that resulted in student participation in a research symposium.

Highlife Adventures Inc. June 2006- August 2008

Events Manager – Montgomery Sauder

Planning a monthly calendar of 75-85 events per month for a 3,000 person membership base. Managing an in-house staff or 5 people and a contract staff of 15. Responsibilities also include maintenance of vendor and customer relations, creating and maintaining departmental budgets and bonus programs.

Lodge Management Group

May 2001-April 2008

Bartender – Ronda Culver

Developed and implemented an employee training program. Responsibilities also include customer service, inventory control, and management of employees.

PUBLICATIONS

Brett, M-E., Hoffman, J., Merrill, B., and Eddington, D. T. (2012). A microfluidic device for in vitro culture of gastrulation stage mouse embryos. In Preparation.

Brett, M-E., Sinkala, E., Sukumar, M., Stone,D.E., and Eddington, D. T. (2012). A fully automated microfluidic platform for gradient generation in an agarose pad for the study of yeast chemotropism. In Preparation.

DeFlorio, R., Apollinari, E., Brett, M-E., Metodiev, M., Dubrovskyi, O. and Eddington, D.T. Stone, D. E. (2012). G-beta phosphorylation is critical for efficient chemotropism in yeast. JCS. In review.

Brett, M-E., DeFlorio, R., Stone, D. E., and Eddington, D. T. (2012). A microfluidic device that forms and redirects pheromone gradients to study chemotropism in yeast. *Lab Chip*. 12, 3127-3134.

Brett, M-E., Zhao, S., Stoia, J.L., and Eddington, D.T. (2011). Controlling flow in microfluidic channels with a manually actuated pin valve. *Biomed Microdevices* 13(4), 633-9.

Cheng, G., Brett, M-E., and He, B. (2002). Signals that dictate nuclear, nucleolar, and cytoplasmic shuttling of the gamma (1)34.5 protein of herpes simplex virus type 1. *J. Virol.* 76(18), 9434-9445.

Cheng, G., Brett, M-E., and He, B. (2001). Val^{193} and Phe^{195} of the $\gamma_1$34.5 Protein of Herpes Simplex Virus 1 Are Required for Viral Resistance to Interferon-α/β. *Virology* 290(1), 115-120.

Cheng, G., Gross, M., Brett, M-E., and He, B. (2001). AlaArg motif in the carboxyl terminus of the $g_1$34.5 protein of herpes simplex virus type 1 is required for the formation of a high-molecular-weight complex that dephosphorylates eIF-2a. *J. Virol.* 75(8), 3666-3674.

CONFERENCES

Brett, M-E., Hoffman, J., Merrill, B., Eddington, D. T. A microfluidic device for in vitro culture of gastrulation stage mouse embryos. Biomedical Engineering Society (BMES) 2012 Annual Meeting scheduled for October 24-27 in Atlanta, Georgia. Poster.

Brett, M-E., DeFlorio, R., Stone, D. E., and Eddington, D. T. Saccharomyces cerevisiae Response to a Rapidly Rotating Pheromone Gradient in a Microfluidic Device. SLAS 2012, February 4-8 in San Diego, CA. Poster.

Brett, M-E., DeFlorio, R., Stone, D. E., and Eddington, D. T. The Response of Yeast Cells to a Change in the Direction of a Pheromone Gradient in a Microfluidic Device. MicroTAS 2011 Conference, Seattle, Washington, USA, October 2-6, 2011. Poster.

Brett, M-E., DeFlorio, R., Stone, D. E., and Eddington, D. T. The Response of Yeast Cells to a Change in the Direction of a Pheromone Gradient in a Microfluidic Device. Chicago Biomedical Consortium's (CBC) 9th annual symposium "Engineering Biology: From Tools to Insights." Chicago, IL, October 21, 2011. Poster.

Brett, M-E., Hoffman, J., Merrill, B., Eddington, D. T. Culture of Mouse Embryos in a Microfluidic Device. Third Stem Cell and Regenerative Medicine Program. Chicago, IL, May 20, 2011

Brett, M-E., Zhao, S., Stoia, J.L., and Eddington, D.T. Pin Valve for Microfluidics. Lab Automation (LA) 2011 Annual conference January 29 – February 2, 2011. Poster.

Brett, M-E., Zhao, S., Stoia, J.L., Mittal, G., and Eddington, D.T. Push Valve for Microfluidic Devices. 2010 Biomedical Engineering Society (BMES) Annual Meeting October 6-9, 2010 in Austin, Texas. Poster.

AWARDS

Graduate Student Council Travel Award from the UIC Graduate Student Council for the Biomedical Engineering Society (BMES) 2012 Annual Meeting scheduled for October 24-27 in Atlanta, Georgia.

Tony B. Academic Travel Award from the Society for Laboratory Automation and Screening (SLAS) for the 2012 Annual Conference February 4-8 in San Diego, CA.

Graduate Student Council Travel Award from the UIC Graduate Student Council for the Lab Automation (LA) 2011 Annual Conference January 29 – February 2, 2011.

Graduate College Travel Award from the UIC Graduate College for the Lab Automation (LA) 2011 Annual Conference January 29 – February 2, 2011.

SERVICE

Graduate Student Council Representative for Department of Bioengineering 2011-2012

Graduate Student Council Social Committee Chair 2011-2012

Graduate Student Representative in Faculty Senate 2011-2012

Volunteer for Helping Hands Girl Scout Program 2008- Present

SOFTWARE SKILLS

Microsoft Word, Power Point, Excel, Sigma Stat, Sigma Plot, Adobe CS4, Pro-Engineer, and Comsol.

Works Cited

1. Whitesides, G.M., *The origins and the future of microfluidics.* Nature, 2006. **442**(7101): p. 368-73.
2. Brittain, S., et al., *Soft lithography and microfabrication.* Physics World, 1998. **11**(5): p. 31-36.
3. Love, J.C., et al., *Microscope projection photolithography for rapid prototyping of masters with micron-scale features for use in soft lithography.* Langmuir, 2001. **17**(19): p. 6005-6012.
4. Odom, T.W., et al., *Improved pattern transfer in soft lithography using composite stamps.* Langmuir, 2002. **18**(13): p. 5314-5320.
5. Xia, Y.N. and G.M. Whitesides, *Soft lithography.* Angewandte Chemie-International Edition, 1998. **37**(5): p. 551-575.
6. Kane, R.S., et al., *Patterning proteins and cells using soft lithography.* Biomaterials, 1999. **20**(23-24): p. 2363-2376.
7. Leclerc, E., Y. Sakai, and T. Fujii, *Microfluidic PDMS (polydimethylsiloxane) bioreactor for large-scale culture of hepatocytes.* Biotechnology Progress, 2004. **20**(3): p. 750-755.
8. El-Ali, J., P.K. Sorger, and K.F. Jensen, *Cells on chips.* Nature, 2006. **442**(7101): p. 403-411.
9. Raja, S.G., et al., *Saphenous vein grafts: to use or not to use?* Heart Lung Circ, 2004. **13**(4): p. 403-9.
10. Suchkov, D.V., et al., *Polarization of the yeast pheromone receptor requires its internalization but not actin-dependent secretion.* Mol Biol Cell, 2010. **21**(10): p. 1737-52.
11. Metodiev, M.V., et al., *Regulation of MAPK function by direct interaction with the mating-specific Galpha in yeast.* Science, 2002. **296**(5572): p. 1483-6.
12. Lemke, G., *Glial control of neuronal development.* Annu Rev Neurosci, 2001. **24**: p. 87-105.
13. Ray, S.M., S.S. Park, and A. Ray, *Pollen tube guidance by the female gametophyte.* Development, 1997. **124**(12): p. 2489-98.
14. Tessier-Lavigne, M. and C.S. Goodman, *The molecular biology of axon guidance.* Science, 1996. **274**(5290): p. 1123-33.
15. Segall, J.E., *Polarization of yeast cells in spatial gradients of alpha mating factor.* Proc Natl Acad Sci U S A, 1993. **90**(18): p. 8332-6.
16. Vallier, L.G., J.E. Segall, and M. Snyder, *The alpha-factor receptor C-terminus is important for mating projection formation and orientation in Saccharomyces cerevisiae.* Cell Motil Cytoskeleton, 2002. **53**(4): p. 251-66.
17. Paliwal, S., et al., *MAPK-mediated bimodal gene expression and adaptive gradient sensing in yeast.* Nature, 2007. **446**(7131): p. 46-51.
18. Moore, T.I., et al., *Robust Spatial Sensing of Mating Pheromone Gradients by Yeast Cells.* Plos One, 2008. **3**(12).
19. Hao, N., et al., *Regulation of cell signaling dynamics by the protein kinase-scaffold Ste5.* Molecular Cell, 2008. **30**(5): p. 649-56.
20. Kim, S., H.J. Kim, and N.L. Jeon, *Biological applications of microfluidic gradient devices.* Integr Biol (Camb), 2010. **2**(11-12): p. 584-603.

21. Jones, E.A., et al., *Dynamic in vivo imaging of postimplantation mammalian embryos using whole embryo culture.* Genesis, 2002. **34**(4): p. 228-35.
22. Tam, P.P.L., *Postimplantation mouse development: whole embryo culture and micro-manipulation.* International Journal of Developmental Biology, 1998. **42**(7): p. 895-902.
23. Tam, P.P. and R.R. Behringer, *Mouse gastrulation: the formation of a mammalian body plan.* Mech Dev, 1997. **68**(1-2): p. 3-25.
24. Oh, K.W. and C.H. Ahn, *A review of microvalves.* Journal of Micromechanics and Microengineering, 2006. **16**(5): p. R13-R39.
25. Gu, W., et al., *Computerized microfluidic cell culture using elastomeric channels and Braille displays.* Proceedings of the National Academy of Sciences of the United States of America, 2004. **101**(45): p. 15861-15866.
26. Weibel, D.B., et al., *Torque-actuated valves for microfluidics.* Analytical Chemistry, 2005. **77**(15): p. 4726-4733.
27. Chou, H.-P., M.A. Unger, and S.R. Quake, *A Microfabricated Rotary Pump.* Biomed Microdevices, 2001. **3**(4): p. 323-330.
28. Hansen, C. and S.R. Quake, *Microfluidics in structural biology: smaller, faster... better.* Current Opinion in Structural Biology, 2003. **13**(5): p. 538-544.
29. Ahn, C.H., et al., *Disposable Smart lab on a chip for point-of-care clinical diagnostics.* Proceedings of the Ieee, 2004. **92**(1): p. 154-173.
30. Godino, N., et al., *Integration of a zero dead-volume PDMS rotary switch valve in a miniaturised (bio)electroanalytical system.* Lab on a Chip, 2010. **10**(14): p. 1841-1847.
31. Beebe, D.J., et al., *Functional hydrogel structures for autonomous flow control inside microfluidic channels.* Nature, 2000. **404**(6778): p. 588-+.
32. Sershen, S.R., et al., *Independent optical control of microfluidic valves formed from optomechanically responsive nanocomposite hydrogels.* Advanced Materials, 2005. **17**(11): p. 1366-+.
33. Markov, D.A., et al., *Tape underlayment rotary-node (TURN) valves for simple on-chip microfluidic flow control.* Biomedical Microdevices, 2010. **12**(1): p. 135-144.
34. Weibel, D.B., et al., *Pumping fluids in microfluidic systems using the elastic deformation of poly(dimethylsiloxane).* Lab on a Chip, 2007. **7**(12): p. 1832-1836.
35. Hulme, S.E., S.S. Shevkoplyas, and G.M. Whitesides, *Incorporation of prefabricated screw, pneumatic, and solenoid valves into microfluidic devices.* Lab on a Chip, 2009. **9**(1): p. 79-86.
36. Lo, J.F., E. Sinkala, and D.T. Eddington, *Oxygen gradients for open well cellular cultures via microfluidic substrates.* Lab on a Chip, 2010. **10**(18): p. 2394-2401.
37. Oppegard, S.C., et al., *Modulating temporal and spatial oxygenation over adherent cellular cultures.* Plos One, 2009. **4**(9): p. e6891.
38. Oppegard, S.C., et al., *Precise control over the oxygen conditions within the Boyden chamber using a microfabricated insert.* Lab on a Chip, 2010. **10**(18): p. 2366-2373.
39. Chow, D.C., et al., *Modeling pO(2) distributions in the bone marrow hematopoietic compartment. I. Krogh's model.* Biophysical Journal, 2001. **81**(2): p. 675-684.
40. Ito, Y., *Surface micropatterning to regulate cell functions.* Biomaterials, 1999. **20**(23-24): p. 2333-2342.
41. Kofoed, H., et al., *Bone-Marrow Circulation after Osteotomy - Blood-Flow, Po2, Pco2, and Pressure Studied in Dogs.* Acta Orthopaedica Scandinavica, 1985. **56**(5): p. 400-403.

42. Joddar, B., et al., *Arterial pO(2) stimulates intimal hyperplasia and serum stimulates inward eutrophic remodeling in porcine saphenous veins cultured ex vivo.* Biomech Model Mechanobiol, 2011. **10**(2): p. 161-75.
43. Fermor, B., et al., *Oxygen, nitric oxide and articular cartilage.* Eur Cell Mater, 2007. **13**: p. 56-65; discussion 65.
44. Cairns, R.A., T. Kalliomaki, and R.P. Hill, *Acute (cyclic) hypoxia enhances spontaneous metastasis of KHT murine tumors.* Cancer Research, 2001. **61**(24): p. 8903-8908.
45. Joyeux-Faure, M., et al., *Chronic intermittent hypoxia increases infarction in the isolated rat heart.* Journal of Applied Physiology, 2005. **98**(5): p. 1691-1696.
46. Grist, S.M., L. Chrostowski, and K.C. Cheung, *Optical Oxygen Sensors for Applications in Microfluidic Cell Culture.* Sensors, 2010. **10**(10): p. 9286-9316.
47. Maxwell, P.H. and P.J. Ratcliffe, *Oxygen sensors and angiogenesis.* Seminars in Cell & Developmental Biology, 2002. **13**(1): p. 29-37.
48. Kim, K.W., et al., *Insulin-like growth factor II induced by hypoxia may contribute to angiogenesis of human hepatocellular carcinoma.* Cancer Research, 1998. **58**(2): p. 348-351.
49. Wang, G.L., et al., *Hypoxia-Inducible Factor-1 Is a Basic-Helix-Loop-Helix-Pas Heterodimer Regulated by Cellular O-2 Tension.* Proceedings of the National Academy of Sciences of the United States of America, 1995. **92**(12): p. 5510-5514.
50. Sowter, H.M., et al., *Predominant role of hypoxia-inducible transcription factor (Hif)-1 alpha versus Hif-2 alpha in regulation of the transcriptional response to hypoxia.* Cancer Research, 2003. **63**(19): p. 6130-6134.
51. Semenza, G.L., *HIF-1 and human disease: one highly involved factor.* Genes & Development, 2000. **14**(16): p. 1983-1991.
52. Carmeliet, P., et al., *Role of HIF-1 alpha in hypoxia-mediated apoptosis, cell proliferation and tumour angiogenesis (vol 394, pg 485, 1998).* Nature, 1998. **395**(6701): p. 525-525.
53. Semenza, G.L., *HIF-1 and tumor progression: pathophysiology and therapeutics.* Trends in Molecular Medicine, 2002. **8**(4): p. S62-S67.
54. Semenza, G.L., *Targeting HIF-1 for cancer therapy.* Nature Reviews Cancer, 2003. **3**(10): p. 721-732.
55. Lo, J.F., et al., *Islet preconditioning via multimodal microfluidic modulation of intermittent hypoxia.* Anal Chem, 2012. **84**(4): p. 1987-93.
56. Gusic, R.J., et al., *Mechanical properties of native and ex vivo remodeled porcine saphenous veins.* J Biomech, 2005. **38**(9): p. 1770-9.
57. Joddar, B., et al., *Protandim attenuates intimal hyperplasia in human saphenous veins cultured ex vivo via a catalase-dependent pathway.* Free Radic Biol Med, 2011. **50**(6): p. 700-9.
58. Risso, A., et al., *Effect of hypoxia/reoxygenation on the contractility of the isolated bovine digital vein.* Res Vet Sci, 2012. **92**(2): p. 299-305.
59. Dospinescu, C., et al., *Hypoxia sensitivity of a voltage-gated potassium current in porcine intrapulmonary vein smooth muscle cells.* Am J Physiol Lung Cell Mol Physiol, 2012. **303**(5): p. L476-86.
60. Kahler, R.L., A. Goldblatt, and E. Braunwald, *The effects of acute hypoxia on the systemic venous and arterial systems and on myocardial contractile force.* J Clin Invest, 1962. **41**: p. 1553-63.
61. Hagen, T., et al., *Redistribution of intracellular oxygen in hypoxia by nitric oxide: Effect on HIF1 alpha.* Science, 2003. **302**(5652): p. 1975-1978.

62. Huang, L.E., et al., *Regulation of hypoxia-inducible factor 1 alpha is mediated by an O-2-dependent degradation domain via the ubiquitin-proteasome pathway.* Proceedings of the National Academy of Sciences of the United States of America, 1998. **95**(14): p. 7987-7992.
63. Lennon, D.P., J.M. Edmison, and A.I. Caplan, *Cultivation of rat marrow-derived mesenchymal stem cells in reduced oxygen tension: Effects on in vitro and in vivo osteochondrogenesis.* Journal of Cellular Physiology, 2001. **187**(3): p. 345-355.
64. Allen, J.W., R.S. Johnson, and S.N. Bhatia, *Oxygen modulation of cytochrome P450 pathways: Role of oxygen gradients and HIF-1alpha in hepatocytes in vitro.* Hepatology, 2003. **38**(4): p. 270a-270a.
65. Lee, H.L.T., et al., *Microbioreactor arrays with integrated mixers and fluid injectors for high-throughput experimentation with pH and dissolved oxygen control.* Lab on a Chip, 2006. **6**(9): p. 1229-1235.
66. Mehta, G., et al., *Quantitative measurement and control of oxygen levels in microfluidic poly(dimethylsiloxane) bioreactors during cell culture.* Biomedical Microdevices, 2007. **9**(2): p. 123-134.
67. Tilles, A.W., et al., *Effects of oxygenation and flow on the viability and function of rat hepatocytes cocultured in a microchannel flat-plate bioreactor.* Biotechnology and Bioengineering, 2001. **73**(5): p. 379-389.
68. Vollmer, A.P., et al., *Development of an integrated microfluidic platform for dynamic oxygen sensing and delivery in a flowing medium.* Lab on a Chip, 2005. **5**(10): p. 1059-1066.
69. Baumgardner, J.E. and C.M. Otto, *In vitro intermittent hypoxia: challenges for creating hypoxia in cell culture.* Respiratory Physiology & Neurobiology, 2003. **136**(2-3): p. 131-139.
70. Nam, K.H. and D.T. Eddington, *Size-Based Separation of Microparticles in a Multilayered Microfluidic Device.* Journal of Microelectromechanical Systems, 2010. **19**(2): p. 375-383.
71. Leclerc, E., Y. Sakai, and T. Fujii, *Cell culture in 3-dimensional microfluidic structure of PDMS (polydimethylsiloxane).* Biomedical Microdevices, 2003. **5**(2): p. 109-114.
72. Wheeler, A.R., et al., *Microfluidic device for single-cell analysis.* Analytical Chemistry, 2003. **75**(14): p. 3581-6.
73. Bohl, B., et al., *Multi-layer SU-8 lift-off technology for microfluidic devices.* Journal of Micromechanics and Microengineering, 2005. **15**(6): p. 1125-1130.
74. Chant, J., *Generation of cell polarity in yeast.* Current Opinion in Cell Biology, 1996. **8**(4): p. 557-565.
75. Toshima, J.Y., et al., *Requirements for recruitment of a G protein-coupled receptor to clathrin-coated pits in budding yeast.* Molecular Biology of the Cell, 2009. **20**(24): p. 5039-50.
76. Lee, S.S., et al., *Quantitative and dynamic assay of single cell chemotaxis.* Integr Biol (Camb), 2012. **4**(4): p. 381-90.
77. Bu, M.Q., et al., *A new masking technology for deep glass etching and its microfluidic application.* Sensors and Actuators a-Physical, 2004. **115**(2-3): p. 476-482.
78. Stjernstrom, M. and J. Roeraade, *Method for fabrication of microfluidic systems in glass.* Journal of Micromechanics and Microengineering, 1998. **8**(1): p. 33-38.
79. Iliescu, C., B.T. Chen, and J. Miao, *On the wet etching of Pyrex glass.* Sensors and Actuators a-Physical, 2008. **143**(1): p. 154-161.
80. Du, W., et al., *SlipChip.* Lab Chip, 2009. **9**(16): p. 2286-92.

81. Li, L., et al., *Dead-end filling of SlipChip evaluated theoretically and experimentally as a function of the surface chemistry and the gap size between the plates for lubricated and dry SlipChips.* Langmuir, 2010. **26**(14): p. 12465-71.
82. Allen, P.B. and D.T. Chiu, *Calcium-assisted glass-to-glass bonding for fabrication of glass microfluidic devices.* Anal Chem, 2008. **80**(18): p. 7153-7.
83. Chantiwas, R., et al., *Simple replication methods for producing nanoslits in thermoplastics and the transport dynamics of double-stranded DNA through these slits.* Lab Chip, 2010. **10**(23): p. 3255-64.
84. Hupert, M.L., et al., *Evaluation of micromilled metal mold masters for the replication of microchip electrophoresis devices.* Microfluidics and Nanofluidics, 2007. **3**(1): p. 1-11.
85. Becker, H. and U. Heim, *Hot embossing as a method for the fabrication of polymer high aspect ratio structures.* Sensors and Actuators a-Physical, 2000. **83**(1-3): p. 130-135.
86. Rotting, O., et al., *Polymer microfabrication technologies.* Microsystem Technologies, 2002. **8**(1): p. 32-36.
87. Brett, M.E., et al., *A microfluidic device that forms and redirects pheromone gradients to study chemotropism in yeast.* Lab Chip, 2012. **12**(17): p. 3127-34.
88. Desai, S.P., D.M. Freeman, and J. Voldman, *Plastic masters-rigid templates for soft lithography.* Lab on a Chip, 2009. **9**(11): p. 1631-1637.
89. Meenakshisundaram, G., et al., *Oxygen sensitivity and biocompatibility of an implantable paramagnetic probe for repeated measurements of tissue oxygenation.* Biomedical Microdevices, 2009. **11**(4): p. 817-826.
90. Duffy, D.C., et al., *Rapid prototyping of microfluidic systems in poly(dimethylsiloxane).* Anal Chem, 1998. **70**(23): p. 4974-4984.
91. Kang, H., et al., *An improved method of preparing composite poly(dimethylsiloxane) moulds.* Nanotechnology, 2006. **17**(1): p. 197-200.
92. Piner, R.D., et al., *"Dip-Pen" nanolithography.* Science, 1999. **283**(5402): p. 661-3.
93. Mittal, N., S. Flavin, and J. Voldman, *Patterning of embryonic stem cells using the bio flip chip.* JoVE, 2007(8).
94. Atencia, J., J. Morrow, and L.E. Locascio, *The microfluidic palette: A diffusive gradient generator with spatio-temporal control.* Lab on a Chip, 2009. **9**(18): p. 2707-2714.
95. Sherman, F., Fink, G.R., Hicks, J.B., *Methods in Yeast Genetics*, 1986, Cold Spring Harbor Laboratory Press: Cold Spring Harbor, NY.
96. Andrews, S.S., et al., *Detailed simulations of cell biology with Smoldyn 2.1.* PLoS Comput Biol, 2010. **6**(3): p. e1000705.
97. Nagatani, H., et al., *Interfacial behavior of sulforhodamine 101 at the polarized water/1,2-dichloroethane interface studied by spectroelectrochemical techniques.* Anal Bioanal Chem, 2006. **386**(3): p. 633-8.
98. Sasaki, H., et al., *Parylene-coating in PDMS microfluidic channels prevents the absorption of fluorescent dyes.* Sensors and Actuators B-Chemical, 2010. **150**(1): p. 478-482.
99. Irimia, D., D.A. Geba, and M. Toner, *Universal microfluidic gradient generator.* Analytical Chemistry, 2006. **78**(10): p. 3472-7.
100. Li, C.W., R.S. Chen, and M.S. Yang, *Generation of linear and non-linear concentration gradients along microfluidic channel by microtunnel controlled stepwise addition of sample solution.* Lab on a Chip, 2007. **7**(10): p. 1371-1373.

101. Lin, F., et al., *Generation of dynamic temporal and spatial concentration gradients using microfluidic devices.* Lab on a Chip, 2004. **4**(3): p. 164-167.
102. Groisman, A., *Generation and Applications of Microfluidic Gradients.* 2010.
103. Arkowitz, R.A., *Chemical Gradients and Chemotropism in Yeast.* Cold Spring Harbor Perspectives in Biology, 2009. **1**(2).
104. Zhu, H.X., et al., *Characterization of deep wet etching of fused silica glass for single cell and optical sensor deposition.* Journal of Micromechanics and Microengineering, 2009. **19**(6).
105. Downs, K.M. and T. Davies, *Staging of Gastrulating Mouse Embryos by Morphological Landmarks in the Dissecting Microscope.* Development, 1993. **118**(4): p. 1255-1266.
106. Snow, M.H.L., *Gastrulation in Mouse - Growth and Regionalization of Epiblast.* Journal of Embryology and Experimental Morphology, 1977. **42**(Dec): p. 293-303.
107. Beddington, R.S.P., *An Autoradiographic Analysis of Tissue Potency in Different Regions of the Embryonic Ectoderm during Gastrulation in the Mouse.* Journal of Embryology and Experimental Morphology, 1982. **69**(Jun): p. 265-285.
108. Lawson, K.A. and R.A. Pedersen, *Cell Fate, Morphogenetic Movement and Population-Kinetics of Embryonic Endoderm at the Time of Germ Layer Formation in the Mouse.* Development, 1987. **101**(3): p. 627-652.
109. Tam, P.P., D.A. Loebel, and S.S. Tanaka, *Building the mouse gastrula: signals, asymmetry and lineages.* Curr Opin Genet Dev, 2006. **16**(4): p. 419-25.
110. Nagy, A., et al., *Manipulating the Mouse Embryo : A Laboratory Manual*2003, Cold Spring Harbor, NY: Cold Spring Harbor Laboratory Press.
111. Rivera-Perez, J.A., V. Jones, and P.P. Tam, *Culture of whole mouse embryos at early postimplantation to organogenesis stages: developmental staging and methods.* Methods Enzymol, 2010. **476**: p. 185-203.
112. Garcia, M.D., et al., *Live imaging of mouse embryos.* Cold Spring Harb Protoc, 2011. **2011**(4): p. pdb top104.
113. Piliszek, A., G.S. Kwon, and A.K. Hadjantonakis, *Ex utero culture and live imaging of mouse embryos.* Methods Mol Biol, 2011. **770**: p. 243-57.
114. Williams, M., et al., *Mouse primitive streak forms in situ by initiation of epithelial to mesenchymal transition without migration of a cell population.* Dev Dyn, 2012. **241**(2): p. 270-83.
115. Suh, R.S., et al., *Rethinking gamete/embryo isolation and culture with microfluidics.* Human Reproduction Update, 2003. **9**(5): p. 451-461.
116. Smith, G.D. and S. Takayama, *Gamete and embryo isolation and culture with microfluidics.* Theriogenology, 2007. **68 Suppl 1**: p. S190-5.
117. Raty, S., et al., *Embryonic development in the mouse is enhanced via microchannel culture.* Lab on a Chip, 2004. **4**(3): p. 186-90.
118. Lucchetta, E.M., M.S. Munson, and R.F. Ismagilov, *Characterization of the local temperature in space and time around a developing Drosophila embryo in a microfluidic device.* Lab on a Chip, 2006. **6**(2): p. 185-190.
119. Heo, Y.S., et al., *Dynamic microfunnel culture enhances mouse embryo development and pregnancy rates.* Hum Reprod, 2010. **25**(3): p. 613-22.
120. Choudhury, D., et al., *Fish and Chips: a microfluidic perfusion platform for monitoring zebrafish development.* Lab on a Chip, 2012. **12**(5): p. 892-900.
121. Ohinata, Y., et al., *A Signaling Principle for the Specification of the Germ Cell Lineage in Mice.* Cell, 2009. **137**(3): p. 571-584.

122. Wilkinson, D.G. and M.A. Nieto, *Detection of messenger RNA by in situ hybridization to tissue sections and whole mounts.* Methods Enzymol, 1993. **225**: p. 361-73.